THE UNIVERSITY OF CHICAGO

FUNCTIONALLY GRADED SEMICONDUCTING POLYMERS AS ORGANIC THERMOELECTRICS

A DISSERTATION SUBMITTED TO

THE FACULTY OF THE PRITZKER SCHOOL OF MOLECULAR ENGINEERING

IN CANDIDACY FOR THE DEGREE OF

DOCTOR OF PHILOSOPHY

BY

TENGZHOU MA

CHICAGO, ILLINOIS

MARCH 2022

TABLE OF CONTENTS

LIST OF FIGURES

LIST OF TABLES

ACKNOWLEDGEMENTS

First and foremost, I would like to thank my Ph.D. advisor Professor Shrayesh N. Patel for his trust and support throughout the whole time of my doctorate study. I feel very grateful for joining Professor Patel's group and being one of his first students. Starting from day one, I have learnt so much from his profound knowledge and enthusiasm in science. Thank you for being an excellent professor and mentor. I would also like to thank Professor Paul F. Nealey, Professor Sihong Wang, Professor Juan de Pablo and Professor Stuart J. Rowan for being on my Defense Committee or Candidacy Committee and supporting me as a candidate. It is a great honor for me to present my work to these excellent scientists.

Next, I would like to thank all current and former members in Patel group. I want to give my special thanks to Garrett Grocke who has been an amazing labmate and generously helping me set up, design and build anything I need, to Dr. Ban Dong who has been an amazing collaborator and patiently helping me in my research. I would like to thank William Kent, Dr. Zhongyang Wang and Killian Tracy for all the valuable discussion and contribution to my research. I would like to thank Mark DiTusa for bringing much joy and fun into the office during the past four years and Dr. Junseop Lee for his encouragement during my early days in UChicago. I also would like to thank Arvin Sookezian, Zijing Xia, Peter Bennington, Veronica Burnett, Priya Mirmira, Hongyi Zhang, Dr. Zhongbo Zhang, Nicholas Boynton and Sam Kopfinger for being incredible colleagues.

I would also like to thank Dr. Philip Griffin at the Soft Matter Characterization Facility in PME and Dr. Justin Juller at the Materials Research Science and Engineering Center for the assistance in the physical characterization. I would like to thank Dr. Joseph Strzalka at the

Advanced Photon Source of the Argonne National Laboratory for the help in X-ray scattering measurements.

Last but not the least, I would like to thank my family. Thank my parents for their unconditional trust and love throughout my life. Without them, I would never become who I am. Thank my wife and my best friend, Xi Chen, for always believing in me and supporting me through ups and downs. This work is dedicated to my family whole-heartedly.

ABSTRACT

With the solution and thermal processability and coupled with the ability to tuning electronic properties through molecular doping, semiconducting conjugated polymers (CPs) have been increasingly explored in enabling organic thermoelectric (TE) for thermal energy harvesting and management. While the effort has been focused on optimizing TE material performance, functionally graded materials (FGMs) where the material properties are spatially controlled have been proven to further improve TE device performance, especially as thermoelectric (Peltier) coolers for thermal energy management and cooling applications. However, the concept of FGMs has not been explored in the context of organic materials.

In this thesis, we aim to enable organic FGMs by leveraging molecularly doped semiconducting CPs through two approaches. The first approach is to spatially control the dopant composition across the film where the first series of organic FG polymer films, i.e., double-segmented and continuously graded thin films are achieved. Specifically, the focus of the Chapter 2 centers around a fundamental understanding of spatial structure-transport properties of molecularly doped poly(2,5-bis(3-alkyl-2-thienyl)thieno[3,2-b]thiophene) (PBTTT) through characterizations of double-segmented thin films. Moreover, Chapter 3 reports on continuously graded thin films relevant to improved thermoelectric (Peltier) cooling. Spatial compositional control of the molecular dopant, F4TCNQ (2,3,5,6-tetrafluoro-7,7,8,8-tetracyanoquinodimethane), in PBTTT yield 1D profiles in electrical conductivity and Seebeck coefficient (σ and α). First principle calculations based on linear Onsager theory and conservation of charge and energy are used to model the cooling performance using the experimentally derived

σ and α spatial profiles. The grading σ and α profiles allow for efficient redistribution of the Joule heating and Peltier cooling effects to improve cooling compared to equivalent uniform films.

For the second route, we utilize the thermal processing to vary the microstructure of polymer films in order to enable the functional gradient. The variation in microstructure is first investigated in uniform poly(dodecyl-quaterthiophene) (PQT) thin films where polymorphs with interdigitated side chains coexist. The interdigitation of side-chain significantly affects the doping efficiency, which leads to a large variation in thermoelectric properties upon vapor doping with F4TCNQ. Chapter 5 follows the work from the previous chapter and realize spatial gradient in σ and α by coupling microstructure change in PQT with molecular doping. The variation in microstructure is achieved by apply a temperature gradient across the polymer film, which is captured directly through IR imaging. The cooling performance of the graded PQT film is predicted to be greater than the uniform equivalent.

Lastly, we look into the $\alpha - \sigma$ relationship of doped thiophene-based polymers by applying Kang-Snyder charge transport model in Chapter 6. This fundamental investigation in modelling $\alpha - \sigma$ relationship of conjugated polymers enables more possibilities of future functional grading designs by precisely tailoring the values and profiles of conductivity and Seebeck coefficient to achieve enhanced device performance in TE applications.

Chapter 1: INTRODUCTION

Semiconducting conjugated polymers (CPs) have demonstrated great potential for low-cost, light-weight, and flexible organic electronic devices such as organic photovoltaics (OPVs), organic light-emitting diodes (OLEDs) and thin film transistors (TFTs).[1–6] The family of such polymers has the advantages in its low weight and solution-processing ability compared to inorganic semiconductors and organic π-conjugated small molecules.[7,8] In addition, the solution processability provides the opportunity to industrial manufacturing of large-area devices such as roll-to-roll processing and printing technologies.[9,10]

One emerging application of semiconducting CPs involves organic thermoelectrics (OTEs), which interconverts heat and electricity.[11,12] Polyacetylene is the simplest and one of the earliest studied conjugated polymer.[13] It was found that polyacetylene could have thermoelectric performance comparable to inorganic materials upon exposure to halogens and other oxidizing agents.[13] However, doped polyacetylene is insoluble in most solvents and has poor stability in ambient condition, which limited the realization of its promise. Therefore, the focus has been shifted to more stable semiconducting CPs, such as poly(3-alkylthiophenes) (P3HT) and poly[2,5-bis(3-tetradecylthiophen-2-yl)thieno[3,2-b]thiophene] (PBTTT).

Molecular doping process is a major approach to improve thermoelectric (TE) properties of semiconducting CPs, which is achieved by the addition of small molecules as dopants into the polymer.[14–17] Sequential doping method where a dopant infiltrates into polymer matrix from solution or vapor phase has been a promising approach to maintains the crystalline order and long-range chain connectivity, which leads to high carrier mobility and thus better electrical

performance.[18–20] There have been studies on charge transport mechanisms in doped CPs to understand the connection between two key properties that define the performance of TE materials, Seebeck coefficient (α) and electrical conductivity (σ). The strategies are to investigate the correlation using charge transport models, which will benefit the design of future polymer – dopant systems, leading to improved TE material performance.

Along with the effect to increase the material properties and performance, the use of functionally graded materials (FGMs) opens up alternative pathway to further enhance the TE device performance. Compared to inorganic materials, semiconducting polymers has the inherent advantage to spatially tune their material properties by leveraging the control of dopant composition as well as polymer microstructure. By utilizing FGMs, it enables more efficient distribution of heat and leads to better TE performance, especially in the case of thermoelectric (Peltier) cooling applications.

The scope of this dissertation will focus on developing organic functionally graded materials as organic thermoelectrics by leveraging molecularly doped semiconducting polymers and investigating the performance of such functionally graded polymer thin films as TE (Peltier) coolers.

1.1 Basic of Thermoelectrics

Thermoelectric (TE) is a technology that interconverts heat and electricity. By definition, thermoelectric effect is the direct conversion between a temperature gradient and electric voltage.[21] TE materials exhibit Seebeck and Peltier effect, which are reversible effect of the same physical process:

1. Seebeck effect, which was found in 1821, disclosed the generation of an electric voltage gradient when a temperature gradient is applied. The temperature gradient serves as a driving force for charge carriers to diffuse from hot end to the cold end, resulting in an electric field across the TE material. Seebeck effect is used for power generation by capturing heat or temperature gradient as a thermoelectric generator (TEG) (Figure 1.1a).
2. Peltier effect was discovered in 1834 which demonstrated the presence of heating or cooling at the junction when an external electric field is applied. This effect can be used for cooling applications as a thermoelectric cooler (TEC), also referring as a Peltier cooler (Figure 1.1b).

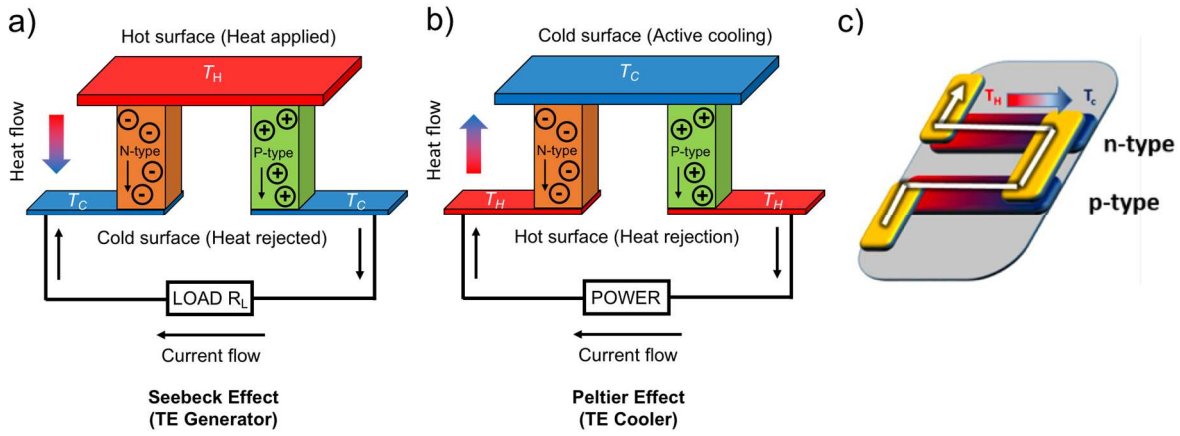

Figure 1.1: Schematic showing the operating principles of TE devices: (a) Seebeck effect for the power generation as TE generator, (b) Peltier effect for the active refrigeration as TE cooler. c) In-plane (printable) TE architecture from Ref. [22].

A thermoelectric device comprises multiple pairs of *n*-type and *p*-type semiconductor legs that are connected thermally in parallel and electrically in series. For a conventional inorganic TE device, it consists of pairs of bulk pellets that are built on the ceramic substrates as demonstrated by the schematics in Figure 1.1. Suggested by this geometry, the thermal/temperature gradient is perpendicular to the substrate. However, this geometry is not suitable for many solution processable organic materials that follows an in-plane architecture. As shown in Figure 1.1c, the

thermal gradient and charge transport direction are both in the plane of the substrate, which benefits the development of alternative fabrication and processing methods to realize more flexible and conformal OTE devices.

The performance of a TE material is characterized by a combination of its thermal and electrical properties, including Seebeck coefficient, electrical conductivity and thermal conductivity.

1 Seebeck coefficient (S), also referred as thermopower (α), is defined as $\alpha = -\Delta V/\Delta T$, and quantifies the induced voltage in response to a temperature gradient across the TE material. Seebeck coefficient can be a positive or negative value, depending on whether the charge carriers are electrons (n-type, negative α) or holes (p-type, positive α). The SI unit of α is volts per kelvin (V/K), but it is more often given in microvolts per kelvin (μV/K)

2 Electrical conductivity, denoted as σ, is the measure of how easily the charge carriers can move within a material. σ is directly proportional to charge carrier concentration, n, and carrier mobility, μ, as $\sigma = ne\mu$, where e is the unit charge (1.602×10^{-19} C). The SI unit of σ is siemens per meter (S/m), although siemens per centimeter (S/cm) is used in this dissertation.

3 Thermal conductivity, κ, measures the ability of heat flux moving across a material. Thermal conductivity consists of two components: $\kappa = \kappa_L + \kappa_e$, where κ_L is lattice contribution, and κ_e is electronic contribution, representing for two heat transport mechanisms: (1) through the crystal lattice vibration, and (2) through the charge carrier transport.[23] The SI unit of κ is watts per meter-kelvin (W/mK).

TE materials performance is characterized by the dimensionless figure of merit, *ZT*, by combining these three material properties at temperature, *T*, through Equation 1.1:

$$ZT = \frac{\alpha^2 \sigma}{\kappa} T \qquad (1.1)$$

A good thermoelectric material should have a high *ZT*, which requires a high α to ensure a large induced voltage and needs to be a good electrical conductor (a high σ), and a poor thermal conductor (a low κ). However, the TE properties are interrelated as functions of carrier concentration, *n*.[24] Seebeck coefficient is related to the density of states of a material, and reflects the average entropy transported per charge carrier. This indicates that α decreases with increasing *n*. Electrical conductivity is directly proportional to *n* and κ also increases with *n*. The key challenge in developing inorganic thermoelectric materials is lowering κ while not sacrificing their electrical transport properties (α and σ). However, in the case of organic materials, the disordered morphology of semiconducting polymers leads to a low lattice contribution of thermal conductivity, and the electronic contribution of the thermal conductivity for polymers is not significant until large electrical conductivities (> 500 S/cm). Therefore, enhancing the power factor value ($PF = \alpha^2 \sigma$) has been recognized as a primary strategy in optimizing the *ZT* value in the case of semiconducting CPs. So far, the organic material with best TE material performance reported has been poly(3,4-ethylenedioxythiophene):poly(styrene sulfonate) (PEDOT:PSS) thin films with a $ZT = 0.75$.[25] For non-PEDOT p-type conjugated polymer, the highest reported *PF* is around 2000 $\mu W/m^1K^2$ for chain aligned PBTTT, which results in a *ZT* of 0.5 based on the thermal conductivity reported.[20] The state of art *PF* and *ZT* values reported for various conjugated polymers are highlighted in Table 1.1.

Overall, the materials properties (α and σ) of semiconducting CPs has strong dependence with molecular design, chemistry of polymers as well as processing approaches such as molecular doping and structure control. The effect on charge transport in CPs and TE properties of molecularly doped polymers are discussed in the following section.

Table 1.1: State-of-the-art thermoelectric performance among the organic material candidates.

Material	Type	Dopant or counterion	α (μV/K)	σ (S/cm)	PF ($\mu W/m^1K^2$)	κ (W/mK)	ZT	Ref.
PA	p	I_2	28.4	1.1×10^5	896	0.7	0.38	[26]
PEDOT	p	Tos	~200	~80	324	0.37	0.25	[27]
PEDOT	p	PSS	~65	~1600	754	0.3	0.75	[25]
P3HT	p	$FeCl_3$	5.4	570	21			[20]
PBTTT	p	$FeCl_3$	9.4	2.2×10^5	1944	1.2	0.5	[20]
Poly[K_x(Ni-ett)]	n		-151.7	63.1	145	0.31	0.2*	[28]

*ZT at 450 K

1.2 Molecular Doping of Semiconducting Polymers

Semiconducting polymers possess alternating single and double carbon-carbon bonds along the polymer backbone (referred as conjugated backbone), which contains delocalized π and π* symmetry molecular orbitals serving as valence and conduction bands. The electrons in the unoccupied p-orbitals are mobile and can transport along the conjugated backbone. The energy gap between the highest occupied molecular orbital (HOMO) and the lowest unoccupied molecular orbital (LUMO) is called the band gap, which can be modified by varying the conformation and synthetic architecture of polymers. A range of semiconducting conjugated polymers are shown in Figure 1.2. Side chains are usually added onto the conjugated backbones to improve the solubility

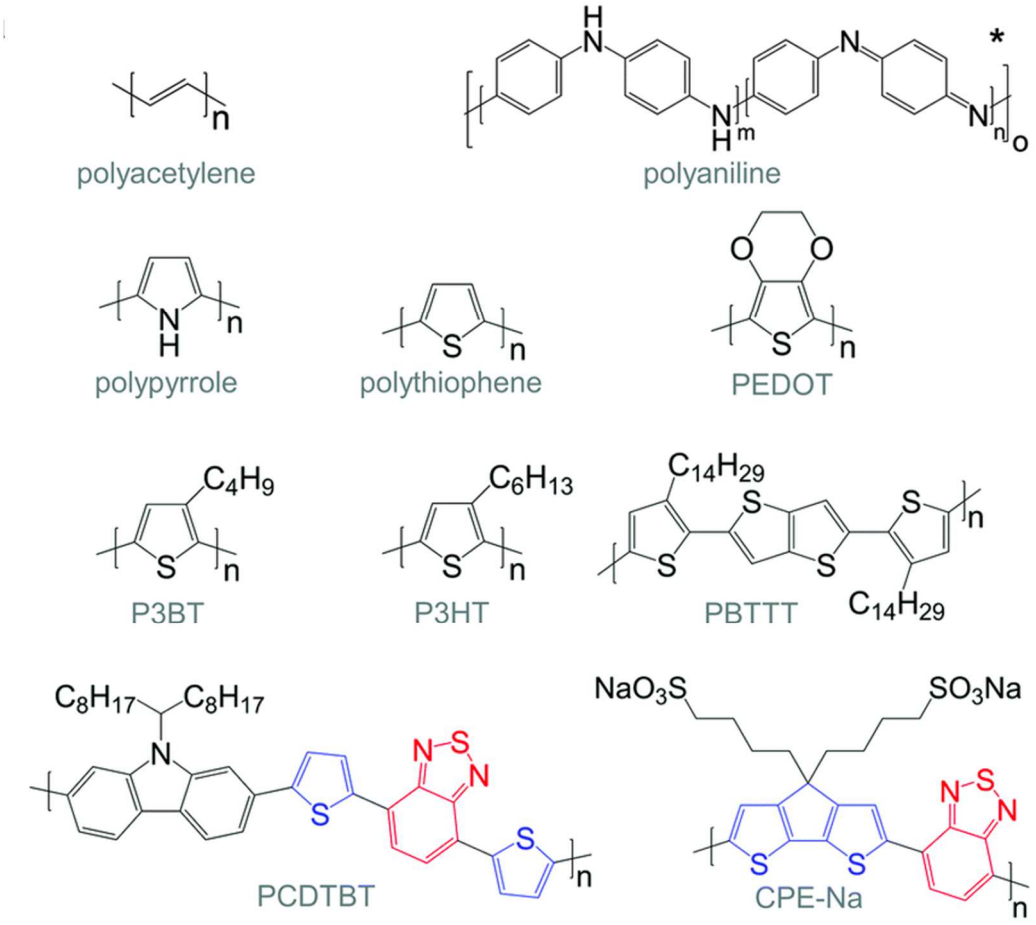

Figure 1.2: Chemical structures of conjugated polymers from Ref. [29]. For the donor–acceptor architectures, donor and acceptor moieties are indicated in blue and red, respectively.

of such polymers in organic solvent as well as lower the melting point to enhance processability. Semiconducting CPs with alkyl side chains, such as P3HT, poly[bis(3-dodecyl-2-thienyl)-2,2'-dithiophene-5,5'-diyl] (PQT) and PBTTT, have been widely investigated as organic thermoelectric materials in literatures. The addition of side chains to the polymer backbone helps control the molecular packing and thus electronic transport in semiconducting CPs. The electronic transport in CPs is highly anisotropic and depends on the transport direction. The fastest transport occurs along the conjugated backbones. The π-π stacks that arises from electronic interaction between planar backbones also facilitate electron transport through interchain hopping. The transport along the insulting alkyl side chains or lamellar stacking direction is inhibited.

However, just conjugation is not enough to enable conjugated polymers as TE applications as the pristine state of CP is still insulating. For example, the σ of pristine state P3HT is at the order of 10^{-5} S/cm. Therefore, additional charge carriers need to be introduced into polymers in the form of holes or electrons. This process is known as 'doping', which was first proposed by Heeger, MacDiarmid and Shirakawa in 1977 when they introduced halogen vapor to oxidize polyacetylene and improve the conductivity over 100 times.[13,30] This discovery on enhancing conductivity of CPs opened up the possibility of leveraging doped conjugated polymers as thermoelectric applications. Since then, researchers have investigated on the doping process of semiconducting CPs, including molecular design of host polymers and dopants, appropriate doping methods development, understanding of doping mechanism and optimization of TE properties of molecularly doped polymers (Figure 1.3).

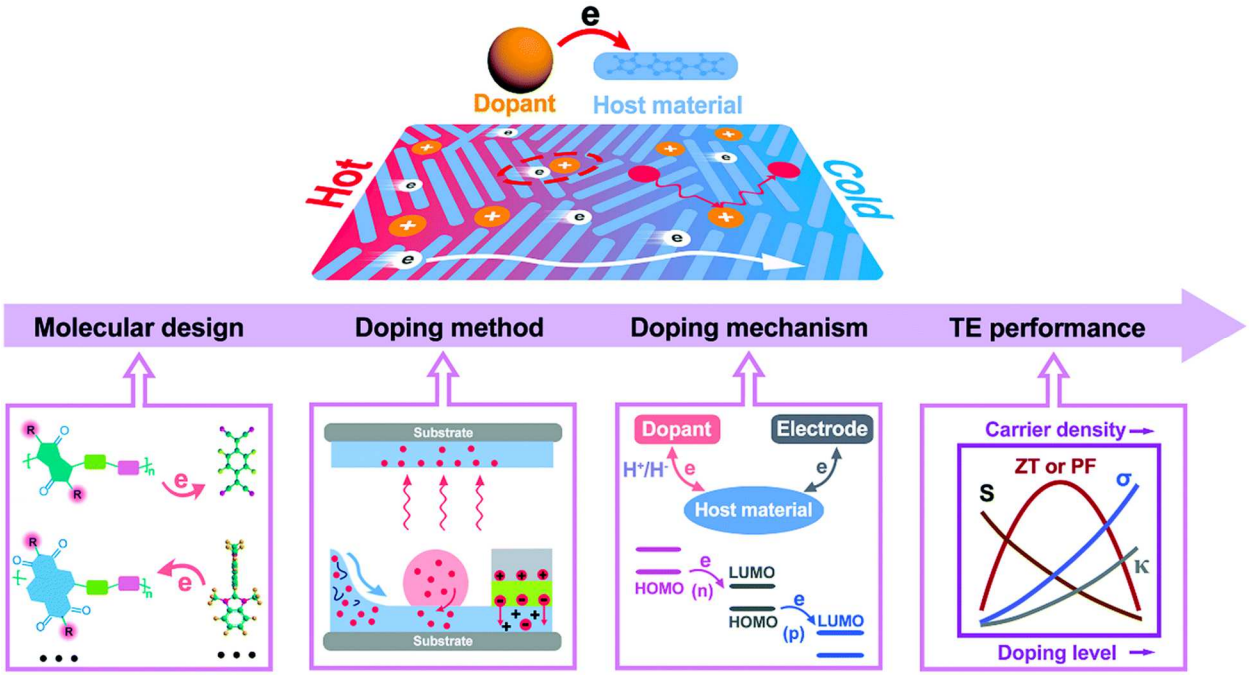

Figure 1.3: The schematic illustration of doping engineering in semiconducting conjugated polymers toward TE applications from Ref. [14].

The doping process is accomplished by introducing a dopant as either an oxidizing (*p*-type doping) or reducing (*n*-type doping) agent into the polymer.[14–17] It is challenging to synthesize and design *n*-type dopants due to their instability under ambient condition. In this thesis, I focus on p-type doping of semiconducting polymers using a common *p*-type dopant, 2,3,5,6-tetrafluoro-7,7,8,8-tetracyanoquinodimethane (F4TCNQ) and its fluorinated-derivatives. In general, the p-type doping process is energetically favorable when the HOMO level of the semiconducting polymer is higher than the LUMO level of the dopant, as shown in Figure 1.3. This energy gap enables the charge transfer, i.e., the electron transfer from HOMO level of the polymer to the LUMO level of the dopant, leaving behind the positively charged carriers, polaron (holes), in the semiconducting polymer. The molecular structures and LUMO levels of some *p*-type dopants are shown in Figure 1.4. The dopant molecule extracts the electron and becomes negatively charged

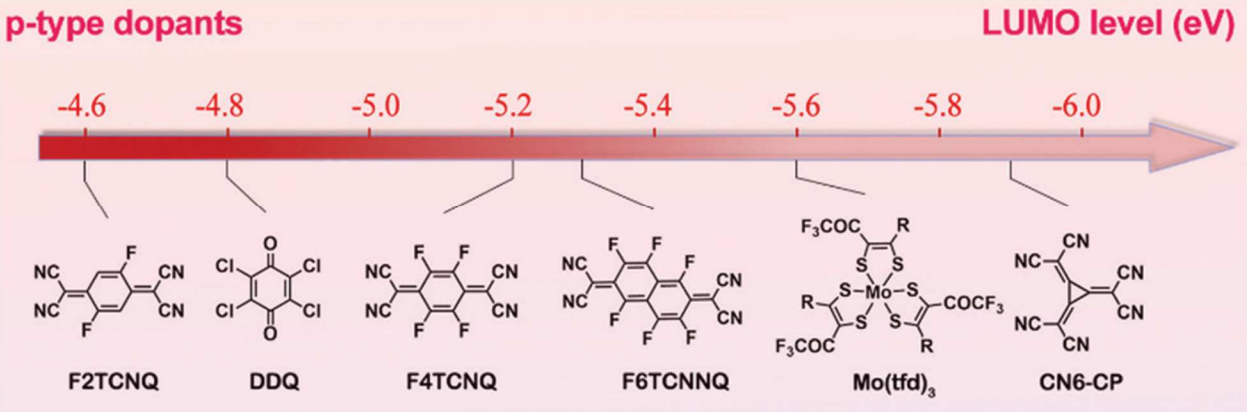

Figure 1.4: Molecular structures and corresponding LUMO levels of *p*-type dopants from Ref. [14].

anion. When the extent of doping, i.e., the ratio of dopant molecule to polymer monomer, is larger enough, two polarons can be pair up to form a bipolaron, which is a +2 positively charged species.[31,32] It is worth noting that at initial stage of doping, i.e., the ratio of dopant to polymer monomer is small, dianion could be formed when the energy level of dopant anion is still lower or approaching the HOMO level of the polymer.[33]

However, unlike inorganic semiconductor materials that have crystalline structures, the pristine polymers already possess a semicrystalline microstructure where the ordered (aggregates) and disordered (amorphous) regions coexist. The polymer chains form amorphous regions outside of the crystallites, which leads to electronic disorder. Specifically, the reduced conjugation length of amorphous parts leads to a broader band gap compared to the order region, resulting in lower carrier mobility and prohibiting transport from aggregates to amorphous regions. It is shown that the charge carriers can only move across the amorphous regions via single polymer chains referred as tie chains.[34,35] Upon doping, the dopants infiltrate into the polymer matrix, affecting the solid-state structure as well as the processability of the polymer.[17] The generated charge carriers are delocalized along the backbone, which stiffen the polymer chains.[36,37] Therefore, the processing and doping methods used will have strong effect on the film microstructure and thus the thermoelectric properties of semiconducting polymers.

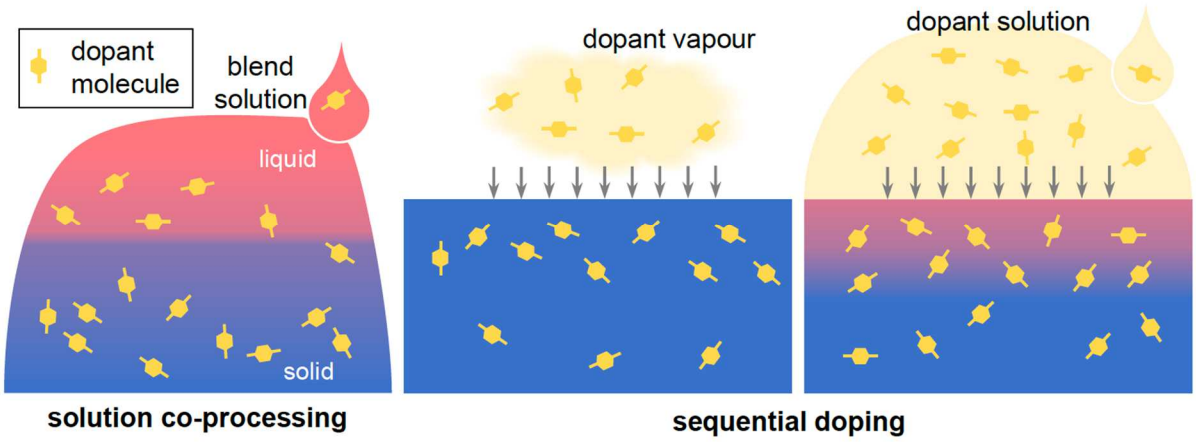

Figure 1.5: Schematic of solution co-processing (left) and sequential doping by dopant vapor (middle) and solution (right) from Ref. [46].

In general, there are two approaches to introduce dopant molecules into the polymer matrix (Figure 1.5). The first one, known as solution mixing method, dissolves the polymer and dopant

in the same solvent and cast the doped film from the solution mixtures. This approach takes advantage of solution processability and precise control of amount of dopant input. However, the resulting polymer and film morphology is hard to control due to the formation of charged polymers, leading to precipitation or aggregation. This undesirable microstructure often results in limited materials performance, e.g. low conductivity values.[38,39] An alternative approach to overcome these problems is the sequential doping method where the dopant can be infiltrated into the polymer matrix through an orthogonal solvent or from the vapor phase.[19,39–45] Through sequential doping, the polymer morphology is being preserved as nanostructure formation is controlled before the dopant infiltration, which leads to better electrical properties. Patel et al. has shown that sequentially doped PBTTT thin films by F4TCNQ leads to a *PF* of *c.a.* 120 $\mu Wm^{-1}K^{-2}$, which is over two orders of magnitude higher than a PBTTT thin film doped through solution mixing approach.[41] More recently, Brinkmann and co-workers have presented a record *PF* of around 2000 $\mu Wm^{-1}K^{-2}$ for solution processable semiconducting polymers by sequentially doping of a chain aligned PBTTT.[20] Sequential vapor doping method is applied for all studies in this thesis.

1.3 Charge Transport Models

By compiling extensive molecularly doped semiconducting polymer studies from the past literature, there have been fundamental research on thermoelectric properties of such polymers, particularly in the context of understanding the correlation between α and σ by investigating charge transport mechanisms.[23,47–58] Two models pioneered by Mott were first used to describe the transport in polymer semiconductors.[49,50,53] The variable hopping model represents carriers hopping between localized states and yields a Seebeck coefficient on the order of 10 μV/K, which is much smaller than the actual values for doped polymers. Mott's mobility edge model is characterized by a mobility edge above which the charge carriers are mobile. However, this model

also fails to predict the α - σ relation compared to experimental observations as it only takes account the mobile free charge carriers. Later on, Glaudell et al. presented an empirical relation as shown as dashed line in Figure 1.6a where $\alpha \sim \sigma^{-1/4}$ by compiling series studies of doped thiophene-based polymers.[23] This correlation fitted well for two very different doping methods in their study (solution mixing and sequential vapor doping), suggesting the TE properties are dominated primarily by the polymer:dopant system, rather than the doping mechanism. However, the authors did not specify the physical explanation for this empirical relationship.

More recently, there have been increasing interests in utilizing the charge transport model proposed by Kang and Snyder (referred as Kang-Snyder model) to study α - σ relation and understand the charge transport mechanism of conducting and semiconducting polymers (Figure 1.6c).[47,52,54,55] The Kang-Snyder model takes into account both mobile charge carriers and carriers in the localized states by introducing a transport edge, E_t. Unlike the mobility edge in Mott's transport model, E_t does not limit on metal-like free carrier transport above the edge but it still accounts for hopping transport between localized states.[47] This model has two characteristic parameter: s is an energy dependent parameter, which is related to energetic disorder nature of polymers and determine the shape of the α-σ curve (Figure 1.6b) and σ_{E0} is called the transport coefficient, which is independent with energy. The value of σ_{E0} reflects the magnitude of electrical conductivity and serves as a weighted carrier mobility, which affects the horizontal position of the α-σ curve as shown in bottom graph of Figure 1.6b. By applying the Kang-Snyder model, past literatures including my own research have found good fits with the α - σ relationship of semiconducting conjugated polymers over a significant range of σ from 10^{-6} S/cm to 10^{3} S/cm. More detailed charge transport study on specific conjugated polymer with polar side chains using Kang-Snyder model can be found in Chapter 6 of this dissertation.

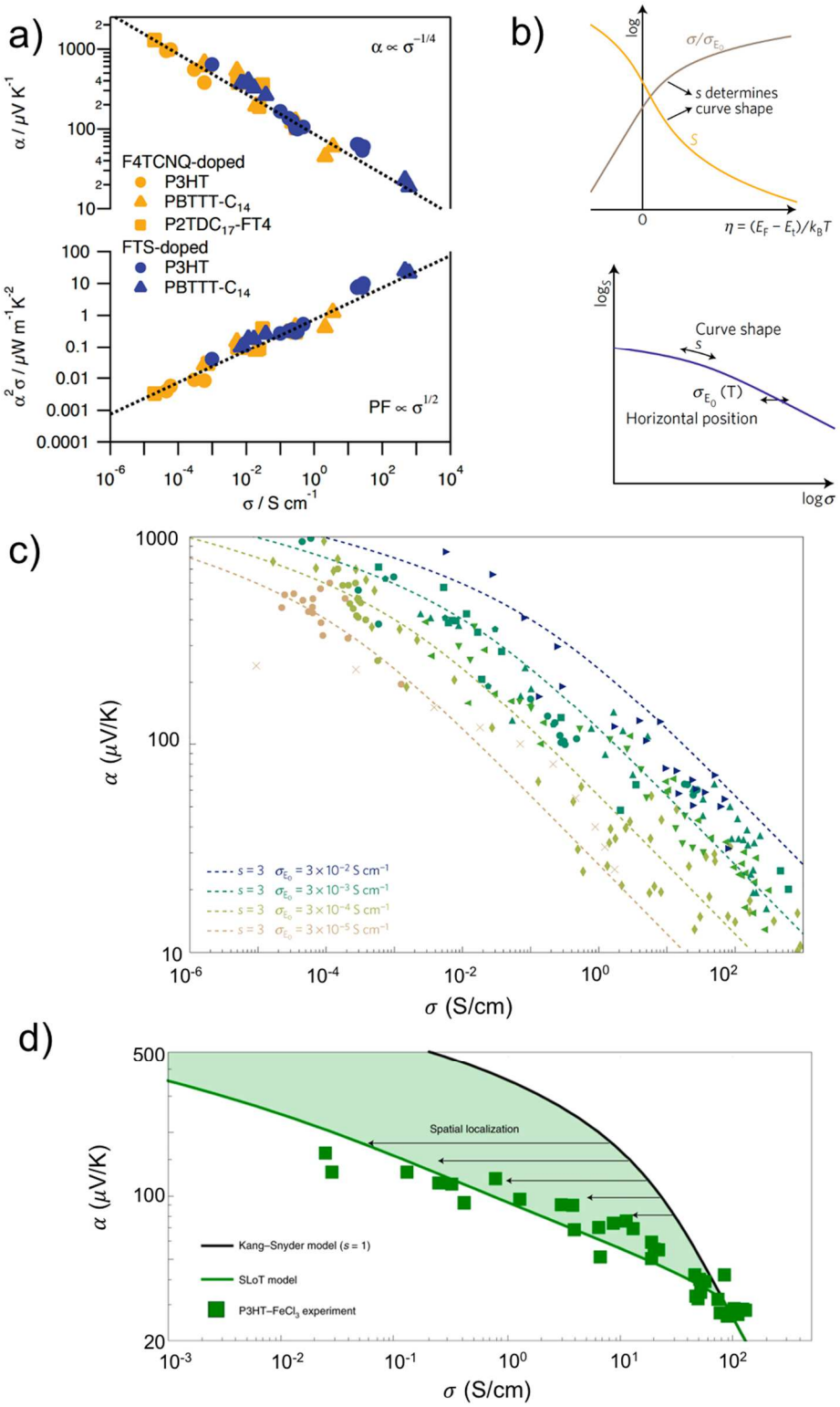

Figure 1.6: (a) Seebeck coefficient (top) and *PF* (bottom) as a function of electrical conductivity for F4TCNQ-doped polymers (yellow) and FTS-doped polymers (blue) from Ref. [23]. The

Figure 1.6 continued: dashed lines indicate an empirical fit of α proportional to $\sigma^{-1/4}$ and *PF* proportional to $\sigma^{1/2}$ (b) Top: The measured electrical conductivity (normalized byσ_{E0}) and Seebeck coefficient will depend on the reduced chemical potential η as described with the model curve. The curve shape depends only on the transport parameter *s*. Bottom: The Seebeck coefficient versus conductivity relation obtained by eliminating the parameter η in top graph. The curve has only two fitting parameters: s determines the curve shape and the transport coefficient σ_{E0} determines the magnitude of the conductivity. (c) Compilation of literature data showing the range of σ_{E0} values found in polymer semiconductors. The dashed lines are obtained with the Kang-Snyder *s* = 3 model.[47] (d) α - σ plot showing that a nominal *s* = 1 Kang–Snyder model (black line) cannot explain the P3HT–$FeCl_3$ experimental data (green squares, each data point representing a unique sample measurement). The SLoT model (green line) accounts for a localization energy that decreases with increasing carrier concentration.[51]

In addition, there are other studies on understanding charge transport in semiconducting polymers. Built upon Kang-Snyder model, Gregory et al. have proposed a semi-localized transport (SLoT) model where they modified the transport coefficient, σ_{E0} as a function of both temperature and carrier concentration.[51] The SLoT model captures a large spectrum of transport in polymers and emphasizes the localized to delocalized transition, which helps tailor thermoelectric properties of molecularly doped polymers more accurately (Figure 1.6d). Moreover, the charge transport mechanisms in doped semiconducting CPs have been examined with respect to the homogeneity of dopant distribution[48] as well as the paracrystallinity[56] in polymers. Both studies simulated the relation between the degree of disorder and the density of states and highlighted the importance of controlling dopant distribution and degree of disorder for high performing organic TE, motivating further investigations on the role of polymer-dopants interaction on thermoelectric properties of molecularly doped semiconducting polymers.

Going forward, the fundamental studies on charge transport relationship in doped semiconducting polymer will lead to strategies towards proper polymer and dopant systems that balance the correlation between TE properties, and thus ultimate PF and ZT for better TE material performance.

So far, there have been numerous studies on uniform polymer films to optimize material performance by understanding the fundamentals of processing-structure-properties relationship of semiconducting CPs. Researchers have investigated various processing methods to achieve diverse polymer morphologies. Coupled with the benefit of structural control, molecular doping is also applied to modulate carrier concentration in the polymer film to improve thermoelectric properties and thus material performance (*ZT* or *PF*). In addition to increasing TE material properties, new architecture designs of TE modules offer alternative pathway to realize and enhance their TE performance. In particular, the ease in solution and thermal processability of semiconducting CPs enables spatial control of TE properties across the length of the polymer films, e.g. formation of gradients in dopant composition or polymer microstructure. Materials with such graded configurations are known as functionally graded materials (FGMs). To date, FGMs as thermoelectric have been studied exclusively in the context of inorganic materials and proved to improve the TE device performance compared to their uniform/homogenous counterpart, which will be discussed in more details in the following section. The approaches to achieve FGMs by leveraging molecularly doped semiconducting CPs are potentially easier than in inorganic materials and will be the major focus of my thesis work.

1.4 Functionally Graded Materials as Thermoelectrics

1.4.1 Functionally Graded Materials Concept

The concept of functionally graded material (FGM) has been proposed to achieve favorable gradients in chemical, magnetic, mechanical, thermal and electrical properties, which results from gradually tuning the composition, microstructure or pore size/porosity spatially across the volume of a material.[59] FGMs are inhomogeneous materials that are designed as segmented or

continuously graded structures, depending on the areas of application and with the aim of performing specific functions.[60–63] Functionally graded materials are utilized in variety of industries and have demonstrated great potential in other emerging applications. Currently, FGMs are being applied in the areas including automobile, aerospace, biomedical, electronic/electrical and energy applications.[59,64–68]

Of particular interest in the field of thermoelectric, there has been significant effort to enhance the performance of single-phase/homogeneous TE materials. Along with the efforts to improve the material performance (i.e. *ZT* and *PF*), introducing FGMs provides alternative pathways to further improve the TE device performance as well as overcome some of the difficulties associated with homogenous materials.[69–71] Essentially, TE materials possess strong temperature-dependent material properties (α and σ), which leads to operation issue that device with homogeneous material can only operate efficiently over a limited temperature range. This is due to the variation in *ZT* values over temperature. Therefore, the position-dependent TE properties ($\alpha(x)$, $\sigma(x)$ and $\kappa(x)$) needs to be taken into account when working with TE devices over a wide temperature range to achieve local optimization of TE performance.

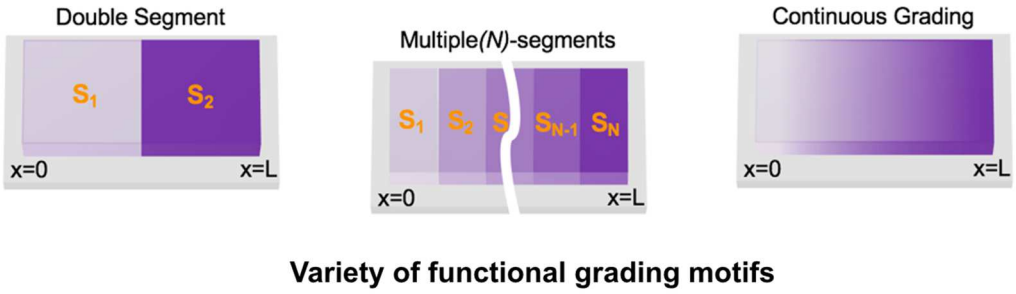

Figure 1.7: Configurations of Functionally Graded Materials

FGMs for TE can be classified as segmented structures (e.g. staging, segmentation or cascading) or continuously graded structure along the operation gradient (Figure 1.7). Major types

of FGMs includes material species graded, dopant concentration graded, composition graded, and microstructure graded. Throughout the years, researches have been carried out to realize functionally graded motifs based on inorganic materials by leveraging proper material selection, joining technology and fabrication methods.[61,63,72,73] However, fabrication and processing of inorganic materials require high pressure and temperature, which could prevent such materials from being candidates in achieving appropriate segmented or gradient configurations.[63,74–78] Instead, most research has been focused on the theoretical modeling and simulation with conventional inorganic TE materials to elaborate optimal gradients in TE properties and establish the theoretical limits of TE performance.[79–86] Simulation works based on inorganic material database as well as fabrication process on inorganic FGMs as TE devices will be further discussed in the following section.

1.4.2 Studies on Functionally Graded Materials as TE Applications

Theoretical studies of functionally graded TE materials and devices aims to provide guidelines for optimal graded configuration of TE materials which results in optimum device operation.[79–82,86–93] Specifically, FGMs has been implemented in thermoelectric cooling applications by leveraging inorganic TE materials. In principle, the heat is absorbed from the environment at the cold side of a TEC and transferred to the hot side by charge carrier diffusion. The absorbed heat has three contributions, the Peltier cooling effect, which removes heat from the cold side, the Joule heating that uniformly heats the material, and the thermal conduction that transports heat from the hot side to the cold side. The functional gradient in TE properties leads to more effective redistribution of Joule heating and Peltier cooling effects, which enables larger cooling temperatures, resulting in better device coefficient of performance (*C.O.P.*) of compared to single or homogeneous TEC.[79,87,88] It is worth noting that, in most of the theoretical studies, the

TE device is consider as an ideal device with no thermal losses and no contact resistance. In addition, one dimensional transport is adapted, indicating the heat flux and electrical current are parallel to each other. For simplicity, previous studies normally considered a TE leg as a single-element TE device with fixed length and cross-sectional area to investigate the functional grading strategies by following the linear Onsager theory.[94] More detailed analysis and derivation can be found in Chapter 3, Chapter 5 and in the literatures.[82,86,87,93] Based on different boundary conditions and varying profiles of material properties, temperature gradient across the TE device, *T(x)*, and *C.O.P.* of the device can be determined, leading to evaluation of TE performance.

Theoretical and numerical studies on FGMs have been carried out since 1990s to investigate the design and performance of such materials in TE applications. Back in 1991, Mahan proposed the idea of inhomogeneous thermoelectrics where the material properties (α, σ and κ) were continuously varied throughout the length of a TE device. The *C.O.P.* of inhomogeneous profile was calculated to be higher than its homogeneous equivalent.[89] Muller and his coworkers have conducted a series of studies on probing local optimal composition and property profiles for FGMs as thermoelectrics and also developed a finite element script to numerically solve the temperature profiles and TE device performance of FGMs.[82,86,87,90–93] Through modelling, Muller et al. have demonstrated the 3D plot of *C.O.P.* of a continuously graded TE element as a function of current density and the cold side temperature (Figure 1.8a) and also shown the improvement in cooling temperature of the continuously graded profile compared to uniform equivalent (Figure 1.8b). Moreover, there are studies that focused on designated TE property profiles where analytical solution can be modeled. Bian, Shakouri and coworkers have proposed specific $\alpha(x)$ and $\sigma(x)$ profiles as shown in Figure 1.8c with power factor, $PF = \alpha(x)^2\sigma(x) = C$ remaining constant as well as constant thermal conductivity, where they calculated that the maximum cooling performance of

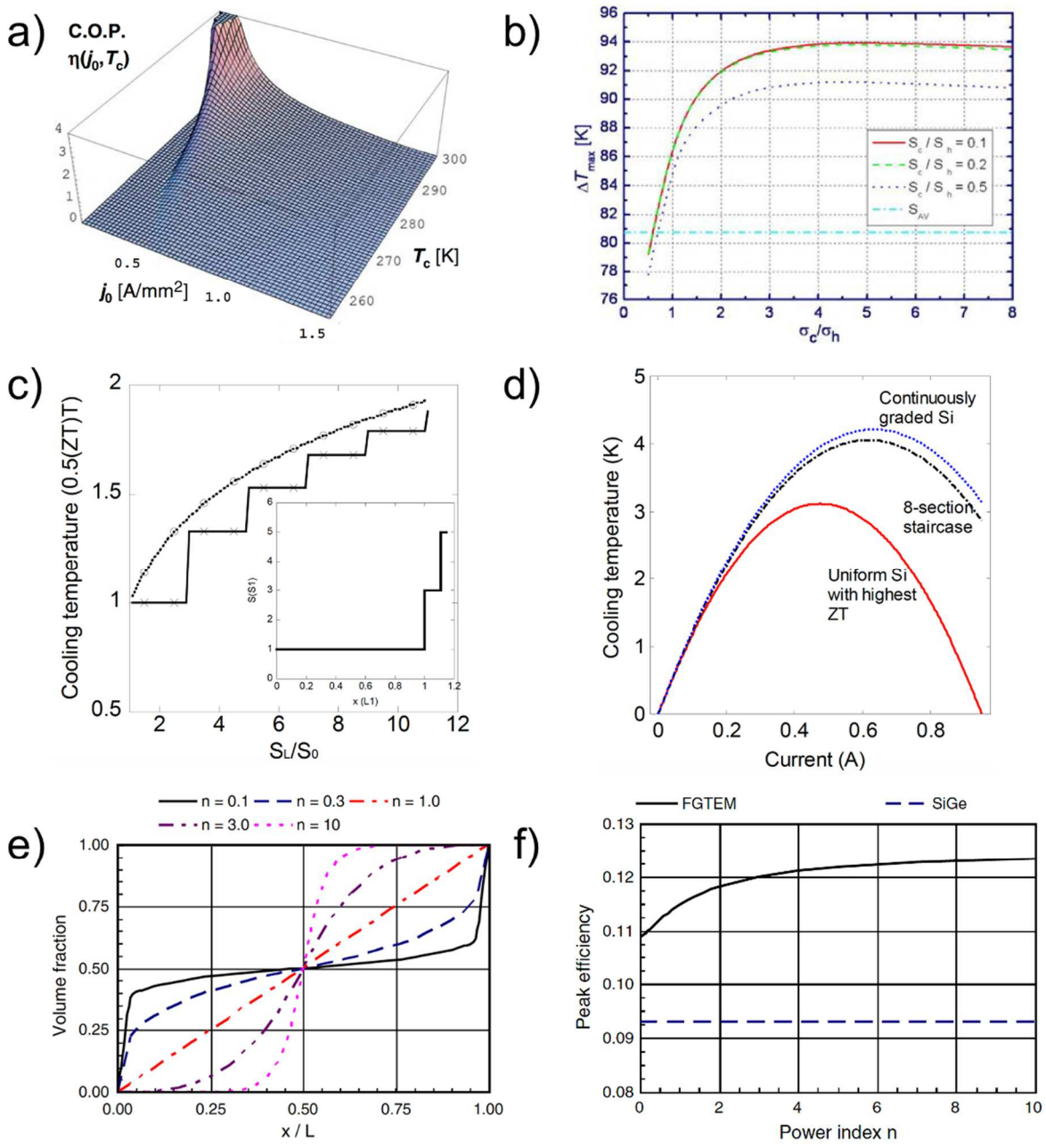

Figure 1.8: Examples of theoretical studies on FGMs enhancing TE performance. (a) C.O.P. of a continuously graded element at T_h = 300 K as a function of current density and the cold side temperature. The material properties: σ = 650 S/cm, κ = 1.35 W/(m K) with a linear profile of the Seebeck coefficient as ⟨S⟩ = 157.5 μV/K and the ratio S_c/S_h = 0.5. (b) Cooling temperature of a continuously graded element. Material parameters: ⟨S⟩ = 180 μV/K, ⟨σ⟩ = 1400 $(\Omega\ cm)^{-1}$, κ = 1.35 W/(m K), independently of temperature. (a) and (b) from Ref. [86] (c) Cooling enhancement of staircase Seebeck profile (x) and the continuously graded material (○). Inset shows the Seebeck profile of the staircase configuration as a function of distance. (d) The cooling curves of the uniform Silicon with the largest ZT, and the average of 8-section profiles

Figure 1.8 continued: and the continuously graded material according to its linear fitting. (c) and (d) from Ref. [79] (e) Sigmoid gradation profiles. (f) Peak efficiency versus the property gradation parameter (power index) for a PbTb–SiGe graded nanocomposite. (e) and (f) from Ref. [97]

graded (both segmented and continuously graded) profiles is always greater than uniform materials (Figure 1.8d).[79,80,88] Zabrocki et al presented the modelling with a linear continuous gradient in α and κ but constant σ and observed the enhancement in power output.[95] Jin et al investigated the effect of exponential gradients in α, σ and κ on the TEG efficiency and reported an improvement of 30% in efficiency when the material properties gradients are selected so that the value of *ZT* increases towards the hot end of the device.[96] Following the previous work, Jin and Wallace also reported on the enhancement of sigmoid property gradients (profiles as in Figure 1.8e) on the performance of functionally graded TE device.[97] They have proved that the device efficiency of FG thermoelectric are always higher than the homogeneous one over the power index of the sigmoid function ranging from 0.01 to 10.0 as shown in Figure 1.8f.

In parallel to theoretical studies, there have been efforts on achieving segmented or continuously graded TE materials through fabrication and processing methods of inorganic materials over the past two decades. Kuznetsov et al. has developed a Bi_2Te_3-based FGM by control the dopant gradient across the TE leg and observed an increase in energy conversion efficiency from 8.8% to over 10% under operation temperature gradient.[98] Muller et al achieved a five-layer segmented TE material by doping iron disilicide with aluminum, cobalt or manganese. The segmented FGM was fabricated by hot pressing powder mixtures of doped and non-doped $FeSi_2$ at specific weight ratios.[75] In 2014, an *n*-type FGM based on phase-separated matrix of $(Pb_{0.95}Sn_{0.05}Te)_{0.92}(PbS)_{0.08}$ was developed by Hazan et al., where they applied simultaneous hot pressing coupled with PbI_2 doping at two different compositions.[74] By finite element simulation, the authors have observed enhanced device efficiency of FGM compared to both non-graded doped

materials. In 2016, Li et al. has proposed a one-step spark plasma sintering method to fabricate both *n*-type and *p*-type segmented TE legs based on Bi_2Te_3.[99] They found in the study that interfacial resistance between each segments has a significant effect on the overall electrical resistance of the TE legs and would result in a depression in the actual power output and device efficiency.

Overall, the fabrication of inorganic materials requires high temperature (~1000 K) and pressure (~50 MPa), which could prohibit the functional grading designs. In contrast, organic materials, especially semiconducting polymers which possess good solution processability, are better candidates to explore variety functionally graded motifs. Compositional gradient can be achieved by spatial control of doping process while thermal processing enables the gradient in polymer microstructure. To best of our knowledge, the principles of functional grading have not been explored for organic thermoelectric materials. Our goal is to develop organic functionally graded materials that can be used in TE applications through a single uniform material by leveraging molecularly doped semiconducting polymers. In this dissertation, I aim to investigate on different forms of functionally graded polymer thin films achieved by two approaches: 1. Control of molecular dopant composition and 2. Control of polymer microstructure.

1.5 References

(1) Knopfmacher, O.; Hammock, M. L.; Appleton, A. L.; Schwartz, G.; Mei, J.; Lei, T.; Pei, J.; Bao, Z. Highly Stable Organic Polymer Field-Effect Transistor Sensor for Selective Detection in the Marine Environment. *Nat. Commun.* **2014**, *5*, 2954.

(2) Chen, C. C.; Chang, W. H.; Yoshimura, K.; Ohya, K.; You, J.; Gao, J.; Hong, Z.; Yang, Y. An Efficient Triple-Junction Polymer Solar Cell Having a Power Conversion Efficiency Exceeding 11%. *Adv. Mater.* **2014**, *26* (32), 5670–5677.

(3) Kaltenbrunner, M.; Sekitani, T.; Reeder, J.; Yokota, T.; Kuribara, K.; Tokuhara, T.; Drack, M.; Schwödiauer, R.; Graz, I.; Bauer-Gogonea, S.; Bauer, S.; Someya, T. An Ultra-Lightweight Design for Imperceptible Plastic Electronics. *Nature* **2013**, *499* (7459), 458–463.

(4) White, M. S.; Kaltenbrunner, M.; Głowacki, E. D.; Gutnichenko, K.; Kettlgruber, G.; Graz, I.; Aazou, S.; Ulbricht, C.; Egbe, D. A. M.; Miron, M. C.; Major, Z.; Scharber, M. C.; Sekitani, T.; Someya, T.; Bauer, S.; Sariciftci, N. S. Ultrathin, Highly Flexible and Stretchable PLEDs. *Nat. Photonics* **2013**, *7* (10), 811–816.

(5) Sirringhaus, H. *25th Anniversary Article: Organic Field-Effect Transistors: The Path beyond Amorphous Silicon*. *Advanced Materials*. March 2014, pp 1319–1335.

(6) Li, Y.; Tatum, W. K.; Onorato, J. W.; Zhang, Y.; Luscombe, C. K. Low Elastic Modulus and High Charge Mobility of Low-Crystallinity Indacenodithiophene-Based Semiconducting Polymers for Potential Applications in Stretchable Electronics. *Macromolecules* **2018**, *51* (16), 6352–6358.

(7) Heeger, A. J. Semiconducting and Metallic Polymers: The Fourth Generation of Polymeric Materials. *Curr. Appl. Phys.* **2001**, *1* (4–5), 247–267.

(8) Wang, H.; Xu, Y.; Yu, X.; Xing, R.; Liu, J.; Han, Y. *Structure and Morphology Control in Thin Films of Conjugated Polymers for an Improved Charge Transport*; 2013; Vol. 5.

(9) Yue, W.; Larsen-Olsen, T. T.; Hu, X.; Shi, M.; Chen, H.; Hinge, M.; Fojan, P.; Krebs, F. C.; Yu, D. Synthesis and Photovoltaic Properties from Inverted Geometry Cells and Roll-to-Roll Coated Large Area Cells from Dithienopyrrole-Based Donor–Acceptor Polymers. *J. Mater. Chem. A* **2013**, *1* (5), 1785–1793.

(10) Krebs, F. C. Polymer Solar Cell Modules Prepared Using Roll-to-Roll Methods: Knife-over-Edge Coating, Slot-Die Coating and Screen Printing. *Sol. Energy Mater. Sol. Cells* **2009**, *93* (4), 465–475.

(11) Russ, B.; Glaudell, A.; Urban, J. J.; Chabinyc, M. L.; Segalman, R. A. Organic Thermoelectric Materials for Energy Harvesting and Temperature Control. *Nat. Rev. Mater.* **2016**, *1* (10), 16050.

(12) Cowen, L. M.; Atoyo, J.; Carnie, M. J.; Baran, D.; Schroeder, B. C. Review—Organic Materials for Thermoelectric Energy Generation. *ECS J. Solid State Sci. Technol.* **2017**, *6*

(3), N3080–N3088.

(13) Chiang, C. K.; Fincher, C. R.; Park, Y. W.; Heeger, A. J.; Shirakawa, H.; Louis, E. J.; Gau, S. C.; MacDiarmid, A. G. Electrical Conductivity in Doped Polyacetylene. *Phys. Rev. Lett.* **1977**, *39* (17), 1098–1101.

(14) Zhao, W.; Ding, J.; Zou, Y.; Di, C. A.; Zhu, D. Chemical Doping of Organic Semiconductors for Thermoelectric Applications. *Chem. Soc. Rev.* **2020**, *49* (20), 7210–7228.

(15) Kroon, R.; Mengistie, D. A.; Kiefer, D.; Hynynen, J.; Ryan, J. D.; Yu, L.; Müller, C. Thermoelectric Plastics: From Design to Synthesis, Processing and Structure-Property Relationships. *Chem. Soc. Rev.* **2016**, *45* (22), 6147–6164.

(16) Tam, T. L. D.; Xu, J. Strategies and Concepts in N-Doped Conjugated Polymer Thermoelectrics. *J. Mater. Chem. A* **2021**, *9* (9), 5149–5163.

(17) Jacobs, I. E.; Moulé, A. J. *Controlling Molecular Doping in Organic Semiconductors*. *Advanced Materials*. 2017.

(18) Patel, S. N.; Glaudell, A. M.; Peterson, K. A.; Thomas, E. M.; O'Hara, K. A.; Lim, E.; Chabinyc, M. L. Morphology Controls the Thermoelectric Power Factor of a Doped Semiconducting Polymer. *Sci. Adv.* **2017**, *3* (6), e1700434.

(19) Jacobs, I. E.; Aasen, E. W.; Oliveira, J. L.; Fonseca, T. N.; Roehling, J. D.; Li, J.; Zhang, G.; Augustine, M. P.; Mascal, M.; Moulé, A. J. Comparison of Solution-Mixed and Sequentially Processed P3HT:F4TCNQ Films: Effect of Doping-Induced Aggregation on Film Morphology. *J. Mater. Chem. C* **2016**, *4* (16), 3454–3466.

(20) Vijayakumar, V.; Zhong, Y.; Untilova, V.; Bahri, M.; Herrmann, L.; Biniek, L.; Leclerc, N.; Brinkmann, M. Bringing Conducting Polymers to High Order: Toward Conductivities beyond 105 S Cm−1 and Thermoelectric Power Factors of 2 MW M−1 K−2. *Adv. Energy Mater.* **2019**, *9* (24), 1900266.

(21) Kuomoto, K.; Mori, T. Thermoelectric Nanoparticles : Materials Design and Applications; 2013; pp 365–382.

(22) Glaudell, A. M. Understanding Charge Transport in Polymers for Thermoelectric Applications. *ProQuest Diss. Theses* **2016**, No. June 2016, 155.

(23) Glaudell, A. M.; Cochran, J. E.; Patel, S. N.; Chabinyc, M. L. Impact of the Doping Method on Conductivity and Thermopower in Semiconducting Polythiophenes. *Adv. Energy Mater.* **2015**, *5* (4).

(24) Snyder, G. J.; Toberer, E. S. Complex Thermoelectric Materials. *Nat. Mater.* **2008**, *7* (2), 105–114.

(25) Fan, Z.; Du, D.; Guan, X.; Ouyang, J. Polymer Films with Ultrahigh Thermoelectric Properties Arising from Significant Seebeck Coefficient Enhancement by Ion Accumulation on Surface. *Nano Energy* **2018**, *51*, 481–488.

(26) Xuan, Y.; Liu, X.; Desbief, S.; Leclère, P.; Fahlman, M.; Lazzaroni, R.; Berggren, M.; Cornil, J.; Emin, D.; Crispin, X. Thermoelectric Properties of Conducting Polymers: The Case of Poly(3-Hexylthiophene). *Phys. Rev. B - Condens. Matter Mater. Phys.* **2010**, *82* (11), 115454.

(27) Bubnova, O.; Khan, Z. U.; Malti, A.; Braun, S.; Fahlman, M.; Berggren, M.; Crispin, X. Optimization of the Thermoelectric Figure of Merit in the Conducting Polymer Poly(3,4-Ethylenedioxythiophene). *Nat. Mater.* **2011**, *10* (6), 429–433.

(28) Sun, Y.; Sheng, P.; Di, C.; Jiao, F.; Xu, W.; Qiu, D.; Zhu, D. Organic Thermoelectric Materials and Devices Based on P- and n-Type Poly(Metal 1,1,2,2-Ethenetetrathiolate)S. *Adv. Mater.* **2012**, *24* (7), 932–937.

(29) Kroon, R.; Mengistie, D. A.; Kiefer, D.; Hynynen, J.; Ryan, J. D.; Yu, L.; Müller, C. Thermoelectric Plastics: From Design to Synthesis, Processing and Structure–Property Relationships. *Chem. Soc. Rev.* **2016**, *45* (22), 6147–6164.

(30) Shirakawa, H.; Louis, E. J.; MacDiarmid, A. G.; Chiang, C. K.; Heeger, A. J. Synthesis of Electrically Conducting Organic Polymers: Halogen Derivatives of Polyacetylene, (CH)X. *J. Chem. Soc. Chem. Commun.* **1977**, No. 16, 578–580.

(31) Bredas, J. L.; Street, G. B. Polarons, Bipolarons, and Solitons in Conducting Polymers. *Acc. Chem. Res.* **1985**, *18* (10), 309–315.

(32) Pingel, P.; Neher, D. Comprehensive Picture of P-Type Doping of P3HT with the Molecular Acceptor F4TCNQ. *Phys. Rev. B - Condens. Matter Mater. Phys.* **2013**, *87* (11).

(33) Kiefer, D.; Kroon, R.; Hofmann, A. I.; Sun, H.; Liu, X.; Giovannitti, A.; Stegerer, D.; Cano, A.; Hynynen, J.; Yu, L.; Zhang, Y.; Nai, D.; Harrelson, T. F.; Sommer, M.; Moulé, A. J.; Kemerink, M.; Marder, S. R.; McCulloch, I.; Fahlman, M.; Fabiano, S.; Müller, C. Double Doping of Conjugated Polymers with Monomer Molecular Dopants. *Nat. Mater.* **2019**, *18* (2), 149–155.

(34) Noriega, R.; Rivnay, J.; Vandewal, K.; Koch, F. P. V; Stingelin, N.; Smith, P.; Toney, M. F.; Salleo, A. A General Relationship between Disorder, Aggregation and Charge Transport in Conjugated Polymers. *Nat. Mater.* **2013**, *12* (11), 1038–1044.

(35) Himmelberger, S.; Salleo, A. Engineering Semiconducting Polymers for Efficient Charge Transport. *MRS Commun.* **2015**, *5* (03), 383–395.

(36) Harrelson, T. F.; Cheng, Y. Q.; Li, J.; Jacobs, I. E.; Ramirez-Cuesta, A. J.; Faller, R.; Moulé, A. J. Identifying Atomic Scale Structure in Undoped/Doped Semicrystalline P3HT Using Inelastic Neutron Scattering. *Macromolecules* **2017**, *50* (6), 2424–2435.

(37) Ghosh, R.; Chew, A. R.; Onorato, J.; Pakhnyuk, V.; Luscombe, C. K.; Salleo, A.; Spano, F. C. Spectral Signatures and Spatial Coherence of Bound and Unbound Polarons in P3HT Films: Theory Versus Experiment. *J. Phys. Chem. C* **2018**, *122* (31), 18048–18060.

(38) Duong, D. T.; Wang, C.; Antono, E.; Toney, M. F.; Salleo, A. The Chemical and Structural Origin of Efficient P-Type Doping in P3HT. *Org. Electron. physics, Mater. Appl.* **2013**, *14*

(5), 1330–1336.

(39) Scholes, D. T.; Hawks, S. A.; Yee, P. Y.; Wu, H.; Jeffrey, R.; Tolbert, S. H.; Schwartz, B. J.; Lindemuth, J. R.; Tolbert, S. H.; Schwartz, B. J. Overcoming Film Quality Issues for Conjugated Polymers Doped with F4TCNQ by Solution Sequential Processing: Hall Effect, Structural, and Optical Measurements. *J. Phys. Chem. Lett.* **2015**, *6* (23), 4786–4793.

(40) Fontana, M. T.; Stanfield, D. A.; Scholes, D. T.; Winchell, K. J.; Tolbert, S. H.; Schwartz, B. J. Evaporation vs Solution Sequential Doping of Conjugated Polymers: F4TCNQ Doping of Micrometer-Thick P3HT Films for Thermoelectrics. *J. Phys. Chem. C* **2019**, *123* (37), 22711–22724.

(41) Patel, S. N.; Glaudell, A. M.; Peterson, K. A.; Thomas, E. M.; O'Hara, K. A.; Lim, E.; Chabinyc, M. L. Morphology Controls the Thermoelectric Power Factor of a Doped Semiconducting Polymer. *Sci. Adv.* **2017**, *3* (6), e1700434.

(42) Lim, E.; Peterson, K. A.; Su, G. M.; Chabinyc, M. L. Thermoelectric Properties of Poly(3-Hexylthiophene) (P3HT) Doped with 2,3,5,6-Tetrafluoro-7,7,8,8-Tetracyanoquinodimethane (F4TCNQ) by Vapor-Phase Infiltration. *Chem. Mater.* **2018**, *30* (3), 998–1010.

(43) Ma, T.; Dong, B. X.; Grocke, G. L.; Strzalka, J.; Patel, S. N. Leveraging Sequential Doping of Semiconducting Polymers to Enable Functionally Graded Materials for Organic Thermoelectrics. *Macromolecules* **2020**, *53* (8), 2882–2892.

(44) Hynynen, J.; Kiefer, D.; Yu, L.; Kroon, R.; Munir, R.; Amassian, A.; Kemerink, M.; Müller, C. Enhanced Electrical Conductivity of Molecularly P-Doped Poly(3-Hexylthiophene) through Understanding the Correlation with Solid-State Order. *Macromolecules* **2017**, *50* (20), 8140–8148.

(45) Kang, K.; Watanabe, S.; Broch, K.; Sepe, A.; Brown, A.; Nasrallah, I.; Nikolka, M.; Fei, Z.; Heeney, M.; Matsumoto, D.; Marumoto, K.; Tanaka, H.; Kuroda, S.-I.; Sirringhaus, H. 2D Coherent Charge Transport in Highly Ordered Conducting Polymers Doped by Solid State Diffusion. *Nat. Mater.* **2016**.

(46) Kiefer, D. *Molecular Doping of Polar Conjugated Polymers*; 2019.

(47) Dongmin Kang, S.; Jeffrey Snyder, G. Charge-Transport Model for Conducting Polymers. *Nat. Mater.* **2017**, *16* (2), 252–257.

(48) Boyle, C. J.; Upadhyaya, M.; Wang, P.; Renna, L. A.; Lu-Díaz, M.; Pyo Jeong, S.; Hight-Huf, N.; Korugic-Karasz, L.; Barnes, M. D.; Aksamija, Z.; Venkataraman, D. Tuning Charge Transport Dynamics via Clustering of Doping in Organic Semiconductor Thin Films. *Nat. Commun.* **2019**, *10* (1), 2827.

(49) Kaiser, A. B. Electronic Transport Properties of Conducting Polymers and Carbon Nanotubes. *Reports Prog. Phys.* **2001**, *64* (1), 1–49.

(50) Bisquert, J. Interpretation of Electron Diffusion Coefficient in Organic and Inorganic Semiconductors with Broad Distributions of States. *Phys. Chem. Chem. Phys.* **2008**, *10* (22),

3175–3194.

(51) Gregory, S. A.; Hanus, R.; Atassi, A.; Rinehart, J. M.; Wooding, J. P.; Menon, A. K.; Losego, M. D.; Snyder, G. J.; Yee, S. K. Quantifying Charge Carrier Localization in Chemically Doped Semiconducting Polymers. *Nat. Mater.* **2021**.

(52) Thomas, E. M.; Popere, B. C.; Fang, H.; Chabinyc, M. L.; Segalman, R. A. Role of Disorder Induced by Doping on the Thermoelectric Properties of Semiconducting Polymers. *Chem. Mater.* **2018**, *30* (9), 2965–2972.

(53) Mott, N. F.; Davis, E. A. *Electronic Processes in Materials*; Oxford Classic Texts in the Physical Sciences; OUP Oxford, 1963; Vol. 276.

(54) Kang, K.; Schott, S.; Venkateshvaran, D.; Broch, K.; Schweicher, G.; Harkin, D.; Jellett, C.; Nielsen, C. B.; McCulloch, I.; Sirringhaus, H. Investigation of the Thermoelectric Response in Conducting Polymers Doped by Solid-State Diffusion. *Mater. Today Phys.* **2019**, *8*, 112–122.

(55) Lee, Y.; Park, J.; Son, J.; Woo, H. Y.; Kwak, J. Degenerately Doped Semi-Crystalline Polymers for High Performance Thermoelectrics. *Adv. Funct. Mater.* **2021**, *31* (9), 2006900.

(56) Abutaha, A.; Kumar, P.; Yildirim, E.; Shi, W.; Yang, S. W.; Wu, G.; Hippalgaonkar, K. Correlating Charge and Thermoelectric Transport to Paracrystallinity in Conducting Polymers. *Nat. Commun.* **2020**, *11* (1), 1737.

(57) Tanaka, H.; Kanahashi, K.; Takekoshi, N.; Mada, H.; Ito, H.; Shimoi, Y.; Ohta, H.; Takenobu, T. Thermoelectric Properties of a Semicrystalline Polymer Doped beyond the Insulator-to-Metal Transition by Electrolyte Gating. *Sci. Adv.* **2020**, *6* (7), eaay8065.

(58) Watanabe, S.; Ohno, M.; Yamashita, Y.; Terashige, T.; Okamoto, H.; Takeya, J. Validity of the Mott Formula and the Origin of Thermopower in π-Conjugated Semicrystalline Polymers. *Phys. Rev. B* **2019**, *10* (24), 241201.

(59) Mahamood, R. M.; Akinlabi, E. T. Types of Functionally Graded Materials and Their Areas of Application. In *Topics in Mining, Metallurgy and Materials Engineering*; Mahamood, R. M., Akinlabi, E. T., Eds.; Springer International Publishing: Cham, 2017; pp 9–21.

(60) Kieback, B.; Neubrand, A.; Riedel, H. Processing Techniques for Functionally Graded Materials. *Mater. Sci. Eng. A* **2003**, *362* (1–2), 81–106.

(61) Cramer, C. L.; Wang, H.; Ma, K. Performance of Functionally Graded Thermoelectric Materials and Devices: A Review. *J. Electron. Mater.* **2018**, *47* (9), 5122–5132.

(62) Müller, E.; Drašar, Č.; Schilz, J.; Kaysser, W. A. Functionally Graded Materials for Sensor and Energy Applications. *Mater. Sci. Eng. A* **2003**.

(63) Sallehin, N. Z. I. M.; Yatim, N. M.; Suhaimi, S. A Review on Fabrication Methods for Segmented Thermoelectric Structure. **2018**, *030003*, 030003.

(64) Thieme, M.; Wieters, K. P.; Bergner, F.; Scharnweber, D.; Worch, H.; Ndop, J.; Kim, T. J.; Grill, W. Titanium Powder Sintering for Preparation of a Porous Functionally Graded Material Destined for Orthopaedic Implants. *J. Mater. Sci. Mater. Med.* **2001**, *12* (3), 225–231.

(65) Kato, K.; Kurimoto, M.; Shumiya, H.; Adachi, H.; Sakuma, S.; Okubo, H. Application of Functionally Graded Material for Solid Insulator in Gaseous Insulation System. *IEEE Trans. Dielectr. Electr. Insul.* **2006**, *13* (2), 362–371.

(66) Li, Y.; Jian, S.; Min, Z. Application of Ceramics Metal Functionally Graded Materials on Green Automobiles. *Key Eng. Mater.* **2007**, *280–283*, 1925–0.

(67) Kumar, S.; Murthy Reddy, K. V. V. S.; Kumar, A.; Rohini Devi, G. Development and Characterization of Polymer-Ceramic Continuous Fiber Reinforced Functionally Graded Composites for Aerospace Application. *Aerosp. Sci. Technol.* **2013**, *26* (1), 185–191.

(68) Bharti, I.; Gupta, N.; Gupta, K. M. Novel Applications of Functionally Graded Nano, Optoelectronic and Thermoelectric Materials. *Int. J. Mater. Mech. Manuf.* **2013**, *1*, 221–224.

(69) Zhang, Q.; Sun, Y.; Xu, W.; Zhu, D. Organic Thermoelectric Materials: Emerging Green Energy Materials Converting Heat to Electricity Directly and Efficiently. *Adv. Mater.* **2014**, *26* (40), 6829–6851.

(70) He, M.; Qiu, F.; Lin, Z. Towards High-Performance Polymer-Based Thermoelectric Materials. *Energy Environ. Sci.* **2013**, *6* (6), 1352–1361.

(71) Bonnassieux, Y.; Brabec, C. J.; Cao, Y.; Carmichael, T. B.; Chabinyc, M. L.; Cheng, K.-T.; Cho, G.; Chung, A.; Cobb, C. L.; Distler, A.; Egelhaaf, H.-J.; Grau, G.; Guo, X.; Haghiashtiani, G.; Huang, T.-C.; Hussain, M. M.; Iniguez, B.; Lee, T.-M.; Li, L.; Ma, Y.; Ma, D.; McAlpine, M. C.; Ng, T. N.; Österbacka, R.; Patel, S. N.; Peng, J.; Peng, H.; Rivnay, J.; Shao, L.; Steingart, D.; Street, R. A.; Subramanian, V.; Torsi, L.; Wu, Y. The 2021 Flexible and Printed Electronics Roadmap. *Flex. Print. Electron.* **2022**, *6* (2), 023001.

(72) Teraki, J.; Hirano, T. A Design Procedure of Functionally Graded Thermoelectric Materials; Shiota, I., Miyamoto, Y. B. T.-F. G. M. 1996, Eds.; Elsevier Science B.V.: Amsterdam, 1997; pp 483–488.

(73) Bergmann, C. P. *Functionally Graded Materials 1996*; 1997.

(74) Hazan, E.; Ben-Yehuda, O.; Madar, N.; Gelbstein, Y. Functional Graded Germanium-Lead Chalcogenide-Based Thermoelectric Module for Renewable Energy Applications. *Adv. Energy Mater.* **2015**, *5* (11), 1–8.

(75) Müller, E.; Drašar, Č.; Schilz, J.; Kaysser, W. A. Functionally Graded Materials for Sensor and Energy Applications. *Mater. Sci. Eng. A* **2003**, *362* (1–2), 17–39.

(76) Hung, L. T.; Van Nong, N.; Snyder, G. J.; Viet, M. H.; Balke, B.; Han, L.; Stamate, E.; Linderoth, S.; Pryds, N. High Performance P-Type Segmented Leg of Misfit-Layered Cobaltite and Half-Heusler Alloy. *Energy Convers. Manag.* **2015**, *99*, 20–27.

(77) Hedegaard, E. M. J.; Mamakhel, A. A. H.; Reardon, H.; Iversen, B. B. Functionally Graded (PbTe) 1– x (SnTe) x Thermoelectrics. *Chem. Mater.* **2018**, *30* (1), 280–287.

(78) Zhang, Q.; Liao, J.; Tang, Y.; Gu, M.; Ming, C.; Qiu, P.; Bai, S.; Shi, X.; Uher, C.; Chen, L. Realizing a Thermoelectric Conversion Efficiency of 12% in Bismuth Telluride/Skutterudite Segmented Modules through Full-Parameter Optimization and Energy-Loss Minimized Integration. *Energy Environ. Sci.* **2017**, *10* (4), 956–963.

(79) Bian, Z.; Shakouri, A.; Cruz, S. Cooling Enhancement Using Inhomogeneous Thermoelectric Materials. *Int. Conf. Thermoelectr. ICT, Proc.* **2006**, No. 1, 264–267.

(80) Bian, Z.; Wang, H.; Zhou, Q.; Shakouri, A. Maximum Cooling Temperature and Uniform Efficiency Criterion for Inhomogeneous Thermoelectric Materials. *Phys. Rev. B - Condens. Matter Mater. Phys.* **2007**, *75* (24), 1–7.

(81) Vikhor, L. N.; Anatychuk, L. I. Theoretical Evaluation of Maximum Temperature Difference in Segmented Thermoelectric Coolers. *Appl. Therm. Eng.* **2006**, *26* (14), 1692–1696.

(82) Seifert, W.; Ueltzen, M.; Müller, E. One-Dimensional Modelling of Thermoelectric Cooling. *Phys. Status Solidi Appl. Res.* **2002**, *194* (1), 277–290.

(83) Thiébaut, E.; Goupil, C.; Pesty, F.; D'Angelo, Y.; Guegan, G.; Lecoeur, P. Maximization of the Thermoelectric Cooling of a Graded Peltier Device by Analytical Heat-Equation Resolution. *Phys. Rev. Appl.* **2017**, *8* (6), 64003.

(84) Jin, Z. H.; Wallace, T. T. Functionally Graded Thermoelectric Materials with Arbitrary Property Gradations: A One-Dimensional Semianalytical Study. *J. Electron. Mater.* **2015**, *44* (6), 1444–1449.

(85) Shen, L.; Zhang, W.; Liu, G.; Tu, Z.; Lu, Q.; Chen, H.; Huang, Q. Performance Enhancement Investigation of Thermoelectric Cooler with Segmented Configuration. *Appl. Therm. Eng.* **2020**, *168* (August 2019), 114852.

(86) Müller, E.; Walczak, S.; Seifert, W. Optimization Strategies for Segmented Peltier Coolers. *Phys. Status Solidi Appl. Mater. Sci.* **2006**, *203* (8), 2128–2141.

(87) Müller, E.; Zabrocki, K.; Goupil, C.; Snyder, G. J.; Seifert, W. Functionally Graded Thermoelectric Generator and Cooler Elements. **2012**.

(88) Bian, Z.; Shakouri, A. Beating the Maximum Cooling Limit with Graded Thermoelectric Materials. *Appl. Phys. Lett.* **2006**, *89* (21), 2004–2007.

(89) Mahan, G. D. Inhomogeneous Thermoelectrics. *J. Appl. Phys.* **1991**, *70* (8), 4551–4554.

(90) Schilz, J.; Helmers, L.; Müller, W. E.; Niino, M. A Local Selection Criterion for the Composition of Graded Thermoelectric Generators. *J. Appl. Phys.* **1998**, *83* (2), 1150–1152.

(91) Helmers, L.; Müller, E.; Schilz, J.; Kaysser, W. A. Graded and Stacked Thermoelectric Generators - Numerical Description and Maximisation of Output Power. *Mater. Sci. Eng.*

B **1998**, *56 B56* (1), 60–68.

(92) Muller, E.; Walczak, S.; Seifert, W.; Stiewe, C.; Karpinski, G. Numerical Performance Estimation of Segmented Thermoelectric Elements. In *ICT 2005. 24th International Conference on Thermoelectrics, 2005.*; 2005; pp 364–369.

(93) Seifert, W.; Müller, E.; Walczak, S. Generalized Analytic One-Dimensional Description of Non-Homogeneous TE Cooler and Generator Elements Based on the Compatibility Approach. *Int. Conf. Thermoelectr. ICT, Proc.* **2006**, 714–719.

(94) Onsager, L. Reciprocal Relations in Irreversible Processes. I. *Phys. Rev.* **1931**, *37* (4), 405–426.

(95) Zabrocki, K.; Müller, E.; Seifert, W. One-Dimensional Modeling of Thermogenerator Elements with Linear Material Profiles. *J. Electron. Mater.* **2010**, *39* (9), 1724–1729.

(96) Jin, Z. H.; Wallace, T. T.; Lad, R. J.; Su, J. Energy Conversion Efficiency of an Exponentially Graded Thermoelectric Material. *J. Electron. Mater.* **2014**, *43* (2), 308–313.

(97) Jin, Z. H.; Wallace, T. T. Functionally Graded Thermoelectric Materials with Arbitrary Property Gradations: A One-Dimensional Semianalytical Study. *J. Electron. Mater.* **2015**, *44* (6), 1444–1449.

(98) Kuznetsov, V. L.; Kuznetsova, L. A.; Kaliazin, A. E.; Rowe, D. M. High Performance Functionally Graded and Segmented Bi2Te3-Based Materials for Thermoelectric Power Generation. *J. Mater. Sci.* **2002**, *37* (14), 2893–2897.

(99) Li, S.; Pei, J.; Liu, D.; Bao, L.; Li, J. F.; Wu, H.; Li, L. Fabrication and Characterization of Thermoelectric Power Generators with Segmented Legs Synthesized by One-Step Spark Plasma Sintering. *Energy* **2016**, *113*, 35–43.

Chapter 2: LEVERAGING SEQUENTIAL DOPING OF SEMICONDUCTING POLYMERS TO ENABLE FUNCTIONALLY GRADED MATERIALS FOR ORGANIC THERMOELECTRICS

With the ability to modulate electronic properties through molecular doping coupled with ease in processability, semiconducting polymers are at the forefront in enabling organic thermoelectric devices for thermal energy management. In contrast to uniform thermoelectric material properties, an alternative route focuses on functionally graded materials (FGMs) where one spatially controls and optimizes transport properties across the length of a thermoelectric material. While primarily studied in the context of inorganic materials, the concept of FGMs for organic thermoelectrics has not been explored. Herein, we introduce how molecular doping of semiconducting polymers enables spatial compositional control of thin-film FGMs. Specifically, we utilize sequential vapor doping of poly[2,5-bis(3-tetradecylthiophen-2-yl) thieno [3,2-b]thiophene] (PBTTT) with the small molecule acceptor 2,3,5,6-tetrafluoro-7,7,8,8-tetracyanoquinodimethane (F4TCNQ) to fabricate the simplest form of FGMs – double-segmented thin films. The two thin-film segments are of equal length (7.5 mm), but each set to different doping levels. Our study focuses on understanding the thermoelectric properties (Seebeck coefficient, α, and electronic conductivity, σ) and structural properties (through X-ray scattering, UV-vis-NIR spectroscopy, and Raman spectroscopy) within and across the two segments. We observe the presence of a small diffuse interfacial region of 0.5 – 1 mm between the two segments

where the doping level and transport properties vary continuously. Despite the diffuse interface, the measured effective Seebeck coefficient (αeff) across the two segments is simply the average of α within each segment. Importantly, this experimental result is consistent with reported mathematical models describing αeff in graded thermoelectric materials. Our results demonstrate the facile fabrication and characterization of functionally graded organic thermoelectric materials, providing guidelines for further development on more complex FGMs.

2.1 Introduction

Molecular doping is an essential process in controlling charge carrier concentration, and in turn, the electronic transport properties of conjugated polymeric semiconductors.[1,2] Doped semiconducting polymers are of broad interesting spanning organic electronic and energy applications.[1,3] Recently, doped semiconducting polymers have emerged as promising materials for thermoelectrics – devices that interconvert heat and electricity.[3–10] Polymers for thermoelectrics span poly(ethylene dioxythiophene) (PEDOT), polythiophene derivatives (*e.g.*, poly(2,5-bis(3-alkyl-2-thienyl)thieno[3,2-b]thiophene) [PBTTT] and poly(3-alkythiophene) [P3AT]), and more advanced polymers based on donor-acceptor conjugated moieties. Organic thermoelectrics based on these polymers can enable new device geometries and architectures that are challenging to achieve through traditional inorganic-based materials. By leveraging the processability of polymers, modules may be flexible and conformable.[11–13] In turn, unique designs, such as annular or corrugated modules facilitate broader implementation towards waste heat harvesting, local temperature control (cooling), and low-power wearable electronics.[14–17]

Fundamentally, challenges lie in controlling the highly interrelated material properties that dictate thermoelectric performance, which include electronic conductivity (σ), Seebeck coefficient (or thermopower) (α), and thermal conductivity (κ).[18] The thermal-to-electrical energy conversion

efficiency is related to the dimensionless figure of merit, $ZT = \alpha^2\sigma T/\kappa$, where T is the temperature in Kelvin and $\alpha^2\sigma$ is the power factor (*PF*). Unifying each transport property is the connection to the charge carrier concentration (n). In principle, the magnitude of σ increases as function of n while, in contrast, the magnitude of α decreases with n.[3,18] For the case of thiophene-based semiconducting polymers, the quantitative addition of a molecular *p*-dopant such as a small organic acceptor (F4TCNQ, 2,3,5,6-tetrafluoro-7,7,8,8-tetracyanoquinodimethane) leads to an electron transfer between the host polymer and dopant molecule, which modulates n.[19] In addition, the introduction of the dopant must maintain the underlying hierarchical structure (crystalline order, orientation, and long-range morphology) enabling efficient charge transport in semiconducting polymers.

Therefore, how the dopant molecule is introduced into the polymer matrix is critical to controlling the thermoelectric material properties.[20,21] One approach includes casting films from solution mixtures of the polymer and dopant. While this process takes advantage of solution processability, controlling the morphology of films is difficult due to the formation of charged polymers, which results in significant aggregation or precipitation at high dopant loadings that leads to poor quality films.[22] An alternative and most promising approach is the sequential doping method where one first casts a neat thin film and then the dopant is infiltrated into the polymer matrix either with an orthogonal solvent or from the vapor phase.[22–29] It has been shown when casting a thin film of PBTTT and then vapor doping with F4TCNQ leads to a thermoelectric *PF* around 120 $\mu Wm^{-1}K^{-2}$, which is substantially higher relative to a film cast from a polymer/dopant solution (1.3 $\mu Wm^{-1}K^{-2}$).[20] The high *PF* is achieved because the infiltration of the dopant into the polymer matrix maintains the crystalline order, orientation, and long-range chain connectivity permitting high charge carrier mobility.[20] Applying a similar approach, a recent publication from

Brinkmann and co-workers has shown that sequential doping of chain aligned PBTTT leads to a *PF* of about 2000 $\mu Wm^{-1}K^{-2}$ – a record for modern solution-processable semiconducting polymers.[30]

Inspired by facile processability of semiconducting polymers and the utility of the sequential doping process, we are exploring a new direction towards functionally graded forms of doped semiconducting polymers. Functionally graded materials (FGMs) are engineered materials where properties are varied spatially either continuously or a step-by-step (segmented) fashion throughout the volume of the material.[31–33] Spatial control through composition, microstructure, and orientation can tune local properties across the FGM.[32] Implementation of the functional grading principles offers an opportunity of increasing the efficiency of thermoelectric devices for power generation or cooling by employing appropriate distribution of *n* and microstructure.[34–44] The effectiveness of FGMs has been exclusively investigated with inorganic thermoelectric materials (*e.g.*, Bi_2Te_3, PbTe).[18,36,45] For perspective, a wide operating temperature range (up to *c.a.* 1000 K) for power generation through inorganic materials leads to thermoelectric properties to be a strong function of temperature.[18] Therefore, by tuning the dopant composition (carrier density) or microstructure across the operating temperature gradient permits local optimization of thermoelectric properties.[35] Alternatively, spatial variation of the thermoelectric properties enables more efficient distribution of heat when operating thermoelectrics as Peltier coolers.[37,39] This design, referred to as the distributed Peltier effect, leads to larger cooling temperature gradients and coefficient of performance. Utilization of FGMs in the context of thermoelectric cooling applications (*e.g.*, medical cooling devices, seat coolers, and thermal management for batteries) where the operating temperatures amenable to polymeric materials (*e.g.*, ~60 °C - 0 °C) will be most promising.

To understand the influence of segmented to continuously graded thermoelectric properties, significant focus has been on developing mathematical models of FGMs based on first principles in order to establish the theoretical limits of performance.[37–39,42,46,47] Experimentally, these models provide guiding principles for the fabrication and implementation of FGMs. However, the experimental synthesis and processing of conventional inorganic thermoelectric materials typically require high temperature (~1000 K) and pressure (50 MPa) conditions to produce ingots with appropriate gradient in dopant concentration or microstructure. Therefore, executing the principles of functional grading can be prohibitive due to extreme synthetic and processing conditions. In contrast, solution processability of semiconducting polymers and low temperature thermal processing conditions permits a deeper exploration of various forms of functionally graded motifs through a single material. In particular, gradient in microstructure can be achieved with solvent or thermal annealing while the sequential doping method enables spatial control of dopant composition. To best of our knowledge, the principles of functional grading have not been explored for organic thermoelectric materials.

To this end, we report on the fabrication, structure, and thermoelectric properties (σ and α) of symmetric double-segmented thin films – simplest form of a 1D functionally graded thin films. By design, the focus of the work is not motivated by device optimization, but centered around a fundamental understanding of spatial structure-transport properties of molecularly-doped semiconducting polymers through double-segmented thin films. We utilize the high mobility semiconducting polymer poly(2,5-bis(3-tetradecylthio-phen-2-yl)thieno[3,2-b]thiophene) (PBTTT). The approach for this study employs compositional control of the molecular dopant F4TCNQ to modulate doping level (carrier concentration) within each macroscopic segment. Through a custom-designed vapor doping apparatus, we show how sequential vapor doping leads

to facile fabrication of compositionally controlled double-segmented thin films. Through a combination of grazing incidence wide angle x-ray scattering (GIWAXS) and Raman spectroscopy, we characterize the local order and the lateral spatial distribution of the dopant within and across the boundary of the two segments. In addition, the spatial distribution of σ is measured through an array of microfabricated electrodes. The measurements reveal a more complex picture encompassing multiple forms of functional gradients across multiple length scale. In particular, the fabrication process leads to the formation of diffuse interface at the boundary of two segments comprising a sigmoidal-like profile in doping and electronic conductivity. Lastly, the macroscopic α is measured within and between the segments to provide insight on the spatial average of α.

2.2 Results and Discussion

2.2.1 Fabricating Double-Segmented Films through Sequential Vapor Doping

For facile fabrication of symmetric double-segmented PBTTT:F4TCNQ thin films, we employ sequential vapor doping to spatially control dopant composition in the lateral direction (Figure 2.1). It has been established that thin film processing controls the thermoelectric transport properties of molecular-doped semiconducting polymers like PBTTT. Therefore, for consistency, all neat PBTTT thin films are processed in the same manner in this study: spin-coated from chlorobenzene solution and soft annealed at 80 °C (as-cast thin films of *c.a.* 30 nm). By focusing on the thin film regime, we can ensure uniform composition of dopant through the thickness of the film (out-of-plane direction),[27] and thus, spatial variation only occurs in the lateral direction (1D profile). In Figure 2.1b, we show a schematic of our home-built apparatus for controlled vapor doping of polymer thin films in an argon atmosphere glovebox. More details are provided in the methods section and supporting information. In short, a pellet of F4TCNQ in an alumina crucible

is placed at the bottom of the doping chamber where the base is heated to ~200 °C to sublime F4TCNQ. The dopant vapor infiltrates a PBTTT thin film that has been placed in a Teflon holder at the top of the doping chamber. The extent of doping is controlled through vapor dopant exposure time.

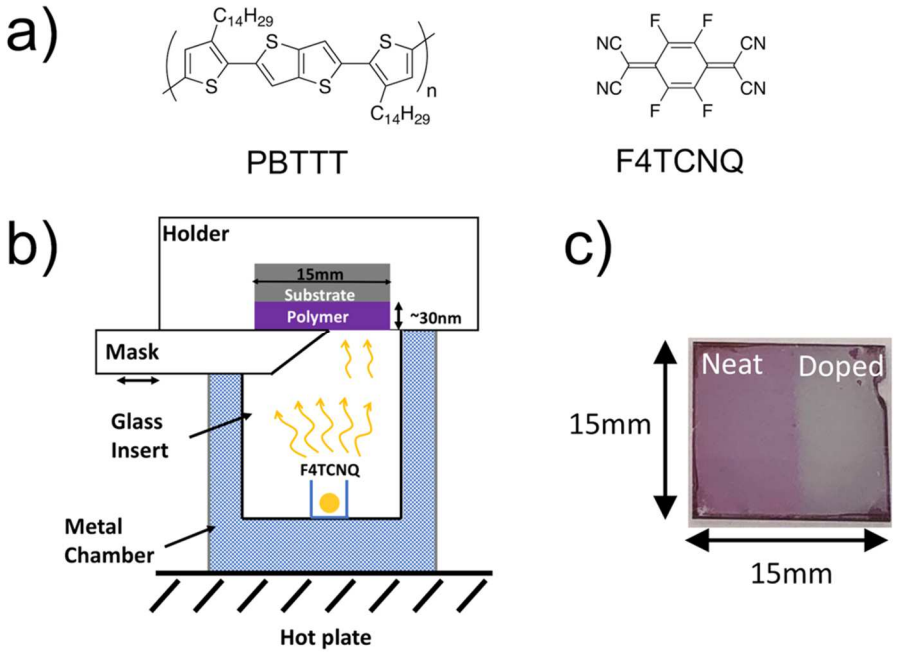

Figure 2.1: a) Chemical structure of PBTTT and F4TCNQ. b) Schematic of fabrication process used in this study to achieve double-segmented PBTTT thin films. c) Picture of a double-segmented thin film.

We calibrated our doping chamber to determine the extent of doping and conductivity as function of F4TCNQ vapor exposure time. Figure 2.2a shows a semi-log plot for the evolution of the four-probe electronic conductivity. We observe the typical superlinear increase in conductivity where the conductivity rapidly increases and then eventually plateauing at longer doping times. The values for conductivity are 0.10 S/cm at 1.5 min, 8 S/cm at 2 min, and 200 S/cm at 4 min. The corresponding UV-vis-NIR absorption spectra are shown in Figure 2.2b indicating efficient charge transfer between PBTTT and F4TCNQ. For neat PBTTT, the primary absorption peak is observed

at 2.3 eV and a broad shoulder at 2.1 eV. After vapor exposure, absorption intensity of the primary peak decreases along with the appearance of absorption structure in vicinity of 0.5 eV corresponding to the positive polaron of PBTTT and the appearance of peaks near 1.4 and 1.6 eV corresponding to the radical anion of F4TCNQ.[19] These absorption features reveal the integer charge transfer doping mechanism.[1]

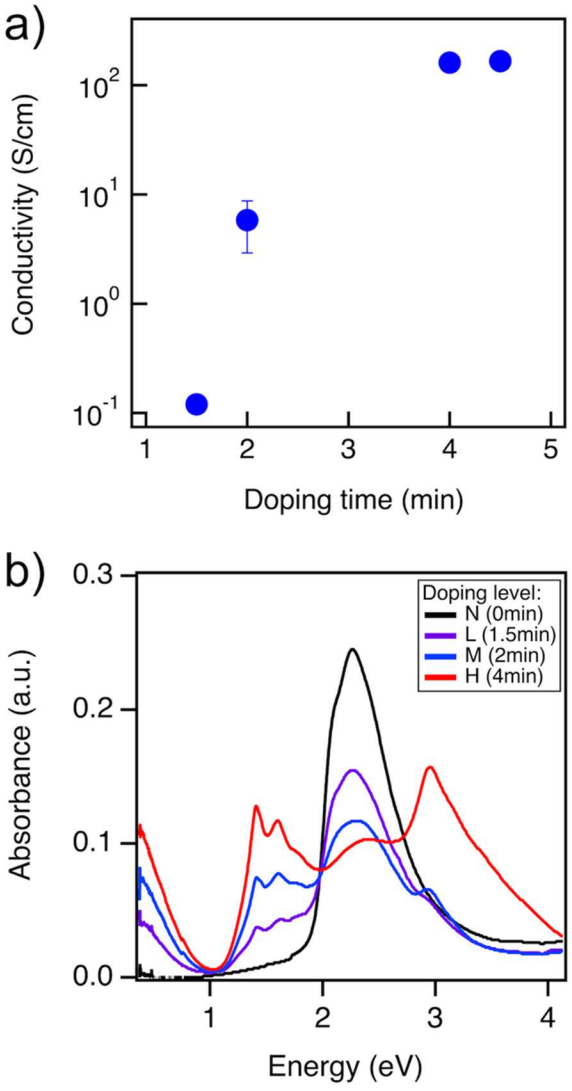

Figure 2.2: a) Electronic conductivity of PBTTT thin films doped with F4TCNQ via vapor doping method for various times. Conductivity of neat PBTTT was measured to be 1.5×10^{-5} S/cm. b) UV-VIS-NIR spectra of PBTTT thin films vapor-doped with F4TCNQ for various times. **N** = neat, **L** = low, **M** = medium, and **H** = high doping levels.

The doping levels in our films were estimated with the deconvoluted UV-Vis-NIR spectra using Beer's law (Figure 2.3). The F4TCNQ anion concentration was determined using the F4TCNQ anion molar extinction coefficient at 1.4 eV (ε = 50000 L mol^{-1} cm^{-1})[48] and the underlying monomer concentration was estimated from PBTTT extinction coefficient at 2.3eV (ε = 50000 L mol^{-1} cm^{-1}) (see Appendix for detailed calculation). The estimated molar ratio (MR) of the dopant anion to monomer (F4TCNQ anion:PBTTT monomer) are 0.04, 0.09, 0.23 for 1.5 min doped, 2 min doped and 4 min doped films, respectively. The high doping level is approaching reported studies of PBTTT doped with F4TCNQ where the maximum MR is in the range of 0.25-0.30.[20,27,29] With these results, we designate four doping and conductivity levels for our study: neat (undoped) (**N**), MR = 0.04 = low (**L**), MR = 0.09 = medium (**M**), and MR = 0.23 = high (**H**). To generate segmented films, we utilized a Teflon bar to mask parts of the film from exposure to the dopant vapor (Figure 2.1b). More details are provided in the experimental methods section. Going forward, we will focus on the characterization of neat-high (**NH**), low-high (**LH**), and medium-high (**MH**) double-segmented samples.

2.2.2 Influence of Molecular Doping on Local Structure and Dopant Distribution

By performing grazing incidence wide angle X-ray (GIWAXS) scattering experiments, we can determine how molecular doping influences the local ordering of the polymer chains and provide insight on the distribution of the dopant within and across the two segments. The GIWAXS images of our neat PBTTT thin film conveys the characteristic scattering pattern for as-cast PBTTT (Figure 2.4). The GIWAXS image indicates side-chain stacking (h00) peaks up to the 4th order in the out-of-plane direction along with the backbone reflection ($\bar{1}\,1\,\bar{3}$) as well as the reflection (110) related to the π-π stacking in the in-plane direction.[49–51] This observation indicates

a preferential edge-on orientation of polymer crystallites, resulting from the casting conditions used in this particular study.

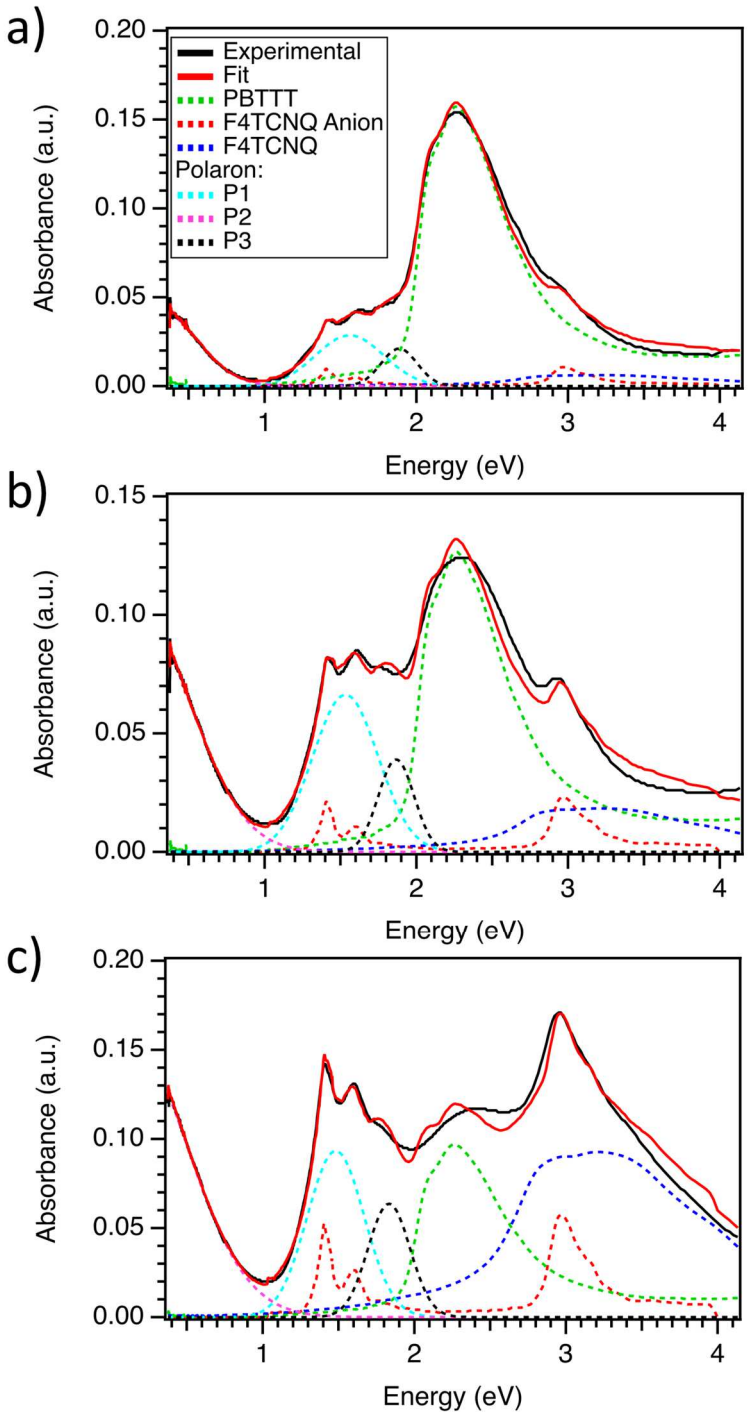

Figure 2.3: Absorption spectra fits for PBTTT thin films vapor doped with F4TCNQ for various times. (a) 1.5 min = low (**L**), (b) 2 min = medium (**M**), and (c) 4 min = high (**H**).

For F4TCNQ-doped films, representative GIWAXS images are shown for the **LH** segmented film in Figure 2.5a and for the **NH** and **MH** segmented films in Figure 2.6. Overall, the scattering patterns for all segmented films are qualitatively similar to neat PBTTT. This indicates that vapor infiltration with F4TCNQ only causes minimal disruption to the underlying semicrystalline morphology of PBTTT, which is consistent with previous reports.[20] Quantitative changes upon vapor doping are seen through the side-chain stacking and π-π stacking distances. We focus on the (200) reflection to due to background scattering from the beamstop and substrate reflectivity present near the (100) reflection. In segment **H**, we observe an increase in the side-chain spacing distance (d_{200}) to 1.14 nm relative to 1.06 nm for neat PBTTT. In addition, we observe a compression of the π-π stacking distance to 0.354 nm relative to 0.371 nm for neat PBTTT.

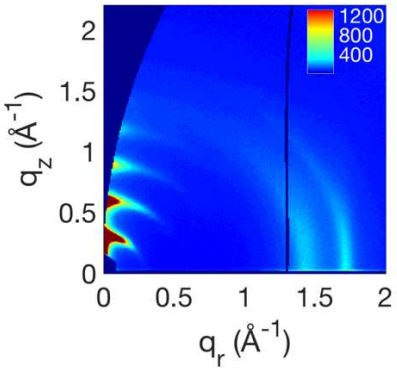

Figure 2.4: 2D GIWAXS image of neat PBTTT.

These changes are consistent to recent reports showing that dopant F4TCNQ anion resides within regions of the aliphatic side chains where an expansion of the side-chain stacking direction (*h*00) and compression of the π-π stacking distance are observed.[20,29] The decrease in the π-π stacking distance upon doping is widely observed in molecularly doped conjugated polymers.[19,23,52,53] Recently, it has been shown that doping-induced polaron delocalization between adjacent backbones leads to electrostatically attractive intermolecular interactions, and, thus,

accounts for the reduction in the π–π stacking distance.[54] Moreover, the extent of the changes in the distances is a function of doping level. Therefore, we can use the relative changes in side-chain and π-π stacking distances to monitor the compositional distribution of the dopant.

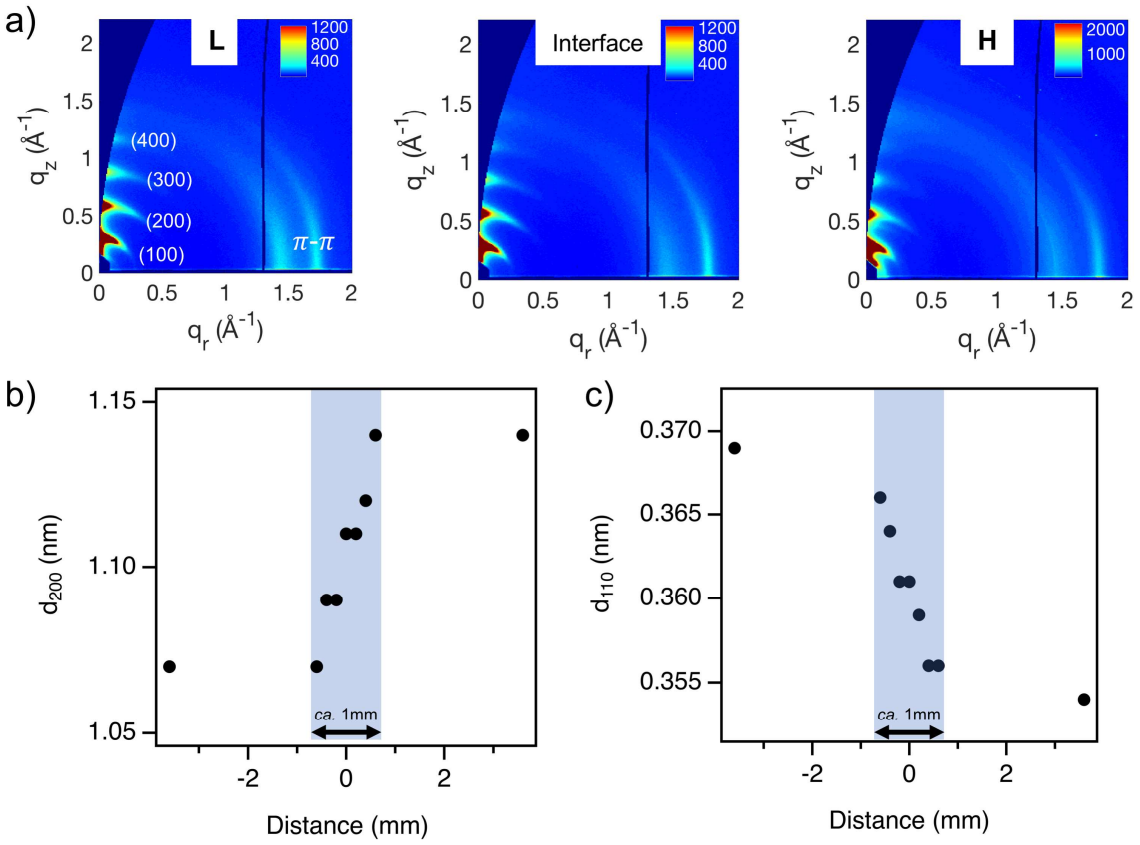

Figure 2.5: a) 2D GIWAXS images collected at L (low doping) segment, interface and H (high doping) segment, respectively; Domain spacing of b) (200) peak, d_{200}, and c) (110) peak, d_{110}, at different positions on LH segmented thin films obtained from GIWAXS.

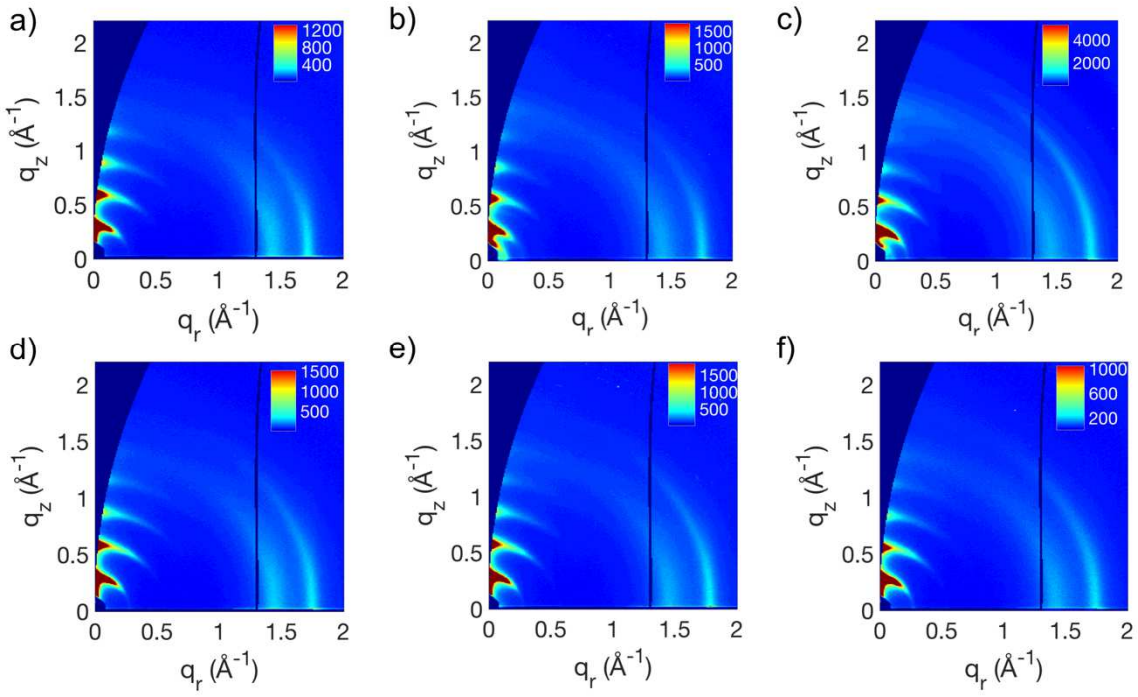

Figure 2.6: 2D GIWAXS images collected on **NH** segmented film at (a) **N** segment, (b) interface and (c) **H** segment, respectively. 2D GIWAXS images collected on **MH** segmented film at (d) **M** segment, (e) interface and (f) **H** segment, respectively.

GIWAXS experiments as function of angle of incidence were performed to determine the dopant composition through the thickness of the film (out-of-plane direction). In Figures 2.7, we show the scattering profiles measured at different angles of incidence for segments **L** and **H**. Overall, the changes to side-chain stacking and π-π stacking distances are the same at each angle of incidence, which signifies uniform distribution of dopant through the thickness of the film. These results are consistent with previous reports for PBTTT thin films used in this study (*c.a.*, 30 nm).[20]

The lateral distribution of both side-chain stacking and π-π stacking distances are shown in Figure 2.5b and 2.5c, respectively, for the **LH** segmented film and in for **NH** and **MH** segmented films. Measurements were carried out on nine different spots laterally across the double-segmented film (7.2 mm distance). The center location (x = 0 mm) was designated as the location of edge of

the Teflon bar during vapor doping, which establishes the interface between the two segments. Seven measurements were conducted across the interface of the segments. The distance between adjacent spots is approximately 200 μm, which is the width of the X-ray beam. Measurements within each segment were 3 mm away from the edge of the interface of the two segments.

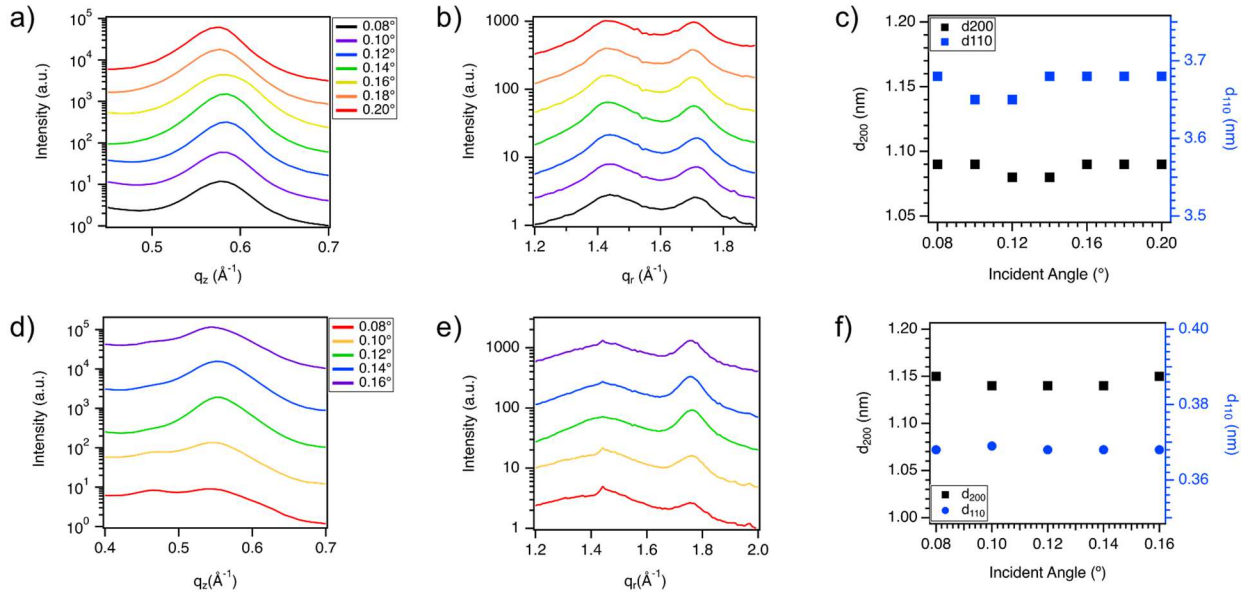

Figure 2.7: (a) Out-of-plane and (b) In-plane scattering profiles of **L** segment at different incident angles; (c) Alkyl stacking spacing (d_{200}) and π-stacking spacing (d_{110}) at different incident angles. (d) Out-of-plane and (e) In-plane scattering profiles of **H** segment at different incident angles; (f) Alkyl stacking spacing (d_{200}) and π-stacking spacing (d_{110}) at different incident angles. The critical angle of PBTTT is about 0.12°, and the critical angle of the Si substrate is about 0.166°. The scattering profiles have been vertically shifted for clarity. Note the difference in the scattering intensity is on the account variation in scattering volume at different angle of incidence.

Starting from within segment **L** (x = -3.6 mm), the 2nd order side-chain spacing, d_{200}, is 1.07 nm and maintains this value when approaching the interface (x = -0.6 mm). Importantly, finer spatial measurements across the interface and towards segment **H** revealed a steady increase in d_{200} where the value reaches 1.14 nm at x = +0.6 mm. This d_{200} is equal to the value within segment **H** (x = +3.6 mm). The distribution can be qualitatively described to follow a sigmoidal-like profile. As shown in Figure 2.5c, the spatial distribution for π-π stacking distance shows similar sigmoidal-profile, but inversely correlated. The profile reveals that while the doping level is homogenous

within each segment, there exist a thin diffuse interface where the doping level gradually changes. This distribution was also observed in **NH** and **MH** segmented films (Figures 2.8 and 2.9). Overall, the width of the diffuse interface is *c.a.* 1 mm for **NH** and **LH**, and *c.a.* 0.5 mm for **MH** segmented films.

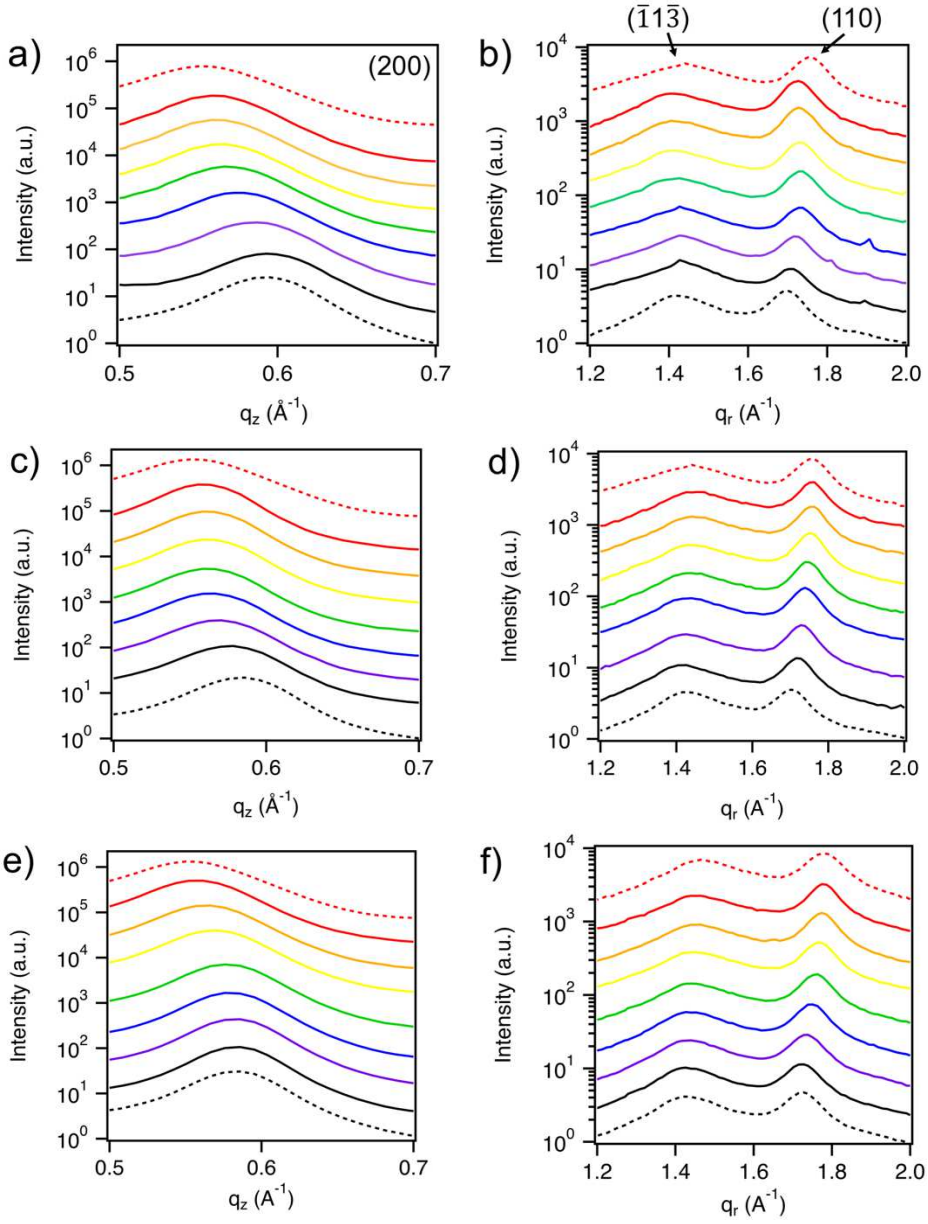

Figure 2.8: Out-of-plane (200) scattering peak profiles at different positions on (a) **NH**, (c) **LH** and (e) **MH** segmented films. In-plane scattering profiles for $(\bar{1}1\bar{3})$ and (110) at different positions on (b) **NH**, (d) **LH** and (f) **MH** segmented films. Dotted lines represent the measurements in the segments and solid lines represent the measurements across the interface.

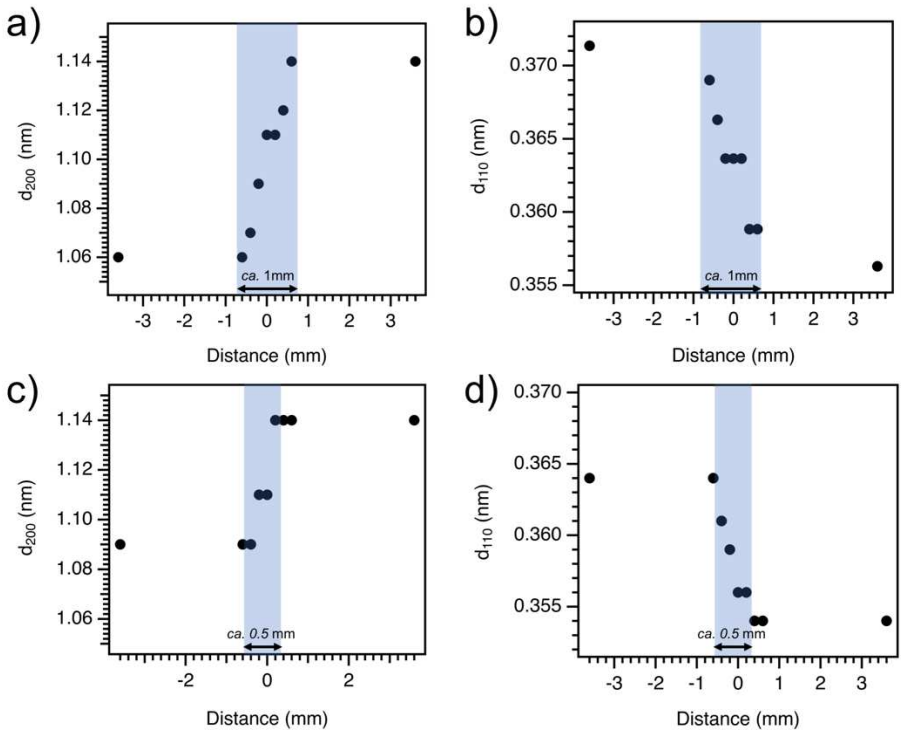

Figure 2.9: (a), (c) Alkyl stacking spacing (d_{200}) and (b), (d) π-stacking spacing (d_{110}) at different positions on **NH** and **MH** double-segmented PBTTT thin films obtained from GIWAXS.

2.2.3 Raman Spectroscopy Reveals Spatial Distribution of Charge Carriers

Raman spectroscopy was used to further characterize the spatial distribution of charge carriers (doping level) within and across the double-segmented PBTTT thin films. Charge carriers here correspond to the formation of positive polarons, which can be observed through changes in Raman vibrational modes of the conjugated core of PBTTT. Note that the determination of positive polarons through Raman spectroscopy is used to quantify the local doping level and should not be equated to be free charge carriers contributing to conduction.[55] Raman spectra of neat PBTTT and PBTTT:F4TCNQ thin films at various vapor doping times are shown in Figure 2.10b. For neat PBTTT, we observe four major Raman modes, appearing at 1394 cm^{-1} (mode A), 1415 cm^{-1} (mode B), 1460 cm^{-1} (mode C) and 1490 cm^{-1} (mode D). These modes are in good agreement with

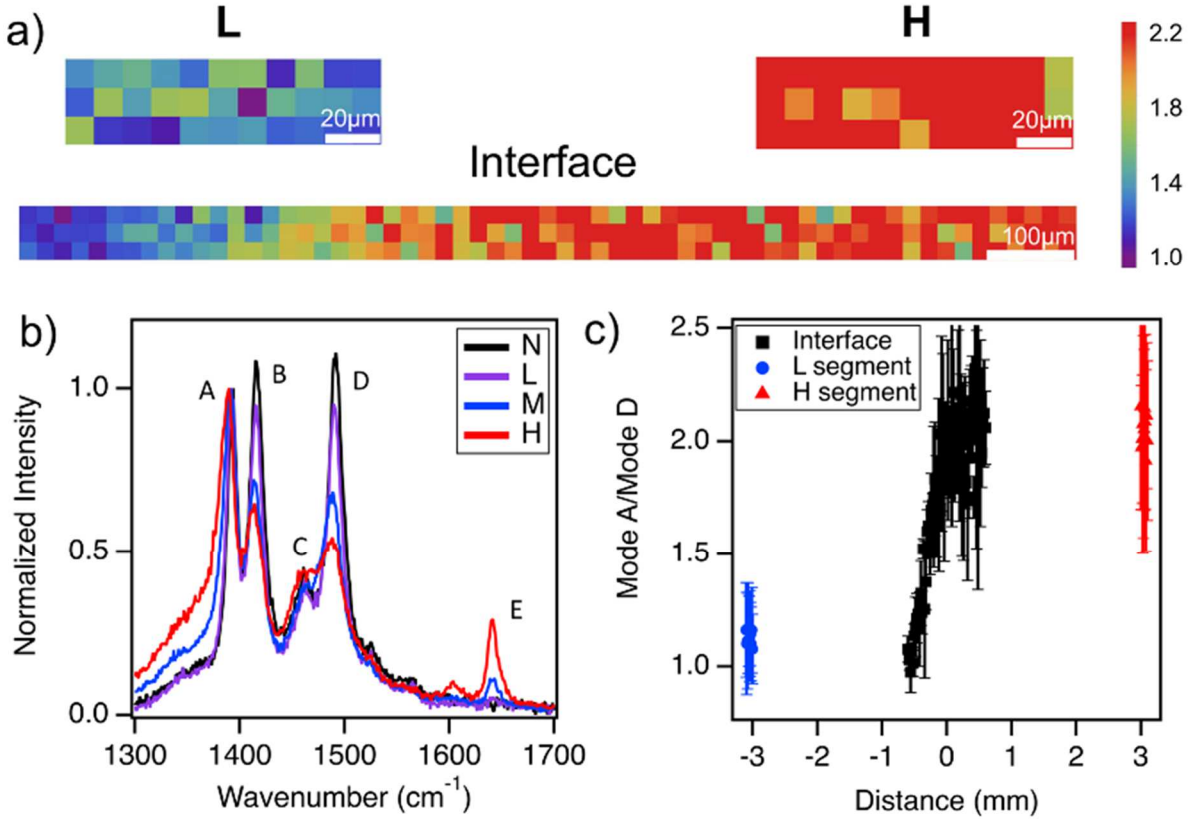

Figure 2.10: a) Raman maps of peak height ratio of mode A/mode D on segment L, segment H, and across the interface, respectively. b) Raman spectra for N, L, M, H films with labeled Raman modes. c) Peak height ratio of mode A/mode D as a function of distance across a LH segmented film. Raman results for NH and MH segmented films are provided in the supporting information.

previous reports[56–58] and are further summarized in Figure 2.11 and Table 2.1. The relevant modes to monitor polaron formation are A and D, which correspond to C=C stretching mode from the thienothiophene core and C=C/C–C stretching/shrinking mode from the outer thiophene rings, respectively.[56–58] Relative intensity change of Mode A indicates the formation of positive polarons (hole carriers) while the change to Mode D relates to neutral (undoped) chains. In tandem, the appearance and growth of the peak at 1642 cm^{-1} corresponds to the formation of F4TCNQ anion (mode E), which further emphasizes the correlation to doping level. To best express relative changes between individual peak modes, we normalized all neat and doped Raman spectra to mode A. With this normalization scheme, the intensity of mode D is shown to decrease significantly

upon doping with F4TCNQ. In turn, taking the peak height ratio of mode A/mode D approximates the positive polaron (hole) concentration. For example, the peak height ratio of mode A to mode D increases from 0.92 for neat PBTTT to 1.9 when PBTTT doped for 4 minutes. This relation provides us a pathway to spatially map out the charge carrier concentration across key regions of the segmented film.

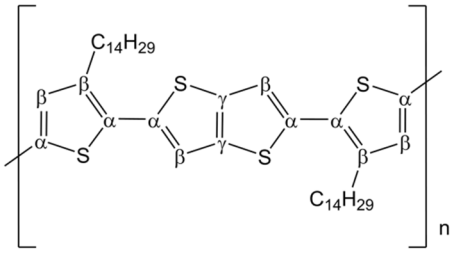

Figure 2.11: Chemical structure of PBTTT

Table 2.1: Raman mode assignment for neutral and F4TCNQ vapor-doped PBTTT

Mode	Wavenumber (cm^{-1})				Description[57]
	Neat	1.5 min	2 min	4 min	
A	1394	1392	1391	1390	C_γ-C_γ intra-ring stretch
B	1415	1415	1413	1414	C_β-C_β intra-ring stretch
C	1461	1461	1461	1461	C_α-C_α inter-ring stretch
D	1490	1490	1489	1489	C_α-C_β intra-ring
E	N/A	N/A	1642	1642	F_4TCNQ anion

Figure 2.10a shows the Raman maps of peak height ratio of A/D for different spots of the **LH** segmented film. Note that the spatial resolution of the Raman mapping is approximately 0.65 μm based on the aperture of the microscope and laser wavelength. Moreover, each "pixel" of the color map is "coarse-grained" to a 10 μm by 10 μm square, which is based on the step size for each measurement. Here, purple corresponds to regions of lowest charge carrier concentration while

red corresponds to regions of highest charge carrier concentration. Within segment **H**, we observe near uniform distribution of charge carriers. On the other hand, segment **L** shows a less homogenous charge carrier distribution suggesting dopant segregation at lower doping levels. Raman maps with finer scale (1 μm step size) were also obtained to confirm this inhomogeneity (Figure 2.12). While doping level is uniform when macroscopically-average, the Raman experiments show the inhomogeneity of doping at the sub-micron scale, and thus, the hierarchical nature of compositional dopant control inherent with the sequential vapor doing process.

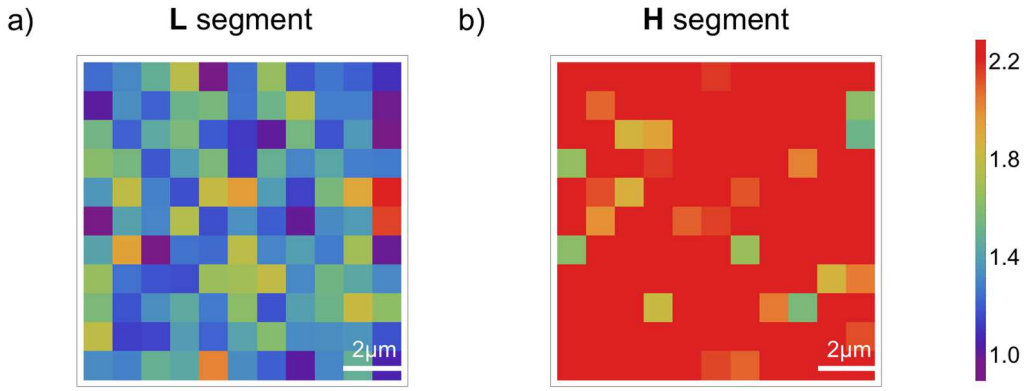

Figure 2.12: Raman maps with finer scale of peak height ratio of mode A/mode D on (a) **L** and (b) **H** segment.

The interfacial region between both segments, moreover, shows a gradual change in charge carrier concentration (Figure 2.10a and Figure 2.13). To quantify width of the gradual change, we plot the lateral average of the ratio of modes A and D (Figure 2.10c, Figure 2.13b and 2.13d). The peak height ratio A/D is 1.1 ± 0.2 within segment **L** while the A/D ratio is 2.0 ± 0.4 within segment **H**. The large error arises from the heterogeneity of the charge carrier distribution. Across the interface region, the peak height ratio gradually increases from 1.0 (average of first three points) near segment **L** to 2.1 (average of last three points) near segment **H**. This gradual change describes a diffuse interface, which occurs across a width of approximately 1 mm for the **LH** segmented

film. The presence of a diffuse interface is consistent with the analysis of the GIWAXS measurements discussed earlier.

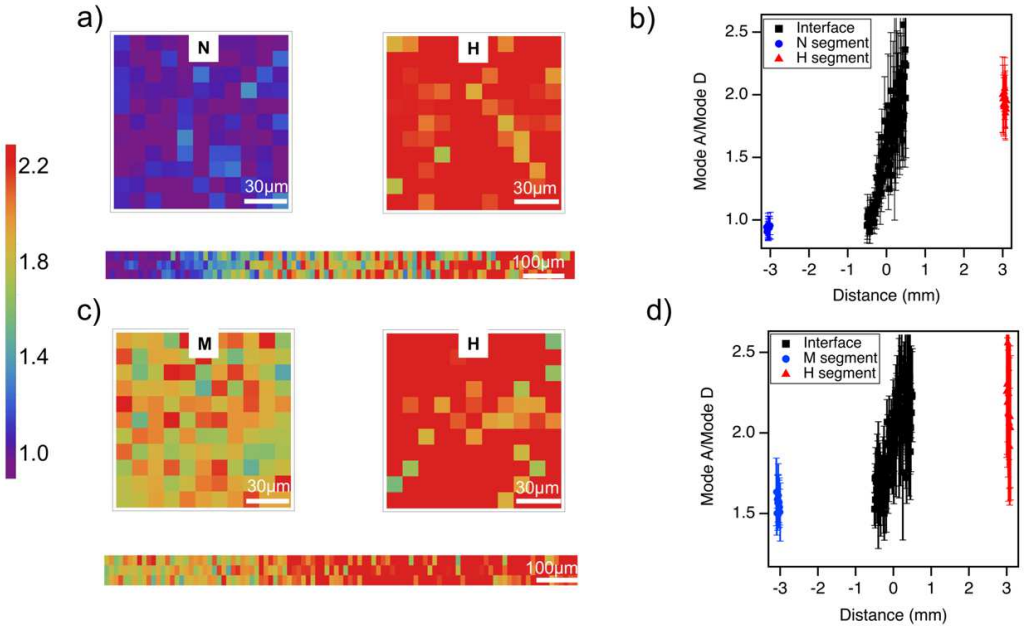

Figure 2.13: a) Raman maps of peak height ratio of mode A/mode D for a) NH and c) MH segmented films, respectively. Peak height ratio of mode A/mode D as a function of distance across b) NH and d) MH segmented films, respectively.

2.2.4 Determination of Spatial Electronic Conductivity

The spatial distribution of the electronic conductivity was characterized within and across the interface of the segments through an array of interdigitated electrodes (IDEs). Note that we designate the center IDE (x = 0) as the spot where the edge of the Teflon mask was located during vapor doping, which establishes the boundary between the two segments. Each IDE measures a 100 μm by 300 μm region and is laterally spaced apart by 200 μm, which yields a total distance of 6 mm (3 mm for each segment). Shown in Figure 2.14 is the spatial electronic conductivity for the three double-segmented thin films. The spatial distribution reveals uniform conductivity within each segment, but with the presence of a diffuse interface that has a sigmoidal-like conductivity

profile. The width of the diffuse interface is dependent on the doping time and is *c.a.* 1.5 mm for **NH**, *c.a.* 1.0 mm for **LH**, and *c.a.* 0.6 mm for **MH** segmented films. Importantly, the conductivity profile within the diffuse interface correlates well with the presence of a graded doping profile as observed through GIWAXS and Raman spectroscopy.

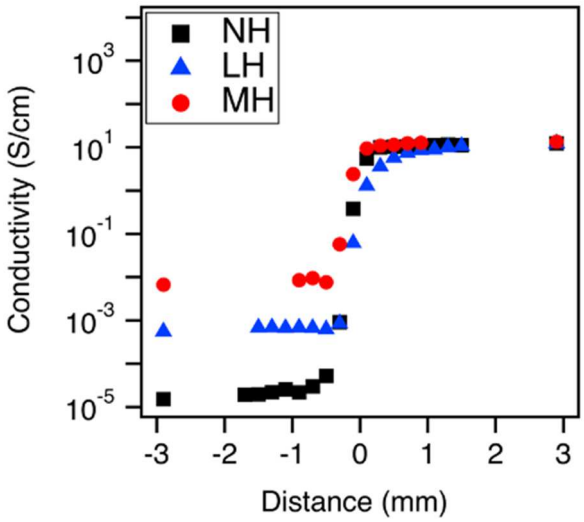

Figure 2.14: Electronic conductivity across the double-segmented films (measured by an array of IDEs, see supporting information). The center spot (0 mm) is as the location where the edge of the Teflon mask was placed during vapor doping.

2.2.5 Description of Functional Gradient Forms in Our Double-Segmented Films

Conductivity, GIWAXS, and Raman experiments reveal that the fabrication of the double-segmented film leads to a more intricate description encompassing multiple forms of functional grading across multiple length scales. Specifically, the description accounts for composition and structural characteristics spatially controlled from nano- to macro-scales. Our functionally graded films comprise macroscopic segments set to a specific doping level. As observed through Raman mapping, the dopant composition is heterogenous in the sub-micron length scale. The heterogeneity and hierarchical dopant composition control the measured macroscopic electronic

conductivity and Seebeck coefficient within each segment. Between the two segments is a diffuse interface where the dopant composition and conductivity vary continuously. Qualitatively, the functional grading profile of our double-segmented film can be described by a Sigmoidal-like curve. The intricate nature of the functional gradient forms in our films will regulate the spatial average of the Seebeck coefficient (to be discussed in the next section). We posit the formation of the diffuse interface arises from the inhomogeneity of dopant infiltration from shadowing effects at edge of the bar and vapor diffusion underneath the microscopic gap between the bar and film surface. While solid-state lateral drift-diffusion can contribute to the diffuse interface, we believe this process is negligible in our experiments (see Appendix for more details). In total, these processes lead to a gradient in dopant concentration across the boundary of the two segments.

2.2.6 Determination of Macroscopic Seebeck Coefficient

In this section, we present and discuss the results for the measured macroscopic α values within and between the two segments. In Figure 2.15a, we show the geometry and arrangement of the gold contacts used to measure the Seebeck coefficient of the double-segmented films. The larger gold pads were used to measure the temperature difference while the narrow gold strips are used to measure the voltage difference. Measurements were taken each 1 mm apart to ensure sufficient voltage response. The Seebeck coefficient was spatially measured at five spots across the double-segmented film. The middle contact pair were for measurements between the interface of the two segments. Note that the distance of 1 mm is approximately similar to or larger than the width of the diffuse interface. In addition, the location of the metal contacts was controlled so that measurement equally weights each segment when measuring across the interface.

Measurements within segments **L** and **H** yielded values of α_{L1}= 177 ± 17 μV/K and α_{L2}= 178 ± 17 μV/K, and α_{H1}= 33 ± 3 μV/K and α_{H2}= 34 ± 3 μV/K. In addition, the **MH** segmented

film yielded values of α_{M1}= 71 ± 7 μV/K and α_{M2}= 70 ± 7 μV/K, and α_{H1}= 33 ± 3 μV/K and α_{H2} = 30 ± 3 μV/K. Overall, these values reveal the homogeneity of the macroscopic Seebeck coefficient within each segment. The measurement of α across the segments yielded values of α_{LH} = 97 ± 9 μV/K and α_{MH}= 48 ± 5 μV/K for the two segmented films. Upon closer inspection, α_{LH} and α_{MH} is the average of the α values of each corresponding homogenous segment **(**Figure 2.15b**)**. This observation holds true when α is measured along a longer distance of 3 mm across the two segments (Figure 2.16).

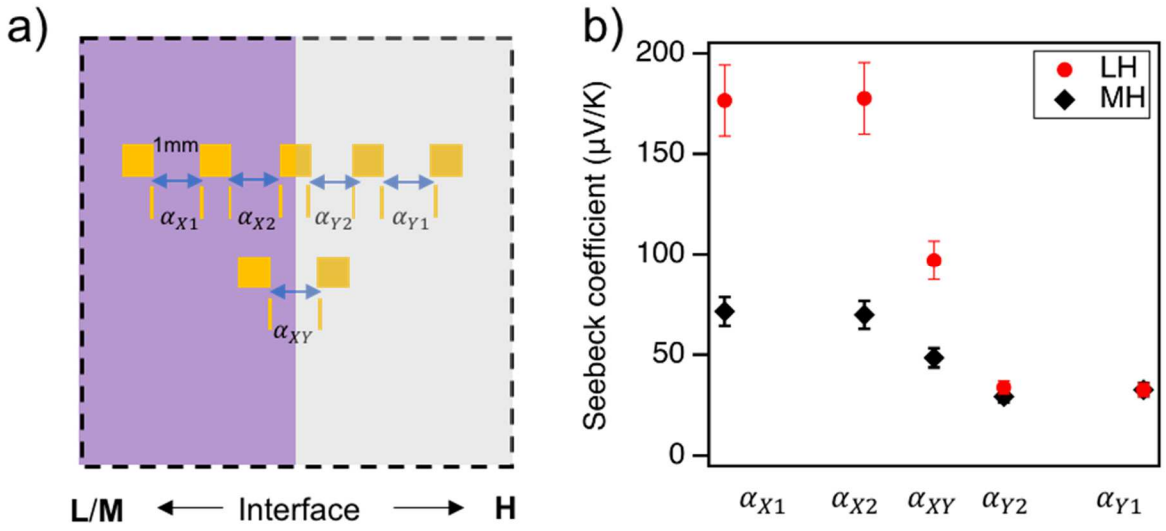

Figure 2.15: a) Schematic of the contact geometry for spatial Seebeck coefficient measurements on LH and MH segmented films; b) Seebeck coefficient at different regions of **LH** and **MH** segmented films. (X = **L** or **M**; Y = **H**).

This averaging effect can be validated by considering the general integral expression for the spatial average (α_{avg}) for a graded α profile:

$$\alpha_{avg} = \frac{1}{L}\int_0^L \alpha(x)dx \qquad (2.1)$$

where $\alpha(x)$ is the spatial distribution function of the graded Seebeck coefficient and L is the total lateral distance of the graded profile.[35] For our symmetric double-segmented films, the integration

can be simplified as the sum of the rectangular integration of each segment ($\alpha_1 L_1 + \alpha_2 L_2$). Dividing by the total length ($L = L_1 + L_2$) leads to the average Seebeck coefficient. Note our double-segmented films are symmetric so $L_1 = L_2$; therefore, Equation 1 simplifies down to $(\alpha_1 + \alpha_2)/2$, or the average of each homogenous segment. Indeed, α_{LH} is measured to be 97 ± 9 μV/K, which is the same as the integrated average, 105 ± 10 μV/K, within error. Similarly, for the **MH** segmented film, the integrated average 51 ± 5 μV/K which is equivalent to the measured α_{MH} = 48 ± 5 μV/K.

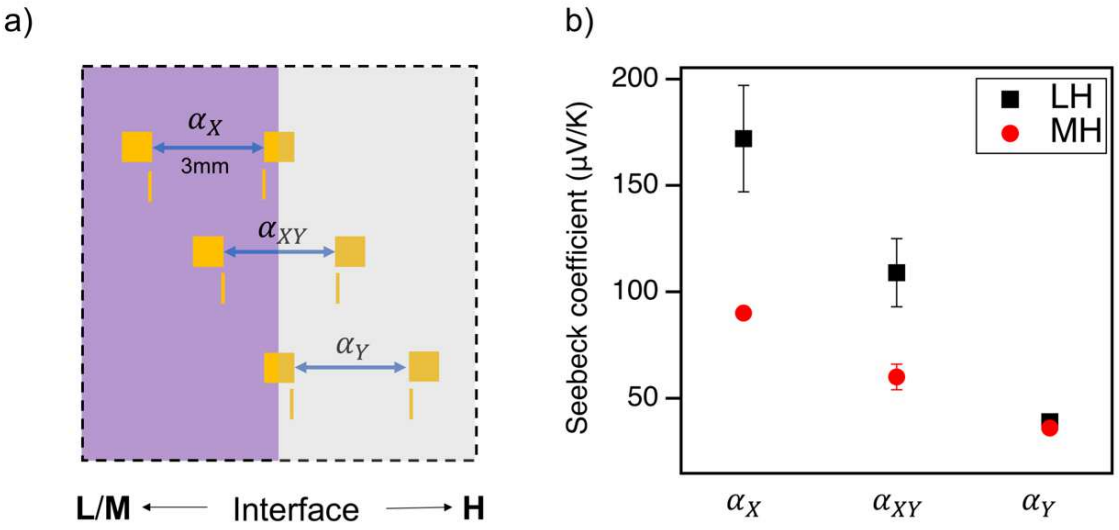

Figure 2.16: a) Schematic of contacts geometry for Seebeck measurements across 3 mm on **LH** and **MH** segmented films; b) Seebeck coefficient at different regions on **LH** and **MH** segmented films. (X = **L** or **M**; Y = **H**).

The above analysis does not account for the small diffuse interface between the two segments where the doping level has a sigmoidal-like profile. While we could not experimentally map out the local Seebeck coefficient, it can be reasonably assumed the spatial distribution for α inversely correlates to the dopant composition and conductivity profiles shown earlier. For discussion purposes, we calculated the spatial α profile using the experimental spatial conductivity in Figure 2.14 and the empirical power law correlation previously reported for polythiophene-

based polymers (α proportional to $\sigma^{-1/4}$, Figure 2.17).[3] The calculated local α spatial profile for the segmented-films are shown in Figure 2.18. With a nearly symmetric sigmoidal-like profile, the average of the two asymptotic values corresponds to the inflection point of the curve. As noted earlier, the experimental measurement distance of 1 mm for α is approximately similar to or larger than the width of the diffuse interface. Consequently, the Au Seebeck contacts reside on the asymptotes of the Sigmoidal-like profile where the asymptotes track each homogenous segment.

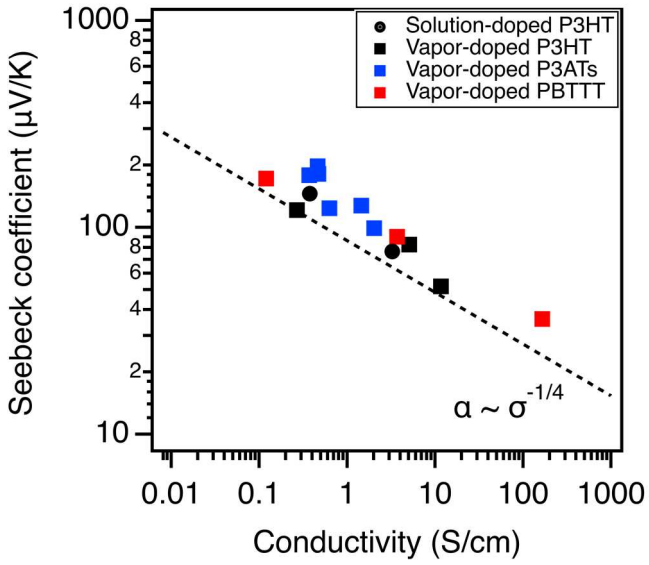

Figure 2.17: Seebeck coefficient as a function of electrical conductivity for F4TCNQ-doped polymers, P3HT (•,■), PBTTT (■) and P3BT, P3OT, P3DDT (■). The black dash line represents the empirical relationship of α proportional to $\sigma^{-1/4}$.

By design, the experimental α measurement equally balances each segment, thus the measured α across the segment is equivalent to the local α at the midpoint point (inflection point) within the diffuse interface. Therefore, due to the symmetry of the α profile and equal weighting of each segment, the spatial distribution of α within the diffuse interface does not impact the determination of the average Seebeck coefficient of our double-segmented films.

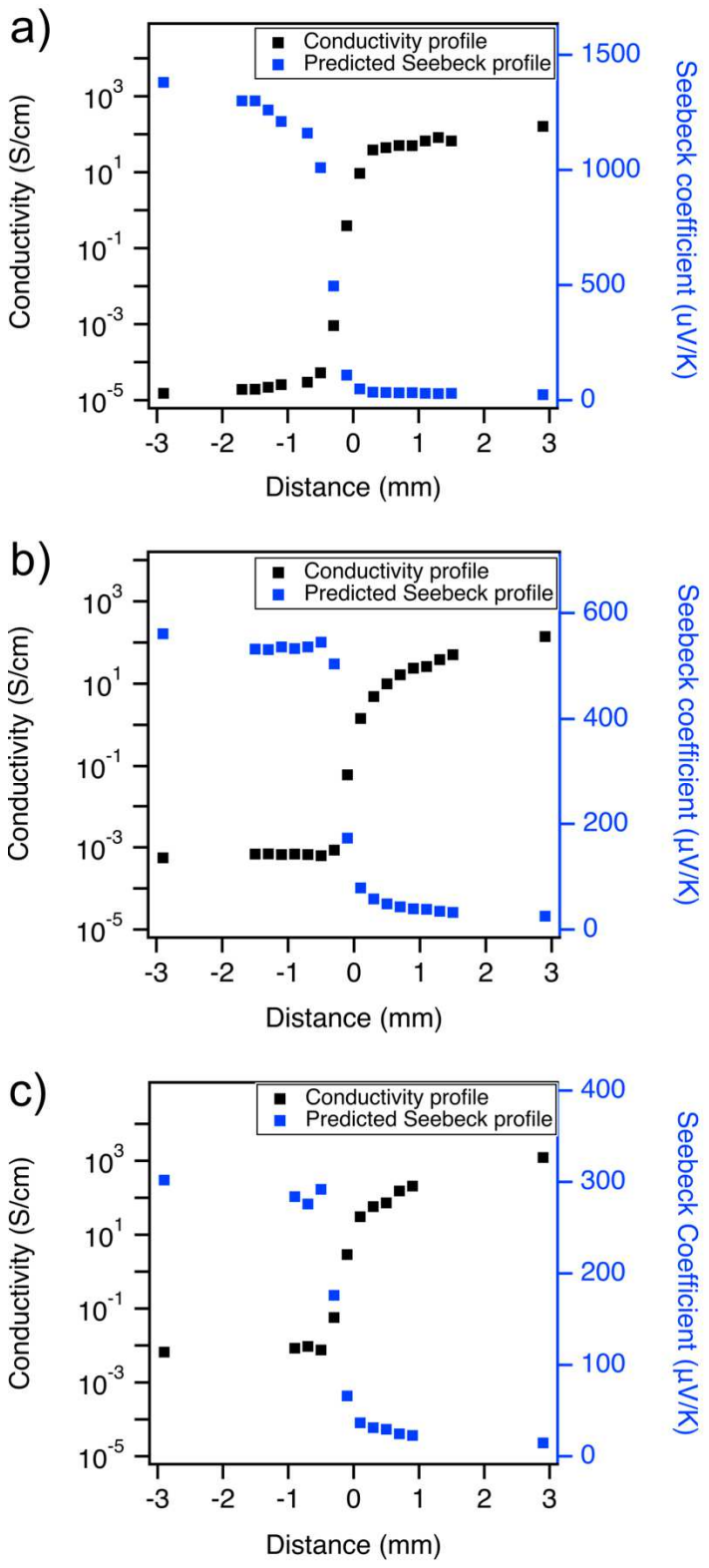

Figure 2.18: Predicted Seebeck profile across the (a) **NH**, (b) **LH** and (c) **MH** segmented film.

2.3 Conclusion

We have presented a facile process in fabricating symmetric double-segmented PBTTT thin films where each segment is sequentially doped with F4TCNQ from the vapor phase. To characterize the lateral dopant composition profile, we correlated the changes in the characteristic side-chain stacking and π-π stacking distances to the presence of dopant anion molecules. While uniform side-chain stacking and π-π stacking distance were seen within each segment (uniform doping level), a gradual change in these characteristic spacings was seen across the interface of the segments (gradient in doping level). Of note, the length of this diffuse interface is 0.5 – 1 mm between the two segments. In addition, Raman spectroscopy provided complementary details in the localized doping level. While Raman mapping revealed inhomogeneity of doping at the sub-micron scale, the macroscopic average of the spatial doping profile follows the trends observed with GIWAXS. Spatial conductivity measurements through an array of microelectrodes indicate sigmoidal-like profile tracking well with the dopant compositional profile Lastly, the Seebeck coefficient (α) was measured within and the across the segments. The measurements reveal homogeneity of the macroscopic Seebeck coefficient within each segment. Even with presence of the diffuse interface, the spatiality integrated α is simply the average of the α values of the segments.

Our work showcases how sequential vapor doping is an enabling technique for applying the principles of functional grading for organic thermoelectrics. While this study is limited to symmetric double-segmented films, going forward, more complex designs spanning multi-segments to continuously-graded profiles are possible. Moreover, for judicious selection of graded profiles, the design process can be coupled with mathematical transport models revealing theoretical limits of thermoelectric performance. Overall, semiconducting polymers as FGMs are

an enabling platform to further advance our understanding of structure-transport properties and the development of more efficient organic thermoelectric devices.

2.4 Experimental Methods

Materials. Poly(2,5-bis(3-tetradecylthiophen-2-yl)thieno[3,2-b]thiophene) (PBTTT) and anhydrous chlorobenzene (CB) was purchased from Sigma-Aldrich (M_w 40,000-80,000) and used as received without further purification. 2,3,5,6-tetrafluoro-7,7,8,8-tetracyanoquinodimethane (F4TCNQ, >98%) was purchased from TCI Chemicals.

Thin Film Preparation. Thin film samples for GIWAXS experiments were prepared on silicon with native oxide wafer substrates (15 mm × 15 mm × 0.5 mm, University Wafer). Thin film samples for UV-VIS-NIR spectroscopy, Raman spectroscopy, and electrical characterization were prepared on quartz substrates (15 mm × 15 mm × 0.5 mm, University Wafer). All substrates were cleaned by sonicating in acetone and isopropanol for 10 min each, followed by plasma-cleaning for 3 min. For neat PBTTT thin film preparation, PBTTT was dissolved in anhydrous CB (10 mg/mL), and the solution was heated at 80 ℃ for 2 hours to fully dissolve the polymer. Then thin films were spin-coated using SCS G3P spin coater from the heated solution (80 ℃) using a two-step spin condition of 2000 rpm for 40s followed by 3000 rpm for 25s. Films were heated at 80 ℃ for 10 min to remove residual solvent. All solution preparation, spin-coating, and drying steps were performed in an Argon glovebox. Thickness of neat films were measured via ellipsometry, which was determined to be approximately 30 nm.

Vapor Doping Process. Vapor doping was performed in an Argon glovebox. Approximately 2 mg of F4TCNQ powder was pressed into a pellet (approximately 3 mm in diameter) and placed in an aluminum oxide crucible (OD 6.8 mm x H 4 mm from Government Scientific Source Inc.), which was in turn placed in a glass insert (diameter ~ 5 cm, height ~ 4.5

cm). A stainless-steel container was then preheated for 30 min on a hot plate to allow the chamber to reach a steady temperature at 200 ℃ (measured vial thermocouple at the base of the chamber). The glass insert with the dopant inside was put into the metal chamber to produce dopant vapor. For uniform doping of films (unsegmented films), a neat PBTTT thin film was held in a Teflon holder and placed on the top of the doping chamber. The doping level was controlled as a function of dopant exposure time. For this study, we define four doping levels: neat (**N**, 0 min), low (**L**, ~1.5 min), medium (**M**, ~2 min), and high (**H**, ~4 min) (Figure 2.2).

Double-segmented films were fabricated through a sequential vapor doping process. First, the whole polymer film was exposed to F4TCNQ vapor to achieve **L** doping level or **M** doping level. Second, the Teflon holder being was removed from the chamber and a Teflon bar (see dimensions in Figure 2.19 in Appendix) was then used as a mask to cover half of the film. Then, the holder was put back onto the chamber to further expose the uncovered half of the film to F4TCNQ vapor. For the film at **L** doping level, the film was exposed to F4TCNQ vapor for an additional 3 min to achieve an **LH** segmented film. For the film at **M** doping level, the film was exposed to F4TCNQ vapor for an additional 2 min to achieve a **MH** segmented film. Starting with a neat film, the films was exposed to F4TCNQ vapor for 4 min to achieve an **NH** segmented film.

UV-VIS-NIR. UV-VIS-NIR spectra of neat PBTTT and vapor-doped thin films on quartz substrates were obtained using the Shimadzu UV-3600 Plus UV-VIS-NIR Dual Beam Spectrophotometer housed in the Soft Matter Characterization Facility (SMCF) (Pritzker School of Molecular Engineering, University of Chicago). Measurements were taken within a wavelength range of 300 to 3300 nm.

Grazing Incidence Wide Angle X-ray Diffraction. GIWAXS experiments were conducted at the Advanced Photon Source (Argonne National Laboratory) at beamline 8-ID-E.

The energy of the incident beam was at 10.91 keV, and a Pilatus 1MF pixel array detector (pixel size = 172 μm) was used.[59] The measurement time for one image was 10 seconds. All samples were placed and measured in a low vacuum chamber (10^{-3} mbar) to reduce the air scattering as well as to minimize beam radiation damage. There are multiple rows of inactive pixels between the detector modules when the images were collected at one position. To fill these inactive gaps, the detector was moved down to a pre-set new position along the vertical direction after each measurement. After the image was collected at the new spot, the data from these two detector positions were combined using the GIXSGUI package for MATLAB to fill the inactive gaps.[60] The absence of artifacts in the combined image demonstrates that the scattering from the sample does not change during the exposure. The GIXSGUI package was also used to output the GIWAXS signals as intensity maps in (q_r, q_z) space, and take the linecuts along out-of-plane (q_z) and in-plane directions (q_r).

GIWAXS images of segmented thin films were taken at a grazing incident x-ray angle of 0.14°, which is above the critical angle of the polymer film and below the critical angle of the silicon substrate. GIWAXS images measured laterally across nine different spots for the double-segmented films. One measurement within each segment were 3 mm away from the interface of the segmented film. Other seven measurements were conducted laterally across the interface of the segmented films. The distance between adjacent spots is 200 μm, which is the width of the X-ray beam. Lastly, for the depth dependent experiments on doped PBTTT thin films, images were taken across a range of incidence angles (0.08°, 0.10°, 0.12°, 0.14°, 0.16°, 0.18°, 0.20°) to obtain scattering from the surface, bulk, and the polymer/substrate interface of doped PBTTT thin films (Figures 2.7).

Raman Spectroscopy. Raman spectroscopy experiments were performed under ambient conditions using the Horiba LabRAM HR Evolution NIR confocal Raman microscope housed in Chicago Materials Research Center. Raman spectra of neat and doped PBTTT thin films was collected using a 100◊ objective and a 532 nm wavelength laser. The Raman spectra on segmented thin films were collected using 50◊ objective and the same 532 nm wavelength laser. The spatial resolution of each measurement is dependent on the numerical aperture of the microscope objective, the wavelength of the laser used, and the pinhole size of the confocal imaging mode. In our configuration, the spatial resolution of each Raman spectra is calculated to be 0.65 μm. Laser power and accumulation time was set to 1% and 10 s to minimize local heating and material degradation. Spatial Raman spectra within each segment were acquired using a step size of 10 μm for a 100 μm x 100 μm region or using a step size of 1 μm for a 10 μm x 10 μm region for finer measurements. Spatial Raman spectra across the interface of the two segments were acquired using a step size of 10 μm for 1000 μm x 20 μm region. The time to collect a Raman map of 100 μm x 100 μm is about 5 – 6 minutes. This minimized possible degradations that occurred during the measurement.

To generate a Raman color map, the ratio of peak intensity of mode A (representing the C=C stretching mode on the thienothiophene core) and mode D (representing the C=C stretching localized on the thiophene rings) was recorded for every Raman spectrum. The recorded ratios were autosaved in text file by the software, and then exported into Wolfram Mathematica to plot as color maps. The color scale for every Raman map followed a rainbow color scheme where purple represents neat (ratio = 0.9) and red represents highly doped (ratio = 2.2).

Conductivity and Seebeck Measurements. Gold electrical contacts (75 nm thick) for electronic conductivity (σ) and Seebeck coefficient (α) measurements were deposited onto either

uniform or segmented PBTTT thin films via thermal evaporation through shadow masks designed in our lab. Electronic conductivity was measured in the in-plane direction using four probe geometry with a 0.2 mm spacing between electrodes and electrodes length of 1 mm. Seebeck coefficient was measured with two 1 mm^2 gold pads, which are either 3 mm or 1 mm apart. A detailed schematic is provided in Figure 2.20. Four probe conductivity measurements were performed using a custom-designed probe station in an Argon glovebox. Voltage and current measurements were performed using a Keithley 2400 source meter and Keithley 6221 precision current source. A constant current was applied to the outer contacts, and the resultant steady-state voltage response was recorded from the two inner contacts. The resistance (R; ohms) of the sample was extracted from the slope of the IV sweep using Ohm's law ($V = IR$). The thin film conductivity σ was then calculated using the following equation:

$$\sigma = \frac{\ln 2}{\pi h R}$$

where h = 30 nm is the thickness of the sample.

The Seebeck coefficient measurements were performed on the same probe station. Two Peltier elements were placed 5 mm apart to provide the temperature difference ($\Delta T = T_H - T_C$). Two thermocouples were used to collect the hot and cold side temperatures, and two probes were used to measure the corresponding voltage value. A minimal amount of thermally conductive silicone paste was applied to the tips of the thermocouple to ensure good thermal contact between the thermocouple and the gold pads. A delay of 200 s was used for voltage measurements to ensure that a steady-state temperature gradient and voltage was reached. The Seebeck coefficient was calculated from the slope of a linear fit for the ΔV versus ΔT plot. A representative plot can be found in Figure 2.21. The measurements were taken within an approximate ΔT of ± 3 K around

300 K so that the Seebeck coefficient did not change significantly over T ± ΔT. A series of measurements on Nickel foil (0.03mm, >99.9%) were carried out at 25 °C to determine the systematic error (Figure 2.22). The measured Seebeck coefficient of Ni is –20.3 ± 1.3 μV/K, which matched with reported value in literatures (–19 μV/K at 25 °C). [61–63]

The spatial measurements of the electronic conductivity were performed using an array of interdigitated electrodes (IDEs). Interdigitated electrode devices were fabricated at Pritzker Nanofabrication Facility, University of Chicago (see detailed fabrication process in Appendix and Figure 2.23). The measurements were performed using DC measurement method. The extracted resistance R was then used to calculate the electronic conductivity σ_{IDE} according to the following equation:

$$\sigma_{IDE} = \frac{1}{R}\frac{d}{l(N-1)h}$$

Here, d = 8 μm is the separation distance between electrodes, l = 100 μm is the electrode length, N = 40 is the number of electrodes and h = 30 nm is the thickness of the film.

2.5 Acknowledgments

This work was primarily supported by the University of Chicago Materials Research Science and Engineering Center, which is funded by National Science Foundation under award number DMR-1420709. B.X.D. was supported by NSF DMREF Award Number 1922259. This research used resources of the Advanced Photon Source, an Office of Science User Facility operated for the U.S. Department of Energy (DOE) by Argonne National Laboratory under Contract No. DE-AC02-06CH11357. Parts of this work were carried out at the Soft Matter Characterization Facility of the University of Chicago.

2.6 Appendix

Determination of doping level

The doping level (MR), the molar ratio of F4TCNQ anion to PBTTT monomer repeat unit, was determined through Beer's law by using the absorption intensity of the F4TCNQ anion at 1.4 eV and the primary absorption peak of neat PBTTT at 2.3 eV. The absorption spectra of all doped samples were deconvoluted to the neutral, anion, and polaron components using the peak shape and relative intensities (Figure 2.3). Then, the dopant concentration (C_{F4^-}) was estimated using Beer's law with the F4TCNQ anion molar extinction coefficient (ε = 50000 L mol^{-1} cm^{-1})[48] and the underlying monomer concentration was estimated from PBTTT extinction coefficient at 2.3eV (ε = 50000 L mol^{-1} cm^{-1}).

PBTTT molar extinction coefficient calculation

Density of PBTTT is calculated from mass of repeat unit per unit cell. The unit cell volume of PBTTT, V_{uc}, is calculated as:

$$V_{uc} = abc\sqrt{1 - cos(\alpha)^2 - cos(\beta)^2 - cos(\gamma)^2 + 2 \bullet \cos(\alpha) \bullet \cos(\beta) \bullet \cos(\gamma)} = 1060 \text{ Å}^3$$

with the following parameters[64,65] : a = 21.5 Å, b = 5.4 Å, c = 13.5 Å, α = 137°, β = 86°, and γ = 89°.

Density of PBTTT, ρ_{PBTTT}, is then calculated as:

$$\rho_{PBTTT} = \frac{M_{BTTT} \times N_{ru}}{N_A \times V_{uc}} = \frac{694\ g \bullet mol^{-1}}{6.022 \times 10^{23} mol^{-1} \times 1060 \times 10^{-24}\ cm^3} \approx 1.1\ g \bullet cm^{-3}$$

where, M_{BTTT} is the molar mass of repeat unit, N_{ru} is the number of repeat units per unit cell (1 in the case of PBTTT) and N_A is the Avogadro constant.

With density of PBTTT as 1.1 g/cm^3, the molar concentration of PBTTT, C_{PBTTT}, is found to be:

$$C_{PBTTT} = \frac{\rho_{PBTTT}}{M_{BTTT}} = 1.58\ mol \bullet L^{-1}$$

Using Beer's law, the molar extinction coefficient of PBTTT at 2.3 eV is estimated as:

$$\varepsilon_{PBTTT} = \frac{A_{PBTTT}}{C_{PBTTT} \times L} \approx 50000\ L \bullet mol^{-1} \bullet cm^{-1}$$

Where, A_{PBTTT} is the absorption of neat PBTTT at 2.3eV and L is the optical path length, in this case, the polymer film thickness (30 nm).

Origin of the formation of interface region

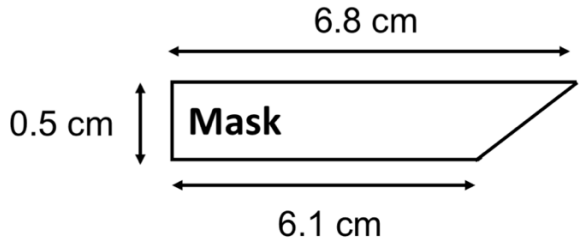

Figure 2.19: Schematic of the Teflon mask used in fabrication of double – segmented thin films.

Since conductivity measurement, GIWAXS and Raman experiments all confirmed the existence of a diffuse interface region between the two segments of our samples, it is important to understand the origin of the formation of this interfacial region. One possible explanation is the diffusion of dopant/anion during vapor doping process or after the segmented film is established. While the specific diffusion coefficient of F4TCNQ in PBTTT has not been reported yet, the

diffusion process of F4TCNQ in a similar thiophene-based polymer, P3HT upon thermal annealing has been studied.[66] Assuming that the diffusion coefficients of F4TCNQ dopant/anion in PBTTT is the same as in P3HT, we can estimate that the diffusion length of dopant/anion at 60 ℃ (during vapor doping) or under room temperature (after establishing segmented film) lies in the micrometer scale which is much lower than the observed width of the interfacial region in our study. Therefore, the formation of this interface is unlikely due to dopant or anion diffusion. We thus attribute the origin of the formation of the interface region to our specific fabrication process. In our experiments, the Teflon mask was placed slightly above the polymer surface to avoid scratches on the film. We suspect that this minor gap between the bar and polymer allowed a small amount of dopant vapor to diffuse underneath the bar, leading to the formation of the diffuse interface. This also explains why the interface regions are narrower in **LH** and **MH** segmented films as the time for dopant vapor diffusion is shorter.

Set-up and calibration for Seebeck measurement

Figure 2.20 shows the customized setup of the Seebeck coefficient measurement. Two peltier elements were placed 5 mm apart to provide the temperature difference ($\Delta T = T_H - T_C$). Gold contact pads 1 mm or 3 mm apart were evaporated onto the sample. The sample was placed in a way where the midpoint between gold pads was approximately the midline of the gap between the Peltier elements.

The thermocouples for temperature measurements and the tungsten tips for voltage measurements were aligned at the same vertical position when we did our Seebeck measurements. The thermocouple tip was placed at the edge of the gold pad, which was in vertical alignment with the strip for the voltage probe. This setup would allow the distance between the thermocouple

probes to be the same as distance between voltage tips in all of the measurements, which led to accurate Seebeck measurements. A minimal amount of thermal conductive silicon paste was applied to the thermocouple beads to ensure good thermal contact between the thermocouple and the sample. The Peltier elements were connected to make one side hot and one side cold when +1V applied and reverse the temperature gradient under –1V. There was a 200s settling time to reach the steady-state temperature gradient. At each temperature gradient, five consecutive measurements were taken 1 s apart. A typical Seebeck measurement scan is shown in Figure 2.21. For each sample, both forward and reverse scan were carried out to obtain an average Seebeck value.

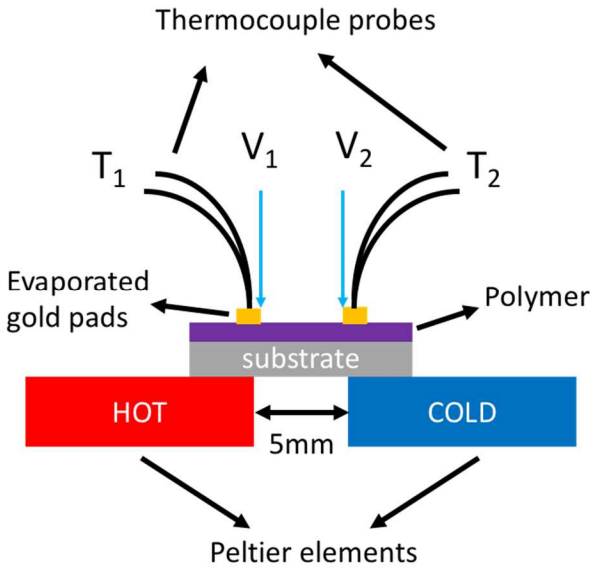

Figure 2.20: Schematic of Seebeck measurement setup.

Calibration measurements were carried out on multiple Nickel (>99.9%) samples from the same foil (Figure 2.22). After subtracting Seebeck coefficient of gold at 25 °C (+1.94 μV/K)[67], the average Seebeck coefficient of Ni was calculated to be –20.3 ± 1.3 μV/K, which matched well with previous literatures (–19 μV/K at 25 °C).[61–63] The systematic error was estimated from the standard deviation of the measurements, which is approximately 10%. Seebeck coefficients of

F4TCNQ-doped thiophene based polymers were measured using our Seebeck set-up (Figure 2.17). The dash line is an empirical relation between α and σ, which obeys a power law as α proportional to $\sigma^{-1/4}$ and matches with previous study on transport properties.[3]

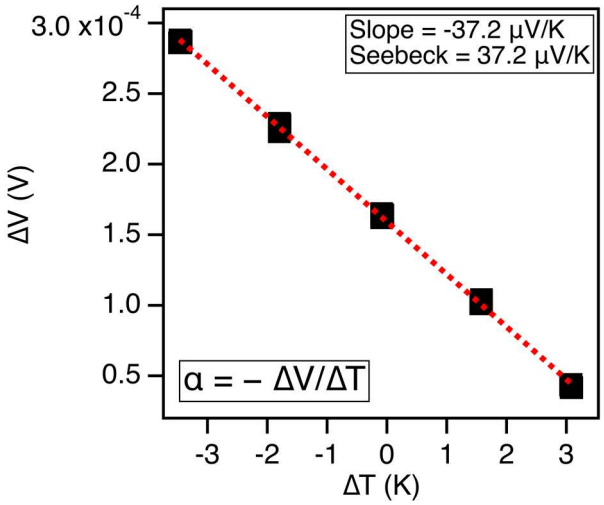

Figure 2.21: Typical Seebeck coefficient measurement curve (4 min doped PBTTT). Seebeck coefficient is the negative of the slope from the linear fit through the (ΔT, ΔV) points. 5 measurements for each steady-state ΔT are recorded.

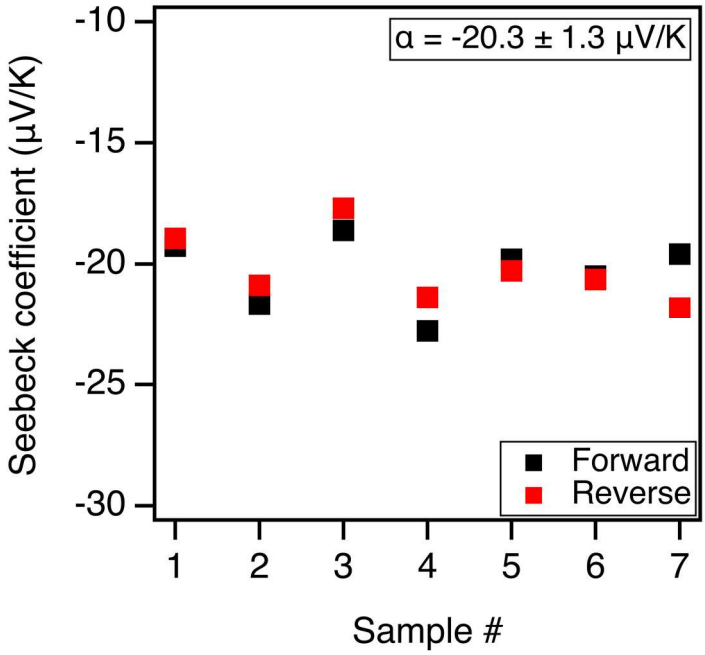

Figure 2.22: Seebeck coefficients of Nickel measured at 25°C.

Interdigitated electrode (IDE) fabrication

Si wafers with 1 μm of thermal oxide were first cleaned with a 300W oxygen plasma. A monolayer of hexamethyldisilazane (HMDS) is then deposited on the wafer in a vacuum oven at 110 °C under N2 flow to promote photoresist adhesion. AZ nlof 2020 negative photoresist was spun cast at 3500 rpm for 45 seconds onto the wafer. IDE pattern was written with a Heidelberg MLA150 Direct Write Lithographer and AZ 300 MIF developer (tetramethylammonium hydroxide in water) was used to remove the patterned areas of the photoresist. E-beam evaporation of 5 nm titanium followed by 95 nm of gold was then applied to create the electrodes using an Angstrom EvoVac electron-beam evaporator. Liftoff of the excess metal and removal of the remaining photoresist was achieved by soaking the wafer in an 80 °C bath of n-methyl-2-pyyrolidone (NMP) overnight followed by sonication in fresh NMP. Wafers were subsequently rinsed with acetone, IPA, and deionized water. A single 4" wafer contains as many as 24 IDE devices. The work flow for fabrication of the IDEs is shown in Figure 2.23.

Figure 2.23: Workflow for fabrication of micron sized IDEs.

2.7 References

(1) Salzmann, I.; Heimel, G.; Oehzelt, M.; Winkler, S.; Koch, N. Molecular Electrical Doping of Organic Semiconductors: Fundamental Mechanisms and Emerging Dopant Design Rules. *Acc. Chem. Res.* **2016**, *49* (3), 370–378.

(2) Jacobs, I. E.; Moulé, A. J. Controlling Molecular Doping in Organic Semiconductors. *Adv. Mater.* **2017**, *29* (42), 1703063.

(3) Glaudell, A. M.; Cochran, J. E.; Patel, S. N.; Chabinyc, M. L. Impact of the Doping Method on Conductivity and Thermopower in Semiconducting Polythiophenes. *Adv. Energy Mater.* **2015**, *5* (4), 1401072.

(4) Kroon, R.; Mengistie, D. A.; Kiefer, D.; Hynynen, J.; Ryan, J. D.; Yu, L.; Müller, C. Thermoelectric Plastics: From Design to Synthesis, Processing and Structure–Property Relationships. *Chem. Soc. Rev.* **2016**, *45* (22), 6147–6164.

(5) Zhang, Q.; Sun, Y.; Xu, W.; Zhu, D. What To Expect from Conducting Polymers on the Playground of Thermoelectricity: Lessons Learned from Four High-Mobility Polymeric Semiconductors. *Macromolecules* **2014**, *47* (2), 609–615.

(6) Guo, J.; Li, G.; Reith, H.; Jiang, L.; Wang, M.; Li, Y.; Wang, X.; Zeng, Z.; Zhao, H.; Lu, X.; Schierning, G.; Nielsch, K.; Liao, L.; Hu, Y. Doping High-Mobility Donor–Acceptor Copolymer Semiconductors with an Organic Salt for High-Performance Thermoelectric Materials. *Adv. Electron. Mater.* **2020**, *6* (3), 1900945.

(7) Liu, J.; Garman, M. P.; Dong, J.; van der Zee, B.; Qiu, L.; Portale, G.; Hummelen, J. C.; Koster, L. J. A. Doping Engineering Enables Highly Conductive and Thermally Stable N-Type Organic Thermoelectrics with High Power Factor. *ACS Appl. Energy Mater.* **2019**, *2* (9), 6664–6671.

(8) Untilova, V.; Biskup, T.; Biniek, L.; Vijayakumar, V.; Brinkmann, M. Control of Chain Alignment and Crystallization Helps Enhance Charge Conductivities and Thermoelectric Power Factors in Sequentially Doped P3HT:F4TCNQ Films. *Macromolecules* **2020**.

(9) Serrano-Claumarchirant, J. F.; Culebras, M.; Muñoz-Espí, R.; Cantarero, A.; Gómez, C. M.; Collins, M. N. PEDOT Thin Films with N-Type Thermopower. *ACS Appl. Energy Mater.* **2020**, *3* (1), 861–867.

(10) Lu, Y.; Wang, J.-Y.; Pei, J. Strategies To Enhance the Conductivity of N-Type Polymer Thermoelectric Materials. *Chem. Mater.* **2019**, *31* (17), 6412–6423.

(11) Russ, B.; Glaudell, A.; Urban, J. J.; Chabinyc, M. L.; Segalman, R. A. Organic Thermoelectric Materials for Energy Harvesting and Temperature Control. *Nat. Rev. Mater.* **2016**, *1* (10), 16050.

(12) Bahk, J.-H.; Fang, H.; Yazawa, K.; Shakouri, A. Flexible Thermoelectric Materials and Device Optimization for Wearable Energy Harvesting. *J. Mater. Chem. C* **2015**, *3* (40), 10362–10374.

(13) Chen, Y.; Zhao, Y.; Liang, Z. Solution Processed Organic Thermoelectrics: Towards Flexible Thermoelectric Modules. *Energy Environ. Sci.* **2015**, *8* (2), 401–422.

(14) Fang, H.; Popere, B. C.; Thomas, E. M.; Mai, C.-K.; Chang, W. B.; Bazan, G. C.; Chabinyc, M. L.; Segalman, R. A. Large-Scale Integration of Flexible Materials into Rolled and Corrugated Thermoelectric Modules. *J. Appl. Polym. Sci.* **2017**, *134* (3).

(15) Ryan, J. D.; Mengistie, D. A.; Gabrielsson, R.; Lund, A.; Müller, C. Machine-Washable PEDOT:PSS Dyed Silk Yarns for Electronic Textiles. *ACS Appl. Mater. Interfaces* **2017**, *9* (10), 9045–9050.

(16) Elmoughni, H. M.; Menon, A. K.; Wolfe, R. M. W.; Yee, S. K. A Textile□Integrated Polymer Thermoelectric Generator for Body Heat Harvesting. *Adv. Mater. Technol.* **2019**, *4* (7), 1800708.

(17) Jin, W.; Liu, L.; Yang, T.; Shen, H.; Zhu, J.; Xu, W.; Li, S.; Li, Q.; Chi, L.; Di, C.; Zhu, D. Exploring Peltier Effect in Organic Thermoelectric Films. *Nat. Commun.* **2018**, *9* (1), 3586.

(18) Snyder, G. J.; Toberer, E. S. Complex Thermoelectric Materials. *Nat. Mater.* **2008**, *7* (2), 105–114.

(19) Cochran, J. E.; Junk, M. J. N.; Glaudell, A. M.; Miller, P. L.; Cowart, J. S.; Toney, M. F.; Hawker, C. J.; Chmelka, B. F.; Chabinyc, M. L. Molecular Interactions and Ordering in Electrically Doped Polymers: Blends of PBTTT and F 4 TCNQ. *Macromolecules* **2014**, *47* (19), 6836–6846.

(20) Patel, S. N.; Glaudell, A. M.; Peterson, K. A.; Thomas, E. M.; O'Hara, K. A.; Lim, E.; Chabinyc, M. L. Morphology Controls the Thermoelectric Power Factor of a Doped Semiconducting Polymer. *Sci. Adv.* **2017**, *3* (6), e1700434.

(21) Lim, E.; Glaudell, A. M.; Miller, R.; Chabinyc, M. L. The Role of Ordering on the Thermoelectric Properties of Blends of Regioregular and Regiorandom Poly(3□ hexylthiophene). *Adv. Electron. Mater.* **2019**, 1800915.

(22) Scholes, D. T.; Hawks, S. A.; Yee, P. Y.; Wu, H.; Lindemuth, J. R.; Tolbert, S. H.; Schwartz, B. J. Overcoming Film Quality Issues for Conjugated Polymers Doped with F4TCNQ by Solution Sequential Processing: Hall Effect, Structural, and Optical Measurements. *J. Phys. Chem. Lett.* **2015**, *6* (23), 4786–4793.

(23) Jacobs, I. E.; Aasen, E. W.; Oliveira, J. L.; Fonseca, T. N.; Roehling, J. D.; Li, J.; Zhang, G.; Augustine, M. P.; Mascal, M.; Moulé, A. J. Comparison of Solution-Mixed and Sequentially Processed P3HT:F4TCNQ Films: Effect of Doping-Induced Aggregation on

Film Morphology. *J. Mater. Chem. C* **2016**, *4* (16), 3454–3466.

(24) Patel, S. N.; Glaudell, A. M.; Kiefer, D.; Chabinyc, M. L. Increasing the Thermoelectric Power Factor of a Semiconducting Polymer by Doping from the Vapor Phase. *ACS Macro Lett.* **2016**, *5* (3).

(25) Hynynen, J.; Kiefer, D.; Yu, L.; Kroon, R.; Munir, R.; Amassian, A.; Kemerink, M.; Müller, C. Enhanced Electrical Conductivity of Molecularly P-Doped Poly(3-Hexylthiophene) through Understanding the Correlation with Solid-State Order. *Macromolecules* **2017**, *50* (20), 8140–8148.

(26) Lim, E.; A. Peterson, K.; M. Su, G.; L. Chabinyc, M. Thermoelectric Properties of Poly(3-Hexylthiophene) (P3HT) Doped with 2,3,5,6-Tetrafluoro-7,7,8,8-Tetracyanoquinodimethane (F4TCNQ) by Vapor-Phase Infiltration. *Chem. Mater.* **2018**, *30* (3), 998–1010.

(27) Kang, K.; Watanabe, S.; Broch, K.; Sepe, A.; Brown, A.; Nasrallah, I.; Nikolka, M.; Fei, Z.; Heeney, M.; Matsumoto, D.; Marumoto, K.; Tanaka, H.; Kuroda, S.; Sirringhaus, H. 2D Coherent Charge Transport in Highly Ordered Conducting Polymers Doped by Solid State Diffusion. *Nat. Mater.* **2016**, *15* (8), 896–902.

(28) Hamidi-Sakr, A.; Biniek, L.; Bantignies, J.-L.; Maurin, D.; Herrmann, L.; Leclerc, N.; Lévêque, P.; Vijayakumar, V.; Zimmermann, N.; Brinkmann, M. A Versatile Method to Fabricate Highly In-Plane Aligned Conducting Polymer Films with Anisotropic Charge Transport and Thermoelectric Properties: The Key Role of Alkyl Side Chain Layers on the Doping Mechanism. *Adv. Funct. Mater.* **2017**, *27* (25), 1700173.

(29) Vijayakumar, V.; Zaborova, E.; Biniek, L.; Zeng, H.; Herrmann, L.; Carvalho, A.; Boyron, O.; Leclerc, N.; Brinkmann, M. Effect of Alkyl Side Chain Length on Doping Kinetics, Thermopower, and Charge Transport Properties in Highly Oriented F4TCNQ-Doped PBTTT Films. *ACS Appl. Mater. & Interfaces* **2019**, *11* (5), 4942–4953.

(30) Vijayakumar, V.; Zhong, Y.; Untilova, V.; Bahri, M.; Herrmann, L.; Biniek, L.; Leclerc, N.; Brinkmann, M. Bringing Conducting Polymers to High Order: Toward Conductivities beyond 10 5 S Cm −1 and Thermoelectric Power Factors of 2 MW m −1 K −2. *Adv. Energy Mater.* **2019**, 1900266.

(31) Liu, Z.; Meyers, M. A.; Zhang, Z.; Ritchie, R. O. Functional Gradients and Heterogeneities in Biological Materials: Design Principles, Functions, and Bioinspired Applications. *Prog. Mater. Sci.* **2017**, *88*, 467–498.

(32) Müller, E.; Drašar, Č.; Schilz, J.; Kaysser, W. A. Functionally Graded Materials for Sensor and Energy Applications. *Mater. Sci. Eng. A* **2003**.

(33) Almasi, D.; Sadeghi, M.; Lau, W. J.; Roozbahani, F.; Iqbal, N. Functionally Graded Polymeric Materials: A Brif Review of Current Fabrication Methods and Introduction of a Novel Fabrication Method. *Mater. Sci. Eng. C* **2016**, *64*, 102–107.

(34) Kuznetsov, V. L.; Kuznetsova, L. A.; Kaliazin, A. E.; Rowe, D. M. High Performance Functionally Graded and Segmented Bi2Te3-Based Materials for Thermoelectric Power Generation. *J. Mater. Sci.* **2002**, *37* (14), 2893–2897.

(35) Müller, E.; Zabrocki, K.; Goupil, C.; Snyder, G. J.; Seifert, W. Functionally Graded Thermoelectric Generator and Cooler Elements. In *Materials, Preparation, and Characterization in Thermoelectrics*; Rowe, D. M., Ed.; CRC Press, 2017; pp 46–81.

(36) Hedegaard, E. M. J.; Mamakhel, A. A. H.; Reardon, H.; Iversen, B. B. Functionally Graded (PbTe) 1– x (SnTe) x Thermoelectrics. *Chem. Mater.* **2018**, *30* (1), 280–287.

(37) Müller, E.; Walczak, S.; Seifert, W. Optimization Strategies for Segmented Peltier Coolers. *Phys. Status Solidi Appl. Mater. Sci.* **2006**, *203* (8), 2128–2141.

(38) Bian, Z.; Wang, H.; Zhou, Q.; Shakouri, A. Maximum Cooling Temperature and Uniform Efficiency Criterion for Inhomogeneous Thermoelectric Materials. *Phys. Rev. B - Condens. Matter Mater. Phys.* **2007**, *75* (24), 1–7.

(39) Bian, Z.; Shakouri, A. Cooling Enhancement Using Inhomogeneous Thermoelectric Materials. In *2006 25th International Conference on Thermoelectrics*; IEEE, 2006; pp 264–267.

(40) Belov, I. M.; Volkov, V. P.; Manyakin, O. Optimization of Peltier Thermocouple Using Distributed Peltier Effect. *Thermoelectr. 1999. Eighteenth Int. Conf.* **1999**, No. 095, 316–318.

(41) Kim, C.; Kim, D. H.; Kim, J. S.; Han, Y. S.; Chung, J. S.; Kim, H. A Study of the Synthesis of Bismuth Tellurium Selenide Nanocompounds and Procedures for Improving Their Thermoelectric Performance. *J. Alloys Compd.* **2011**, *509* (39), 9472–9478.

(42) Vikhor, L. N.; Anatychuk, L. I. Theoretical Evaluation of Maximum Temperature Difference in Segmented Thermoelectric Coolers. *Appl. Therm. Eng.* **2006**, *26* (14–15), 1692–1696.

(43) Zhang, Q.; Liao, J.; Tang, Y.; Gu, M.; Ming, C.; Qiu, P.; Bai, S.; Shi, X.; Uher, C.; Chen, L. Realizing a Thermoelectric Conversion Efficiency of 12% in Bismuth Telluride/Skutterudite Segmented Modules through Full-Parameter Optimization and Energy-Loss Minimized Integration. *Energy Environ. Sci.* **2017**, *10* (4), 956–963.

(44) Cramer, C. L.; Wang, H.; Ma, K. Performance of Functionally Graded Thermoelectric Materials and Devices: A Review. *J. Electron. Mater.* **2018**, *47* (9), 5122–5132.

(45) Snyder, G. J.; Toberer, E. S. Complex Thermoelectric Materials. *Nat. Mater.* **2008**, *7* (2), 105–114.

(46) Sallehin, N. Z. I. M.; Yatim, N. M.; Suhaimi, S. A Review on Fabrication Methods for Segmented Thermoelectric Structure. In *AIP Conference Proceedings*; 2018; Vol. 030003, p 030003.

(47) Seifert, W.; Ueltzen, M.; Müller, E. One-Dimensional Modelling of Thermoelectric Cooling. *Phys. Status Solidi Appl. Res.* **2002**, *194* (1), 277–290.

(48) Thiébaut, E.; Goupil, C.; Pesty, F.; D'Angelo, Y.; Guegan, G.; Lecoeur, P. Maximization of the Thermoelectric Cooling of a Graded Peltier Device by Analytical Heat-Equation Resolution. *Phys. Rev. Appl.* **2017**, *8* (6), 064003.

(49) Dixon, D. A.; Calabrese, J. C.; Miller, J. S. Crystal and Molecular Structure of the 2:1 Charge-Transfer Salt of Decamethylferrocene and Perfluoro-7,7,8,8-Tetracyano-p-Quinodimethane: [[Fe(C5Me5)2]+.Cntdot.]2[TCNQF4]2-. The Electronic Structure of [TCNQF4]n (n = 0, 1-, 2-). *J. Phys. Chem.* **1989**, *93* (6), 2284–2291.

(50) Chabinyc, M. L.; Toney, M. F.; Kline, R. J.; McCulloch, I.; Heeney, M. X-Ray Scattering Study of Thin Films of Poly(2,5-Bis(3-Alkylthiophen-2-Yl)Thieno[3,2- b]Thiophene). *J. Am. Chem. Soc.* **2007**, *129* (11), 3226–3237.

(51) DeLongchamp, D. M.; Kline, R. J.; Jung, Y.; Germack, D. S.; Lin, E. K.; Moad, A. J.; Richter, L. J.; Toney, M. F.; Heeney, M.; McCulloch, I. Controlling the Orientation of Terraced Nanoscale "Ribbons" of a Poly(Thiophene) Semiconductor. *ACS Nano* **2009**, *3* (4), 780–787.

(52) Mcculloch, I.; Heeney, M.; Chabinyc, M. L.; Delongchamp, D.; Kline, R. J.; Cölle, M.; Duffy, W.; Fischer, D.; Gundlach, D.; Hamadani, B.; Hamilton, R.; Richter, L.; Salleo, A.; Shkunov, M.; Sparrowe, D.; Tierney, S.; Zhang, W. Semiconducting Thienothiophene Copolymers: Design, Synthesis, Morphology, and Performance in Thin-Film Organic Transistors. *Adv. Mater.* **2009**, *21* (10–11), 1091–1109.

(53) Scholes, D. T.; Yee, P. Y.; Lindemuth, J. R.; Kang, H.; Onorato, J.; Ghosh, R.; Luscombe, C. K.; Spano, F. C.; Tolbert, S. H.; Schwartz, B. J. The Effects of Crystallinity on Charge Transport and the Structure of Sequentially Processed F 4 TCNQ-Doped Conjugated Polymer Films. *Adv. Funct. Mater.* **2017**, *27* (44), 1702654.

(54) Kiefer, D.; Kroon, R.; Hofmann, A. I.; Sun, H.; Liu, X.; Giovannitti, A.; Stegerer, D.; Cano, A.; Hynynen, J.; Yu, L.; Zhang, Y.; Nai, D.; Harrelson, T. F.; Sommer, M.; Moulé, A. J.; Kemerink, M.; Marder, S. R.; McCulloch, I.; Fahlman, M.; Fabiano, S.; Müller, C. Double Doping of Conjugated Polymers with Monomer Molecular Dopants. *Nat. Mater.* **2019**, *18* (2), 149–155.

(55) Liu, W.; Müller, L.; Ma, S.; Barlow, S.; Marder, S. R.; Kowalsky, W.; Köhn, A.; Lovrincic, R. Origin of the π–π Spacing Change upon Doping of Semiconducting Polymers. *J. Phys. Chem. C* **2018**, *122* (49), 27983–27990.

(56) Tietze, M. L.; Benduhn, J.; Pahner, P.; Nell, B.; Schwarze, M.; Kleemann, H.; Krammer, M.; Zojer, K.; Vandewal, K.; Leo, K. Elementary Steps in Electrical Doping of Organic Semiconductors. *Nat. Commun.* **2018**, *9* (1), 1182.

(57) Francis, C.; Fazzi, D.; Grimm, S. B.; Paulus, F.; Beck, S.; Hillebrandt, S.; Pucci, A.; Zaumseil, J. Raman Spectroscopy and Microscopy of Electrochemically and Chemically Doped High-Mobility Semiconducting Polymers. *J. Mater. Chem. C* **2017**, *5* (25), 6176–6184.

(58) Fujimoto, R.; Yamashita, Y.; Kumagai, S.; Tsurumi, J.; Hinderhofer, A.; Broch, K.; Schreiber, F.; Watanabe, S.; Takeya, J. Molecular Doping in Organic Semiconductors: Fully Solution-Processed, Vacuum-Free Doping with Metal-Organic Complexes in an Orthogonal Solvent. *J. Mater. Chem. C* **2017**, *5* (46), 12023–12030.

(59) Paternò, G. M.; Robbiano, V.; Fraser, K. J.; Frost, C.; Garciá Sakai, V.; Cacialli, F. Neutron Radiation Tolerance of Two Benchmark Thiophene-Based Conjugated Polymers: The Importance of Crystallinity for Organic Avionics. *Sci. Rep.* **2017**, *7* (January), 1–10.

(60) Jiang, Z.; Li, X.; Strzalka, J.; Sprung, M.; Sun, T.; Sandy, A. R.; Narayanan, S.; Lee, D. R.; Wang, J. The Dedicated High-Resolution Grazing-Incidence X-Ray Scattering Beamline 8-ID-E at the Advanced Photon Source. *J. Synchrotron Radiat.* **2012**, *19* (4), 627–636.

(61) Jiang, Z. GIXSGUI: A MATLAB Toolbox for Grazing-Incidence X-Ray Scattering Data Visualization and Reduction, and Indexing of Buried Three-Dimensional Periodic Nanostructured Films. *J. Appl. Crystallogr.* **2015**, *48*, 917–926.

(62) Beretta, D.; Bruno, P.; Lanzani, G.; Caironi, M. Reliable Measurement of the Seebeck Coefficient of Organic and Inorganic Materials between 260 K and 460 K. *Rev. Sci. Instrum.* **2015**, *86* (7), 75104.

(63) Abadlia, L.; Gasser, F.; Khalouk, K.; Mayoufi, M.; Gasser, J. G. New Experimental Methodology, Setup and LabView Program for Accurate Absolute Thermoelectric Power and Electrical Resistivity Measurements between 25 and 1600 K: Application to Pure Copper, Platinum, Tungsten, and Nickel at Very High Temperatures. *Rev. Sci. Instrum.* **2014**, *85* (9), 95121.

(64) Schmidt, V.; Mensch, P. F. J.; Karg, S. F.; Gotsmann, B.; Das Kanungo, P.; Schmid, H.; Riel, H. Using the Seebeck Coefficient to Determine Charge Carrier Concentration, Mobility, and Relaxation Time in InAs Nanowires. *Appl. Phys. Lett.* **2014**, *104* (1), 12113.

Chapter 3: CONTINUOUSLY GRADED DOPED SEMICONDUCTING POLYMERS ENHANCES THERMOELECTRIC COOLING

Reprinted from [Applied Physics Letters 119, 013902 (2021)], with the permission of AIP Publishing.

Spatial control of thermoelectric (TE) material properties through functional grading is a promising strategy in improving cooling performance. Notably, studies on organic-based FGMs for thermoelectrics have been limited compared to their inorganic-based counterparts. In this chapter, we demonstrate how the inherent processability of semiconducting polymers coupled with molecular doping provides for a facile approach in fabricating continuously graded (CG) thin films beneficial for thermoelectric (Peltier) cooling. We achieve CG thin films with 1D profiles in conductivity (σ) and Seebeck coefficient (α) through spatial compositional control of the molecular p-dopant 2,3,5,6-tetrafluoro-7,7,8,8-tetracyanoquinodimethane (F4TCNQ) in semiconducting poly[2,5-bis(3-tetradecylthiophen-2-yl) thieno [3,2-b]thiophene] (PBTTT). Using the experimentally derived σ and α spatial profiles, linear constitutive relations coupled with conservation of charge and energy are used to model the cooling performance of the CG thin films. In comparison to their equivalent uniform (EU) conditions, the CG thin films yield higher cooling temperature ($\Delta T_c = T_H - T_C$) and higher Coefficient of Performance (*C.O.P.*). The enhanced performance arises from efficient redistribution of the Joule heating and Peltier cooling effects. Moreover, the model calculations reveal that the magnitude of the σ profile and the slope of the α profile are specific attributes leading to the enhanced cooling in CG thin films. Overall, this study

highlights a simple yet powerful strategy to enhance the cooling performance of thermoelectric materials through functionally graded doped semiconducting polymers.

3.1 Introduction

Thermoelectric (TE) systems have been a promising technology that interconverts heat and electrical energy.[1–6] TEs can be used for both energy harvesting by capturing waste heat as in thermoelectric generators and thermal energy management by controlling local temperature as in Peltier coolers. The efficiency of TE devices is characterized by its figure of merit, *ZT*, defined as $ZT = \alpha^2 \sigma T/\kappa$; where σ is the electronic conductivity, α is the Seebeck coefficient, κ is the thermal conductivity and T is the temperature in Kelvin.[1] Over the years, researchers have been focusing on enhancing the material's *ZT* to improve the performance of thermoelectric devices. Along with the effort on material optimization, the use of functionally graded materials (FGMs) offers alternative ways to further improve device performance, especially in the case of Peltier coolers. FGMs are engineered materials whose properties are varied spatially either in a continuous or step-by-step (segmented) fashion throughout the volume of the material.[7–9] To date, implementing FGMs in Peltier cooling applications has been exclusively investigated with inorganic TE materials such as Bi_2Te_3 and PbTe.[9–14] In principle, functionally grading motifs with spatial variation in the thermoelectric properties enable more efficient redistribution of the Joule heating and Peltier cooling effects. This redistribution of heat leads to larger cooling temperature gradients and coefficient of performance (*C.O.P.*) compared to thermoelectric materials with uniform properties.[8,15–18] Importantly, modeling and simulations of inorganic FGMs as TE devices have been critical to elaborate optimal gradients in TE properties and establish the theoretical limits of cooling performance.[17,19–25] However, implementing the principles of functional grading using inorganic materials could be prohibitive as the fabrication and processing of conventional

inorganic TE materials would require high temperature and pressure to achieve appropriate graded/segmented configurations.[8,10–12,26,27]

In contrast to inorganic-based materials, semiconducting conjugated polymers with their inherent processability opens the pathway for easier experimental methods of achieving FGMs. Together with solution and thermal processability, principles of molecular doping of semiconducting polymers controls the carrier concentrations modulating thermoelectric properties.[28–31] In recent years, due to their promising performance near room temperature, cooling ability of polymeric materials has been demonstrated to reveal the Pelter effect in organic thin film devices.[32–34] Particularly, for the case of thiophene-based semiconducting polymers, the addition of a molecular *p*-dopant such as a small organic acceptor (e.g. F4TCNQ, 2,3,5,6-tetrafluoro-7,7,8,8-tetracyanoquinodimethane) leads to electron transfer between the host polymer and dopant molecule, which modulates the carrier concentration and therefore tuning the thermoelectric properties.[35,36] In our prior work, we showcased the first report on organic FGM for thermoelectrics by first casting a thin film of poly[2,5-bis(3-tetradecylthiophen-2-yl) thieno [3,2-b]thiophene] (PBTTT) and then infiltrating with F4TCNQ via the vapor doping method.[37] By using a home-built vapor doping apparatus, we were able to achieve a macroscopic double segmented FGMs where each segment were tuned to have different doping level. Our work showcased the facile fabrication and characterization of functionally graded polymer thin films for TE materials, which opened pathways for further development on more complex FGMs.

In this chapter, we report on continuously graded (CG) thin films relevant to improved thermoelectric (Peltier) cooling. Spatial compositional control of the molecular *p*-dopant F4TCNQ in semiconducting PBTTT yield 1D profiles in σ and α. Moreover, first principle calculations based on linear Onsager theory and conservation of charge and energy are used to model the

cooling performance of using the experimentally derived σ and α spatial profiles to demonstrate the utility of the CG thin films.

3.2 Results and Discussion

3.2.1 Fabricating Continuously Graded Films through Sequential Vapor Doping

CG thin films of PBTTT:F4TCNQ, *i.e.* samples that have an in-plane, 1D lateral compositional gradient in molecular doping, were fabricated through sequential vapor doping (Figure 3.1). In the vapor doping process, a neat PBTTT thin film is spin coated prior to the addition of F4TCNQ. As reported previously, this process largely preserves the molecular and long-range order of the polymer thin film, resulting in higher σ compared to films made through the solution-mixing doping process.[35,38–40] Importantly, sequential vapor doping allows for a relatively simple approach in achieving doping gradients along the in-plane, lateral direction of the thin film. Figure 3.1b shows a schematic of our home-built apparatus for controlled vapor doping of polymer thin films in an argon atmosphere glovebox. We use a cover mask where the side facing the PBTTT thin film has a *c.a.* 0.10° wedge grading angle that leaves a narrow gap between PBTTT thin film surface and the mask. This gap controls the mass flux of F4TCNQ to the thin film and, thus, controls the doping level gradient as a function of doping time.

To first demonstrate the feasibility of this approach in achieving CG thin films, a neat PBTTT thin film (*ca.* 30 nm) was vapor doped by F4TCNQ with the cover mask using a doping time of 4 min (see Figure 2.3 and Table 3.1 for the correlation of doping time and doping level in PBTTT:F4TCNQ films).[37] Spatial distribution of σ for the resulting PBTTT:F4TCNQ thin film was measured through arrays of interdigitated electrodes (IDEs) across the dopant graded thin film in order to determine the presence of a continuous gradient in σ (Figure 3.1c). There are in total 20 IDEs and each IDE measures a 100 μm by 300 μm region and is laterally spaced apart by 200

μm, thus measuring spatially across a total distance of 4 mm. This spatial distribution reveals the presence of a gradual gradient in σ where σ increases across the graded region from the neat side to the doped side of the film.

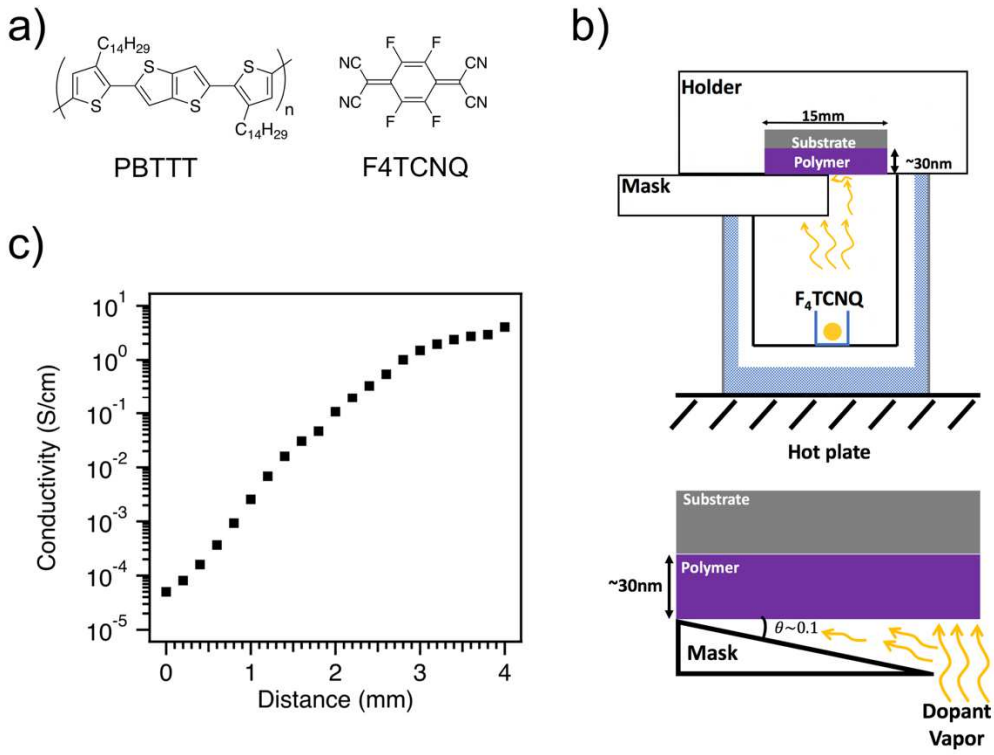

Figure 3.1: a) Chemical structures of the semiconducting polymer (PBTTT) and the molecular p-dopant (F4TCNQ). b) Schematic drawing of setup used to vapor dope PBTTT with F4TCNQ to achieve continuously graded (CG) thin films. The bottom schematic highlights the small wedge grading angle (*c.a.* 0.10°) of the cover mask which controls the mass flux of F4TCNQ to the thin film, which allows for an in-plane, 1D lateral compositional gradient in doping. c) 1D conductivity profile of as a function of distance along the doping gradient for a representative CG thin film.

Table 3.1: Doping time and molar ratio at different doping times

Doping Time (min)	MR
0	0
1.5	0.04
2	0.09
4	0.23

To verify the gradient in σ arises from the compositional gradient of the dopant, grazing incidence wide angle X-ray scattering (GIWAXS) experiments were performed on a representative CG thin film. GIWAXS images of PBTTT:F4TCNQ neat to doped graded films are shown in Figure 3.2. The overall scattering patterns are qualitatively similar to neat PBTTT, which indicates that vapor infiltration with F4TCNQ largely preserves the semicrystalline morphology of PBTTT and is consistent with previous reports.[35,37,41]

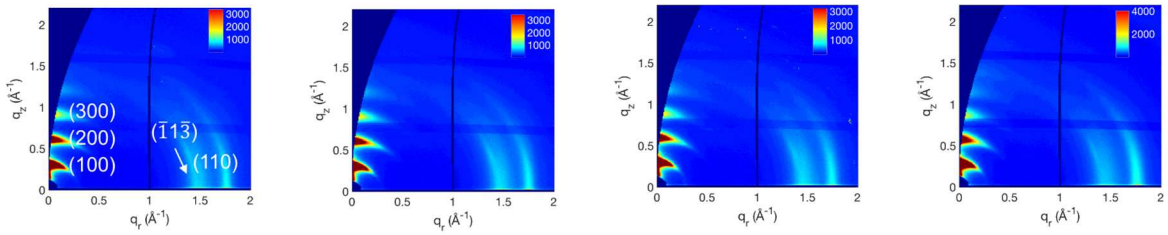

Figure 3.2: 2D GIWAXS images collected at different positions across PBTTT:F4TCNQ continuously graded film every 2 mm from neat to doped side.

By taking linecuts along the out-of-plane and in-plane directions (Figure 3.3), we can observe quantitative changes through the characteristic side-chain stacking (d_{100}) and π-π stacking ($d_{\pi\text{-}\pi}$) distances measured from neat side of the film to the doped side. Starting from neat side, d_{100} = 2.05 nm and maintains this value within the first 2 mm. Then, we observe a gradual increase of d_{100} to 2.27 nm over a total 4 mm distance until stabilizing at the doped side of the film (Figure 3.4a). As shown in Figure 3.4b, the spatial distribution $d_{\pi\text{-}\pi}$ shows similar trend, but inversely correlated. These changes d_{100} and $d_{\pi\text{-}\pi}$ are arises from the dopant F4TCNQ anion residing within regions of the side chain domain where an expansion of d_{100} and compression $d_{\pi\text{-}\pi}$ are observed. Therefore, both spatial profiles of d_{100} and $d_{\pi\text{-}\pi}$ indicate a gradient in dopant distribution of *c.a.* 4 mm, which correlates well with the gradient profile distance as observed in IDE conductivity measurements.

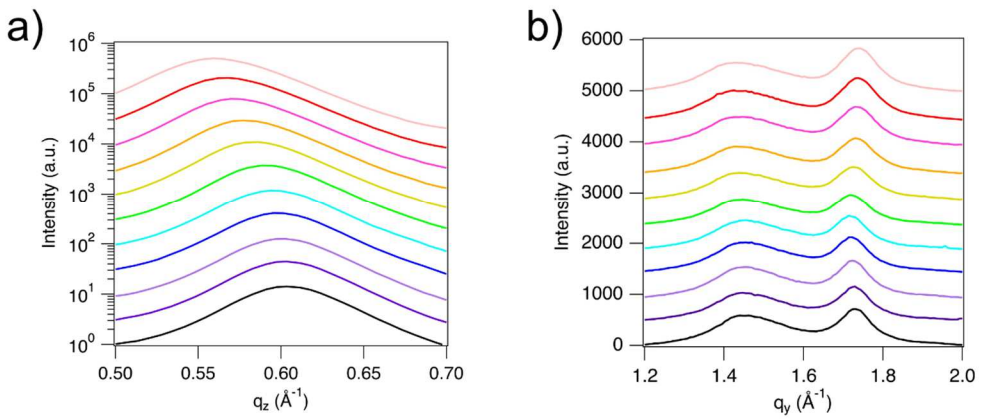

Figure 3.3: (a) Out-of-plane (200) scattering peak profiles and (b) In-plane scattering profiles for $(\bar{1}1\bar{3})$ and (110) across the continuously graded films every 400 µm. The black curve represents the measurement on neat side and light pink curve represents the measurement on doped side.

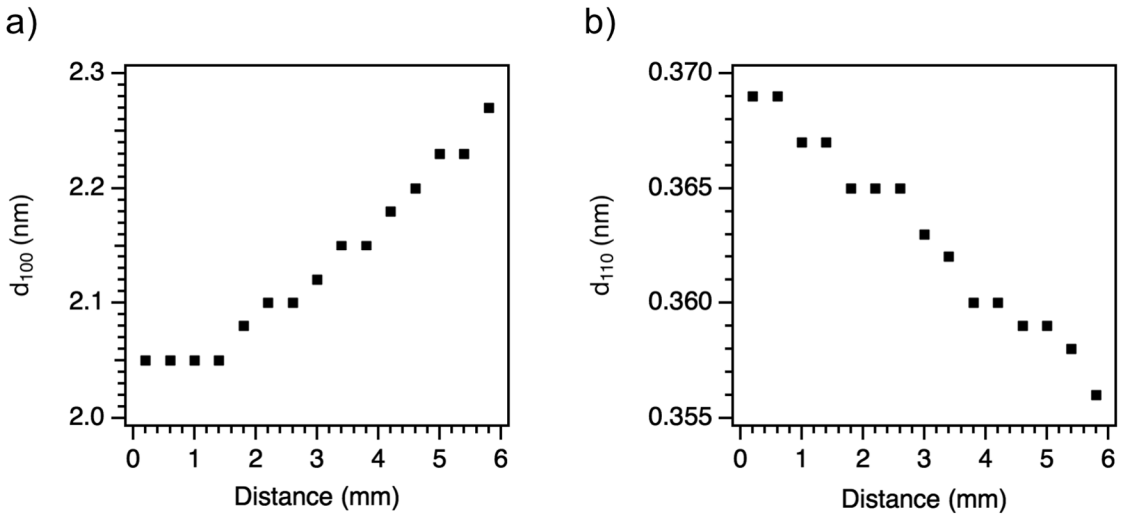

Figure 3.4: a) Side chain stacking spacing (d_{100}) and b) π-stacking spacing (d_{110}) across graded PBTTT thin films obtained from GIWAXS.

3.2.2 Continuously Graded Profiles in Seebeck Coefficient and Conductivity

To explore different gradient profiles, we fabricated three CG thin films with varying magnitudes in gradient of both σ and α across a 4 mm distance. These different gradients were achieved by varying the vapor doing time in our fabrication process described above. The graded profiles of the three thin films are shown in Figure 3.5 and are assigned CG1, CG2 and CG3.

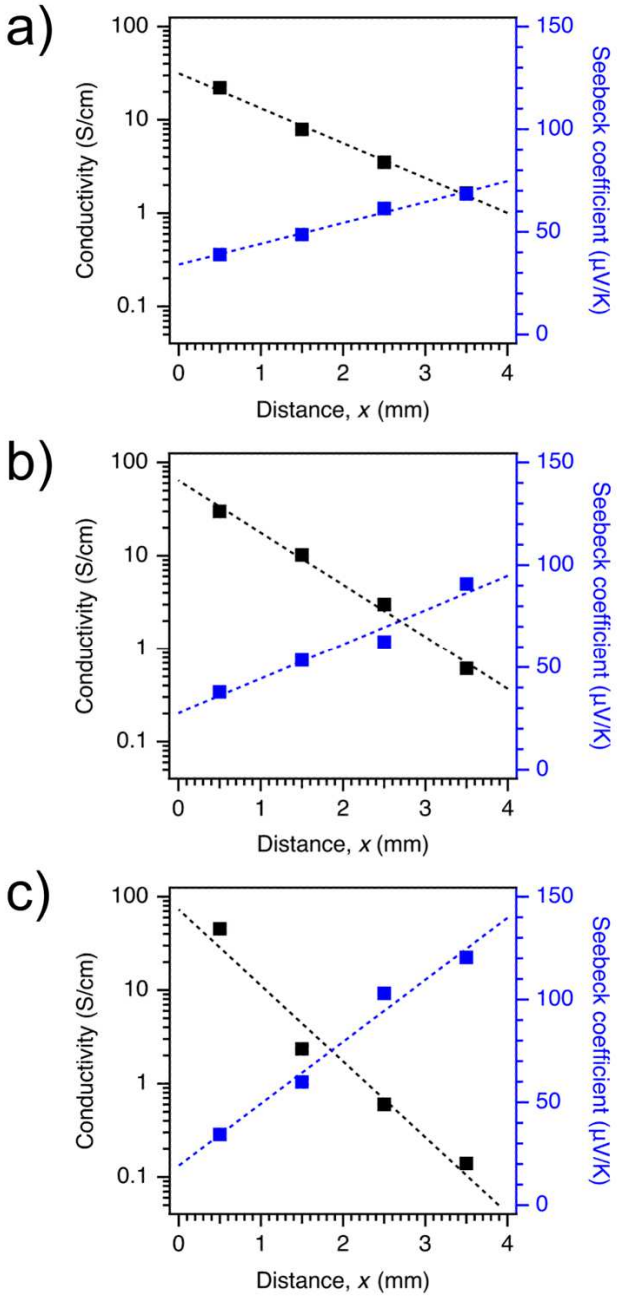

Figure 3.5: Experimentally measured Seebeck coefficient (α, blue square) and conductivity (σ, black square) values along the 1D gradient distance, x, for three CG thin films exhibiting different extent of grading: (a) CG1 (b) CG2 and (c) CG3 thin films. The dashed lines represent fits to α and σ data from x = 0 to x = 4 mm. α(x) follows a linear profile while σ(x) follows an exponential profile (note log-scale on the plot). Fit values are summarized in Table 1. In this profile, hot side (T_H) is set at x = 4 and the cold side (T_C) set at x = 0.

Both α and σ were spatially measured at four spots along the desired in-plane, lateral gradient direction (Figure 3.6). The measured values of σ and α across CG thin films are summarized in Table 3.2 & 3.3. As seen in Figure 3.5, α follows a linear profile whereas the conductivity follows an exponential trend (note the log-scale of the conductivity axis). The spatial distribution in $\alpha(x)$ was fit to a linear equation $[\alpha(x) = kx + m]$ and the spatial distribution in $\sigma(x)$ was fit to an exponential equation $[\sigma(x) = a\exp(bx)]$, where *k, m, a* and *b* has the unit of μV/mm·K, μV/K, S/cm and mm^{-1}, respectively. The fit values for these equations are provided in the Table 3.4. The slope of the $\alpha(x)$ profile increases from CG1 to CG3. Specifically, $\alpha(x)$ slopes are 10.1, 16.8 and 30.1 μV/mm·K for CG1, CG2 and CG3, respectively. Moreover, the decay in $\sigma(x)$ profile increases from CG1 to CG3. The spatial averages of the conductivity (σ_{avg}) and Seebeck coefficient (α_{avg}) for CG thin film were calculated by integrating the gradient profile expressions across the total lateral distance (L) of 4 mm (see details in Appendix).

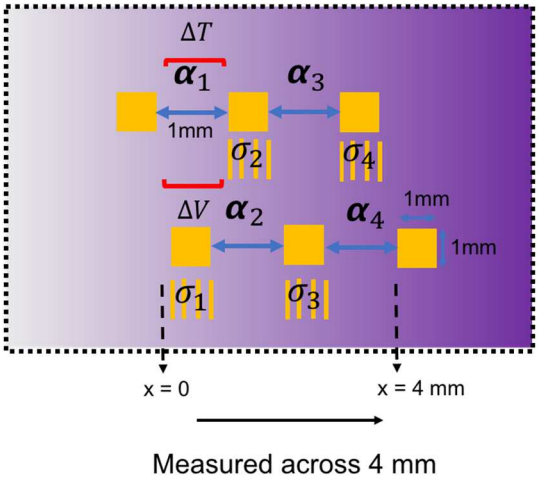

Figure 3.6: Geometry of gold contacts for Seebeck coefficients and conductivity measurements of continuously graded films. Seebeck coefficient and conductivity were measured with across a 1 mm interval at 4 positions along the graded film.

Table 3.2: Seebeck coefficient data across the continuously graded PBTTT:F4TCNQ films

Sample	α_1 (μV/K) (x = 0.5 mm)	α_2 (μV/K) (x = 1.5 mm)	α_3 (μV/K) (x = 2.5 mm)	α_4 (μV/K) (x = 3.5 mm)	α_{avg} (μV/K)
CG1	38.9	48.7	61.4	68.5	54.4
CG2	37.9	53.5	62.5	90.8	61.2
CG3	34.4	59.9	103.0	120.4	79.4

Table 3.3: Conductivity data across the continuously graded PBTTT:F4TCNQ films

Sample	σ_1 (S/cm) (x = 0.5 mm)	σ_2 (S/cm) (x = 1.5 mm)	σ_3 (S/cm) (x = 2.5 mm)	σ_4 (S/cm) (x = 3.5 mm)	σ_{avg} (S/cm)
CG1	22.0	7.91	3.51	1.64	3.58
CG2	29.9	10.2	3.00	0.610	1.92
CG3	45.3	2.35	0.600	0.140	0.308

Table 3.4: Thermoelectric Transport Properties and Model Calculated Cooling Temperature (ΔT_c) of CG PBTTT:F4TCNQ Thin Films

CG Thin Film	**$\sigma(x)$[a] (S/cm)**	**$\alpha(x)$[a] (μV/K)**	**σ_{avg} (S/cm)**	**α_{avg} (μV/K)**	**ΔT_c (K) j = 3 mA/mm^2**	**ΔT_c (K) $C.O.P$ = 0.8**
CG1	$31.5\exp(-0.86x)$	$10.1x + 34.1$	3.58	54.4	0.75	10.5
CG2	$64.2\exp(-1.29x)$	$16.8x + 27.6$	1.92	61.2	1.64	9.78
CG3	$72.9\exp(-1.87x)$	$30.1x + 19.2$	0.308	79.4	12.8	3.51

[a] x is in the unit of mm.

Here, these spatial average values were used to define an equivalent uniform (EU) condition for each corresponding experimentally derived CG thin film.

3.2.3 Model-Based Calculations of Cooling Performance for the Experimentally Derived Continuously Graded Films

To better understand the utility of the experimentally derived CG profiles compared to their EU values, we modeled the cooling performance through first principle calculations based on linear Onsager theory and conservation of charge and energy.[42] Following the work of Müller and co-workers,[22] the generalized constitutive equations for isotropic conditions are as follows

$$\boldsymbol{j} = \sigma \boldsymbol{E} - \sigma\alpha \boldsymbol{\nabla} T \qquad (3.1)$$

$$\boldsymbol{q} = \alpha T \boldsymbol{j} - \kappa \boldsymbol{\nabla} T \qquad (3.2)$$

where, $\boldsymbol{j}$ is the current density, $\boldsymbol{E}$ is the electrical field, $\boldsymbol{q}$ is the heat flux, T is temperature, σ is the electronic conductivity, α is the Seebeck coefficient, κ is the thermal conductivity. Additionally, at steady-state conditions, conservation of charge and energy are the following:

$$\boldsymbol{\nabla} \cdot \boldsymbol{j} = 0 \qquad (3.3)$$

$$\boldsymbol{\nabla} \cdot \boldsymbol{q} = \boldsymbol{j} \cdot \boldsymbol{E} \qquad (3.4)$$

Based on the experimentally derived CG profiles, the constitutive equations can be reasonably simplified to model the case of 1D transport along the x-direction as shown in Equation 3.5. More detailed derivation of this equation and explanation on contribution of the different heat fluxes in a Peltier cooler can be found in the Appendix.

$$-\kappa \frac{\partial^2 T(x)}{\partial x^2} = \frac{j^2}{\sigma(x)} - j \frac{d\alpha(x)}{dx} T(x) \qquad (3.5)$$

The term on the left-hand side of the equation ($-\kappa \frac{\partial^2 \mathrm{T(x)}}{\partial \mathrm{x}^2}$) refers to thermal conduction, the first term on the right-hand side ($\frac{\mathrm{j}^2}{\sigma(\mathrm{x})}$) refers to Joule heating and the second term on the right-hand

side ($-j\frac{d\alpha(x)}{dx}T(x)$) refers to Peltier cooling. Importantly, the derivation of Equation 3.5 assumes κ is constant across the length of the CG film where composition of dopant varies. While such an assumption is valid for the range in doping levels used this study based on reported values of κ for PBTTT:F4TCNQ thin films,[43] it is important to note that other material with higher doping levels and σ will need to account for the doping level dependence in κ.

Integration of Equation 3.5 was performed to calculate the 1D temperature profile $T(x)$ at specific values of j for two cases: *Case 1* – EU conditions where σ and α are spatially constant and *Case 2* – CG profiles of $\sigma(x)$ and $\alpha(x)$. Note that $T(x)$ is calculated assuming no heat transfer between the thin film and glass substrate. For *Case 1*, Equation 3.5 can be further simplified, and an analytical solution can be obtained (see Appendix for details). The values of σ and α when solving for Case 1 were determined through spatial averaging of $\sigma(x)$ and $\alpha(x)$ (Equations S3.1 and S3.2) as described earlier and reported in Table 3.4. For *Case 2*, the inclusion of the spatial dependence of $\sigma(x)$ and $\alpha(x)$ leads to non-linear differential equation requiring numerical integration of Equation 3.5, which was done using custom Python code. For both cases, a mixed boundary condition was applied where the hot side T_H ($x = L$) is fixed to 300 K and the heat flux on the hot side is constant. Upon determining the $T(x)$ profile, the cooling temperature, ΔT_c, is calculated from T_H minus the resulting temperature at the cold side ($T_C = T(x=0)$).

To calibrate for the range of j values in determining $T(x)$ and ΔT_c, the coefficient of performance (*C.O.P.*) were calculated using the gradient profiles of the CG thin films. *C.O.P.* is a metric used for cooling efficiency and is defined as the cooling power (absorbed heat per time per cross-sectional area) divided by the net power input density (electrical power input per cross-sectional area):

$$C.O.P. = \frac{\left[\alpha(x)T(x)\ j - \kappa\frac{\partial T(x)}{\partial x}\right]_{x=0}}{\int_0^L [\alpha(x) j\frac{\partial T(x)}{\partial x} + \frac{j^2}{\sigma(x)}]dx} \quad (3.6)$$

where, L is the length of the CG profile (4 mm). Note that Equation 3.6 is specific to materials with a linear spatial gradient in TE properties. In comparison to the *C.O.P.* of a uniform material (Equation 3.7), the Joule heating term in the numerator is eliminated at the cold side due to the distributed Joule heating effect. In Figure 3.7, *C.O.P* of the three CG thin films are plotted against j. The value of j is within a reasonable range as the absolute current is in the order of μA, which is unlikely to cause any damage to the thin films. For all CG thin films, shape of the *C.O.P.* curve is similar where it increases and plateaus at higher j. For example, at j = 3 mA/mm^2, the *C.O.P.* is 0.35, 0.55, 0.89 for CG1, CG2, and CG3, respectively. Overall, CG3 yields the highest *C.O.P.* across the full range of j.

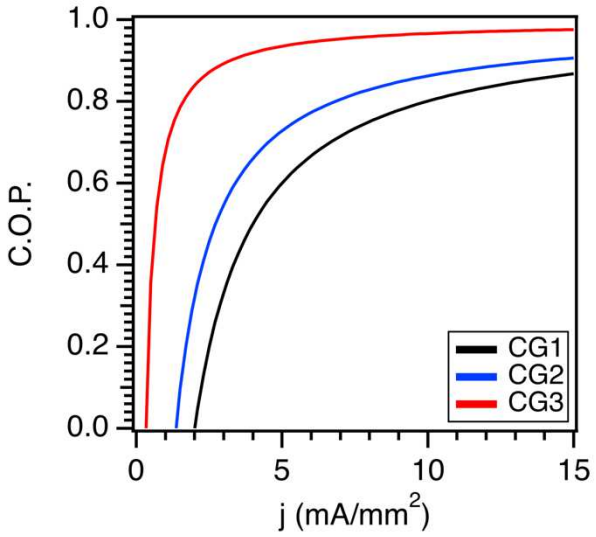

Figure 3.7: Model calculated Coefficient of Performance (C.O.P.) using Equation 3.6 for the CG thin films as a function of current density (j).

For comparison, *C.O.P.* of conventional materials with uniform properties can be calculated through the following equation:

$$C.O.P. = \frac{\alpha T_C j - \frac{1}{2} j^2 \frac{L}{\sigma} - \kappa \frac{\Delta T}{L}}{\alpha j \Delta T + j^2 \frac{L}{\sigma}} \qquad (3.7)$$

As shown in Figure 3.8 for the EU conditions, the *C.O.P.* profile show a different trend where C.O.P decreases with j until reaching negative values. Note that for the uniform case, the Joule heating term ($\frac{1}{2} j^2 \frac{L}{\sigma}$) increases more rapidly than the Peltier effect term ($\alpha T_C j$), which will eventually lead to a negative *C.O.P* value at higher j (at 0.2 mA/mm^2 for EU3). Meaning, the applied electrical current is producing more heat than that the heat being pumped by the Peltier effect, which leads to a net temperature increase. The transition to negative *C.O.P.* highlights the limited utility of the EU thin films based on the calculated σ_{avg} and α_{avg}. The difference in *C.O.P.* behavior between the CG and EU conditions illustrates an advantage for FGMs where the redistributed Joule heating and Peltier cooling allows for a wider operational range of high efficiency.

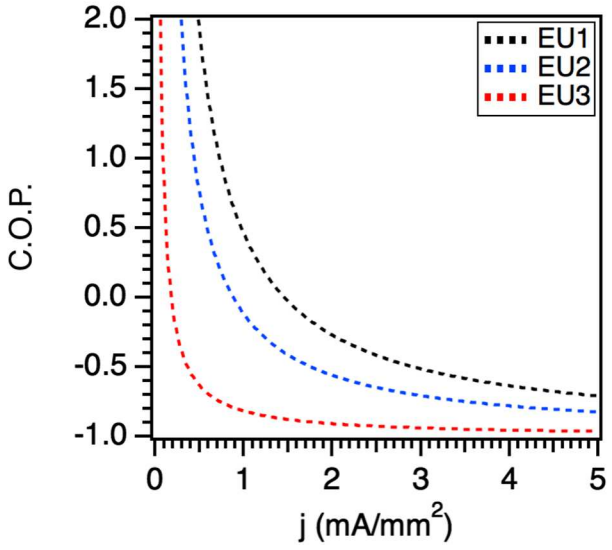

Figure 3.8: Model calculated Coefficient of Performance (C.O.P.) using Equation 3.7 for the equivalent uniform (EU) as a function of current density (j).

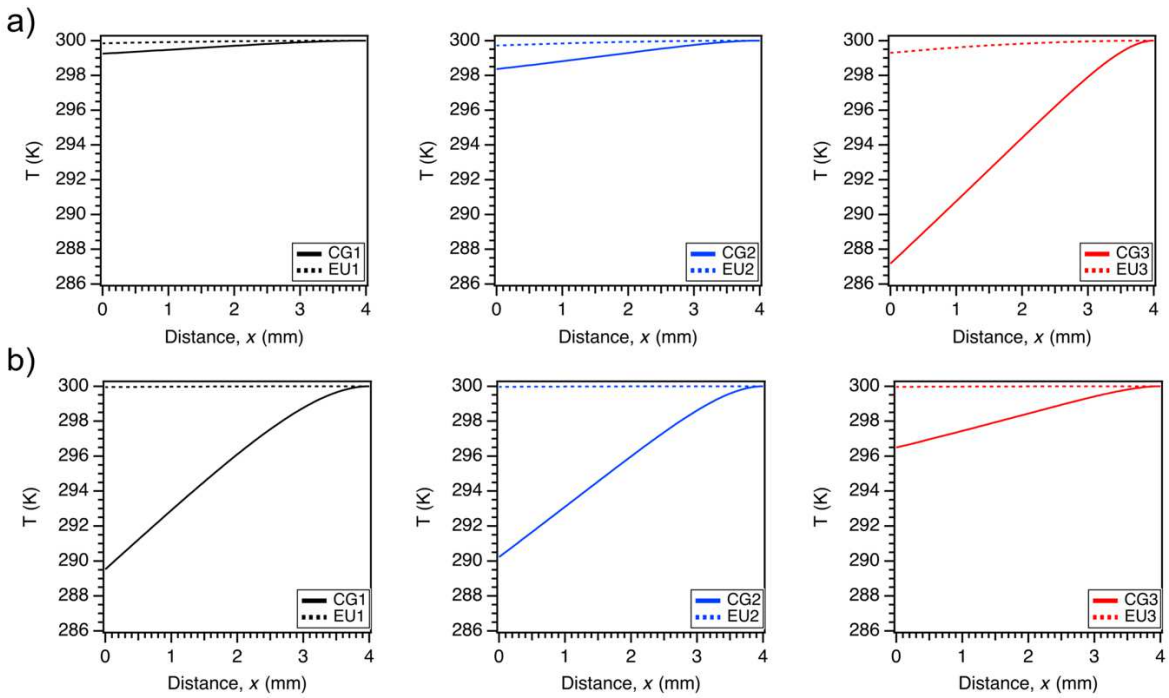

Figure 3.9: Temperature profiles, T(x), for the three continuously graded (CG) thin films and their corresponding equivalent uniform (EU) condition at (a) constant j of 3 mA/mm^2 and (b) constant C.O.P. of 0.80. The hot side (T_H = 300 K) is at x = 4 and cold side (T_C) is at x = 0.

The model calculated $T(x)$ and ΔT_c were determined upon integrating Equation 3.5 for two cases: (1) j = 3.0 mA/mm^2 and (2) *C.O.P.* = 0.80. $T(x)$ profiles of CG and EU conditions are shown in Figure 3.9 and the corresponding ΔT_c are shown in Figure 3.10 and summarized in Table 3.4. It is clear the EU condition exhibit negligible cooling for both cases where, for example, ΔT_c is 0.15 K, 0.29 K, and 0.71 K at j = 3.0 mA/mm^2 for EU1, EU2, and EU3, respectively. On the other hand, all three CG thin films yield marked improvement in cooling. Compared to the EU conditions, the $T(x)$ profile exhibits greater extent of curvature from the hot side to the cold side arising from improved heat pumping across the length of the gradient. At j = 3.0 mA/mm^2, ΔT_c of the CG thin films are 0.75 K, 1.64 K and 12.8 K for CG1, CG2 and CG3, respectively. It's clear that CG3 profile leads to the highest ΔT_c. At a fixed *C.O.P.* = 0.80, the corresponding j are 10 mA/mm^2, 6.9 mA/mm^2, and 1.6 mA/mm^2 for CG1, CG2 and CG3, respectively. In turn, the resulting ΔT_c is 10.5 K for CG1, 9.8 K for CG2, and 3.5 K for CG3. The higher ΔT_c of CG1 and CG2 arises from the

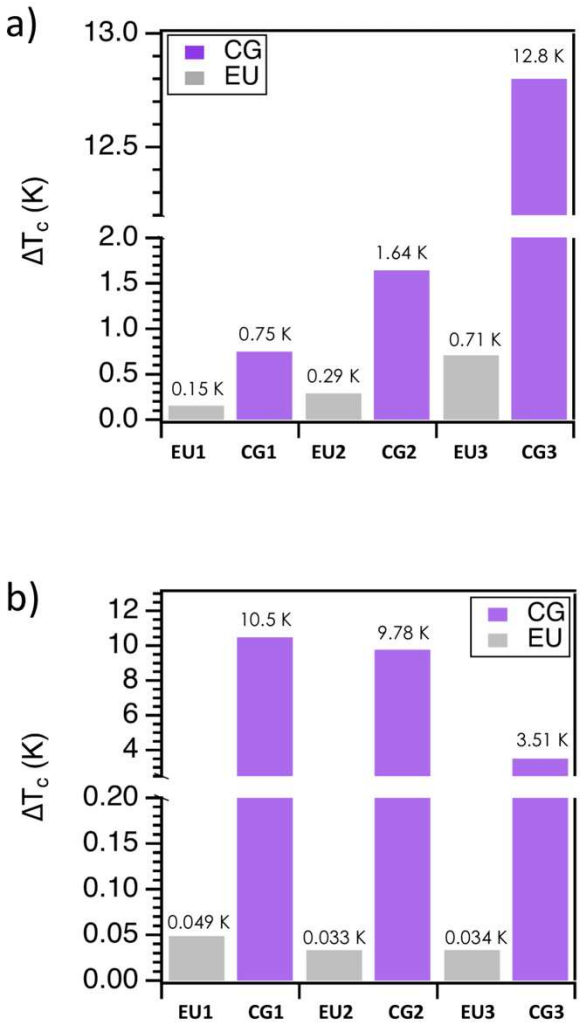

Figure 3.10: Model calculated cooling temperatures ($\Delta T_c = T_H - T_C$) of continuously graded (CG) thin films and their equivalent uniform (EU) conditions at (a) constant current density (j) of 3 mA/mm^2 and (b) constant C.O.P. of 0.80.

larger j providing more heat pumping power. Moreover, while ΔT_c of CG3 is lower at this condition, a higher ΔT_c can be achieved at comparatively lower j; for example, ΔT_c = 10.5 K is achieved at j = 2.7 mA/mm^2 for CG3. It should be noted that ΔT_c continues to increase with j for all CG thin films, especially CG3 (Figure 3.11). This continuous increase in ΔT_c likely arises from the assumption in solving Equation 3.5 where TE properties are independent of temperature and the application of a mixed boundary condition where the heat flux is constant at the hot side. One should take these ΔT_c values as the idealized upper bound in the cooling temperature. Overall, the

results of the two conditions emphasizes CG thin films allows for significant improvements in Peltier cooling and where the specific gradient profile of CG3 yields comparatively higher performance (more than an order of magnitude improvement in ΔT_c).

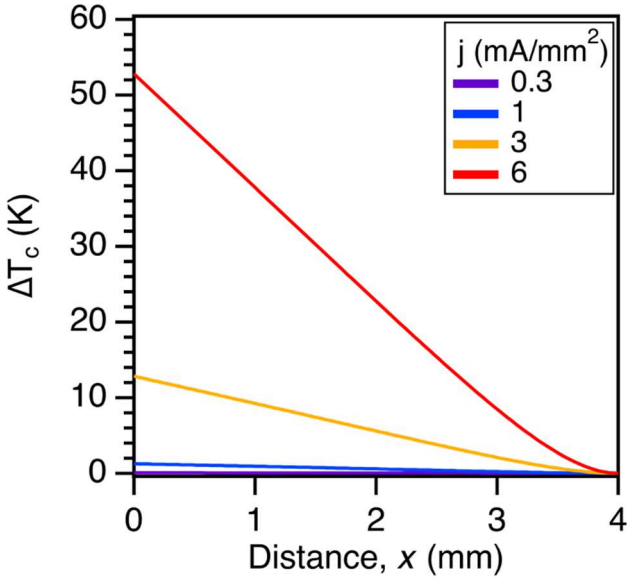

Figure 3.11: Cooling temperatures (ΔT_c) of CG3 graded sample at various input current density.

Analysis of the model-based calculations reveals important features of the $\sigma(x)$ and $\alpha(x)$ profiles leading to higher cooling temperature. Specifically, we compare the two extreme cases of CG1 and CG3. As seen from Equation 3.5, the cooling temperature T(x) is strongly dependent on $\sigma(x)$ and the spatial gradient of $\alpha(x)$, $\frac{d\alpha(x)}{dx}$. First, the exponential $\sigma(x)$ profile of CG3 has a higher σ at the cold side and a wider range in σ (72.9 S/cm at $x = 0$ to 0.0411 S/cm at $x = L$) compared to CG1 (31.5 S/cm at $x = 0$ to 1.01 S/cm at $x = L$). Additionally, the decay in σ is greater near the colder side for CG3 compared to CG1. These features in $\sigma(x)$ reduces the magnitude in Joule heating closer to the colder side. Second, the value of $\frac{d\alpha(x)}{dx}$ of the linear $\alpha(x)$ profile is higher for CG3 (30.1 μV/mm·K) compared to CG1 (10.1 μV/mm·K). This higher $\frac{d\alpha(x)}{dx}$ is an important

feature to provide for a larger contribution from Peltier effect term to offset the contribution from Joule heating. Lastly, while the experimental validation of improved cooling is difficult with thin film system used in this study (see Appendix for more details), future studies should consider alternative strategies with thicker films and full devices to demonstrate functional-grading cooling effect with sufficient power.

3.3 Conclusion

In summary, sequential vapor of PBTTT with F4TCNQ has been described as a straightforward approach of fabricating compositionally controlled continuously graded (CG) thin films. This approach leverages the inherent processibility of polymers and molecular dopants to yield various gradient profiles. In turn, we specifically fabricated three CG thin films with varying magnitudes in 1D gradient profiles of both σ and α across a 4 mm distance to explore how different gradient profiles control cooling performance. By applying model-based calculations through coupled energy and charge transport relations, we predicted the cooling temperature (ΔT_c) and coefficient of performance (*C.O.P.*) of the CG thin films compared to their equivalent uniform (EU) conditions. Specifically, CG3 profile leads to the highest ΔT_c of 12.8 K compared to 0.71 K for the corresponding EU condition. The enhancement in cooling arises from the magnitude of the σ profile and the slope of the α profile distinctive to the CG3 thin film. In turn, these features allow for efficient redistribution of the Joule heating and Peltier cooling effects to improve cooling. Overall, this work together with Chapter 2 showcase that semiconducting polymers as FGMs are promising directions to further advance the development of more efficient organic thermoelectric devices.

3.4 Experimental Methods

Materials and uniform thin film preparation are following the description in Chapter 2.

Vapor Doping Process. Vapor doping was performed in an Argon glovebox. Approximately 2 mg of F4TCNQ powder was pressed into a pellet (approximately 3 mm in diameter) and placed in an aluminum oxide crucible (OD 6.8 mm x H 4 mm from Government Scientific Source Inc.), which was in turn placed in a glass insert (diameter ~ 5 cm, height ~ 4.5 cm). A stainless-steel container was then preheated for 30 min on a hot plate to allow the chamber to reach a steady temperature at 200 °C (measured vial thermocouple at the base of the chamber). The glass insert with the dopant inside was put into the metal chamber to produce dopant vapor.

Continuously graded samples used for conductivity and Seebeck measurements (CG1, CG2, CG3) were fabricated through a sequential vapor doping process. First, the whole polymer film was exposed to F4TCNQ vapor for 2 min, 1.5 min and 1 min for CG1, CG2 and CG3, respectively. Second, a cover mask with a *c.a.* 0.10° wedge grading angle was used to cover half of the film. Then, the sample was put back onto the chamber to further expose the uncovered part of the film to F4TCNQ vapor. For CG1 sample, the film was exposed to F4TCNQ vapor for an additional 2 min to achieve optimal doping level on the doped side. For CG2 and CG3 samples, the films were exposed to F4TCNQ vapor for an additional 2.5 and 3 min, respectively.

GIWAXS Experiments. The detailed setup of GIWAXS experiments is shown in Chapter 2. GIWAXS images of continuously graded thin films were taken at a grazing incident x-ray angle of 0.14°, which is above the critical angle of the polymer film and below the critical angle of the silicon substrate. GIWAXS images measured laterally across 30 different spots for the graded

films. Measurements were conducted laterally across the interface of the segmented films. The distance between adjacent spots is 200 μm, which is the width of the X-ray beam.

Conductivity and Seebeck Measurements. Gold electrical contacts (75 nm thick) for electronic conductivity (σ) and Seebeck coefficient (α) measurements were deposited onto continuously graded PBTTT thin films via thermal evaporation through shadow masks designed in our lab. Electronic conductivity was measured in the in-plane direction using four probe geometry with a 0.2 mm spacing between electrodes and electrodes length of 1 mm. Seebeck coefficient was measured with two 1 mm^2 gold pads, which are 1 mm apart. A detailed schematic is provided in Figure 3.6.

The spatial measurements of the electronic conductivity were performed using an array of interdigitated electrodes (IDEs). Interdigitated electrode devices were fabricated at Pritzker Nanofabrication Facility, University of Chicago following the process in Chapter 2.

3.5 Acknowledgements

This work was supported by the University of Chicago Materials Research Science and Engineering Center, which is funded by National Science Foundation under award number DMR-1420709. This research used resources of the Advanced Photon Source, an Office of Science User Facility operated for the U.S. Department of Energy (DOE) by Argonne National Laboratory under Contract No. DE-AC02-06CH11357. Parts of this work were carried out at the Soft Matter Characterization Facility of the University of Chicago. We thank Han Yang for useful discussion on cooling performance modelling.

3.6 Appendix

Correlation of doping time and doping level

The doping level in the PBTTT:F4TCNQ film was characterized by the molar ratio (MR) of F4TCNQ anion to PBTTT monomer repeat unit, which was estimated by deconvoluting UV-Vis-NIR spectra using Beer's law in Chapter 2. The absorption spectra of all doped samples were deconvoluted to the neutral, anion, and polaron components using the peak shape and relative intensities. MR was calculated using the absorption intensity of the F4TCNQ anion at 1.4 eV and the primary absorption peak of neat PBTTT at 2.3 eV. Table 3.1 summarizes the estimated MR values at selective vapor doping times. By increasing the doping time, MR increases up to 0.23, which is approaching the maximum MR range of 0.25-0.30 as reported in studies of PBTTT doped with F4TCNQ.[44–46]

Seebeck and conductivity profiles

Seebeck coefficients are fitted to follow a linear profile, $\alpha(x) = kx + m$, for each sample while the conductivities are following an exponential profile, $\sigma(x) = a * exp(bx)$. The fitting relations are as follow:

$$\alpha_{G1} = 10.1x + 34.1$$

$$\alpha_{G2} = 16.8x + 27.6$$

$$\alpha_{G3} = 30.1x + 19.2$$

$$\sigma_{G1} = 31.5\exp(-0.86x)$$

$$\sigma_{G2} = 64.2\exp(-1.29x)$$

$$\sigma_{G3} = 72.9\exp(-1.87x)$$

Where, α is in the unit of μV/K, σ is in the unit of S/cm and x is in the unit of mm.

Spatial averages of α and σ for each sample are calculated using Eq. (S3.1) and (S3.2).

$$\alpha_{avg} = \frac{1}{L}\int_0^L \alpha(x)dx \qquad \text{(S3.1)}$$

$$\frac{1}{\sigma_{avg}} = \frac{1}{L}\int_0^L \frac{1}{\sigma(x)}dx \qquad \text{(S3.2)}$$

Derivation of Governing Equation

In this section, we derive the differential equation describing the 1D temperature profile across a thermoelectric film (Equation 3.5). Our continuously graded polymer film is serving as a *p*-type leg of a Peltier cooler. The Peltier effect discussed in this study's framework is based on linear Onsager theory and follows the formulation applied by Müller and co-workers.[22,42]

Considering the gradient is in the in-plane, lateral direction of the thin film, we simplify the expression as a 1D model along the x direction. Additionally, the temperature profile is determined at a constant electrical current density, *j*. From Eq. (3.1), we can get the following:

$$E = \frac{j}{\sigma} + \alpha\frac{\partial T}{\partial x} \qquad \text{(S3.3)}$$

Substituting Eq. (S3.3) into Eq. (3.4) yields

$$\frac{\partial}{\partial \mathrm{x}}q = j \cdot \left(\frac{j}{\sigma} + \alpha\frac{\partial T}{\partial x}\right) \qquad \text{(S3.4)}$$

Substituting Eq. (3.2) into the left-hand side of the Eq. (S3.4) yields

$$\frac{\partial}{\partial \mathrm{x}}\left(\alpha T j - \kappa\frac{dT}{dx}\right) = \frac{j^2}{\sigma} + j\alpha\frac{\partial T}{\partial x} \qquad \text{(S3.5)}$$

Here, we assume thermal conductivity, κ, is a constant value in our system. α and σ are position-dependent following 1D profiles α(x) and σ(x). Note that we assume temperature dependence of α and σ are neglected, which means that properties at each point across our graded

films will remain unchanged when a temperature gradient is presented. Such an assumption is valid for small values of ΔT. In this case, Eq. (S3.5) can be expanded as:

$$j\frac{d\alpha(x)}{dx}T(x) + j\alpha(x)\frac{dT(x)}{dx} - \kappa\frac{\partial^2 T(x)}{\partial x^2} = \frac{j^2}{\sigma(x)} + j\alpha(x)\frac{dT(x)}{dx} \qquad \text{(S3.6)}$$

Further simplification by cancelling out similar terms leads to the following expression

$$j\frac{d\alpha(x)}{dx}T(x) - \kappa\frac{\partial^2 T(x)}{\partial x^2} = \frac{j^2}{\sigma(x)} \qquad \text{(S3.7)}$$

Rearranging Eq. (S3.7), we can get the equation

$$-\kappa\frac{\partial^2 T(x)}{\partial x^2} = \frac{j^2}{\sigma(x)} - j\frac{d\alpha(x)}{dx}T(x) \qquad \text{(S3.8)}$$

The term on the left-hand side of Equation S3.8 ($-\kappa\frac{\partial^2 T(x)}{\partial x^2}$) refers to thermal (heat) conduction, the first term on the right-hand side ($\frac{j^2}{\sigma(x)}$) refers to Joule heating and the second term on the right-hand side ($-j\frac{d\alpha(x)}{dx}T(x)$) refers to Peltier cooling effect. These three components contribute to the heat absorbed at the cold side of the film (a *p*-type leg of a Peltier cooler) as shown in Figure 3.12. The Peltier effect removes heat from the cold side (T_c), the joule heating uniformly heats the leg, and the heat conduction transports heat from the hot side T_h to the cold side.

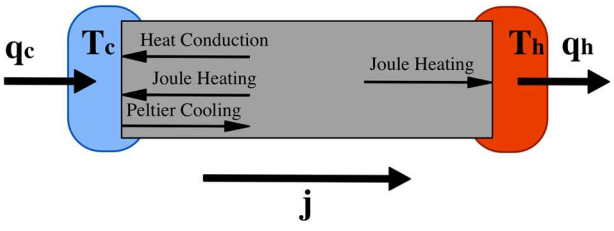

Figure 3.12: Schematic of one *p*-type leg of a Peltier cooler with heat contributions assigned.

Eq. (S3.8) is integrated to determine the 1D temperature profile, which are solved for the following two cases: (1) Uniform profile with constant α and σ, and (2) Gradient profiles of $\alpha(x)$ and $\sigma(x)$. Mixed boundary conditions shown in Eq. (S3.9) are applied to solve $T(x)$ in both cases. We fix hot side temperature, T_h, at 300 K and assume constant heat flux at the hot side of the film.

$$T(x = L) = T_H, \quad q(x = L) = q_H^0 \qquad \text{(S3.9)}$$

For simplicity, we set $q_H^0 = \alpha T_H j$, which yields $\frac{\partial T}{\partial x}(x = L) = 0$

Case 1: Uniform profile with constant α and σ

Considering a uniform Peltier leg with constant material properties, α, σ and κ, the $\mathrm{j}\frac{\mathrm{d}\alpha(\mathrm{x})}{\mathrm{dx}}\mathrm{T}(\mathrm{x})$ term in Eq. (S3.8) goes to zero and the relation will become

$$-\kappa \frac{\partial^2 T(x)}{\partial x^2} = \frac{j^2}{\sigma(x)} \qquad \text{(S3.10)}$$

The analytic solution of Eq. (S3.10) is a parabolic temperature profile

$$T(x) = -\frac{c_0}{2}x^2 + c_1 x + c_2 \qquad \text{(S3.11)}$$

Where $c_0 = \frac{j^2}{\sigma\kappa}$, c_1 and c_2 can be determined by boundary conditions.

Case 2: Gradient profiles of $\alpha(x)$ and $\sigma(x)$

As there is no general analytical solution to Eq. (S3.8), numerical integration of Eq. (S3.8) was done with Python to obtain the solution of temperature across the film, $T(x)$. From the solved $T(x)$ profiles, $\Delta T = T_H - T_C$, was calculated for both continuously graded and uniform profiles. The

results have demonstrated that ΔT of graded samples are significantly improved compared to that of the uniform profile.

Maximum Cooling

It is known that maximum cooling, i.e. maximum temperature difference, ΔT_{max}, is occurring when cooling power is at zero and can be calculated by solving Eq. S3.10 for Peltier leg with constant materials properties, which is equal to $\frac{1}{2}ZT_C^2$.[19] By comparing Eq. (S3.8) and (S3.10), we found that the Peltier term, $j\frac{d\alpha(x)}{dx}T(x)$ is appeared to reduce the Joule heating effect in the continuously graded case. Note that previous studies have chosen specific α and σ profiles to quantitively calculate the maximum in ΔT_c for continuously graded materials. For instance, Bian et al. have proposed $\alpha(x)$ and $\sigma(x)$ profiles with power factors $\alpha(x)^2\sigma(x) = C$ remaining constant, where they calculated $\Delta T_{max} = \frac{1}{2}ZT_C^2 \times F(\alpha)$ with $F(\alpha)$ always greater than 1.[20]

Experimental difficulties on confirming cooling effect

While the model-based calculation reveals enhanced cooling effect of our graded thin films, it would be difficult to experimentally achieve the film conditions stated in our assumptions. For instance, the boundary conditions with constant heat flux and temperature at the hot side would be hard to achieve in reality. In addition, as the graded polymer films we studied are coated on glass substrate, the heat transfer between the graded film and glass substrate needs to be taken into account, which leads to a different cooling scenario. The cooling effect of thicker polymer films (thickness in the range of 2 – 14 μm) have been experimentally studied in the literature where a thermally suspended device was fabricated and tested.[32] With thicker films and full device as

alternative strategies, the functional-grading cooling effect can be demonstrated by leveraging our graded polymer films in the future studies.

3.7 References

(1) Snyder, G. J.; Toberer, E. S. Complex Thermoelectric Materials. *Nat. Mater.* **2008**, *7* (2), 105–114.

(2) Snyder, G. J.; Ursell, T. S. Thermoelectric Efficiency and Compatibility. *Phys. Rev. Lett.* **2003**, *91* (14), 148301/1-148301/4.

(3) Russ, B.; Glaudell, A.; Urban, J. J.; Chabinyc, M. L.; Segalman, R. A. Organic Thermoelectric Materials for Energy Harvesting and Temperature Control. *Nat. Rev. Mater.* **2016**, *1* (10), 16050.

(4) Wang, Y.; Yang, L.; Shi, X.-L.; Shi, X.; Chen, L.; Dargusch, M. S.; Zou, J.; Chen, Z.-G. Flexible Thermoelectric Materials and Generators: Challenges and Innovations. *Adv. Mater.* **2019**, *31* (29), 1807916.

(5) Petsagkourakis, I.; Tybrandt, K.; Crispin, X.; Ohkubo, I.; Satoh, N.; Mori, T. Thermoelectric Materials and Applications for Energy Harvesting Power Generation. *Sci. Technol. Adv. Mater.* **2018**, *19* (1), 836–862.

(6) Beretta, D.; Neophytou, N.; Hodges, J. M.; Kanatzidis, M. G.; Narducci, D.; Martin-Gonzalez, M.; Beekman, M.; Balke, B.; Cerretti, G.; Tremel, W.; Zevalkink, A.; Hofmann, A. I.; Müller, C.; Dörling, B.; Campoy-Quiles, M.; Caironi, M. Thermoelectrics: From History, a Window to the Future. *Mater. Sci. Eng. R Reports* **2019**, *138* (July).

(7) Liu, Z.; Meyers, M. A.; Zhang, Z.; Ritchie, R. O. Functional Gradients and Heterogeneities in Biological Materials: Design Principles, Functions, and Bioinspired Applications. *Prog. Mater. Sci.* **2017**, *88*, 467–498.

(8) Müller, E.; Drašar, Č.; Schilz, J.; Kaysser, W. A. Functionally Graded Materials for Sensor and Energy Applications. *Mater. Sci. Eng. A* **2003**.

(9) Almasi, D.; Sadeghi, M.; Lau, W. J.; Roozbahani, F.; Iqbal, N. Functionally Graded Polymeric Materials: A Brif Review of Current Fabrication Methods and Introduction of a Novel Fabrication Method. *Mater. Sci. Eng. C* **2016**, *64*, 102–107.

(10) Sallehin, N. Z. I. M.; Yatim, N. M.; Suhaimi, S. A Review on Fabrication Methods for Segmented Thermoelectric Structure. **2018**, *030003*, 030003.

(11) Hedegaard, E. M. J.; Mamakhel, A. A. H.; Reardon, H.; Iversen, B. B. Functionally Graded (PbTe) 1– x (SnTe) x Thermoelectrics. *Chem. Mater.* **2018**, *30* (1), 280–287.

(12) Zhang, Q.; Liao, J.; Tang, Y.; Gu, M.; Ming, C.; Qiu, P.; Bai, S.; Shi, X.; Uher, C.; Chen, L. Realizing a Thermoelectric Conversion Efficiency of 12% in Bismuth Telluride/Skutterudite Segmented Modules through Full-Parameter Optimization and

Energy-Loss Minimized Integration. *Energy Environ. Sci.* **2017**, *10* (4), 956–963.

(13) Kuznetsov, V. L.; Kuznetsova, L. A.; Kaliazin, A. E.; Rowe, D. M. High Performance Functionally Graded and Segmented Bi2Te3-Based Materials for Thermoelectric Power Generation. *J. Mater. Sci.* **2002**, *37* (14), 2893–2897.

(14) Kim, C.; Kim, D. H.; Kim, J. S.; Han, Y. S.; Chung, J. S.; Kim, H. A Study of the Synthesis of Bismuth Tellurium Selenide Nanocompounds and Procedures for Improving Their Thermoelectric Performance. *J. Alloys Compd.* **2011**, *509* (39), 9472–9478.

(15) Müller, E.; Zabrocki, K.; Goupil, C.; Snyder, G. J.; Seifert, W. Functionally Graded Thermoelectric Generator and Cooler Elements. **2012**.

(16) Seifert, W.; Müller, E.; Walczak, S. Generalized Analytic One-Dimensional Description of Non-Homogeneous TE Cooler and Generator Elements Based on the Compatibility Approach. *Int. Conf. Thermoelectr. ICT, Proc.* **2006**, 714–719.

(17) Müller, E.; Walczak, S.; Seifert, W. Optimization Strategies for Segmented Peltier Coolers. *Phys. Status Solidi Appl. Mater. Sci.* **2006**, *203* (8), 2128–2141.

(18) Cramer, C. L.; Wang, H.; Ma, K. Performance of Functionally Graded Thermoelectric Materials and Devices: A Review. *J. Electron. Mater.* **2018**, *47* (9), 5122–5132.

(19) Bian, Z.; Shakouri, A.; Cruz, S. Cooling Enhancement Using Inhomogeneous Thermoelectric Materials. *Int. Conf. Thermoelectr. ICT, Proc.* **2006**, No. 1, 264–267.

(20) Bian, Z.; Wang, H.; Zhou, Q.; Shakouri, A. Maximum Cooling Temperature and Uniform Efficiency Criterion for Inhomogeneous Thermoelectric Materials. *Phys. Rev. B - Condens. Matter Mater. Phys.* **2007**, *75* (24), 1–7.

(21) Vikhor, L. N.; Anatychuk, L. I. Theoretical Evaluation of Maximum Temperature Difference in Segmented Thermoelectric Coolers. *Appl. Therm. Eng.* **2006**, *26* (14), 1692–1696.

(22) Seifert, W.; Ueltzen, M.; Müller, E. One-Dimensional Modelling of Thermoelectric Cooling. *Phys. Status Solidi Appl. Res.* **2002**, *194* (1), 277–290.

(23) Thiébaut, E.; Goupil, C.; Pesty, F.; D'Angelo, Y.; Guegan, G.; Lecoeur, P. Maximization of the Thermoelectric Cooling of a Graded Peltier Device by Analytical Heat-Equation Resolution. *Phys. Rev. Appl.* **2017**, *8* (6), 64003.

(24) Jin, Z. H.; Wallace, T. T. Functionally Graded Thermoelectric Materials with Arbitrary Property Gradations: A One-Dimensional Semianalytical Study. *J. Electron. Mater.* **2015**, *44* (6), 1444–1449.

(25) Shen, L.; Zhang, W.; Liu, G.; Tu, Z.; Lu, Q.; Chen, H.; Huang, Q. Performance

Enhancement Investigation of Thermoelectric Cooler with Segmented Configuration. *Appl. Therm. Eng.* **2020**, *168* (August 2019), 114852.

(26) Hazan, E.; Ben-Yehuda, O.; Madar, N.; Gelbstein, Y. Functional Graded Germanium-Lead Chalcogenide-Based Thermoelectric Module for Renewable Energy Applications. *Adv. Energy Mater.* **2015**, *5* (11), 1–8.

(27) Hung, L. T.; Van Nong, N.; Snyder, G. J.; Viet, M. H.; Balke, B.; Han, L.; Stamate, E.; Linderoth, S.; Pryds, N. High Performance P-Type Segmented Leg of Misfit-Layered Cobaltite and Half-Heusler Alloy. *Energy Convers. Manag.* **2015**, *99*, 20–27.

(28) Kroon, R.; Mengistie, D. A.; Kiefer, D.; Hynynen, J.; Ryan, J. D.; Yu, L.; Müller, C. Thermoelectric Plastics: From Design to Synthesis, Processing and Structure–Property Relationships. *Chem. Soc. Rev.* **2016**, *45* (22), 6147–6164.

(29) Zhang, Q.; Sun, Y.; Xu, W.; Zhu, D. What To Expect from Conducting Polymers on the Playground of Thermoelectricity: Lessons Learned from Four High-Mobility Polymeric Semiconductors. *Macromolecules* **2014**, *47* (2), 609–615.

(30) Vijayakumar, V.; Zhong, Y.; Untilova, V.; Bahri, M.; Herrmann, L.; Biniek, L.; Leclerc, N.; Brinkmann, M. Bringing Conducting Polymers to High Order: Toward Conductivities beyond 105 S Cm−1 and Thermoelectric Power Factors of 2 MW M−1 K−2. *Adv. Energy Mater.* **2019**, *9* (24), 1900266.

(31) Salzmann, I.; Heimel, G.; Oehzelt, M.; Winkler, S.; Koch, N. Molecular Electrical Doping of Organic Semiconductors: Fundamental Mechanisms and Emerging Dopant Design Rules. *Acc. Chem. Res.* **2016**, *49* (3), 370–378.

(32) Jin, W.; Liu, L.; Yang, T.; Shen, H.; Zhu, J.; Xu, W.; Li, S.; Li, Q.; Chi, L.; Di, C.; Zhu, D. Exploring Peltier Effect in Organic Thermoelectric Films. *Nat. Commun.* **2018**, *9* (1), 3586.

(33) Sun, Z.; Li, J.; Wong, W.-Y. Emerging Organic Thermoelectric Applications from Conducting Metallopolymers. *Macromol. Chem. Phys.* **2020**, *221* (12), 2000115.

(34) Sun, Y.; Di, C.-A.; Xu, W.; Zhu, D. Advances in N-Type Organic Thermoelectric Materials and Devices. *Adv. Electron. Mater.* **2019**, *5* (11), 1800825.

(35) Patel, S. N.; Glaudell, A. M.; Peterson, K. A.; Thomas, E. M.; O'Hara, K. A.; Lim, E.; Chabinyc, M. L. Morphology Controls the Thermoelectric Power Factor of a Doped Semiconducting Polymer. *Sci. Adv.* **2017**, *3* (6), e1700434.

(36) Cochran, J. E.; Junk, M. J. N.; Glaudell, A. M.; Miller, P. L.; Cowart, J. S.; Toney, M. F.; Hawker, C. J.; Chmelka, B. F.; Chabinyc, M. L. Molecular Interactions and Ordering in Electrically Doped Polymers: Blends of PBTTT and F4TCNQ. *Macromolecules* **2014**, *47* (19), 6836–6846.

(37) Ma, T.; Dong, B. X.; Grocke, G. L.; Strzalka, J.; Patel, S. N. Leveraging Sequential Doping of Semiconducting Polymers to Enable Functionally Graded Materials for Organic Thermoelectrics. *Macromolecules* **2020**, *53* (8), 2882–2892.

(38) Lim, E.; Peterson, K. A.; Su, G. M.; Chabinyc, M. L. Thermoelectric Properties of Poly(3-Hexylthiophene) (P3HT) Doped with 2,3,5,6-Tetrafluoro-7,7,8,8-Tetracyanoquinodimethane (F4TCNQ) by Vapor-Phase Infiltration. *Chem. Mater.* **2018**, *30* (3), 998–1010.

(39) Jacobs, I. E.; Aasen, E. W.; Oliveira, J. L.; Fonseca, T. N.; Roehling, J. D.; Li, J.; Zhang, G.; Augustine, M. P.; Mascal, M.; Moulé, A. J. Comparison of Solution-Mixed and Sequentially Processed P3HT:F4TCNQ Films: Effect of Doping-Induced Aggregation on Film Morphology. *J. Mater. Chem. C* **2016**, *4* (16), 3454–3466.

(40) Scholes, D. T.; Hawks, S. A.; Yee, P. Y.; Wu, H.; Jeffrey, R.; Tolbert, S. H.; Schwartz, B. J.; Lindemuth, J. R.; Tolbert, S. H.; Schwartz, B. J. Overcoming Film Quality Issues for Conjugated Polymers Doped with F4TCNQ by Solution Sequential Processing: Hall Effect, Structural, and Optical Measurements. *J. Phys. Chem. Lett.* **2015**, *6* (23), 4786–4793.

(41) Vijayakumar, V.; Zaborova, E.; Biniek, L.; Zeng, H.; Herrmann, L.; Carvalho, A.; Boyron, O.; Leclerc, N.; Brinkmann, M. Effect of Alkyl Side Chain Length on Doping Kinetics, Thermopower, and Charge Transport Properties in Highly Oriented F4TCNQ-Doped PBTTT Films. *ACS Appl. Mater. & Interfaces* **2019**, *11* (5), 4942–4953.

(42) Onsager, L. Reciprocal Relations in Irreversible Processes. I. *Phys. Rev.* **1931**, *37* (4), 405–426.

(43) Zapata-Arteaga, O.; Perevedentsev, A.; Marina, S.; Martin, J.; Reparaz, J. S.; Campoy-Quiles, M. Reduction of the Lattice Thermal Conductivity of Polymer Semiconductors by Molecular Doping. *ACS Energy Lett.* **2020**, *5* (9), 2972–2978.

(44) Patel, S. N.; Glaudell, A. M.; Peterson, K. A.; Thomas, E. M.; O'Hara, K. A.; Lim, E.; Chabinyc, M. L. Morphology Controls the Thermoelectric Power Factor of a Doped Semiconducting Polymer. *Sci. Adv.* **2017**, *3* (6), e1700434.

(45) Kang, K.; Watanabe, S.; Broch, K.; Sepe, A.; Brown, A.; Nasrallah, I.; Nikolka, M.; Fei, Z.; Heeney, M.; Matsumoto, D.; Marumoto, K.; Tanaka, H.; Kuroda, S.-I.; Sirringhaus, H. 2D Coherent Charge Transport in Highly Ordered Conducting Polymers Doped by Solid State Diffusion. *Nat. Mater.* **2016**.

(46) Untilova, V.; Biskup, T.; Biniek, L.; Vijayakumar, V.; Brinkmann, M. Control of Chain Alignment and Crystallization Helps Enhance Charge Conductivities and Thermoelectric Power Factors in Sequentially Doped P3HT:F4TCNQ Films. *Macromolecules* **2020**.

Chapter 4: POLYMORPHISM CONTROLS THE THERMOELECTRIC PROPERTIES OF MOLECULAR DOPED POLY(DODECYL-QUARTERTHIOPHENE)

This chapter will be published in the future as a journal article.

Molecularly doped conjugated polymers play a vital role in realizing lightweight and flexible organic electronics. To enhance the solution processability of such polymers, linear alkyl side chains have been added to the conjugated backbone. However, long alkyl chains could lead to a polymorphism microstructure where side chains transit from fully extended to partially bended. This interdigitation effect on side chains correlated with structure and charge transport performances of doped conjugated polymers have not been adequately exploited up to date. Herein, by investigating poly(dodecyl-quaterthiophene) (PQT) vapor doped by tetracyanoquinodimethane (F4TCNQ), we show that polymorphs with interdigitated side chains have significant effect on doping efficiency and thus the charge transport properties. Thermal annealing was leveraged as a post-cast treatment to achieve PQT samples having different polymorphs. Two different polymorphs were observed when PQT is recrystallized from annealing temperatures at 100 ℃ and 130 ℃, respectively. Ellipsometry and X-ray scattering experiments were utilized to characterize the conformal order and backbone orientation of polymorphs within both as-cast and annealed polymer thin films. The resulting charge transport properties (Seebeck coefficient and conductivity) of doped PQT films were measured. 130 ℃ annealed samples were found to have a maximum σ as high as 6.1 ± 0.3 S/cm while 100 ℃ annealed samples only exhibit

a σ of (6.1 ± 0.4) × 10^{-3} S/cm due to significantly low doping efficiency resulting from stronger interdigitation of side chain.

4.1 Introduction

Semiconducting conjugated polymers (CPs) are promising for the realization of lightweight, environmentally friendly and flexible electronics.[1–4] In particular, there has been increasing attraction in leveraging such polymers as active layers in organic thermoelectrics (TE).[4–7] The performance of TE devices is defined as the dimensionless figure of merit, $ZT = \alpha^2\sigma T/\kappa$, where α is the Seebeck coefficient, σ is the electrical conductivity, κ is the thermal conductivity, T is the temperature in Kelvin and $\alpha^2\sigma$ is the power factor (PF).[4,8] A promising CP candidate for TE application should simultaneously exhibit high PF and low κ. In principle, PF is related to both α and σ as the magnitude of σ increases positively as function of charge carrier concentration, n while, in contrast, the magnitude of α, which reflects the average entropy transport per charge carrier, decreases with the increase of n.[8,9] Due to the interplay relationship of α and σ, a more practical strategy to improve PF is via tuning the molecular packing (e.g. crystallinity, packing orientation, and polymorphs) of CP to achieve high α and σ at the same time rather than increasing the charge carrier concentration monotonically.

Molecular doping is a powerful approach to control n in CPs by the addition of a molecular dopant to either oxidize (p-type doping) or reduce (n-type doping) the polymer backbone.[5,10–12] For the case of thiophene-based polymers, p-type acceptors, e.g. 2,3,5,6-tetrafluoro-7,7,8,8-tetracyanoquinodimethane (F4TCNQ), are introduced as oxidant molecules, leading to charge transfer between the host polymer and dopant molecule. Doping methods are found to strongly affected the charge transport in CPs where optimal properties are achieved when their underlying

hierarchical structure are maintained. Specifically, sequential doping methods where the dopant is infiltrated into the polymer matrix either from an orthogonal solvent-dopant mixture or from the dopant's vapor phase are promising approaches to preserve the underlying local ordering and morphology.[13–17] In contrast to the solution co-processing method where the formation of aggregation leads to films with poor quality,[13,14] the sequentially doping of the polymer maintains the crystalline order and long-range connectivity, which results in high charge carrier mobility μ, σ and thus higher *PF*.

Previous studies on F4TCNQ-doped polythiophenes have demonstrated that the dopant anions are located between alkyl side chains within crystalline domains,[18] which results in an increase in side chain spacing while a compression in π–π stacking upon doping.[19–23] Hence, it is crucial to understand the interrelation between doping mechanism and the solid-state packing in semiconducting CPs with solubilizing alkyl side chains as well as the subsequent effect on the charge transport properties. Particularly, linear alkyl side chains are the most commonly used side chains in semiconducting CPs, e.g. poly(3-hexylthiophene) (P3HT). Another class of thiophene-based CPs is the poly(dodecyl-quaterthiophene) (PQT) with longer alkyl chains, which provides relatively higher stability compared to P3HT.[24] However, despite improving solubility, long alkyl chains could lead to a polymorphism of thiophene-based derivatives resulting from conformational freedom of these long chains. Specifically, polymorphs exist where side chains transit from fully extended to partially bended. The side chain interdigitation phenomenon was firstly observed and studied in quarterthiophene oligomers.[25] Pan *et al.* demonstrated two polymorphs of quarterthiophene oligomers with long pendant side chains parallel and perpendicular to the quarterthiophene core.[25] Different polymorphs were shown to be tunable by changing the substituent of quarterthiophene core and the crystallization conditions. Later, similar polymorph

conformations were demonstrated in polythiophenes with long alkyl chains.[26–28] For example, Jacobs *et al.* investigated the effect of the polymorphism on molecular doping mechanism in P3HT thin films.[26] The alkyl chains were selectively packed (parallelly and perpendicularly to the backbone) by changing the crystallization conditions of P3HT films. F4TCNQ was used as molecular dopant and integer charge transfer mechanism was enabled by the polymorph with side chain stacking perpendicularly to the polythiophene backbone while fractional charge transfer mechanism was found in the polymorph with side chain stacking parallelly to the polythiophene backbone. As a result, the doped P3HT film with integer charge transfer mechanism shows a two order of magnitude higher electronic conductivity (2.1 S/cm) than that of the P3HT film with fraction charge transfer mechanism. Controlling the polymorph of the polythiophene-based semiconductor with long side chains becomes an imperative approach for achieving high molecular doping efficiency and thus, high electronic conductivity.

It is of great importance in the field of molecularly doped CPs to investigate how the interdigitated packing of side chains affect the doping level and thus the charge transport properties. Strategies used to control the polymorphs are normally as follows. First, changing the substituents on the thiophene backbone or the repeating unit of the thiophene backbone favors one polymorph over another.[25,29,30] Second, control over the crystallization conditions (e.g. film deposition methods, thermal treatment and solvent vapor exposure) will also potentially tune the polymorphs of CPs.[26,31,32] In this work, the overall research objectives are two-fold. First, we examine the formation of the polymorphs and chain orientations in PQT films by thermal treatment and verify the structural changes via grazing incidence wide angle x-ray scattering (GIWAXS) and ellipsometry experiments. Second, we investigated the structural and charge transport properties of as-cast and annealed PQT films coupled with sequential vapor doping of molecular dopant,

F4TCNQ. A combination of spectroscopy technique and GIWAXS were utilized to compare the conformal order and doping efficiency within each polymorph upon doping the PQT thin films with different annealing conditions. The charge transport properties were measured, and samples annealed at 130℃ were found to have a maximum σ of 6.1 ± 0.3 S/cm while samples annealed at 100℃ only exhibit a σ of (6.1 ± 0.4) × 10^{-3} S/cm due to significantly low doping efficiency. On the other hand, α of PQT thin films follow the opposite trend where samples annealed at 100℃ have the largest α at 474 ± 34 μV/K. The results obtained from the structure-property relationship for PQT with different polymorphs will provide new design principle for organic TE.

4.2 Results and Discussion

4.2.1 Polymorphism Structure in PQT Films

Differential scanning calorimetry (DSC) study is carried out to probe the thermal and liquid crystal properties of PQT prior to investigate the annealing effect on microstructure and charge transport of PQT thin films. The DSC thermogram is shown in Figure 4.1b. Note that the first run in DSC was discarded because it contains the thermal history of the polymer. Therefore, we have recorded the second run to minimize the effect of thermal history and to investigate the melt crystallization behavior. Two peaks are clearly observed upon heating cycle at 90 ℃ and 110 ℃, which correspond to transition from the crystalline-solid to the liquid-crystalline phase (melting/disordering of alkyl side chains), and from the anisotropic liquid-crystalline to the isotropic liquid phase (melting/disordering of facial π−π stacking), respectively. Based on the DSC results, PQT as-cast films were thermally annealed above each transition. Specifically, each as-cast film was annealed under Argon atmosphere at either 100 ℃ or 130 ℃ for 10 min and cooled

back to room temperature for recrystallization. As shown in AFM images (Figure 4.2), the as-cast film did not show any clear crystal feature, while both post-treated films showed long crystal nanofibrils. Both thermal treatments for cast PQT-12 films could considerably improve self-assembled nanostructure and its crystallinity, which is consistent as stated in previous studies.[33,34]

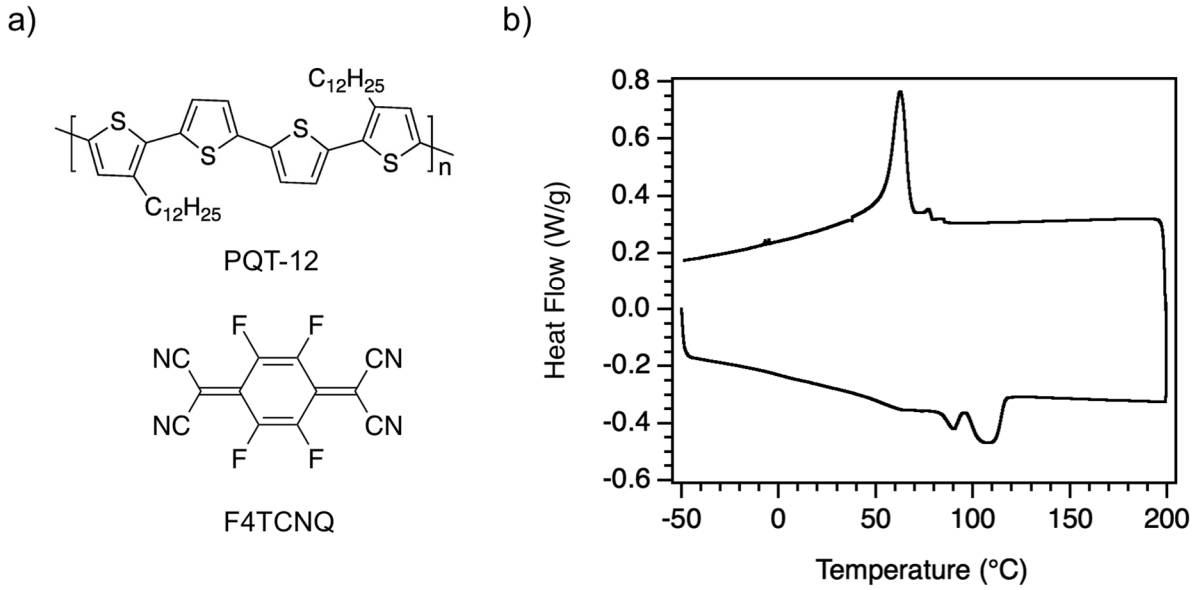

Figure 4.1: a) Chemical structures of PQT and F4TCNQ. b) DSC thermogram of PQT

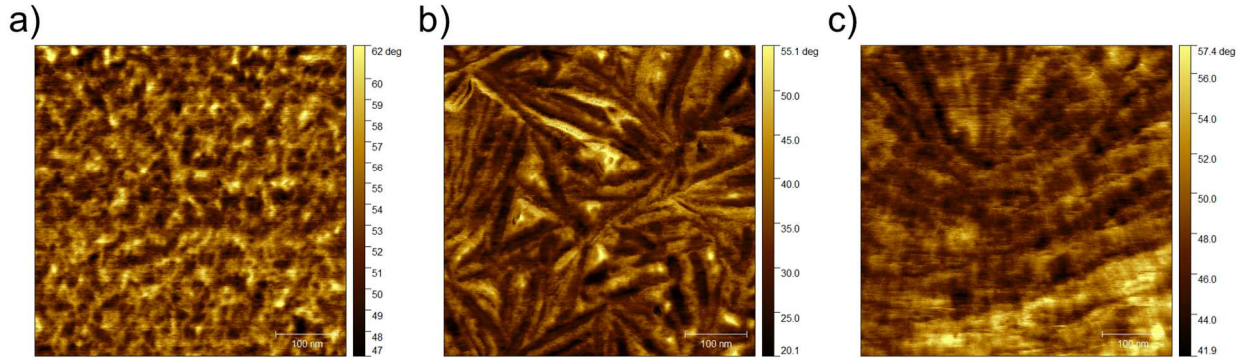

Figure 4.2: AFM phase images of PQT films. (a) as-cast film, (b) and (c): annealed at 100 and 130 °C for 10 min and cooled back to room temperature, respectively.

The local order and crystalline structure of both as-cast and annealed PQT films were investigated by grazing incidence wide angle X-ray scattering (GIWAXS) experiments. 2D

GIWAXS patterns were shown in Figure 4.3. Two side chain stacking peaks, denoted as (100) at smaller *q* value and (100)' at large *q* value, are clearly observed in the scattering pattern of as-cast PQT films (Figure 4.3a), which indicates two polymorphs coexisting in the crystalline region. This polymorphism of PQT is consistent with previous studies.[28,35,36] Quantitative differences in these two polymorphs are seen through the side chain stacking peaks (Figure 4.3d) and calculated side-chain spacings (d_{100} and $d_{100'}$). The first polymorph with d_{100} of 1.83 nm is less interdigitated in side-chain spacing while the second phase has stronger interdigitation between side chains with $d_{100'}$ of 1.17 nm. These two phases are referred to first and second polymorph in further discussion in this study, respectively. It was found that the polymorphic crystals in PQT films competed together, strongly depending on the post film treatments. When annealed at 100 ℃, the second polymorph dominates while the first polymorph disappears in the PQT film as shown in Figure 4.3b. In this case, stronger interdigitation between side chains in the second polymorph will have impact on charge transport in PQT, especially when corporates with molecular dopants as it limits the dopant infiltration capacity. In contrast, both polymorphs remain in the film annealed at 130 ℃. In addition, both (100) and (100)' peaks become narrower compared to the as-cast film, indicating larger domains in both polymorphs, which could lead to better charge transport in annealed PQT film than as-cast sample. It is worth noting that both side-chain and π-stacking peaks are observed along in-plane direction for the 130 ℃ annealed film (Figure 4.3c), which is controversial to conventional edge-on/face-on orientation. We suggest the formation of chain-on orientation with the polymer backbone aligned out-of-plane in the 130 ℃ annealed PQT thin films. The average orientations of PQT backbones were further investigated by spectroscopic ellipsometry measurements. The in-plane and out-of-plane imaginary parts of complex

permittivity ε'' are summarized in Figure 4.4. For as-cast and 100 ℃ annealed samples, both exhibit pronounced anisotropic behavior with stronger in-plane than out-of-plane ε'', suggesting

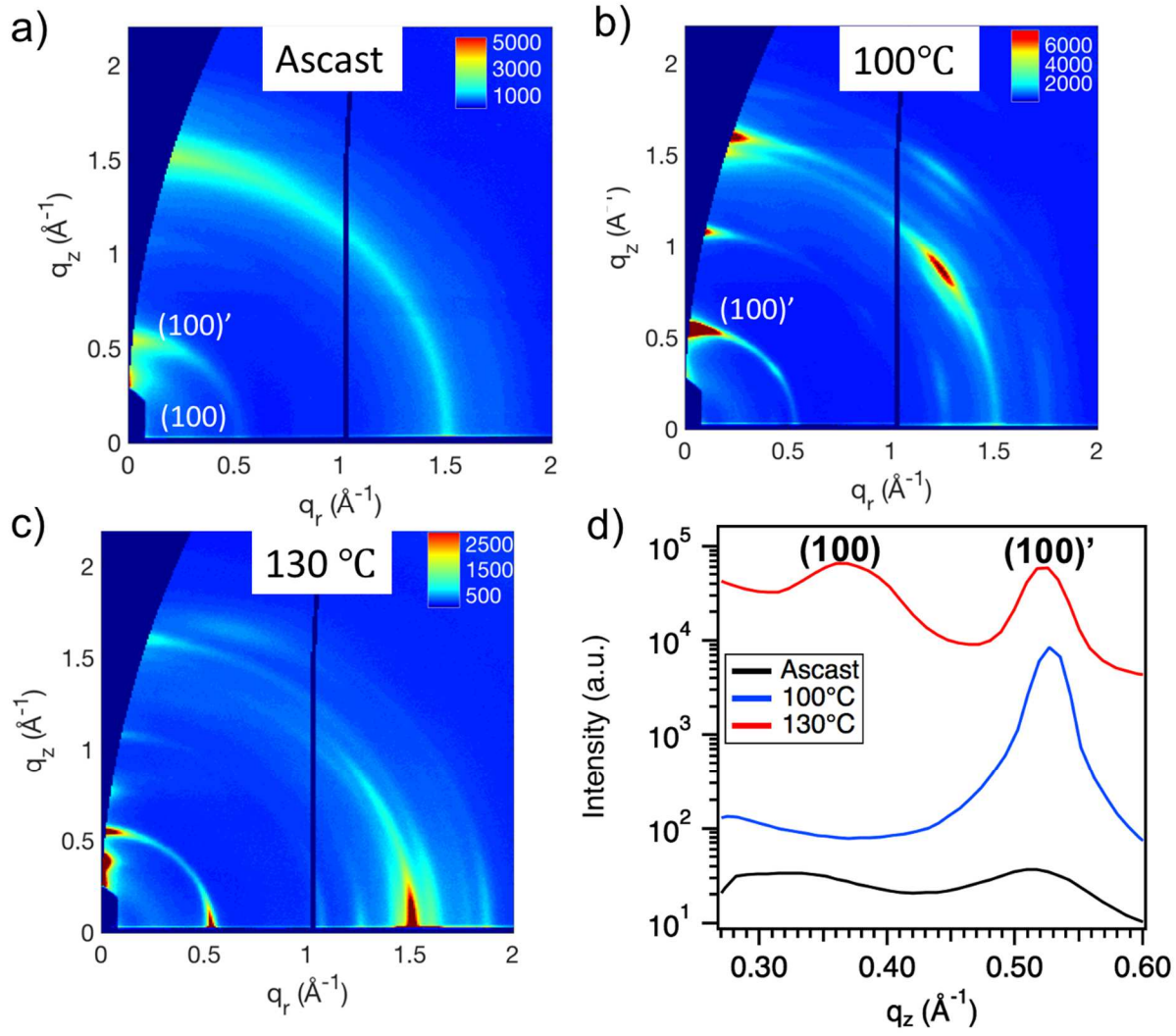

Figure 4.3: PQT GIWAXS patterns of a) as-cast film, b) 100 ℃ annealed and c) 130 ℃ annealed films. d) Out-of-plane (100) and (100)' scattering for as-cast and annealed PQT films.

polymer chains have the tendency of lying parallel to the substrate, which has been widely observed in spin-cast conjugated polymers.[37–39] 130 ℃ annealed sample, however, exhibits a much stronger out-of-plane ε'' than the in-plane component. This indicates that PQT backbones in 130 ℃ annealed sample tend to be perpendicular to the substrate, confirming the chain-on orientation.

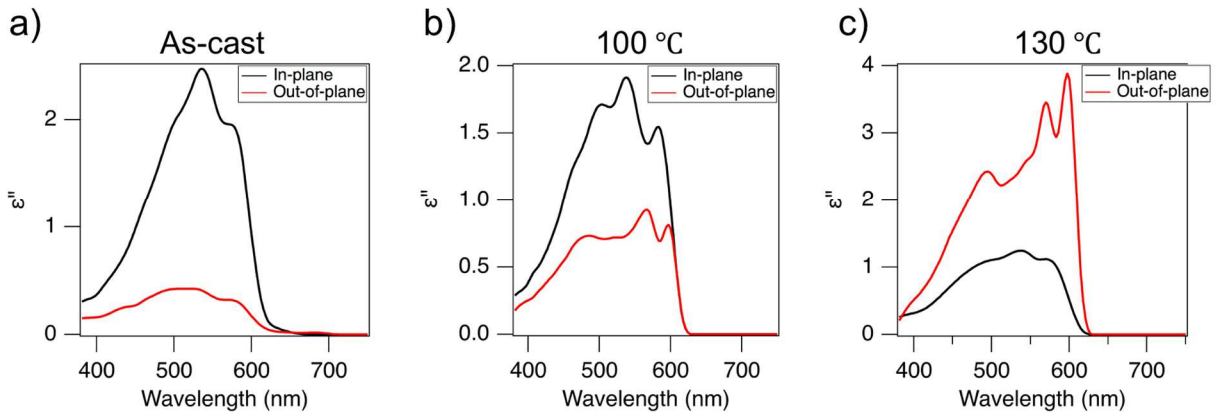

Figure 4.4: In-plane and out-of-plane imaginary permittivities ε'' of (a) as-cast films and films annealed at (b) 100 and (c) 130 °C

4.2.2 Doping Efficiency Affected by Side-Chain Interdigitation

To investigate the doping efficiency and resulting charge transport properties of as-cast and annealed PQT films, we leveraged vapor doping of PQT thin films with *p*-type dopant 2,3,5,6-tetrafluoro-7,7,8,8-tetracyanoquinodimethane (F4TCNQ). UV-vis-NIR absorption spectra of neat and doped PQT films at each condition are shown in Figure 4.5. For neat PQT, the primary absorption peak is observed at 2.2 eV. Upon introducing dopant vapor, as-cast and 130 ℃ annealed samples share a similar charge transfer process between PQT and F4TCNQ as the neutral absorption peak bleaches while the F4TCNQ anion absorption peaks appear near ~1.4 eV together with the neutral F4TCNQ absorption peak near 3.25 eV. As expected, the absorption features due to charge transfer become more pronounced and the absorption of neutral PQT peak diminishes with increasing F4TCNQ vapor doping time, which indicates efficient charge transfer. However, for 100 ℃ annealed samples, only weak anion peaks can be observed upon introducing dopant and the peak intensity does not increase with increasing doping time, suggesting a significant low doping efficiency between 100 ℃ annealed PQT films and F4TCNQ. Side-chain and π-stacking

spacings for all doped samples from GIWAXS experiments were analyzed to probe the dopant distributions in crystalline domains of PQT films as a function of doping time (Figure 4.6). As expected, d_{100} of as-cast and 130℃ annealed films increase upon doping and saturate at 2.2 nm and 2.0 nm, respectively. On the other hand, $d_{100'}$ of the second polymorph shows little increase during the doping process, which confirms the much weaker doping efficiency for the second polymorph.

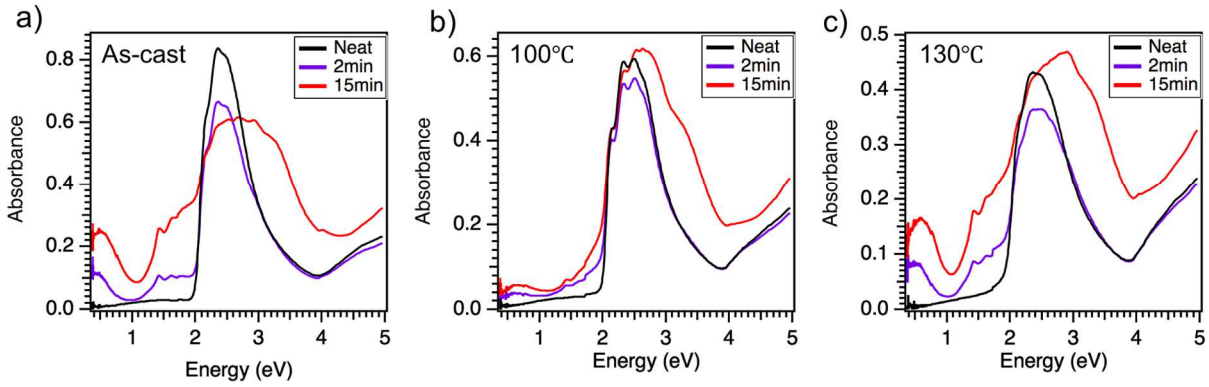

Figure 4.5: UV-Vis spectra of F4TCNQ-doped a) as-cast sample, b) 100 ℃ annealed sample and c) 130 ℃ annealed sample

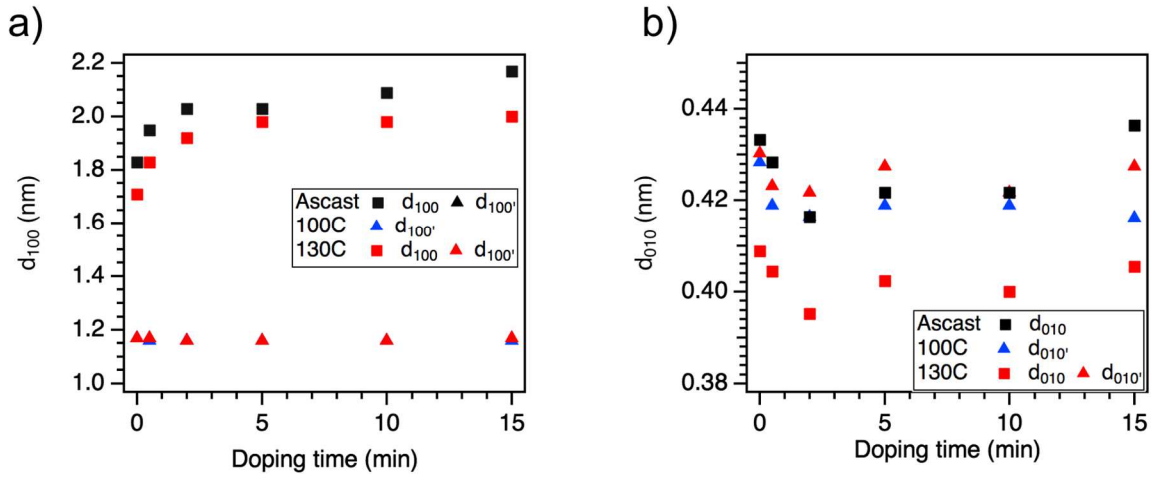

Figure 4.6: (a) Side-chain stacking (d_{100}) and (b) π-stacking distance (d_{010}) of PQT:F4TCNQ thin films as a function of vapor doping time.

The Seebeck coefficient and conductivity of as-cast and annealed PQT as a function of F4TCNQ vapor doping time are summarized in Figure 4.7. For as-cast and 130 ℃ annealed films,

conductivity increases rapidly over two orders of magnitude and saturate after 2 min of doping. Specifically, as-cast and 130 ℃ annealed PQT films have a maximum conductivity of 2.1 ± 1.1 S/cm and 6.1 ± 0.3 S/cm, respectively. On the other hand, 100 ℃ annealed PQT films possess a much lower conductivity upon doping with F4TCNQ due to the low dopant efficiency. The maximum conductivity of 100 ℃ annealed samples is (6.1 ± 0.4) × 10^{-3} S/cm, which is 3 orders of magnitude lower than samples under other conditions.

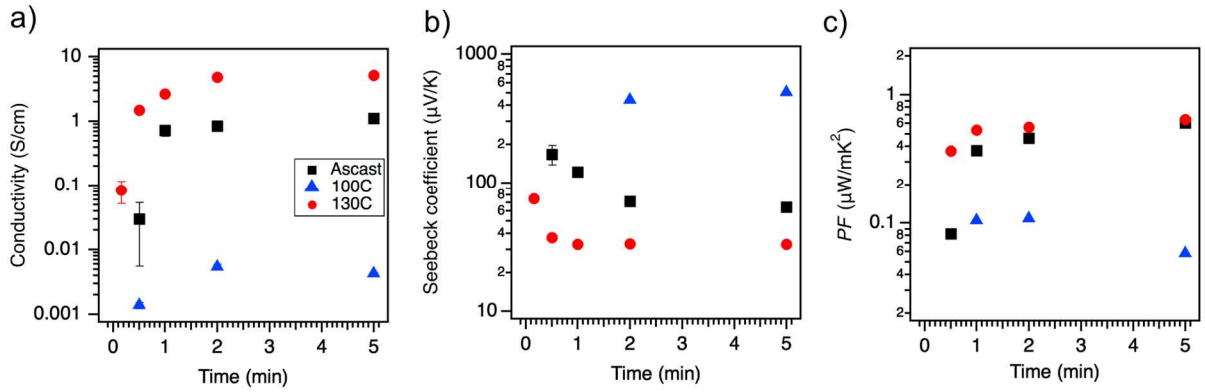

Figure 4.7: (a) Conductivity (σ), (b) Seebeck coefficient (α) and (c) corresponding power factor ($PF = \alpha^2\sigma$) of PQT:F4TCNQ thin films as a function of vapor doping time.

As expected, Seebeck coefficients of doped films show an inverse trend with doping time compared to conductivity profiles. The Seebeck coefficient decreases with increasing vapor doping time and reaches plateau after 2 min of doping (Figure 4.7b). 100 ℃ annealed films thus have a much higher Seebeck than the other samples. The Seebeck coefficients of as-cast, 100 ℃ and 130 ℃ annealed PQT thin films at saturated doping level (15 min) are 83.8 ± 3.5 μV/K, 474 ± 34 μV/K and 39.8 ± 2.6 μV/K, respectively. The resulting PF is calculated and plot in Figure 4.4c. It is worth noting that despite high seebeck coefficient, 100 ℃ annealed sample has the lowest PF (0.1 μW/mK^2) due to significant low conductivity resulting from low doping efficiency. 130 ℃ annealed sample, on the other hand, has a maximum PF of 0.6 μW/mK^2, which is 6 times higher than sample annealed at 100 ℃.

4.3 Conclusion

In summary, we investigated the microstructure change and the resulting charge transport properties of a polythiophene, PQT, via thermal annealing process. Structural characterization (GIWAXS and ellipsometry) reveals the polymorphism and chain orientation in PQT. Upon vapor doping with F4TCNQ, we show that polymorphs with stronger interdigitation in side chains have significant effect on doping efficiency and thus the charge transport properties. 100 ℃ annealed sample has a maximum conductivity of $(6.1 \pm 0.4) \times 10^{-3}$ S/cm due to low doping efficiency, resulting from strong packing of side chains, while 130℃ annealed sample exhibits a σ as high as 6.1 ± 0.3 S/cm. Our findings demonstrate the importance of understanding the interrelation between solid-state packing and doping efficiency of molecularly doped CPs, which could benefit the designs of semiconducting polymers with well-defined doping levels for new organic TE materials.

4.4 Experimental Methods

Materials. Poly (3,3'''-didodecyl quarter thiophene) (PQT, 30 – 80 KDa) was purchased from Solaris Chem. 2,3,5,6-tetrafluoro-7,7,8,8-tetracyanoquinodimethane (F4TCNQ) was purchased from TCI Chemicals.

Thin Film Preparation. Thin film samples for GIWAXS, AFM and Ellipsometry experiments were prepared on silicon with native oxide wafer substrates (15 mm × 15 mm × 0.5 mm, University Wafer). Thin film samples for UV-VIS-NIR spectroscopy and electrical characterization were prepared on quartz substrates (15 mm × 15 mm × 0.5 mm, University Wafer). All substrates were cleaned by sonicating in acetone and isopropanol for 10 min each, followed by plasma-cleaning for 3 min. For as-cast PQT thin film preparation, PQT was dissolved in

chloroform (5 mg/mL), and the solution was stirred overnight to fully dissolve the polymer. Then thin films were spin-coated using SCS G3P spin coater using customized recipes based on thickness requirements. All solution preparation and spin-coating steps were performed in an Argon glovebox. Thickness of neat films were measured via ellipsometry.

Vapor Doping Process. Vapor doping was performed in an Argon glovebox using the custom-built vapor doping chamber, which is introduced in Chapter 2. A Peltier module is added on the top of the holder to provide a constant substrate temperature of 30℃ during the doping process.

Atomic Force Microscopy. The surface topographies of thin film samples were characterized by a Cypher ES AFM (Asylum Research Oxford) with a FS-1500 AuD cantilever at room temperature in Soft Matter Characterization Facility (SMCF) (Pritzker School of Molecular Engineering, University of Chicago). The images were acquired using tapping mode and analyzed by using Gwyddion software.

Ellipsometry. Variable-angle spectroscopic ellipsometry (VASE) measurements were performed using the alpha-SE Ellipsometer (J. A. Woollam Co.,). The experiments were carried out on polymer films deposited using identical conditions onto 3 different Si substrates; one substrate with a thin layer of native oxide and the other 2 with a layer of thermally grown SiO2 that is 500 and 1000 nm thick. The measurements were performed in reflection mode at 55°, 65° and 75°. The data were then fit simultaneously using the CompleteEASE software, provided by J. A. Woollam Co., in order to determine the thickness and optical constants of PQT. To identify the best fit for PQT optical constants, we built a model such that the sample's structure was Si/SiO2/PQT. The optical constants of the Si, native oxide and thermally grown SiO2 were taken

from CompleteEASE software's library database. The multisample analysis was necessary to increase the uniqueness of the fits due to the strong correlations between the fitting parameters.[37,40]

UV-VIS-NIR absorption spectroscopy, GIWAXS experiments, conductivity and Seebeck measurements were conducted in the same manner as in Chapter 2 and 3.

4.5 Acknowledgments

This work was supported by the University of Chicago Materials Research Science and Engineering Center, which is funded by National Science Foundation under award number DMR-1420709. This research used resources of the Advanced Photon Source, an Office of Science User Facility operated for the U.S. Department of Energy (DOE) by Argonne National Laboratory under Contract No. DE-AC02-06CH11357. Parts of this work were carried out at the Soft Matter Characterization Facility of the University of Chicago.

4.6 References

(1) Sirringhaus, H. *25th Anniversary Article: Organic Field-Effect Transistors: The Path beyond Amorphous Silicon*. *Advanced Materials*. March 2014, pp 1319–1335.

(2) Dou, L.; You, J.; Hong, Z.; Xu, Z.; Li, G.; Street, R. A.; Yang, Y. 25th Anniversary Article: A Decade of Organic/Polymeric Photovoltaic Research. *Adv. Mater.* **2013**, *25* (46), 6642–6671.

(3) Walzer, K.; Männig, B.; Pfeiffer, M.; Leo, K. Highly Efficient Organic Devices Based on Electrically Doped Transport Layers. *Chem. Rev.* **2007**, *107* (4), 1233–1271.

(4) Russ, B.; Glaudell, A.; Urban, J. J.; Chabinyc, M. L.; Segalman, R. A. Organic Thermoelectric Materials for Energy Harvesting and Temperature Control. *Nat. Rev. Mater.* **2016**, *1* (10), 16050.

(5) Kroon, R.; Mengistie, D. A.; Kiefer, D.; Hynynen, J.; Ryan, J. D.; Yu, L.; Müller, C. Thermoelectric Plastics: From Design to Synthesis, Processing and Structure-Property Relationships. *Chem. Soc. Rev.* **2016**, *45* (22), 6147–6164.

(6) Goel, M.; Thelakkat, M. Polymer Thermoelectrics: Opportunities and Challenges. *Macromolecules* **2020**, *53* (10), 3632–3642.

(7) Zhang, F.; Di, C. Exploring Thermoelectric Materials from High Mobility Organic Semiconductors. *Chem. Mater.* **2020**, *32* (7), 2688–2702.

(8) Snyder, G. J.; Toberer, E. S. Complex Thermoelectric Materials. *Nat. Mater.* **2008**, *7* (2), 105–114.

(9) Glaudell, A. M.; Cochran, J. E.; Patel, S. N.; Chabinyc, M. L. Impact of the Doping Method on Conductivity and Thermopower in Semiconducting Polythiophenes. *Adv. Energy Mater.* **2015**, *5* (4).

(10) Jacobs, I. E.; Moulé, A. J. *Controlling Molecular Doping in Organic Semiconductors*. *Advanced Materials*. 2017.

(11) Zhao, W.; Ding, J.; Zou, Y.; Di, C. A.; Zhu, D. Chemical Doping of Organic Semiconductors for Thermoelectric Applications. *Chem. Soc. Rev.* **2020**, *49* (20), 7210–7228.

(12) Tam, T. L. D.; Xu, J. Strategies and Concepts in N-Doped Conjugated Polymer Thermoelectrics. *J. Mater. Chem. A* **2021**, *9* (9), 5149–5163.

(13) Scholes, D. T.; Hawks, S. A.; Yee, P. Y.; Wu, H.; Jeffrey, R.; Tolbert, S. H.; Schwartz, B. J.; Lindemuth, J. R.; Tolbert, S. H.; Schwartz, B. J. Overcoming Film Quality Issues for Conjugated Polymers Doped with F4TCNQ by Solution Sequential Processing: Hall Effect, Structural, and Optical Measurements. *J. Phys. Chem. Lett.* **2015**, *6* (23), 4786–4793.

(14) Jacobs, I. E.; Aasen, E. W.; Oliveira, J. L.; Fonseca, T. N.; Roehling, J. D.; Li, J.; Zhang,

G.; Augustine, M. P.; Mascal, M.; Moulé, A. J. Comparison of Solution-Mixed and Sequentially Processed P3HT:F4TCNQ Films: Effect of Doping-Induced Aggregation on Film Morphology. *J. Mater. Chem. C* **2016**, *4* (16), 3454–3466.

(15) Hynynen, J.; Kiefer, D.; Yu, L.; Kroon, R.; Munir, R.; Amassian, A.; Kemerink, M.; Müller, C. Enhanced Electrical Conductivity of Molecularly P-Doped Poly(3-Hexylthiophene) through Understanding the Correlation with Solid-State Order. *Macromolecules* **2017**, *50* (20), 8140–8148.

(16) Patel, S. N.; Glaudell, A. M.; Kiefer, D.; Chabinyc, M. L. Increasing the Thermoelectric Power Factor of a Semiconducting Polymer by Doping from the Vapor Phase. *ACS Macro Lett.* **2016**, *5* (3).

(17) Lim, E.; Peterson, K. A.; Su, G. M.; Chabinyc, M. L. Thermoelectric Properties of Poly(3-Hexylthiophene) (P3HT) Doped with 2,3,5,6-Tetrafluoro-7,7,8,8-Tetracyanoquinodimethane (F4TCNQ) by Vapor-Phase Infiltration. *Chem. Mater.* **2018**, *30* (3), 998–1010.

(18) Hamidi-Sakr, A.; Biniek, L.; Bantignies, J.-L.; Maurin, D.; Herrmann, L.; Leclerc, N.; Lévêque, P.; Vijayakumar, V.; Zimmermann, N.; Brinkmann, M. A Versatile Method to Fabricate Highly In-Plane Aligned Conducting Polymer Films with Anisotropic Charge Transport and Thermoelectric Properties: The Key Role of Alkyl Side Chain Layers on the Doping Mechanism. *Adv. Funct. Mater.* **2017**, *27* (25), 1700173.

(19) Patel, S. N.; Glaudell, A. M.; Peterson, K. A.; Thomas, E. M.; O'Hara, K. A.; Lim, E.; Chabinyc, M. L. Morphology Controls the Thermoelectric Power Factor of a Doped Semiconducting Polymer. *Sci. Adv.* **2017**, *3* (6), e1700434.

(20) Jacobs, I. E.; Aasen, E. W.; Oliveira, J. L.; Fonseca, T. N.; Roehling, J. D.; Li, J.; Zhang, G.; Augustine, M. P.; Mascal, M.; Moulé, A. J. Comparison of Solution-Mixed and Sequentially Processed P3HT:F4TCNQ Films: Effect of Doping-Induced Aggregation on Film Morphology. *J. Mater. Chem. C* **2016**, *4* (16), 3454–3466.

(21) Vijayakumar, V.; Zaborova, E.; Biniek, L.; Zeng, H.; Herrmann, L.; Carvalho, A.; Boyron, O.; Leclerc, N.; Brinkmann, M. Effect of Alkyl Side Chain Length on Doping Kinetics, Thermopower, and Charge Transport Properties in Highly Oriented F4TCNQ-Doped PBTTT Films. *ACS Appl. Mater. & Interfaces* **2019**, *11* (5), 4942–4953.

(22) Scholes, D. T.; Yee, P. Y.; Lindemuth, J. R.; Kang, H.; Onorato, J.; Ghosh, R.; Luscombe, C. K.; Spano, F. C.; Tolbert, S. H.; Schwartz, B. J. The Effects of Crystallinity on Charge Transport and the Structure of Sequentially Processed F4TCNQ-Doped Conjugated Polymer Films. *Adv. Funct. Mater.* **2017**, *27* (44), 1–13.

(23) Kiefer, D.; Kroon, R.; Hofmann, A. I.; Sun, H.; Liu, X.; Giovannitti, A.; Stegerer, D.; Cano, A.; Hynynen, J.; Yu, L.; Zhang, Y.; Nai, D.; Harrelson, T. F.; Sommer, M.; Moulé, A. J.; Kemerink, M.; Marder, S. R.; McCulloch, I.; Fahlman, M.; Fabiano, S.; Müller, C. Double Doping of Conjugated Polymers with Monomer Molecular Dopants. *Nat. Mater.* **2019**, *18* (2), 149–155.

(24) Yuen, A. P.; Hor, A. M.; Jovanovic, S. M.; Preston, J. S.; Klenkler, R. A.; Bamsey, N. M.; Loutfy, R. O. Improved Stability of Solution Processed Photovoltaic Devices Using PQT-12. *Sol. Energy Mater. Sol. Cells* **2010**, *94* (12), 2455–2458.

(25) Pan, H.; Liu, P.; Li, Y.; Wu, Y.; Ong, B. S.; Zhu, S.; Xu, G. Unique Polymorphism of Oligothiophenes. *Adv. Mater.* **2007**, *19* (20), 3240–3243.

(26) Jacobs, I. E.; Cendra, C.; Harrelson, T. F.; Bedolla Valdez, Z. I.; Faller, R.; Salleo, A.; Moulé, A. J. Polymorphism Controls the Degree of Charge Transfer in a Molecularly Doped Semiconducting Polymer. *Mater. Horizons* **2018**, *5* (4), 655–660.

(27) Jimison, L. H.; Salleo, A.; Chabinyc, M. L.; Bernstein, D. P.; Toney, M. F. Correlating the Microstructure of Thin Films of Poly[5,5-Bis(3-Dodecyl-2- Thienyl)-2,2-Bithiophene] with Charge Transport: Effect of Dielectric Surface Energy and Thermal Annealing. *Phys. Rev. B - Condens. Matter Mater. Phys.* **2008**, *78* (12), 125319.

(28) Kang, S. J.; Song, S.; Liu, C.; Kim, D. Y.; Noh, Y. Y. Evolution in Crystal Structure and Electrical Performance of Thiophene-Based Polymer Field Effect Transistors: A Remarkable Difference between Thermal and Solvent Vapor Annealing. *Org. Electron.* **2014**, *15* (9), 1972–1982.

(29) Koch, F. P. V.; Smith, P.; Heeney, M. "Fibonacci's Route" to Regioregular Oligo(3-Hexylthiophene)S. *J. Am. Chem. Soc.* **2013**, *135* (37), 13695–13698.

(30) Koch, F. P. V.; Heeney, M.; Smith, P. Thermal and Structural Characteristics of Oligo(3-Hexylthiophene)s (3HT)n, n = 4-36. *J. Am. Chem. Soc.* **2013**, *135* (37), 13699–13709.

(31) Schulz, G. L.; Ludwigs, S. Controlled Crystallization of Conjugated Polymer Films from Solution and Solvent Vapor for Polymer Electronics. *Adv. Funct. Mater.* **2017**, *27* (1), 1603083.

(32) Verploegen, E.; Mondal, R.; Bettinger, C. J.; Sok, S.; Toney, M. F.; Bao, Z. Effects of Thermal Annealing upon the Morphology of Polymer-Fullerene Blends. *Adv. Funct. Mater.* **2010**, *20* (20), 3519–3529.

(33) Zhao, N.; Botton, G. A.; Zhu, S.; Duft, A.; Ong, B. S.; Wu, Y.; Liu, P. Microscopic Studies on Liquid Crystal Poly(3,3′- Dialkylquaterthiophene) Semiconductor. *Macromolecules* **2004**, *37* (22), 8307–8312.

(34) Wu, Y.; Liu, P.; Ong, B. S.; Srikumar, T.; Zhao, N.; Botton, G.; Zhu, S. Controlled Orientation of Liquid-Crystalline Polythiophene Semiconductors for High-Performance Organic Thin-Film Transistors. *Appl. Phys. Lett.* **2005**, *86* (14), 1–3.

(35) Grigorian, S.; Escoubas, S.; Ksenzov, D.; Duche, D.; Aliouat, M.; Simon, J. J.; Bat-Erdene, B.; Allard, S.; Scherf, U.; Pietsch, U.; Thomas, O. A Complex Interrelationship between Temperature-Dependent Polyquaterthiophene (PQT) Structural and Electrical Properties. *J. Phys. Chem. C* **2017**, *121* (41), 23149–23157.

(36) Jang, M.; Yang, H. Structural Control over Self-Assembled Crystals of φ-Conjugated Poly(3,3'-Didodecyl-Quaterthiophene) for Organic Field-Effect Transistor Applications. *J.*

Nanosci. Nanotechnol. **2012**, *12* (2), 1220–1225.

(37) Gurau, M. C.; Delongchamp, D. M.; Vogel, B. M.; Lin, E. K.; Fischer, D. A.; Sambasivan, S.; Richter, L. J. Measuring Molecular Order in Poly(3-Alkylthiophene) Thin Films with Polarizing Spectroscopies. *Langmuir* **2007**, *23* (2), 834–842.

(38) Zhang, X.; Bronstein, H.; Kronemeijer, A. J.; Smith, J.; Kim, Y.; Kline, R. J.; Richter, L. J.; Anthopoulos, T. D.; Sirringhaus, H.; Song, K.; Heeney, M.; Zhang, W.; McCulloch, I.; Delongchamp, D. M. Molecular Origin of High Field-Effect Mobility in an Indacenodithiophene- Benzothiadiazole Copolymer. *Nat. Commun.* **2013**, *4* (1), 2238.

(39) Dong, B. X.; Li, A.; Strzalka, J.; Stein, G. E.; Green, P. F. Molecular Organization in MAPLE-Deposited Conjugated Polymer Thin Films and the Implications for Carrier Transport Characteristics. *J. Polym. Sci. Part B Polym. Phys.* **2017**, *55* (1), 39–48.

(40) Dong, B. X.; Amonoo, J. A.; Purdum, G. E.; Loo, Y. L.; Green, P. F. Enhancing Carrier Mobilities in Organic Thin-Film Transistors Through Morphological Changes at the Semiconductor/Dielectric Interface Using Supercritical Carbon Dioxide Processing. *ACS Appl. Mater. Interfaces* **2016**, *8* (45), 31144–31153.

Chapter 5: SEMICONDUCTING POLYMERS WITH A FUNCTIONAL GRADIENT IN MICROSTRUCTURE AND RESULTING IMPACT ON THERMOELECTRIC COOLING

This chapter will be published in the future as a journal article.

Functionally graded materials (FGMs) have been a promising approach to enhance the thermoelectric (TE) cooling performance. However, researches on organic FGMs as TE have been limited compared to their inorganic counterparts. In this work, we enable continuously graded (CG) semiconducting polymer thin films by coupling the solution and thermal processability of such polymer with molecular doping. A custom-built thermal annealing station is used to provide a temperature gradient across the film. We achieve CG poly(dodecyl-quaterthiophene) (PQT) thin films through spatially tuning the polymer microstructure along the temperature gradient. 1D profiles in conductivity (σ) and Seebeck coefficient (α) are captured after vapor doped by molecular *p*-dopant 2,3,5,6-tetrafluoro-7,7,8,8-tetracyanoquinodimethane (F4TCNQ). Cooling performance of the PQT CG thin films are modeled through linear constitutive relations coupled with conservation of charge and energy by using the experimentally derived σ and α spatial profiles. The results show that graded PQT thin films yield higher cooling temperature ($\Delta T_c = T_H - T_c$) compared to their equivalent uniform (EU) condition. Overall, this work showcases the strategy to improve the thermoelectric performance in cooling by leveraging functionally graded semiconducting polymers.

5.1 Introduction

Functionally graded materials (FGMs), whose properties are varied spatially either in a continuous or step-by-step (segmented) fashion throughout the volume of the material[1–3], have been developed to address a large spectrum of application fields.[4–7] In particular, FGMs has opened up alternative pathway to enhance the thermoelectric (TE) device performance along with the effort on optimization of material properties. Thermoelectric has been a promising technology that used both in TE generators for energy harvesting by capturing waste heat and in Peltier coolers for thermal energy management by controlling local temperature.[8–13] The TE energy conversion efficiency is benchmarked by its figure of merit, ZT, which is defined as $ZT = \alpha^2\sigma T/\kappa$, where α is the Seebeck coefficient, σ is the electronic conductivity, κ is the thermal conductivity and T is the temperature in Kelvin.[13]

To date, most of the research on thermoelectric is aiming to design new TE materials with better material performance. However, for some of TE applications, especially (micro)-distributed and localized cooling system, the current state-of-art TE materials are already sufficient to provide competitive performance.[14] FGMs, on the other hand, open up another route to further increase the TE device performance by optimize the configuration in TE properties. So far, FGMs have been investigated as TE cooling applications based on inorganic TE materials such as Bi_2Te_3 and PbTe.[3,7,15–18] The spatial variations in TE properties of FGMs enable efficient redistribution of the Joule heating and Peltier cooling effects, which results in enhanced cooling temperature and coefficient of performance (*C.O.P.*) compared to materials with uniform TE properties.[2,5,19–21] The improvements in cooling performance of inorganic FGMs have been investigated through modeling and simulation studies, leading to elaboration of optimal gradients in TE material properties.[21–28] However, researches on FGMs have shown that it could be prohibitive to realize

functional grading motifs using inorganic materials as the fabrication process would require high temperature and pressure.[2,7,15,16,29,30]

In contrast to inorganic materials, semiconducting conjugated polymers have the ease to experimentally achieve FGMs by leveraging the inherent solution and thermal processability. Recently, polymeric materials have been investigated in Peltier cooling applications as organic thin film devices due to their promising performance in near room temperature environment.[31–33] In particular, for the case of thiophene-based semiconducting polymers, variety of functional grading motifs can be realized by either controlling the molecular dopant composition or tuning the polymer microstructure across the polymer films. In the prior chapters, we present the first series of reports on organic FGMs through dopant compositional control: the double-segmented polymer film and the continuously graded polymer film.[34,35] Both studies leveraged the sequential vapor doping of poly[2,5-bis(3-tetradecylthiophen-2-yl) thieno [3,2-b]thiophene] (PBTTT) by molecular dopant, F4TCNQ. By utilizing a home-built vapor doping apparatus, we were able to achieve variation in dopant distribution across the films, and thus results in gradient profiles of TE properties (α and σ). Our work showcased the facile fabrication and characterization of functionally graded polymer thin films for TE materials, which serves as promising directions to further advance the development of more efficient organic thermoelectric devices.

Together with implementing the principle of molecular doping, functional gradient can also be achieved by tuning the microstructure of semiconducting polymers via thermal processing treatments. Thermal annealing is an effective approach to control the crystallization conditions and thus modulates the molecular packing of CPs. In this work, we report on the fabrication of continuously graded (CG) polymer thin films through the microstructure control that help enhance thermoelectric cooling performance. A temperature gradient is achieved by the custom-built

thermal annealing station (Figure 5.1), which yields a gradient in PQT microstructure across the film. The whole film is doped with the molecular dopant F4TCNQ, resulting in 1D spatial profiles of both σ and α. Moreover, the cooling performances of the CG thin films are modelled by coupling the conservation of charge and energy with linear Onsager theory.

5.2 Results and Discussion

5.2.1 Fabricating Continuously Graded Films through Combination of Thermal Annealing and Molecular Doping.

Poly(dodecyl-quaterthiophene) (PQT) possess unique microstructure at the as-cast state that two polymorphs with different side chain interdigitations coexist, which has been studied in past literatures [36–38] as well as in Chapter 4. Upon thermal annealing above melting transition of PQT side chains (100 ℃) followed by recrystallization, the first polymorph with larger side chain spacing disappears and the second polymorph with stronger side chain interdigitation dominates in the PQT thin film. However, when the film undergoes melting transition of π-stacking (annealed at 130 ℃), both polymorphs still coexist, and the crystallite rearrangement leads to a chain-on orientation. This variation in polymer microstructure resulted from thermal annealing process gives rise to the difference in the ability of PQT to uptake molecular dopant, e.g. F4TCNQ, during the doping process, and thus leads to variation in thermoelectric materials properties (α and σ). In particular, the conductivity values of F4TCNQ-doped PQT films are varying over three orders of magnitude among different annealed states as shown in Figure 5.1.

As PQT microstructure is easily tuned by thermal annealing, a functional graded polymer film can be fabricated by exposing the PQT thin film to a temperature gradient. Variation in the

microstructure of the PQT film along the gradient leads to variation in thermoelectric properties (σ and α) upon optimal doping by F4TCNQ. To realize the functionally graded PQT thin films, a custom thermal annealing stage was fabricated (Figure 5.2, detailed description in Experimental section) wherein one end is set above the PQT transition temperature (i.e., 130 ℃) while the other end is set to near room temperature. Placing the PQT film substrate across an air gap between the two stage ends leads to the development of a one-dimensional temperature gradient along the length of the substrate and the film atop (Figure 5.2b). Using an IR camera, a clear temperature gradient can be observed across the horizontal direction of the film (Figure 5.2c). By selecting regularly-spaced points across the film (every 1 mm), the range of the temperature gradient across the film can be quantified (Figure 5.2d). The temperature profile follows a linear increasing trend from 40 ℃ to 130 ℃ upon equilibrium. After annealing for 10 min, the hot end of the stage is reduced to near room temperature, allowing the film to cool slowly. The annealed film is then vapor doped by F4TCNQ using a custom doping chamber for 5 min, resulting in a previously determined optimal doping across the film.

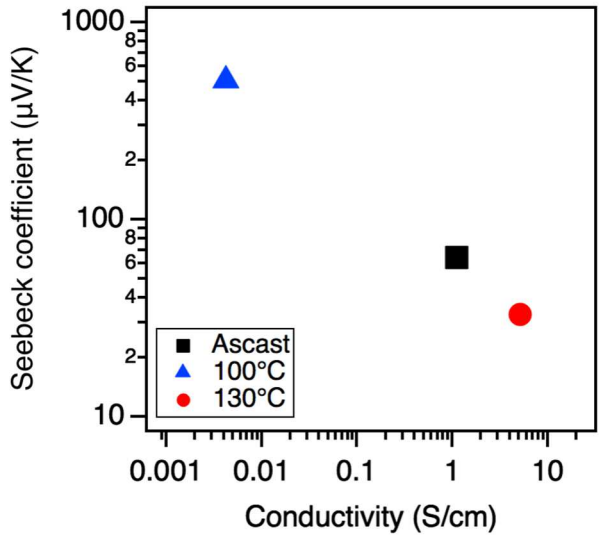

Figure 5.1: Seebeck coefficient and conductivity values of F4TCNQ doped as-cast and annealed PQT thin films.

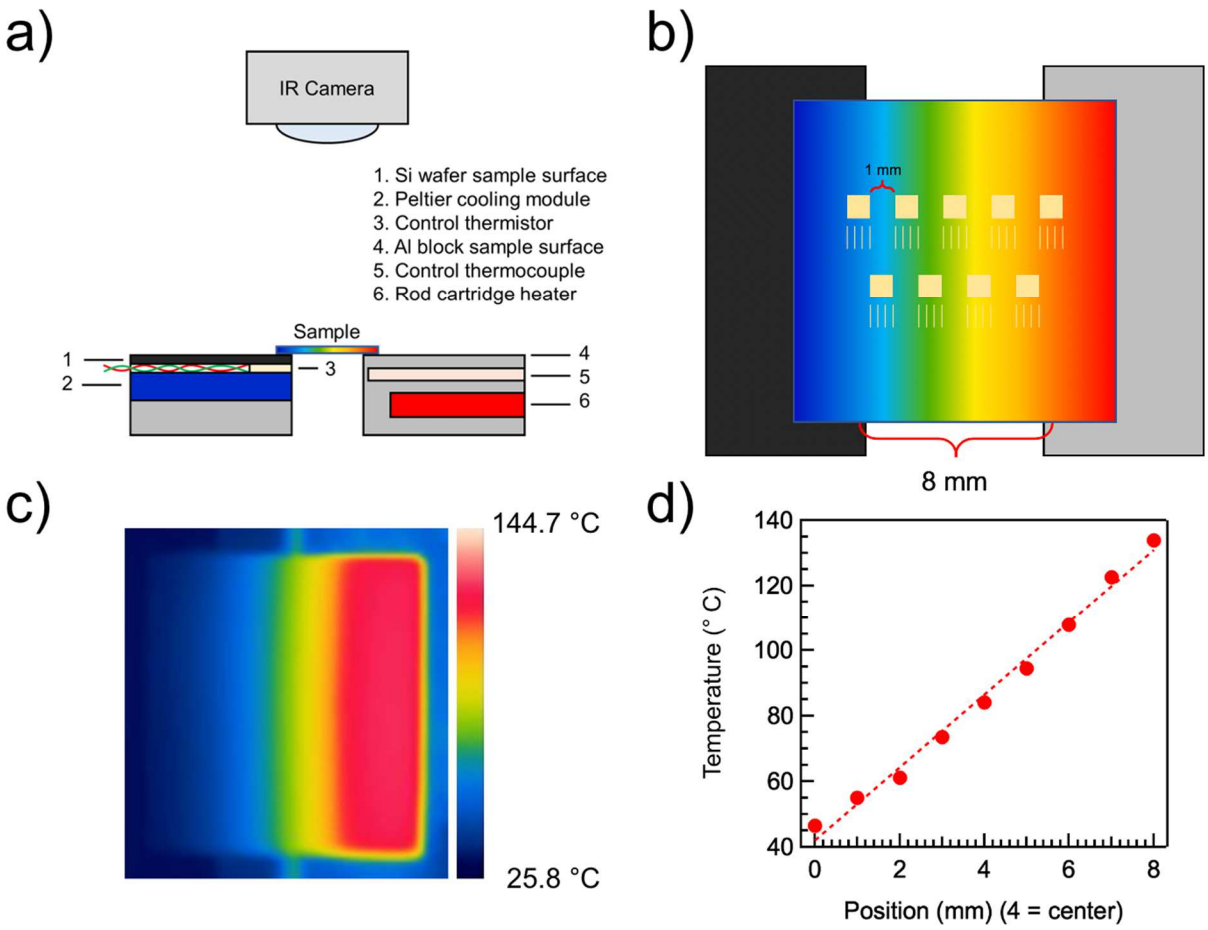

Figure 5.2: (a) Set up of IR Camera and thermal annealing stage. (b) Schematic and (c) IR image of PQT thin film under temperature gradient. (d) Temperature profile along the gradient measured by IR camera

Grazing incidence wide angle X-ray scattering (GIWAXS) experiments were performed on a representative CG thin film to verify the gradient in dopant distribution arises from the variation in PQT microstructure. GIWAXS images of PQT:F4TCNQ 40 – 130 graded films at an interval of 1.6 mm are shown in Figure 5.3. Figure 5.3a is the 2D scattering pattern taken at the 40 ℃ side of the film where two side chain stacking scattering peaks are observed at q values of 0.33 and 0.54 $Å^{-1}$, representing polymorphs with two different side chain stackings referred as (100) and (100)'. The side chain spacing distances are calculated to be 1.90 nm and 1.16 nm, respectively. Upon moving to the right side of the film, the (100) peak becomes less significant while the (100)' peak

dominates with increased intensity (Figure 5.3b, c and d). When approaching the 130 ℃ annealed side of the film, the (100) peak reappears with higher order in the domain and (100)' peak intensity drops as shown in Figure 5.3e. Figure 5.3f summarized the out of plane scattering profiles for both (100) and (100)', which clearly demonstrates the gradual change in the interplay between (100) and (100)', indicating a gradient of *c.a.* 7 mm in PQT microstructure across the PQT:F4TCNQ film.

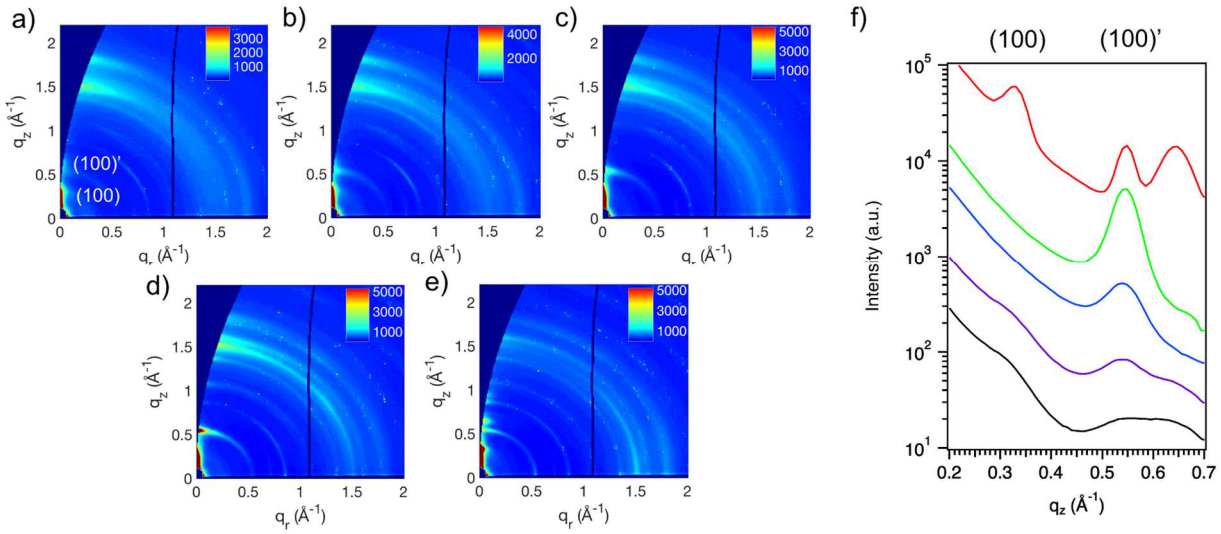

Figure 5.3: (a – e) Representative GIWAXS patterns and (f) Out-of-plane (100) and (100)' profiles along the graded PQT:F4TCNQ film (every 1.6 mm, *red curve is 2.4 mm away from green)

5.2.2 Continuously Graded Profiles in Seebeck Coefficient and Conductivity

To explore different gradient profiles, we fabricated three CG thin films with varying magnitudes in gradients of both σ and α across a 7 mm distance. These different gradients were achieved by varying the hot side and cold side temperatures on the thermal annealing station as described above. Specifically, the temperature ranges are assigned based on the thermal transition temperature of PQT, i.e., from 40 ℃ to 130 ℃, 40 ℃ to 100 ℃ and 100 ℃ to 130 ℃, respectively.

The actual temperature gradients from 40 ℃ to 100 ℃ and 100 ℃ to 130 ℃ across the films can be found in Figure 5.4. After annealing, all CG films are doped with F4TCNQ for 5 min. The measured σ and α profiles of the three graded films are shown in Figure 5.5 and are assigned CG1, CG2 and CG3. Both σ and α were spatially measured every 1 mm at 7 spots along the desired in-plane, lateral gradient direction.

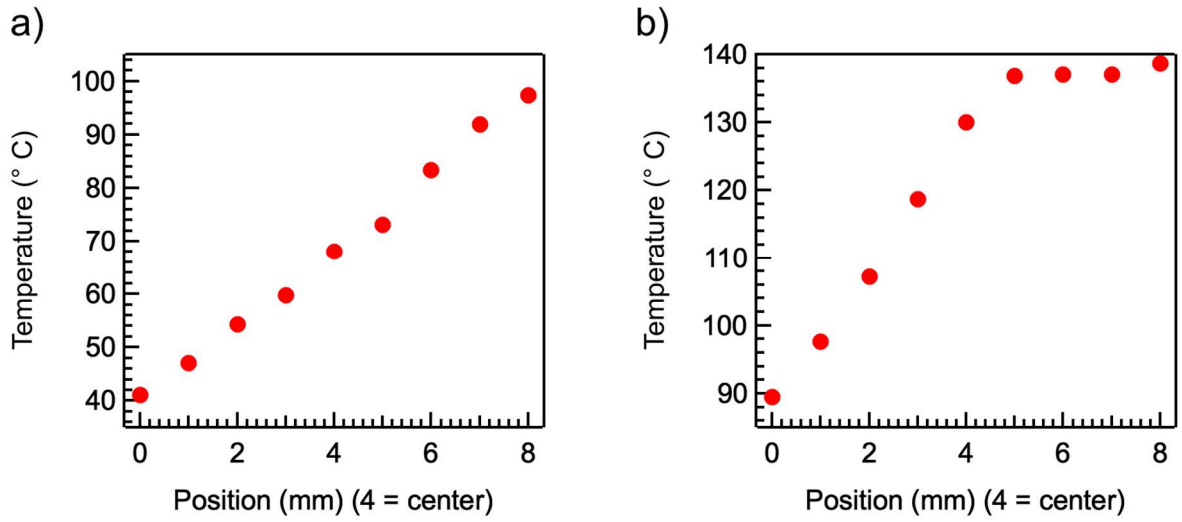

Figure 5.4: Temperature profiles of (a) 40 ℃ – 100 ℃) and (b) 100 ℃ – 130 ℃ samples measured by IR camera.

The measured values of σ and α across CG thin films are summarized in Figure 5.5 and Table 5.1 & 5.2. For CG1 film, starting from the 40 ℃ side (x = 0 mm), the conductivity value gradually drops from 2.5 ± 0.1 S/cm to 0.17 ± 0.04 S/cm in the middle of the film, and then raise up to 4.7 ± 0.5 S/cm when approaching the 130 ℃ annealing side. The values of Seebeck coefficients follow the opposite trend as α varies from 43.7 ± 5.4 μV/K to 111.8 ± 3.1 μV/K and then drops back to 46.9 ± 4.1 μV/K. For CG2 and CG3 films, the σ and α are exhibiting monochromic increase or decrease profiles along the majority part of the film (5 mm) as shown in Figure 5.5b and 5.5c. Specifically, σ decreases from 2.45 ± 0.67 to 0.126 ± 0.043 S/cm and α increases from 42.2 ± 1.2 to 98.1 ± 10 μV/K for CG2, σ decreases from 6.15 ± 0.94 to 0.248 ±

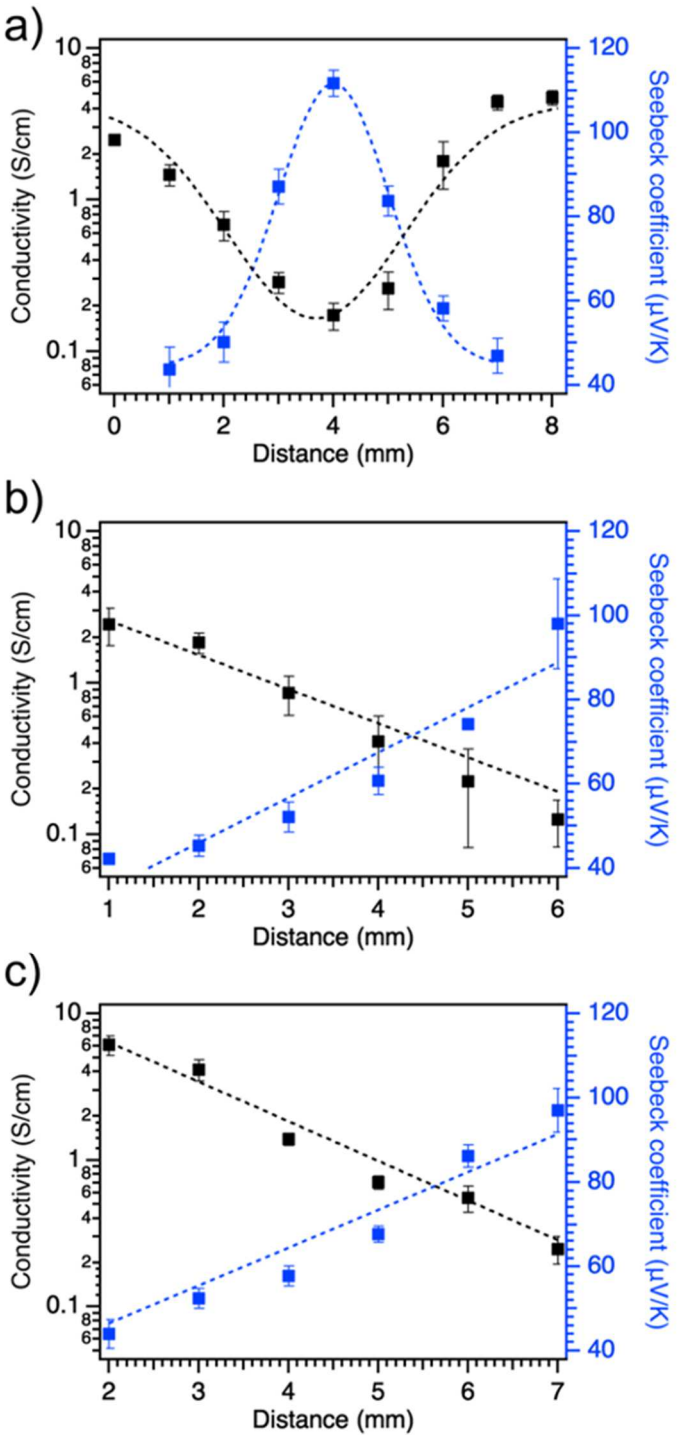

Figure 5.5: Experimentally measured Seebeck coefficient (α, blue square) and conductivity (σ, black square) values along the 1D gradient distance, x, for three CG thin films exhibiting different extent of grading: (a) CG1 (40 ℃ – 130 ℃) (b) CG2 (40 ℃ – 100 ℃) and (c) CG3 (100 ℃ – 130 ℃) thin films. The dashed lines represent fits to α and σ data.

0.053 S/cm and α increases from 43.9 $\pm$ 3.4 to 97.0 $\pm$ 5.2 μV/K for CG3 across 5 mm of the film (see the full spam of σ and α profiles for CG2 & CG3 in Appendix). It is worth noting that for both CG2 and CG3, the conductivity follows an exponential profile while Seebeck coefficient is varying linearly. The spatial distribution in $\alpha(x)$ was fit to a linear equation [$\alpha(x) = kx + m$] and the spatial distribution in $\sigma(x)$ was fit to an exponential equation [$\sigma(x) = a\exp(bx)$], where *k, m, a* and *b* has the unit of μV/mm·K, μV/K, S/cm and mm^{-1}, respectively.

Table 5.1: Seebeck coefficient data across the continuously graded PQT:F4TCNQ films

Sample	α_1 (μV/K) (x = 0 mm)	α_2 (μV/K) (x = 1 mm)	α_3 (μV/K) (x = 2 mm)	α_4 (μV/K) (x = 3 mm)	α_5 (μV/K) (x = 4 mm)	α_6 (μV/K) (x = 5 mm)	α_{avg} (μV/K)
CG2	42.2	45.3	52.2	60.7	74.2	98.1	62.1
CG3	43.9	52.4	57.8	67.7	86.3	97.0	67.5

Table 5.2: Conductivity data across the continuously graded PQT:F4TCNQ films

Sample	σ_1 (S/cm) (x = 0 mm)	σ_2 (S/cm) (x = 1 mm)	σ_3 (S/cm) (x = 2 mm)	σ_4 (S/cm) (x = 3 mm)	σ_5 (S/cm) (x = 4 mm)	σ_6 (S/cm) (x = 5 mm)	σ_{avg} (S/cm)
CG2	2.45	1.85	0.859	0.412	0.223	0.126	0.403
CG3	6.15	4.14	1.40	0.705	0.554	0.248	0.819

The spatial averages of the conductivity (σ_{avg}) and Seebeck coefficient (α_{avg}) for CG2 and CG3 thin film were calculated by integrating the gradient profile expressions across the total lateral distance (*L*) of 5 mm. The values for σ_{avg} and α_{avg} are summarized in Table 5.3. Here, these spatial average values were used to define an equivalent uniform (EU) condition for each corresponding experimentally derived CG thin film.

Table 5.3: Thermoelectric Properties and Model Calculated Cooling Temperature (ΔT_c) of CG PQT:F4TCNQ Thin Films

CG Thin Film	$\sigma(x)$[a] **(S/cm)**	$\alpha(x)$[a] **(μV/K)**	σ_{avg} **(S/cm)**	α_{avg} **(μV/K)**	ΔT_c **(K)** j **= 3 mA/mm²**
CG2	$2.86\exp(-0.63x)$	$10.71x + 35.4$	0.403	62.1	3.0
CG3	$6.25\exp(-0.65x)$	$10.76x + 40.6$	0.819	67.5	1.5

[a] x is in the unit of mm.

5.2.3 Model-Based Calculations of Cooling Performance for CG Films

To better investigate the PQT gradient profiles in terms of Peltier cooling, we modeled the cooling performance of CG2 and CG3 films using first principle calculations based on linear Onsager theory and coupled with charge and energy conservation.[39] The performance of their EU films are also modeled as comparison. From the derivation in Chapter 3 by combining the constitutive equations with the conservation law, the differential equation of 1D temperature profile *T(x)* is shown in Equation 5.1:

$$-\kappa \frac{\partial^2 T(x)}{\partial x^2} = \frac{j^2}{\sigma(x)} - j\frac{d\alpha(x)}{dx}T(x) \qquad (5.1)$$

More detailed derivation of Equation 5.1 and explanation on contribution of the different heat fluxes in a Peltier cooler can be found in Chapter 3. Note that the case of 1D transport along x-direction modelled here is based on the experimentally CG profiles with the assumption of no heat transfer between the thin film and glass substrate. Integration of Equation 5.1 was performed to calculate the $T(x)$ at specific values of j for two cases: *Case 1* – EU conditions where σ and α are spatially constant and *Case 2* – CG profiles of $\sigma(x)$ and $\alpha(x)$. For *Case 1*, an analytical solution can be obtained as the second term on the RHS of the equation ($-j\frac{d\alpha(x)}{dx}T(x)$) goes to zero. The

values of σ and α when solving for the EU case were determined through spatial averaging of $\sigma(x)$ and $\alpha(x)$ as described earlier. For *Case 2*, numerical integration of Equation 5.1 was applied using customized Python code as the inclusion of the spatial dependence of $\sigma(x)$ and $\alpha(x)$ leads to non-linear differential equation. Detailed derivations for both *Case 1* and *Case 2* can be found in Chapter 3. A mix boundary condition is applied for both cases where the hot side temperature, T_H (x = L) is fixed at 300 K and the heat flux on the hot side is constant. After the *T(x)* profile is solved, the cooling temperature, ΔT_c, is calculated from T_H minus the resulting temperature at the cold side ($T_C = T$ (x=0)). The model calculated $T(x)$ and ΔT_c of CG2 film were determined upon integrating Equation 5.1. It is worth noting that ΔT_c continues to increase with j for CG thin films as shown in Figure 5.6. One should treat the ΔT_c values as the idealized upper bound in cooling as we assumed the TE properties are temperature independent when solving Equation 5.1 for *T(x)*. In reality, the values of σ and α vary over temperature and could only be considered as constant within a reasonable temperature range. Therefore, a current density of 3 mA/mm^2 is chosen for following calculations in this study.

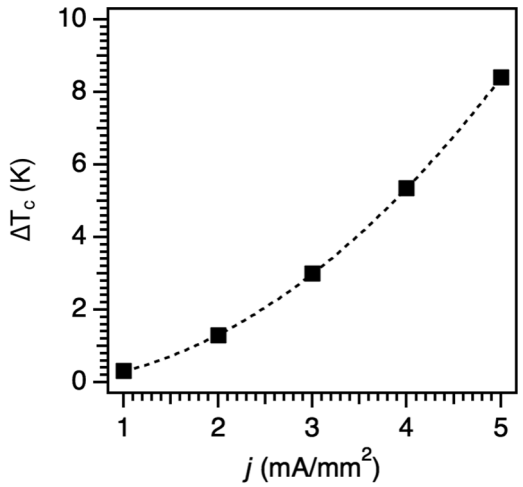

Figure 5.6: Calculated cooling temperatures ($\Delta T_c = T_H - T_c$) for CG2 with j ranging from 1 to 5 mA/mm^2

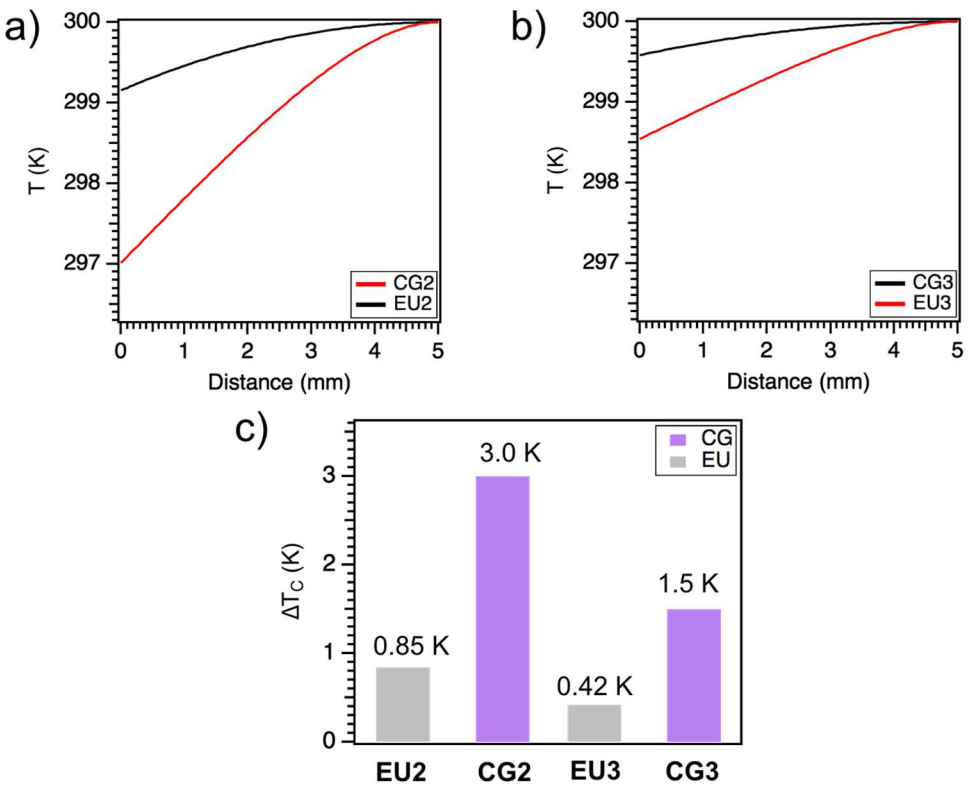

Figure 5.7: Modeled temperature profiles, $T(x)$, for (a) CG2 and (b) CG3 and their corresponding equivalent uniform (EU) condition at constant j of 3 mA/mm^2. (c) calculated cooling temperatures ($\Delta T_c = T_H - T_c$).

$T(x)$ profiles of both CG2 and CG3 and their corresponding EU conditions under input j of 3 mA/mm^2 and the corresponding ΔT_c are shown in Figure 5.7 and summarized in Table 5.3. It is clear that both CG thin films enhance the cooling temperature compared to their EU condition. The $T(x)$ profiles of CG thin films exhibits greater extent of curvature from the hot side to the cold side arising from improved heat pumping across the length of the gradient. At j = 3.0 mA/mm^2, ΔT_c of the CG thin films are 3.0 K and 1.5 K for CG2 and CG3, respectively. The cooling temperatures of both CG films are more than two times higher than their EU conditions, which are 0.85 K for EU2 and 0.42 K for EU3, respectively. Overall, the results of the two conditions emphasizes CG thin films enable improvements in Peltier cooling and break the limitation on material properties. Moreover, the cooling performances of CG thin films are also compared with

the uniform equivalents at the boundary conditions (i.e. EU with $\sigma(0)$ and $\alpha(0)$ and EU with $\sigma(L)$ and $\alpha(L)$, respectively). The model-based calculations of $T(x)$ profiles of CG2 and the uniform conditions at input j of 3 mA/mm^2 are shown in Figure 5.9 in Appendix. The results indicate that the film with the maximum α and minimum σ has the largest cooling temperature despite it possesses the lowest power factor compared to other uniform conditions.

5.3 Conclusion

In summary, we have utilized thermal annealing to achieve microstructure controlled continuously graded (CG) thin films. This approach leverages the inherent polymorphism structure of PQT and coupled with molecular doping to enable various types of gradients. In turn, we specifically fabricated two CG thin films with varying values in 1D gradient profiles of both σ and α across a 5 mm distance to explore how different gradient profiles control cooling performance. Based on the experimental derived profiles, we predicted the cooling temperature (ΔT_c) the CG thin films compared to their equivalent uniform (EU) as well as maximum/minimum uniform conditions by applying 1D transport model. Both CG films show enhancement in ΔT_c compared to their EU conditions, which arises from effective redistribution of the Joule heating and Peltier cooling effects. Overall, this work together with our previous studies showcase essential functional gradings of semiconducting polymers as organic thermoelectrics. Moving forward, more complex designs spanning multi-segments to continuously graded profiles are possible for more efficient organic TE devices.

5.4 Experimental Methods

Materials. Poly (3,3”’-didodecyl quarter thiophene) (PQT, 30 – 80 KDa) was purchased from Solaris Chem. 2,3,5,6-tetrafluoro-7,7,8,8-tetracyanoquinodimethane (F4TCNQ) was purchased from TCI Chemicals.

Thermal Annealing Station Set-up. The thermal annealing stage consists of two parallel platforms of equal height, capable of moving closer or further apart, as seen in Figure 5.2. The cold sink platform consists of Peltier cooling module (Custom Thermoelectric 06311-5L31-06CGQ, Figure 5.2a, #2) mounted to an aluminum base. A small thermistor (TE Technology, Inc. MP-3189, Figure 5.2a, #3) is attached to the Peltier module via thermally conductive adhesive, and copper sheet is placed on either side as a spacer. A silicon wafer (Figure 5.2a, #1) is placed on top the thermistor and copper sheet using thermally conductive adhesive to serve as the cooling surface. The Peltier module is controlled using a TE Technology, Inc. TC-720 temperature controller. The hot source platform consists of an aluminum block (Figure 5.2a, #4) containing an embedded thermocouple probe (Figure 5.2a, #5) and rod heaters (Figure 5.2a, #6). The temperature is regulated via an Omega CS8DPT heater controller. Both platforms are mounted to aluminum posts and insulated with fiberglass felt to ensure uniform heating. Samples are mounted to the stage using thermally conductive adhesive. IR images and video are captured using a FLIR ETS320 thermal imaging camera.

Thin Film Preparation and Vapor Doping Process were conducted the same manner as in Chapter 4. Conductivity and Seebeck measurements were conducted the same manner as in Chapter 3.

Grazing Incidence Wide Angle X-ray Diffraction. The detailed setup of GIWAXS experiments is shown in Chapter 2. GIWAXS images of continuously graded thin films were taken

at a grazing incident x-ray angle of 0.14°, which is above the critical angle of the polymer film and below the critical angle of the silicon substrate. GIWAXS images measured laterally across 10 different spots for the graded films. The distance between adjacent spots is 800 μm.

5.5 Acknowledgements

This work was supported by the University of Chicago Materials Research Science and Engineering Center, which is funded by National Science Foundation under award number DMR-1420709. This research used resources of the Advanced Photon Source, an Office of Science User Facility operated for the U.S. Department of Energy (DOE) by Argonne National Laboratory under Contract No. DE-AC02-06CH11357. Parts of this work were carried out at the Soft Matter Characterization Facility of the University of Chicago.

5.6 Appendix

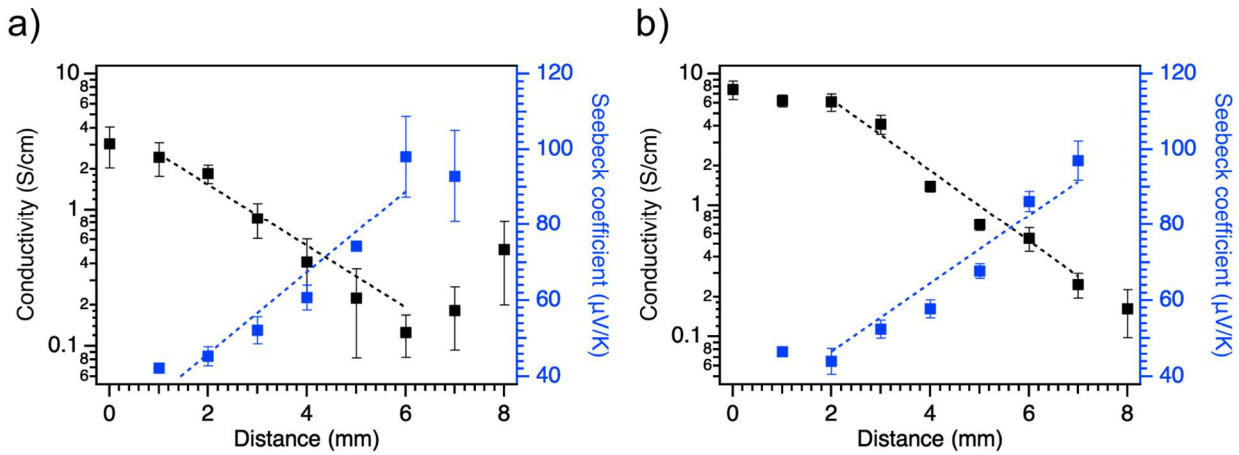

Figure 5.8: Experimentally measured Seebeck coefficient (α, blue square) and conductivity (σ, black square) values along the 1D gradient distance, x, for (a) CG2 (40 °C – 100 °C) and (b) CG3 (100 °C – 130 °C) thin films. The dashed lines represent fits to α and σ data.

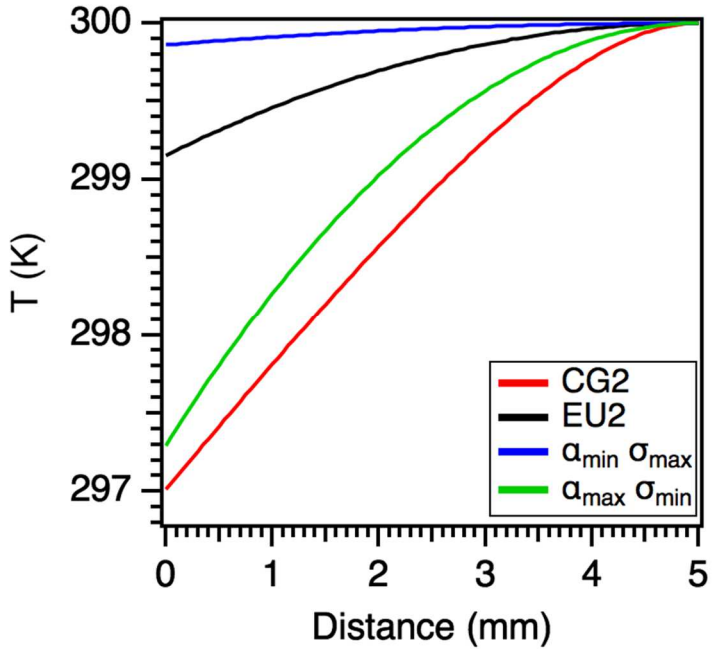

Figure 5.9: Modeled temperature profiles, $T(x)$, for CG2 and corresponding uniform conditions at constant j of 3 mA/mm^2.

5.7 References

(1) Liu, Z.; Meyers, M. A.; Zhang, Z.; Ritchie, R. O. Functional Gradients and Heterogeneities in Biological Materials: Design Principles, Functions, and Bioinspired Applications. *Prog. Mater. Sci.* **2017**, *88*, 467–498.

(2) Müller, E.; Drašar, Č.; Schilz, J.; Kaysser, W. A. Functionally Graded Materials for Sensor and Energy Applications. *Mater. Sci. Eng. A* **2003**, *362* (1–2), 17–39.

(3) Almasi, D.; Sadeghi, M.; Lau, W. J.; Roozbahani, F.; Iqbal, N. Functionally Graded Polymeric Materials: A Brif Review of Current Fabrication Methods and Introduction of a Novel Fabrication Method. *Mater. Sci. Eng. C* **2016**, *64*, 102–107.

(4) Kieback, B.; Neubrand, A.; Riedel, H. Processing Techniques for Functionally Graded Materials. *Mater. Sci. Eng. A* **2003**, *362* (1–2), 81–106.

(5) Cramer, C. L.; Wang, H.; Ma, K. Performance of Functionally Graded Thermoelectric Materials and Devices: A Review. *J. Electron. Mater.* **2018**, *47* (9), 5122–5132.

(6) Müller, E.; Drašar, Č.; Schilz, J.; Kaysser, W. A. Functionally Graded Materials for Sensor and Energy Applications. *Mater. Sci. Eng. A* **2003**.

(7) Sallehin, N. Z. I. M.; Yatim, N. M.; Suhaimi, S. A Review on Fabrication Methods for Segmented Thermoelectric Structure. **2018**, *030003*, 030003.

(8) Snyder, G. J.; Ursell, T. S. Thermoelectric Efficiency and Compatibility. *Phys. Rev. Lett.* **2003**, *91* (14), 148301/1-148301/4.

(9) Russ, B.; Glaudell, A.; Urban, J. J.; Chabinyc, M. L.; Segalman, R. A. Organic Thermoelectric Materials for Energy Harvesting and Temperature Control. *Nat. Rev. Mater.* **2016**, *1* (10), 16050.

(10) Wang, Y.; Yang, L.; Shi, X.-L.; Shi, X.; Chen, L.; Dargusch, M. S.; Zou, J.; Chen, Z.-G. Flexible Thermoelectric Materials and Generators: Challenges and Innovations. *Adv. Mater.* **2019**, *31* (29), 1807916.

(11) Petsagkourakis, I.; Tybrandt, K.; Crispin, X.; Ohkubo, I.; Satoh, N.; Mori, T. Thermoelectric Materials and Applications for Energy Harvesting Power Generation. *Sci. Technol. Adv. Mater.* **2018**, *19* (1), 836–862.

(12) Beretta, D.; Neophytou, N.; Hodges, J. M.; Kanatzidis, M. G.; Narducci, D.; Martin-Gonzalez, M.; Beekman, M.; Balke, B.; Cerretti, G.; Tremel, W.; Zevalkink, A.; Hofmann, A. I.; Müller, C.; Dörling, B.; Campoy-Quiles, M.; Caironi, M. Thermoelectrics: From History, a Window to the Future. *Mater. Sci. Eng. R Reports* **2019**, *138* (July).

(13) Snyder, G. J.; Toberer, E. S. Complex Thermoelectric Materials. *Nat. Mater.* **2008**, *7* (2),

105–114.

(14) Snyder, G. J.; LeBlanc, S.; Crane, D.; Pangborn, H.; Forest, C. E.; Rattner, A.; Borgsmiller, L.; Priya, S. Distributed and Localized Cooling with Thermoelectrics. *Joule* **2021**, *5* (4), 748–751.

(15) Hedegaard, E. M. J.; Mamakhel, A. A. H.; Reardon, H.; Iversen, B. B. Functionally Graded (PbTe) 1– x (SnTe) x Thermoelectrics. *Chem. Mater.* **2018**, *30* (1), 280–287.

(16) Zhang, Q.; Liao, J.; Tang, Y.; Gu, M.; Ming, C.; Qiu, P.; Bai, S.; Shi, X.; Uher, C.; Chen, L. Realizing a Thermoelectric Conversion Efficiency of 12% in Bismuth Telluride/Skutterudite Segmented Modules through Full-Parameter Optimization and Energy-Loss Minimized Integration. *Energy Environ. Sci.* **2017**, *10* (4), 956–963.

(17) Kuznetsov, V. L.; Kuznetsova, L. A.; Kaliazin, A. E.; Rowe, D. M. High Performance Functionally Graded and Segmented Bi2Te3-Based Materials for Thermoelectric Power Generation. *J. Mater. Sci.* **2002**, *37* (14), 2893–2897.

(18) Kim, C.; Kim, D. H.; Kim, J. S.; Han, Y. S.; Chung, J. S.; Kim, H. A Study of the Synthesis of Bismuth Tellurium Selenide Nanocompounds and Procedures for Improving Their Thermoelectric Performance. *J. Alloys Compd.* **2011**, *509* (39), 9472–9478.

(19) Müller, E.; Zabrocki, K.; Goupil, C.; Snyder, G. J.; Seifert, W. Functionally Graded Thermoelectric Generator and Cooler Elements. **2012**.

(20) Seifert, W.; Müller, E.; Walczak, S. Generalized Analytic One-Dimensional Description of Non-Homogeneous TE Cooler and Generator Elements Based on the Compatibility Approach. *Int. Conf. Thermoelectr. ICT, Proc.* **2006**, 714–719.

(21) Müller, E.; Walczak, S.; Seifert, W. Optimization Strategies for Segmented Peltier Coolers. *Phys. Status Solidi Appl. Mater. Sci.* **2006**, *203* (8), 2128–2141.

(22) Bian, Z.; Shakouri, A.; Cruz, S. Cooling Enhancement Using Inhomogeneous Thermoelectric Materials. *Int. Conf. Thermoelectr. ICT, Proc.* **2006**, No. 1, 264–267.

(23) Bian, Z.; Wang, H.; Zhou, Q.; Shakouri, A. Maximum Cooling Temperature and Uniform Efficiency Criterion for Inhomogeneous Thermoelectric Materials. *Phys. Rev. B - Condens. Matter Mater. Phys.* **2007**, *75* (24), 1–7.

(24) Vikhor, L. N.; Anatychuk, L. I. Theoretical Evaluation of Maximum Temperature Difference in Segmented Thermoelectric Coolers. *Appl. Therm. Eng.* **2006**, *26* (14), 1692–1696.

(25) Seifert, W.; Ueltzen, M.; Müller, E. One-Dimensional Modelling of Thermoelectric Cooling. *Phys. Status Solidi Appl. Res.* **2002**, *194* (1), 277–290.

(26) Thiébaut, E.; Goupil, C.; Pesty, F.; D'Angelo, Y.; Guegan, G.; Lecoeur, P. Maximization

of the Thermoelectric Cooling of a Graded Peltier Device by Analytical Heat-Equation Resolution. *Phys. Rev. Appl.* **2017**, *8* (6), 64003.

(27) Jin, Z. H.; Wallace, T. T. Functionally Graded Thermoelectric Materials with Arbitrary Property Gradations: A One-Dimensional Semianalytical Study. *J. Electron. Mater.* **2015**, *44* (6), 1444–1449.

(28) Shen, L.; Zhang, W.; Liu, G.; Tu, Z.; Lu, Q.; Chen, H.; Huang, Q. Performance Enhancement Investigation of Thermoelectric Cooler with Segmented Configuration. *Appl. Therm. Eng.* **2020**, *168* (August 2019), 114852.

(29) Hazan, E.; Ben-Yehuda, O.; Madar, N.; Gelbstein, Y. Functional Graded Germanium-Lead Chalcogenide-Based Thermoelectric Module for Renewable Energy Applications. *Adv. Energy Mater.* **2015**, *5* (11), 1–8.

(30) Hung, L. T.; Van Nong, N.; Snyder, G. J.; Viet, M. H.; Balke, B.; Han, L.; Stamate, E.; Linderoth, S.; Pryds, N. High Performance P-Type Segmented Leg of Misfit-Layered Cobaltite and Half-Heusler Alloy. *Energy Convers. Manag.* **2015**, *99*, 20–27.

(31) Jin, W.; Liu, L.; Yang, T.; Shen, H.; Zhu, J.; Xu, W.; Li, S.; Li, Q.; Chi, L.; Di, C.; Zhu, D. Exploring Peltier Effect in Organic Thermoelectric Films. *Nat. Commun.* **2018**, *9* (1), 3586.

(32) Sun, Z.; Li, J.; Wong, W.-Y. Emerging Organic Thermoelectric Applications from Conducting Metallopolymers. *Macromol. Chem. Phys.* **2020**, *221* (12), 2000115.

(33) Sun, Y.; Di, C.-A.; Xu, W.; Zhu, D. Advances in N-Type Organic Thermoelectric Materials and Devices. *Adv. Electron. Mater.* **2019**, *5* (11), 1800825.

(34) Ma, T.; Dong, B. X.; Grocke, G. L.; Strzalka, J.; Patel, S. N. Leveraging Sequential Doping of Semiconducting Polymers to Enable Functionally Graded Materials for Organic Thermoelectrics. *Macromolecules* **2020**, *53* (8), 2882–2892.

(35) Ma, T.; Kent, W.; Dong, B. X.; Grocke, G. L.; Patel, S. N. Continuously Graded Doped Semiconducting Polymers Enhance Thermoelectric Cooling. *Appl. Phys. Lett.* **2021**, *119* (1), 13902.

(36) Grigorian, S.; Escoubas, S.; Ksenzov, D.; Duche, D.; Aliouat, M.; Simon, J. J.; Bat-Erdene, B.; Allard, S.; Scherf, U.; Pietsch, U.; Thomas, O. A Complex Interrelationship between Temperature-Dependent Polyquaterthiophene (PQT) Structural and Electrical Properties. *J. Phys. Chem. C* **2017**, *121* (41), 23149–23157.

(37) Kang, S. J.; Song, S.; Liu, C.; Kim, D. Y.; Noh, Y. Y. Evolution in Crystal Structure and Electrical Performance of Thiophene-Based Polymer Field Effect Transistors: A Remarkable Difference between Thermal and Solvent Vapor Annealing. *Org. Electron.* **2014**, *15* (9), 1972–1982.

(38) Jang, M.; Yang, H. Structural Control over Self-Assembled Crystals of φ-Conjugated Poly(3,3'-Didodecyl-Quaterthiophene) for Organic Field-Effect Transistor Applications. *J. Nanosci. Nanotechnol.* **2012**, *12* (2), 1220–1225.

(39) Onsager, L. Reciprocal Relations in Irreversible Processes. I. *Phys. Rev.* **1931**, *37* (4), 405–426.

Chapter 6: CORRELATING CONDUCTIVITY AND SEEBECK COEFFICIENT TO DOPED POLY(3-(METHOXYETHOXYETHOXY)THIOPHENE)

This chapter has been published in Ma, T., et al. Correlating conductivity and Seebeck coefficient to doping within crystalline and amorphous domains in poly(3-(methoxyethoxyethoxy)thiophene). J Polym Sci. 2021; 59:2797–2808.

Molecular doping of conjugated polymers (CPs) plays a vital role in optimizing organic electronic and energy applications. For the case of organic thermoelectrics, it is commonly believed that doping CPs with a strong dopant could result in higher conductivity σ and thus better power factor PF. Herein, by investigating thermoelectric performance of a polar side-chain bearing CP poly(3-(methoxyethoxyethoxy)thiophene) (P3MEET) vapor doped with fluorinated-derivative of tetracyanoquinodimethane FnTCNQ (n =1, 2, 4), we show that using strong dopants can in fact have detrimental effects on the thermoelectric performance of CPs. Despite possessing higher electron affinity, doping P3MEET with F4TCNQ only results in a modest increase in σ (27.0 S/cm) compared to samples doped with other two weaker dopants F2TCNQ and F1TCNQ (26.4 S/cm and 20.1 S/cm). Surprisingly, F4TCNQ-doped samples display a marked reduction in Seebeck coefficient α compared to F1TCNQ- and F2TCNQ-doped samples from 42 μV/K to 13 μV/K, leading to an undesirable suppression of PF. Structural characterizations coupled with Kang-Snyder modeling of the α - σ relation show that the reduction of α in F4TCNQ-doped P3MEET samples originates from the generation of low mobility carrier within P3MEET's amorphous domain. Our results demonstrate that factors such as dopant distribution and doping

efficiency within the crystalline and amorphous domains of conjugated polymers should play a crucial role in advancing rational design for organic thermoelectrics.

6.1 Introduction

Molecularly doped semiconducting conjugated polymers (CPs) have been increasingly explored to enabling organic electronic and energy applications.[1–9] The use of molecular dopants allows for effective control of the charge carrier concentration (n), and in turn, the electronic transport properties of CPs. In the case of organic thermoelectrics, key physical properties that define the thermoelectric material performance include Seebeck coefficient (α), electronic conductivity (σ) and thermal conductivity (κ).[10] These properties are a function of n and are highly interrelated. The thermal-to-electrical energy conversion efficiency of thermoelectrics is characterized by the dimensionless figure of merit, $ZT = \alpha^2\sigma T/\kappa$, where T is the temperature in Kelvin and $\alpha^2\sigma$ is the power factor (PF).[11] Organic materials have a potential advantage because of their comparatively low κ, and the community has put a concerted effort in optimizing PF while not sacrificing low κ in order to improve the TE performance.

Doping process of CPs is typically achieved via the addition of a molecular dopant to either oxidize (p-type doping) or reduce (n-type doping) the polymer backbone.[4,12–14] For the case of thiophene-based polymers, p-type acceptors are introduced as oxidant molecules, leading to charge transfer between the host polymer and dopant molecule. This results in negatively charge dopant anion and positively charged polymers (polarons) after doping. Optimal charge transport properties in CPs require doping methods that maintain their underlying hierarchical structure. Specifically, sequential doping methods where the dopant is infiltrated into the polymer matrix either from an orthogonal solvent-dopant mixture or from the dopant's vapor phase are promising approaches to preserve the underlying local ordering and morphology.[15–19] In contrast to the solution co-

processing method where the formation of aggregation leads to films with poor quality,[15,16] the sequentially doping of the polymer maintains the crystalline order and long-range connectivity, which results in high charge carrier mobility μ, σ and thus higher *PF*.

In addition to changing doping methods, improving charge transport can be achieved by permitting efficient polymer-dopant charge transfer by selecting dopants having lowest unoccupied molecular orbital (LUMO) or electron affinity (EA) level close to or deeper than the highest occupied molecular orbital (HOMO) or ionization energy (IE) level of the polymer. For example, Li et al. investigated the doping efficiency of poly(3-hexylthiophene2,5-diyl) (P3HT) doped with F4TCNQ and its ester analogues with lower EA levels.[20] Interestingly, σ of P3HT doped with ester-substituted dopants is higher than P3HT doped with F4TCNQ, which indicates weaker dopants can also lead to efficient doping and thus improvement in σ. In another study, Keifer et al. demonstrated that F4TCNQ and a comparatively stronger dopant, 1,3,4,5,7,8-hexafluoro-tetracyanonaphthoquinodimethane (F6TCNNQ), can transfer two electrons from the CP to the dopant, leading to double doping and an ionization efficiency close to 200%.[21] As for weaker dopants, Patel et al. has shown that the weaker F2TCNQ dopant does not significantly sacrifice σ compared to the stronger F4TCNQ dopant and in turn yields a larger *PF*.[22] Recently, our group has shown that the values σ are within the same order of magnitude for poly 3-(methoxyethoxyethoxy) thiophene (P3MEET) when doping with three different fluorinated tetracyanoquinodimethane dopants (FnTCNQ, n = 1, 2, 4), while the values of σ for poly(3-(methoxyethoxyethoxymethyl)thiophene) (P3MEEMT) decrease significantly with the decreasing fluorination level of the dopants.[23] In this regard, organic dopants such as FnTCNQ are considered to be model dopants since the EA levels of FnTCNQ can be easily manipulated by changing the number of fluorine atoms.[24]

In principle, *PF* is related to both α and σ as the magnitude of σ increases as function of n while, in contrast, the magnitude of α decreases with n.[11,25] Fundamentally, studies of thermoelectric properties of semiconducting polymers have been investigated in the context of charge transport mechanisms where researchers have been exploring the correlation between α and σ.[25–35] In 2014, Glaudell et al. presented an empirical relation where $\alpha \sim \sigma^{-1/4}$ by compiling series studies of doped thiophene-based polymers. The authors, however, did not provide physical explanation of this relationship.[25] More recently, Kang and Snyder have proposed a charge transport model with an energy-dependent parameter s and an energy-independent transport coefficient σ_{E0}, which fits well with the α - σ relationship of conducting polymers over a significant range of σ.[26] Particularly, the authors stated that the transport parameter s is related to energetic disorder of different polymers and thus determine the mechanism of charge transport. However, the factors that affect the value of s in the Kang-Snyder model are still unclear. Gregory et al. have developed a semi-localized transport (SLoT) model modified from Kang-Snyder model where they treat σ_{E0} as a function of temperature and carrier concentration.[29] The SLoT model captures a large spectrum including both hopping-like and metal-like transport in CPs and helps tailor thermoelectric properties of doped CPs more accurately. Moreover, Boyle et al. examined the effect of dopant distribution on CPs' electronic structure, charge transport and the α - σ relationship. They found that CPs having non-uniform dopant distribution led to a heavy tailed DOS, resulting in a flattened α - σ but suppressed α due to the high degree of disorder.[28] The results highlighted the importance of controlling dopant distribution for high performing organic thermoelectrics, motivating further investigations on the role of polymer-dopants interaction, dopant distribution on CPs' thermoelectric properties.

Of particular interest in the field of CPs is studying the role of crystalline (or aggregate) and amorphous phases on charge transport properties. Specifically, understanding how doping occurs within the crystalline and amorphous phases in CP films and the consequent effects on $\alpha - \sigma$ relation and thermoelectric performances still remains poorly understood. To explore this question, in this work we investigate the correlation between conductivity and Seebeck coefficient of a polythiophene derivative with a polar, oligoethylene glycol side-chain, P3MEET (chemical structure shown in Figure 6.1a) vapor-doped with fluorinated-derivatives of tetracyanoquinodimethane (FnTCNQ, n = 1, 2 and 4). P3MEET belongs to a new class of *p*-type semiconducting polymers possessing ethylene oxide polar side chains which has been increasingly used due to its enhanced processability and thermally stability.[21,23,36–41] Additionally, choosing dopants with varying EA not only enables the study of polymer-dopant energy mismatch on charge transport properties but can also systematically change the doping efficiency between the crystalline and amorphous part.

In the first part of this chapter, we study the charge transport and thermoelectric properties of P3MEET thin films vapor doped with FnTCNQ. P3MEET exhibits a maximum σ as high as 27.0 ± 3.7 S/cm upon doping with F4TCNQ, which matches the previous study.[23] Despite having higher EA levels, F2TCNQ/F1TCNQ – doped P3MEET have a comparable maximum σ at 26.4 ± 3.1 S/cm and 20.1 ± 0.77 S/cm, respectively. However, a deviation in α is observed at the high σ region from 42 ± 1 μV/K in F1TCNQ-doped sample to 13 ± 1 μV/K in F4TCNQ-doped sample, which leads to a significant suppression of *PF*. In the second part of the chapter, origin of this observation is explored by using a combination of spectroscopy techniques (UV-vis-NIR and Raman) and grazing incidence wide angle x-ray scattering (GIWAXS). In the last part, we discuss the α - σ relationship of our FnTCNQ-doped P3MEET thin films using Kang-Snyder charge

transport model, which provides insight into the role of crystalline and amorphous domains on charge transport and thermoelectric properties of doped P3MEET polymer thin films.

6.2 Results and Discussion

6.2.1 Fabricating P3MEET:FnTCNQ Films through Sequential Vapor Doping

In this work, thermoelectric properties of P3MEET were investigated upon doping with three dopants, 2,3,5,6-tetrafluoro-7,7,8,8-tetracyanoquinodimethane (F4TCNQ), 2,5,-difluoro-7,7,8,8-tetracyanoquinodimethane (F2TCNQ) and 2-fluoro-7,7,8,8-tetracyanoquinodimethane (F1TCNQ) with different electron affinity (EA). P3MEET having MW of 9.2 kg mol^{-1} and $Đ$ of 1.4 was synthesized by the Kumada catalyst transfer polymerization (KCTP) method as described in our previous publication.[42] Figure 6.1a summarizes the EA values of FnTCNQ (n = 1, 2 or 4) and the ionization energy (IE) of P3MEET determined by solution CV measurements. The IE of P3MEET is found to be 4.92 eV, whereas the EA values of F4TCNQ, F2TCNQ and F1TCNQ are determined to be 5.25 eV, 5.10 eV and 5.01 eV, respectively (see details of CV measurements in Ref. [23]). As expected, the EA level decreases with decreasing fluorination level for three dopants. All dopants have a lower EA than the IE of P3MEET. To introduce molecular dopant into the polymer, we employed sequential vapor doping method where one first casts a neat thin film and then the dopant is infiltrated into the polymer matrix from the vapor phase as shown in Figure 6.1b. For consistency, all neat P3MEET thin films are processed in the same manner in this study: spin-coated from chloroform solution and soft annealed at 80 °C to remove residual solvents within the polymer films (thin films of *c.a.* 40 nm). Figure 6.1b shows a schematic of our home-built apparatus for controlled vapor doping of polymer thin films in an argon atmosphere glovebox. More details are provided in the methods section and previous chapters.

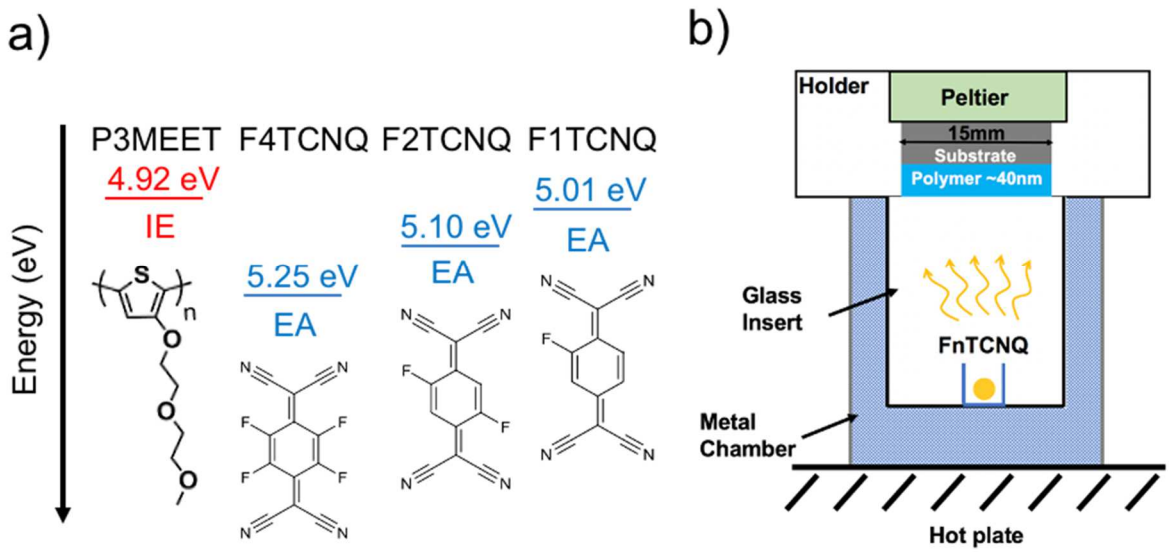

Figure 6.1: a) HOMO level of P3MEET together with LUMO levels of the three dopants, F1TCNQ, F2TCNQ and F4TCNQ used in this work. (b) Schematic of vapor doping chamber.

UV-vis-NIR absorption spectra (Figure 6.2) indicate efficient charge transfer between P3MEET and all three dopant. For neat P3MEET, the primary absorption peak is observed at 2 eV. Notably, there is significant evidence of polaron absorption peaks at around 0.6 eV and 1.5 eV in neat P3MEET, which indicates the presence of intrinsic charge carriers in the neat thin film. Upon introducing dopant vapor, charge transfer process can be observed between P3MEET and FnTCNQ as the neutral absorption peak intensity decreases while the FnTCNQ anion absorption peaks appear and increases near ~1.4 eV together with the neutral FnTCNQ absorption peak near 3.25 eV. Note that for thin films doped beyond 10 min, the neutral FnTCNQ peak becomes significantly pronounced while the polaron and dopant anion peak intensities remain constant, indicating accumulation of neutral dopants on the polymer surface after vapor doping beyond 10 min.

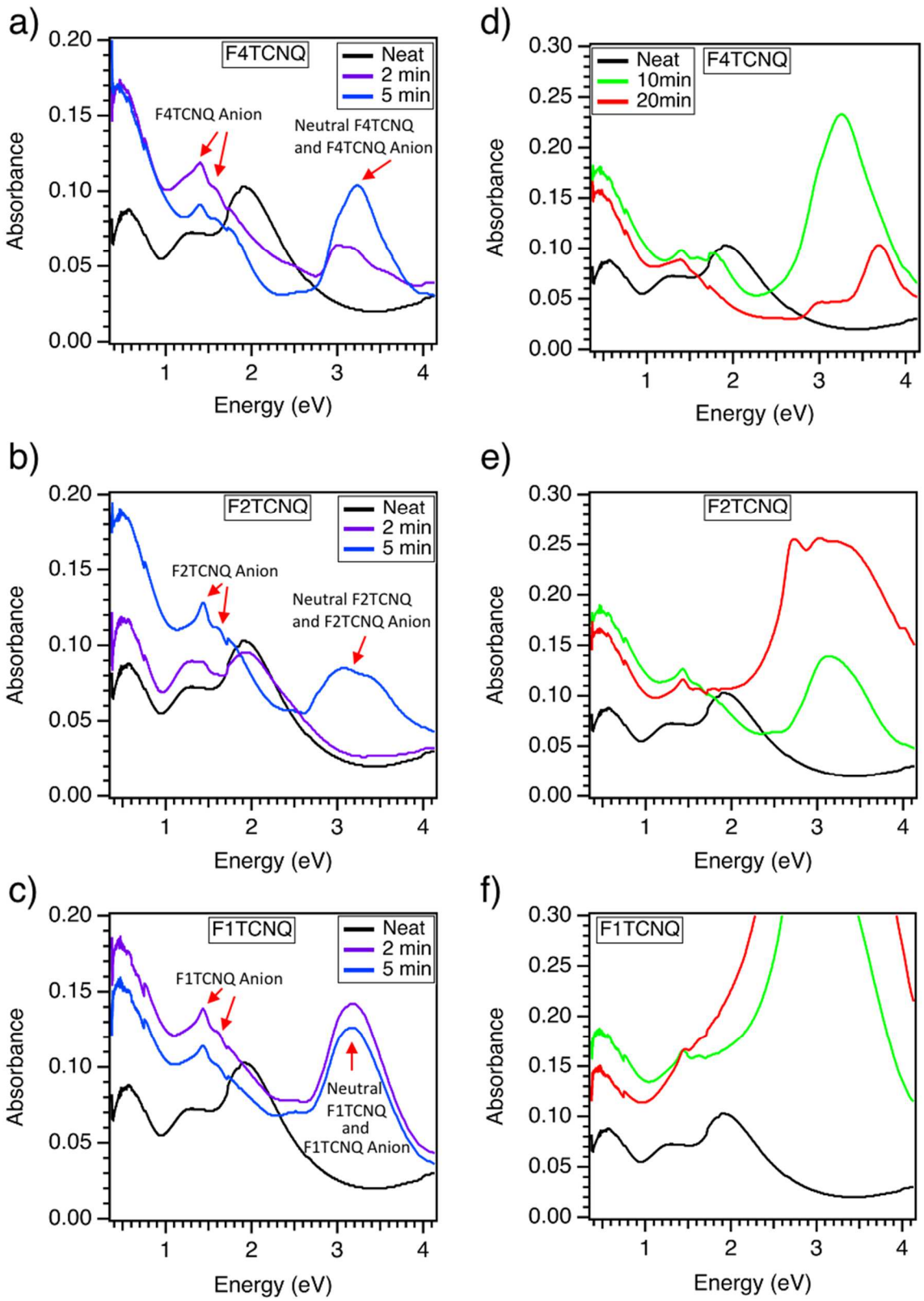

Figure 6.2: UV-Vis-NIR spectra of P3MEET thin films as a function of (a), (d) F4TCNQ, (b), (e) F2TCNQ and (c), (f) F1TCNQ vapor doping time.

6.2.2 Seebeck Coefficient and Conductivity as Function of Vapor Doping Time

The values of α, σ, and the corresponding *PF* of P3MEET as a function of FnTCNQ vapor doping time are summarized in Figure 6.3. Neat P3MEET already processes a σ of *ca.* 0.1 S/cm, which is significantly higher than other thiophene-based polymers. This observation is consistent with our UV-Vis results indicating the presence of intrinsic charge carriers in the film. Having the oxygen atom next to the polythiophene backbone alters the electron-donating ability of the oxygen to the thiophene core, which results in a low ionization energy of P3MEET. Thus, the polymer is prone to oxidation from remaining catalyst and ambient air during the synthesis and handling processes.[42] This leads to much higher "intrinsic" carrier concentration and conductivity at the neat state. The high conductivity generated simply by ambient doping could open up the door for more simple doping methods of CPs via engineering their IE. For all dopants, the conductivity of P3MEET films increases over two orders of magnitude before saturating after doping for 5 min. The difference in conductivity between the neat and doped films originates from the differences in both n and μ. Note that the carrier concentration is not linearly scaled with the conductivity at high doping level as mobile carriers with higher mobility are generated. Conductivity of films doped with F1TCNQ reach the maximum sooner than the other two dopants which is likely due to its faster sublimation rate at a fixed temperature. The conductivities of 10 min F4TCNQ, F2TCNQ and F1TCNQ doped P3MEET thin films are 27.0 ± 3.7 S/cm, 26.4 ± 3.1 S/cm and 20.1 ± 0.77 S/cm, respectively. As expected, α for the doped films show an inverse correlation with doping time compared to σ. The values of α decrease with increasing vapor doping time and reaches a plateau after 5 min of doping (Figure 6.3b). The Seebeck coefficients of 10 min F4TCNQ, F2TCNQ and F1TCNQ doped P3MEET thin films are 13 ± 1 μV/K, 23 ± 1 μV/K and 42 ± 1 μV/K, respectively. It is clearly shown that thin films doped by F4TCNQ have much smaller α compared

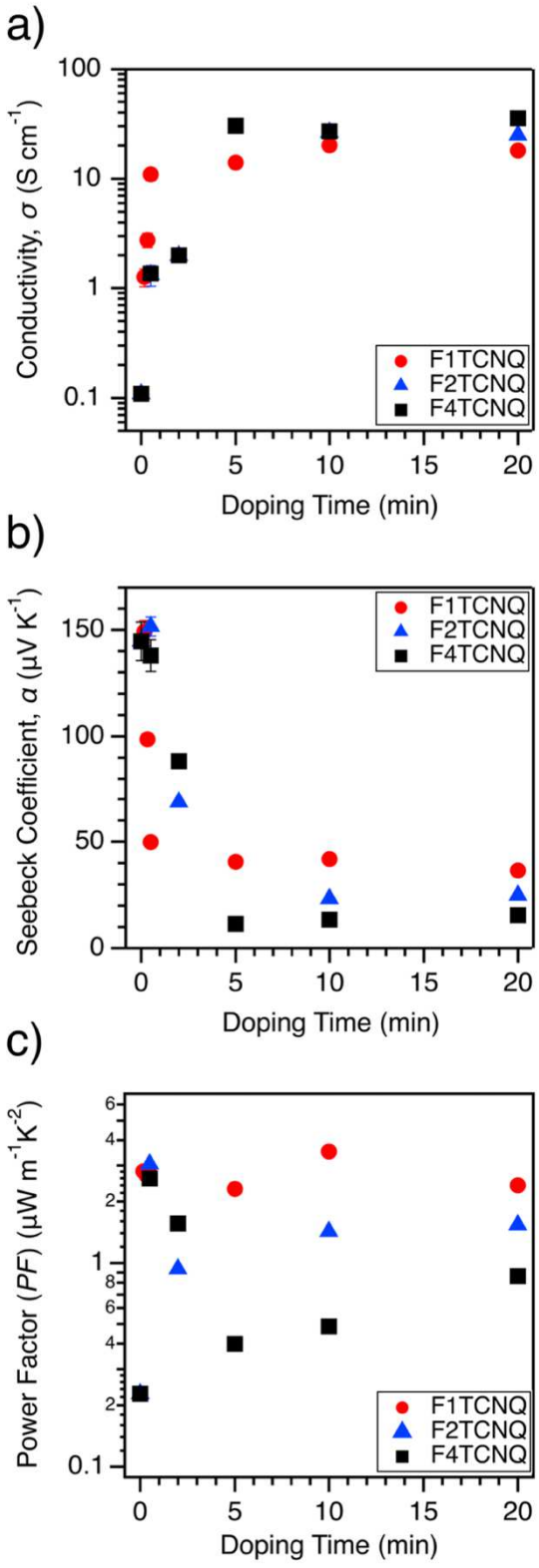

Figure 6.3: (a) Conductivity (σ), (b) Seebeck coefficient (α) and (c) corresponding power factor ($PF = \alpha^2\sigma$) of P3MEET:FnTCNQ thin films as a function of vapor doping time.

to doping with FITCNQ and F2TCNQ at the same doping time.

The *PFs* of all samples are also calculated and plotted in Figure 6.3c. It is worth noting that at the saturated doping time (10 min), *PF* of F1TCNQ doped film (3.5 μW m^{-1} K^{-2}) is higher than those doped by F2TCNQ (1.4 μW m^{-1} K^{-2}) and F4TCNQ (0.48 μW m^{-1} K^{-2}). In particular, F1TCNQ-doped P3MEET has a *PF* that is an order of magnitude higher than F4TCNQ-doped P3MEET. The difference in *PF* is due to the dominance of α in the formula of *PF* where $PF = \alpha^2\sigma$. Thin films doped by F1TCNQ have larger values of α while the difference in σ is not significant. One possible explanation for the difference in α is the variation in *n* between the three doped thin films as α is inversely related to *n*.

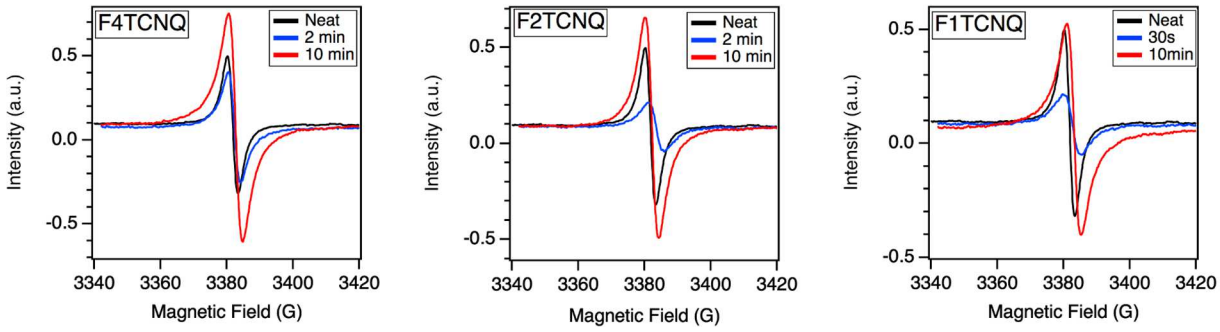

Figure 6.4: EPR spectra of neat and FnTCNQ-doped P3MEET thin films recorded in continuous-wave mode at room temperature.

To provide further insight on *n*, electron paramagnetic resonance (EPR) spectroscopy measurements were performed to quantify the spin concentration (*N*) in FnTCNQ-doped P3MEET thin films. Here, we take *N* as a measurement of the polaronic charge carriers generated after doping. The representative continuous wave (CW) EPR spectra for neat and doped thin films recorded at room temperature are shown in Figure 6.4. The spin concentration in each sample was calculated through double integration of the EPR spectrum divided by the volume of the measured film (Figure 6.5 and Table 6.1). The neat P3MEET film has a spin concentration of (1.9 ± 0.3) ×

10^{19} cm^{-3}, which is relatively high, indicating the polymer is intrinsically doped as suggested by the UV-Vis-NIR and conductivity measurements (Figure 6.2 and Figure 6.3a).

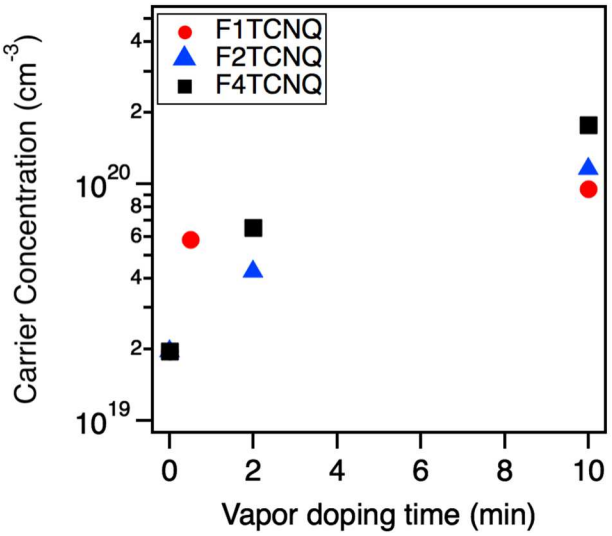

Figure 6.5: Carrier concentration calculated by double integration of EPR spectra as a function of FnTCNQ doping time for P3MEET.

After doping with F4TCNQ for 10 min, the maximum spin concentration of doped P3MEET is $(1.9 \pm 0.3) \times 10^{20}$ cm^{-3}, an order of magnitude higher than neat sample. Note that EPR measurements capture the unpaired electrons that interacted with the applied magnetic field. A decrease in EPR spin concentration could be observed at high doping level when bipolarons are formed, which could lead to underestimation in the calculated carrier concentration.[43] However, the maximum carrier concentrations measured using other techniques (AC Hall effect,[44] XPS,[45,46] and UV-Vis spectroscopy[19,47]) all lie in the order of 10^{20} to 10^{21} cm^{-3}, which is in agreement with our value calculated from EPR, indicating reasonable and commensurable carrier concentrations in this study. As shown in Figure 6.5, the spin concentration in the 10 min F4TCNQ-doped film is more than 50% higher than that in F1TCNQ/F2TCNQ-doped films. This difference indicates greater extent of doping with F4TCNQ compared to other two dopants. However, larger spin concentration does not lead to a significantly higher σ. We posit that a portion of charge carriers

generated in F4TCNQ-doped thin films are trapped in the amorphous region of P3MEET, which possesses lower μ and thus leads to an apparent suppression of σ. Therefore, values of σ for F1TCNQ- and F2TCNQ-doped thin films are comparable with those of F4TCNQ-doped thin films. To investigate our hypothesis, we carried out structural characterization experiments to probe dopant distribution and polymer chain conformational order in P3MEET thin films.

Table 6.1: Summary of experimental values for conductivity (σ), Seebeck Coefficient (α), Power Factor (PF), spin concentration (N), η and Kang-Snyder model fit parameter σ_{E0}.

Sample	σ* **(S cm^{-1})**	α* **(μV K^{-1})**	PF* **(μWm^{-1}K^{-2})**	N **(cm^{-3})* from EPR**	η* **(s = 1)**	σ_{E0} **(s = 1) (S cm^{-1})**	σ_{E0} **(s = 3) (S cm^{-1})**
F1TCNQ -doped	20.1 ± 0.77	42 ± 1	3.5	9.5×10^{19}	6.8	2.3 ± 0.2	$(1.7 \pm 0.2) \times 10^{-3}$
F2TCNQ -doped	26.4 ± 3.1	23 ± 1	1.4	1.1×10^{20}	12.2	2.0 ± 0.2	$(5.7 \pm 0.3) \times 10^{-4}$
F4TCNQ -doped	27.0 ± 3.7	13 ± 1	0.42	1.9×10^{20}	21.2	1.4 ± 0.1	$(9.7 \pm 2.0) \times 10^{-5}$

*Taken at 10 min doping time.

6.2.3 Influence of Molecular Doping on Local Molecular Order in Crystalline Phase

Grazing incidence wide angle X-ray scattering (GIWAXS) experiments were performed to investigate how molecular doping influences the local molecular order in crystalline domains of P3MEET. 2D GIWAXS images of neat and FnTCNQ-doped P3MEET thin films were shown in Figure 6.6. The diffraction pattern of neat P3MEET suggests the face-on orientation of P3MEET as the side-chain stacking peak (100) lies along in-plane direction and the π-stacking peak (010) along out-of-plane direction. In addition, the lack of higher order side-chain diffraction peak

together with the broad, diffuse diffraction peaks in GIWAXS patterns indicates highly disordered structure in P3MEET, consistent with our prior studies. Upon introducing dopant into polymer, the GIWAXS patterns appear similar to the neat sample, indicating that doping with vapor FnTCNQ induces minimal changes to molecular order and crystallite orientation.

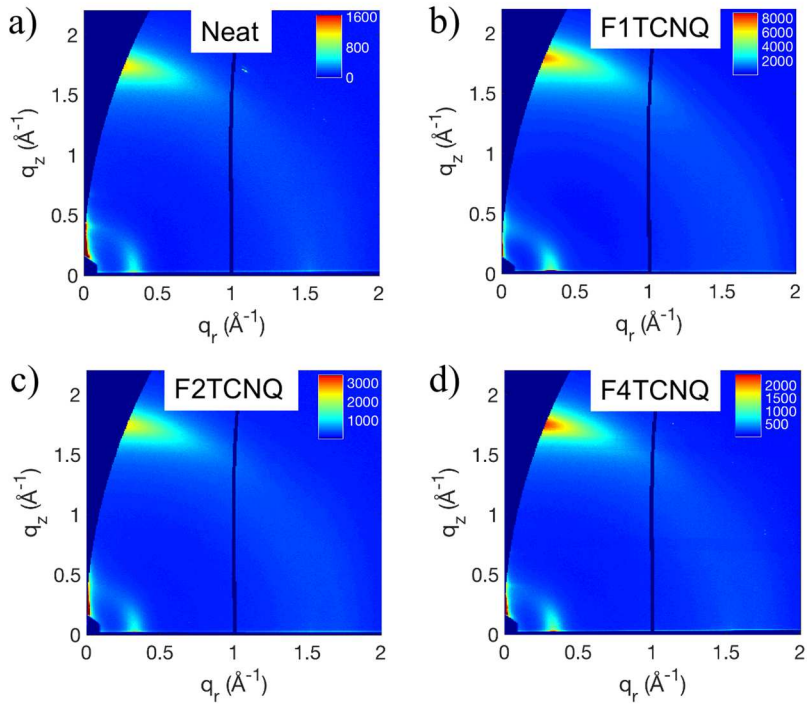

Figure 6.6: Representative 2D images of a) neat and b), c) and d) FnTCNQ-doped P3MEET thin films.

Quantitative changes upon vapor doping by FnTCNQ are seen through the side-chain stacking and π-π stacking distances. We calculate side-chain distance $d_{100} = 2\pi/q_{100}$ as a function of FnTCNQ doping time, the result of which is shown in Figure 6.7a. Upon introducing FnTCNQ we observe an increase in d_{100} for all three dopants due to the intercalation of dopant into the side-chain spacing, a widely observed phenomenon in polythiophene-based polymers.[17,22,48–50] Specifically, d_{100} increases initially from 1.79 nm for neat P3MEET to 1.94 nm, 2.01 nm and 2.06 nm for F1TCNQ, F2TCNQ and F4TCNQ-doped thin films, respectively. For all three dopants,

d_{100} follow the same trend and reach plateaus beyond ca. 10 min of vapor deposition. Along with the increase in d_{100}, we also observe a decrease in the π-stacking distance, d_{010} during the vapor doping process, as illustrated in Figure 6.7b. Notably, decrease in d_{010} is 4.7 % in P3MEET after 20 min of doping with F4TCNQ, which is more prominent than in F1TCNQ (3.5 %) and F2TCNQ (3.1 %), consistent with higher doping efficiency by F4TCNQ.

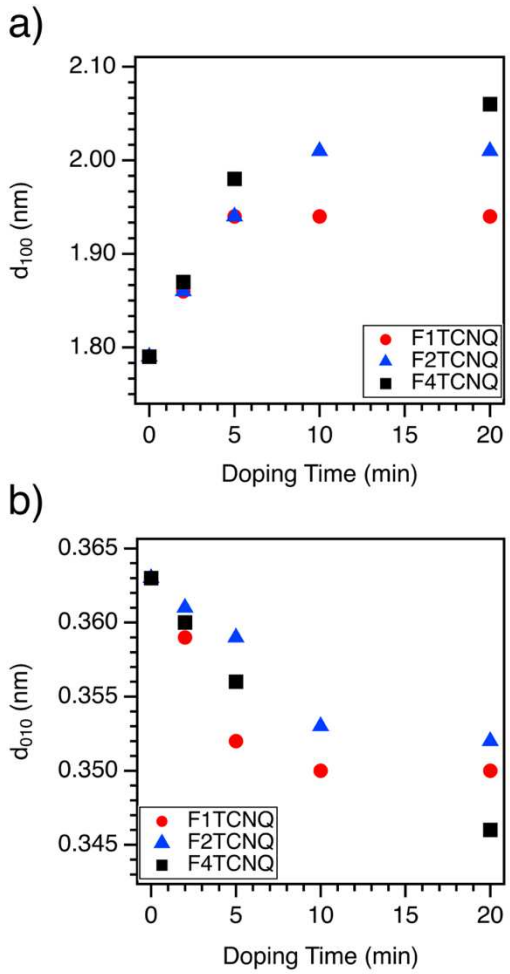

Figure 6.7: (a) Side-chain stacking (d_{100}) and (b) π-stacking distance (d_{010}) of P3MEET:FnTCNQ thin films as a function of vapor doping time.

6.2.4 Raman Spectroscopy Reveals Charge Transfer between Dopants and Amorphous Domain

We performed Raman spectroscopy to preferentially investigate the chain conformational order in the amorphous regions of neat and FnTCNQ-doped P3MEET thin films. Note that because F1TCNQ sublimated much faster than other two dopants, the accumulation of neutral F1TCNQ on polymer thin film surface is more rapid as indicated in the UV-Vis-NIR spectra. Therefore, we chose to compare Raman spectra of 5 min F1TCNQ-doped thin film with 10 min F2TCNQ- and F4TCNQ-doped thin films as they possess similar amount of dopant during vapor doping time. The excitation wavelength was chosen to be in resonance with the amorphous fraction of the P3MEET thin film,[51] which is 532 nm based on the UV-Vis absorption spectra of solution and thin film (Figure 6.8).

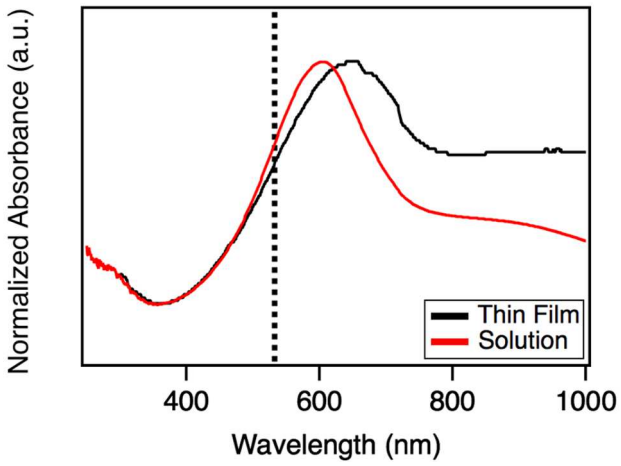

Figure 6.8: Absorption spectra of both solution (chloroform) and thin film states in P3MEET (dashed straight line represents 532 nm).

The normalized Raman spectra of the neat and FnTCNQ-doped P3MEET thin films are shown in Figure 6.9. For neat P3MEET, two strong peaks are observed at 1390 cm^{-1} and 1445 cm^{-1}, which are assigned to thiophene C – C bond stretching and the symmetric C = C bond stretching, respectively. In addition, the shoulder at 1415 cm^{-1} corresponds to polymer chains with higher

conformational order. We attribute the appearance of this shoulder to the stiffening of disordered polymer chains arising from the planar polaronic molecular structure in neat P3MEET, which is consistent with previous reports.[47,52,53]

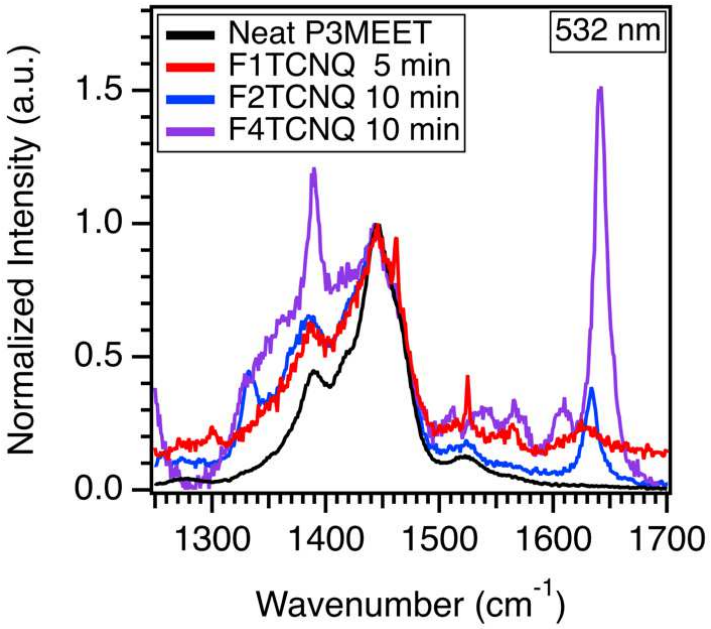

Figure 6.9: Raman spectra of neat and FnTCNQ-doped P3MEET thin films at the excitation wavelength of 532 nm. This excitation wavelength is preferentially in resonance with the amorphous regions of the P**3**MEET thin film.

Upon vapor doping by all three dopants, the characteristic peak positions remain unchanged compared with the neat P3MEET while the peaks of doped films are slightly broader than the neat peaks with a relative intensity change of the C – C bond stretching peak. The relative intensity changes upon introducing dopants into the polymer indicates the formation of additional positive charge carriers (polarons) in P3MEET. These features are consistent among FnTCNQ-doped films, which means that amorphous region of P3MEET can be doped by all three dopants to a certain extent. However, the shoulder at 1415 cm^{-1} in Raman spectrum of F4TCNQ-doped P3MEET has a much higher intensity, indicating a more efficient charge transfer between F4TCNQ and amorphous P3MEET. The more efficient charge transfer results in more charge

carriers in amorphous region when doped by F4TCNQ compared to the other two dopants, which can be confirmed by a much larger F4TNCQ anion peak around 1650 cm^{-1} compared to F1TCNQ and F2TCNQ anion peaks.[54] This difference can be explained as the more disordered polymer chains in the amorphous domain of P3MEET has a lower HOMO level compared to crystalline P3MEET, which can limit the charge transfer with F1TCNQ or F2TCNQ.

6.2.5 Modelling α - σ relation Reveals Charge Transport Mechanism in P3MEET:FnTCNQ

To study the charge transport relation in FnTCNQ-doped P3MEET thin films, we plotted α as a function of σ and compared with previous relations observed for numerous doped CPs. Figure 6.10a represents an empirical fitting (dash line) proposed by Glaudell et al.[25], where the α vs. σ was fit to a power law relation:

$$\alpha = \frac{k_B}{e}\left(\frac{\sigma}{\sigma_\alpha}\right)^{-1/4} \qquad (6.1)$$

where, k_B/e is the Boltzmann constant divided by unit charge, or the natural unit of thermopower 86.17 μV K^{-1}. The parameter σ_α is an empirical constant and fit to approximately 1 S cm^{-1}. The magnitude of σ_α is independent of carrier concentration in the range covered. It is clearly shown in Figure 6.10a that α continuously decreases with increasing σ at low doping regime following this relation. In the higher doping regime, however, we found deviations from the linear trends of both transport relationships, similar to observation by Muller et al. where they also found a deviation from the $\alpha \sim \left(\frac{\sigma}{\sigma_\alpha}\right)^{-1/4}$ relation in a molecularly-doped glycolated side chain bearing conjugated polymer p(g42T-T).[36]

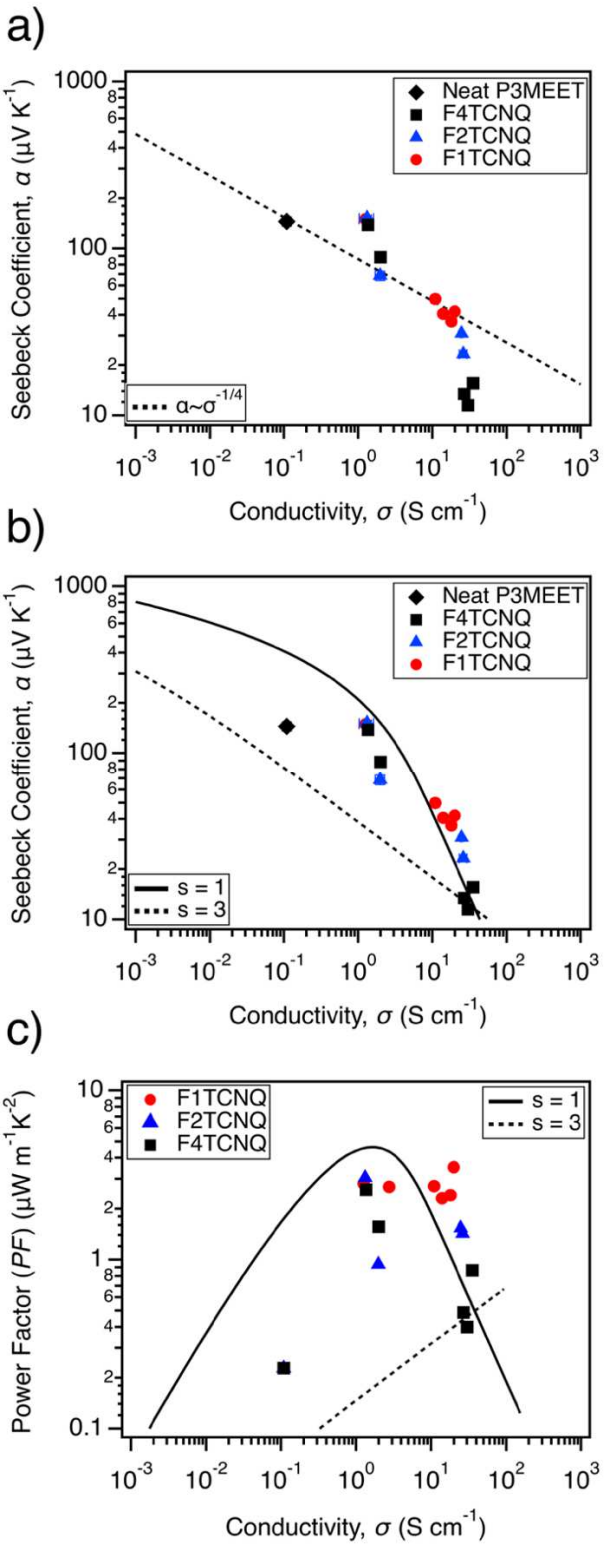

Figure 6.10: Compilation of Seebeck coefficient (α) vs conductivity (σ) data from this study: (a) Power law relations ($\alpha \sim \sigma^{-1/4}$) from Glaudell et al. (dashed line) and (b) Kang and Snyder charge transport model; (c) Compilation of PF vs σ from this study. [s = 1 (solid curve) or s = 3 (dashed curve)].

Recently, the charge transport model proposed by Kang and Snyder has been increasingly used to model α - σ relation for understanding the charge transport mechanism of conducting polymers.[26,30,32,33] In that model, the transport edge, E_t, was introduced where the hopping transport was also taken into account. E_t is similar to the mobility edge model but does not require metal-like transport above the edge while still accounting for hopping conduction between localized states. Fundamentally, α and σ can be described using the following equations:

$$\sigma = \int \sigma_E \left(-\frac{\partial f}{\partial \mathrm{E}}\right) \mathrm{d}E \quad (6.2)$$

$$\alpha = \frac{k_B}{e} \int \frac{E-E_F}{k_B T} \frac{\sigma_E}{\sigma} \left(-\frac{\partial f}{\partial \mathrm{E}}\right) \mathrm{d}E \quad (6.3)$$

Here, σ_E is the transport function, $f(E)$ is the Fermi-Dirac distribution, E_F, T are the Fermi energy level and temperature, respectively. In Kang-Snyder model, σ_E is assumed to have a power law energy dependence above the transport edge, E_T, with a power of s as shown in Equation 6.4:

$$\sigma_E(E,T) = \sigma_{E_0}(T) \times \left(\frac{E-E_t}{k_B T}\right)^s \quad (E > E_t)$$

$$= 0 \ (E < E_t) \quad (6.4)$$

Here, σ_{E0} is called the transport coefficient, which is an energy-independent parameter. s is the transport parameter, which is determined by fitting experimental data. α and σ of samples can be calculated in terms of s and η, where $\eta = \left(\frac{E_F-E_t}{k_B T}\right)$ is defined as reduced chemical potential and represents the relative position of the Fermi level with respect to E_t. α - σ relations of FnTCNQ-doped P3MEET are fitted using Kang-Snyder model for s = 1 or 3 and are summarized in Figure 6.10b and Figure 6.11. Overall, s = 1 model gives better fits than s = 3 for all dopants. In particular, F4TCNQ-doped thin films have the largest deviation using the s = 3 model. This deviation is also observed when we fit all data of three dopants together (Figure 6.10b). As stated in Kang and

Snyder's work, the s = 1 case was only considered for PEDOT-based materials where they suggested that charge transport in this type of materials is mainly affected by acoustic-phonon scattering rather than impurity scattering (s = 3). More recently, Lee et al. also proposed s = 1 model for α - σ relation of $FeCl_3$-doped thiophene-based polymers.[33] They assigned the s = 1 mechanism with materials possessing a narrow density of states (DOS) which results from high crystallinity and/or degenerate energy states ($\eta >> 1$) due to high carrier concentration generated by $FeCl_3$. As seen in Figure 6.6b, fitting with s = 1 gives the better fit than s = 3 for our thin films which might suggest a narrow DOS in the P3MEET-FnTCNQ systems. In addition, the relationship between PF and σ is summarized in Figure 6.10c, which follows s = 1 better than s = 3.

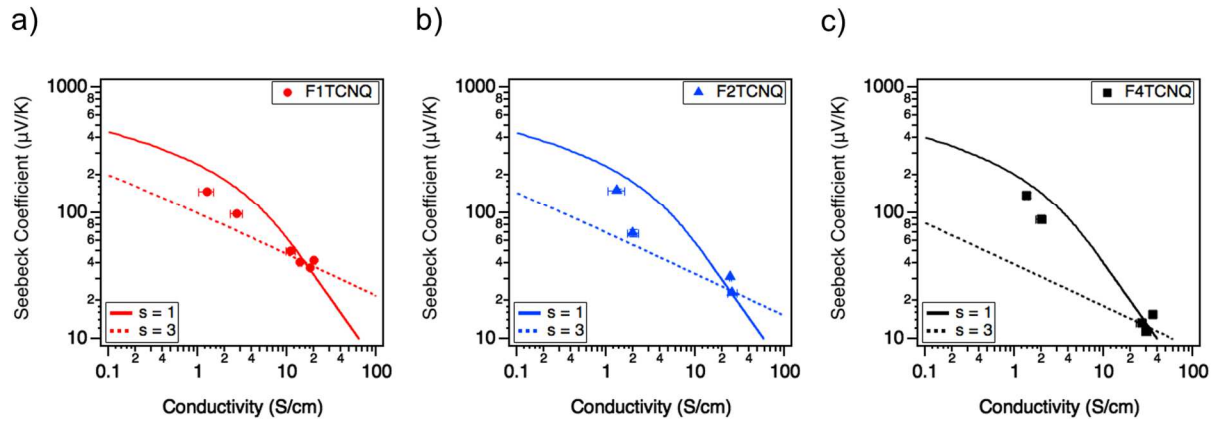

Figure 6.11: α - σ relationships of P3MEET films doped by (a) F1TCNQ, (b) F2TCNQ and (c) F4TCNQ. Solid line (s = 1) and dash line (s = 3) are fits to the Kang-Snyder model.[26]

The values of η for FnTCNQ-doped thin films are determined using s = 1 model and summarized in Figure 6.13 and Table 6.1. The neat P3MEET thin film has an η of 1.2. It is clear that η increases with charge carrier as approximated through EPR measurements, which is consistent with previous study on PBTTT-F4TCNQ by Kang et al.[32] η represents the relative energetic difference between the Fermi level and the transport edge and serves as an indicator of

the electronic bandwidth of the polymer. The largest η in our system is around 20 ($E_F - E_t$ = 0.5 eV), which is physically reasonable, as the full electronic bandwidth of CPs reported in the literature are 0.5 – 1 eV.[26,55–58] In our system, F4TCNQ-doped thin film has a larger η (η = 21.2) than F2TCNQ (η = 12.2) and F1TCNQ (η = 6.8) doped thin films, indicating more carriers generated in F4TCNQ-doped P3MEET. However, despite the difference in η and charge carrier concentration, there is little variation in the maximum conductivity for three dopants. We attribute this to the difference in μ as σ is affected by both charge carrier concentration and μ. Importantly, the value of transport coefficient σ_{E0} is directly related to μ and determines the magnitude of σ. As determined by fitting our data, F1TCNQ-doped thin films have the largest value of σ_{E0} (2.3 ± 0.2 S cm^{-1}) whereas F4TCNQ-doped thin films have the lowest σ_{E0} (1.4 ± 0.1 S cm^{-1}) in the *s* = 1 model. The trend in σ_{E0} indicates that doping with F4TCNQ leads to lower overall average mobility. We note that while *s* = 1 gives better fits than *s* = 3 for all dopants, we observe the same trend in σ_{E0} among the 3 dopants regardless of the value of *s* (Table 6.1). This trend is consistent with our hypothesis as thin films doped by F4TCNQ generate more charge carriers in the amorphous regions, which naturally have lower mobility due to the short conjugation length and more disordered structure compared to the charge carriers generated in crystalline domain. As F4TCNQ dopes the amorphous region more than the other two dopants, the overall charge carriers generated by F4TCNQ is higher and thus leads to a lower α value. However, a larger portion of charge carriers are in the amorphous regions when doped by F4TCNQ, which does not contribute significantly to σ due to the inherently lower μ in the amorphous regions. This explains that there is little variation in σ for P3MEET doped by different dopants at their highest doping level.

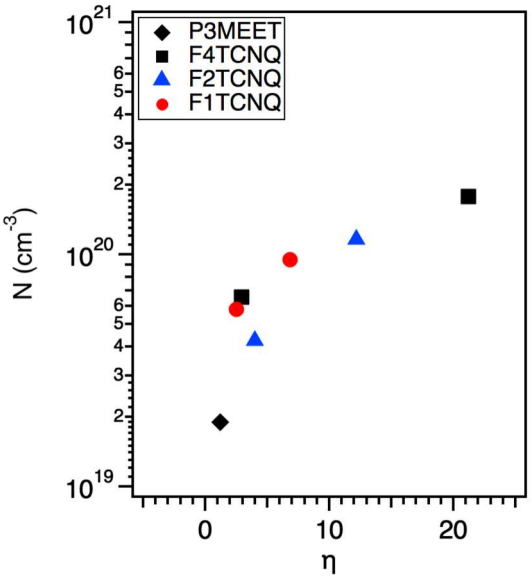

Figure 6.12: Charge carrier concentration in P3MEETT:FnTCNQ, N, counted by EPR measurements variation with η determined from Kang-Snyder Model calculation.[26]

Balancing the contribution of charge transport between the crystalline and amorphous regions is a promising strategy in controlling thermoelectric properties. Specifically, our study indicates preferential doping of the crystalline regions through weaker dopants is needed to achieve high *PF* in P3MEET. A recent study by Liang et al. have demonstrated how to control the sign of α by balancing charge carrier concentration and charge-carrier mobilities in the crystalline and amorphous regions of a doped CP film.[59] Therefore, going forward, strategies towards proper CP and dopant pairing need to consider the doping level between the crystalline and amorphous regions to balance the correlation between α and σ, and the ultimate *PF*.

6.3 Conclusion

In summary, we investigated the charge transport and thermoelectric properties of a polythiophene derivative with a polar side-chain, P3MEET, doped with the *p*-type molecular dopants FnTCNQ (n = 1, 2 and 4). Upon doping, electronic conductivity (σ) increased and plateaus to a similar value (20 - 27 S/cm) for all three dopants at the maximum doping level. On the other

hand, the Seebeck coefficient (α) for F1TCNQ-doped P3MEET thin film (α = 42 ± 1 μV/K) was threefold higher than the F4TCNQ-doped P3MEET thin film (α = 13 ± 1 μV/K). We assigned this variation to the difference in doping efficiency, which results in larger carrier concentration in F4TCNQ-doped P3MEET thin film. A combination of X-ray scattering and spectroscopy (UV-Vis-NIR and Raman) indicated extent of doping between the crystalline and amorphous regions. F4TCNQ possess the highest doping efficiency among three dopants within both crystalline and amorphous domains while F1TCNQ and F2TCNQ primarily doped the crystalline regions. Lastly, we modeled the α - σ relationship of our FnTCNQ-doped P3MEET thin films using Kang-Snyder model where *s* = 1 (transport parameter) was found to give the best fit. Despite having the lowest electron affinity, P3MEET thin films doped with F1TCNQ were found to have the highest σ_{E0} (2.3 ± 0.2 S/cm) which is indictive of higher charge carrier mobility, resulting from less carriers generated in the amorphous region, which eventually led to an optimized *PF*. Our findings illustrate the importance of understanding the role of doping in the crystalline and amorphous domains when considering the thermoelectric transport properties of existing and newly synthesized semiconducting conjugated polymers.

6.4 Experimental Methods

Materials. Poly 3-(methoxyethoxyethoxy) thiophene (P3MEET) was synthesized by first synthesizing the monomers 2,5-dibromo-3-(methoxyethoxyethoxy) thiophene [3MEET], then polymerizing using Kumada Catalyst Transfer Polymerization (KCTP). Additional synthetic details are provided elsewhere.[42] Tetracyanoquinodimethane (FnTCNQ, n = 1, 2 and 4) were purchased from TCI Chemicals.

Thin Film Preparation. Substrates preparations are the same as previous chapters. For neat P3MEET thin film preparation, P3MEET was dissolved in chloroform (10 mg/mL), and the

solution was stirred overnight to fully dissolve the polymer. Then thin films were spin-coated using SCS G3P spin coater using a two-step spin condition of 2000 rpm for 40s followed by 3000 rpm for 25s. All solution preparation and spin-coating steps were performed in an Argon glovebox. Thickness of neat films were measured via ellipsometry, which was determined to be approximately 40 nm.

Vapor Doping Process. Vapor doping was performed in an Argon glovebox. Approximately 2 mg of FnTCNQ powder was pressed into a pellet (approximately 3 mm in diameter) and placed in an aluminum oxide crucible (OD 6.8 mm x H 4 mm from Government Scientific Source Inc.), which was in turn placed in a glass insert (diameter ~ 5 cm, height ~ 4.5 cm). A stainless-steel container was then preheated for 30 min on a hot plate to allow the chamber to reach a steady temperature (200 °C for F4TCNQ, 180 °C for F2TCNQ and 160 °C for F1TCNQ). The glass insert with the dopant inside was put into the metal chamber to produce dopant vapor. The Peltier on top of the holder is used to keep the substrate temperature at 30 °C during the vapor doping process.

The following experiments (EPR, Raman, UV-Vis, GIWAXS, conductivity and Seebeck measurements) were all performed at room temperature.

Electron Paramagnetic Resonance Spectroscopy (EPR). Continuous wave (CW) X-band (9–10GHz) EPR experiments were carried out with a Bruker ELEXSYS II E500 EPR spectrometer (Bruker Biospin, Rheinstetten, Germany), equipped with a TE102 rectangular EPR resonator (Bruker ER 4102ST). Measurements were performed at room temperature (T = 295 K). Thin films on the substrate with dimensions 2 mm x 15 mm were placed in the EPR quartz tubes with 4 mm i.d. For spin quantification a single crystal of CuSO4*H2O with known spin concentration was used as a reference sample. Spin quantifications were done by comparing

double integrals of the experimental and reference EPR signals. For EPR measurement, we estimate a relative error of *ca.* 20% for each sample due to variations from experimental conditions.

Raman Spectroscopy. Raman spectroscopy experiments were performed under ambient conditions using the Horiba LabRAM HR Evolution NIR confocal Raman microscope housed in Chicago Materials Research Center. Raman spectra of neat and doped P3MEET thin films were collected using a 100x objective at excitation wavelength of 532 nm. The spatial resolution of each measurement is dependent on the numerical aperture of the microscope objective, the wavelength of the laser used, and the pinhole size of the confocal imaging mode. In our configurations, the spatial resolution of each Raman spectrum is calculated to be ~0.65 μm. Laser power and accumulation time was set to 1% and 20 s to minimize local heating and material degradation.

UV-VIS-NIR absorption spectroscopy, GIWAXS experiments, conductivity and Seebeck measurements were conducted in the same manner as in previous chapters.

6.5 Acknowledgements

The authors acknowledge funding support from NSF DMR- 1922259 (J.W.O. and B.X.D.) This research used resources of the Advanced Photon Source, an Office of Science User Facility operated for the U.S. Department of Energy (DOE) by Argonne National Laboratory under Contract No. DE-AC02-06CH11357. Parts of this work were carried out at the Soft Matter Characterization Facility of the University of Chicago. The EPR work was supported by the U.S. Department of Energy (DOE), Office of Basic Energy Sciences, Division of Chemical Sciences, Geosciences, and Biosciences, under Contract no. DE-AC-02-06CH11357.

6.6 References

(1) Salzmann, I.; Heimel, G.; Oehzelt, M.; Winkler, S.; Koch, N. Molecular Electrical Doping of Organic Semiconductors: Fundamental Mechanisms and Emerging Dopant Design Rules. *Acc. Chem. Res.* **2016**, *49* (3), 370–378.

(2) Fratini, S.; Nikolka, M.; Salleo, A.; Schweicher, G.; Sirringhaus, H. Charge Transport in High-Mobility Conjugated Polymers and Molecular Semiconductors. *Nat. Mater.* **2020**, *19* (5), 491–502.

(3) Lüssem, B.; Keum, C. M.; Kasemann, D.; Naab, B.; Bao, Z.; Leo, K. Doped Organic Transistors. *Chem. Rev.* **2016**, *116* (22), 13714–13751.

(4) Tam, T. L. D.; Xu, J. Strategies and Concepts in N-Doped Conjugated Polymer Thermoelectrics. *J. Mater. Chem. A* **2021**, *9* (9), 5149–5163.

(5) Yan, H.; Manion, J. G.; Yuan, M.; García de Arquer, F. P.; McKeown, G. R.; Beaupré, S.; Leclerc, M.; Sargent, E. H.; Seferos, D. S. Increasing Polymer Solar Cell Fill Factor by Trap-Filling with F4-TCNQ at Parts Per Thousand Concentration. *Adv. Mater.* **2016**, *28* (30), 6491–6496.

(6) Goel, M.; Thelakkat, M. Polymer Thermoelectrics: Opportunities and Challenges. *Macromolecules* **2020**, *53* (10), 3632–3642.

(7) Zhang, F.; Di, C. Exploring Thermoelectric Materials from High Mobility Organic Semiconductors. *Chem. Mater.* **2020**, *32* (7), 2688–2702.

(8) Sommer, M. Development of Conjugated Polymers for Organic Flexible Electronics. In *Organic Flexible Electronics*; Cosseddu, P., Caironi, M. B. T.-O. F. E., Eds.; Woodhead Publishing, 2021; pp 27–70.

(9) Zhang, Y.; Zhou, H.; Seifter, J.; Ying, L.; Mikhailovsky, A.; Heeger, A. J.; Bazan, G. C.; Nguyen, T.-Q. Molecular Doping Enhances Photoconductivity in Polymer Bulk Heterojunction Solar Cells. *Adv. Mater.* **2013**, *25* (48), 7038–7044.

(10) Russ, B.; Glaudell, A.; Urban, J. J.; Chabinyc, M. L.; Segalman, R. A. Organic Thermoelectric Materials for Energy Harvesting and Temperature Control. *Nat. Rev. Mater.* **2016**, *1* (10), 16050.

(11) Snyder, G. J.; Toberer, E. S. Complex Thermoelectric Materials. *Nat. Mater.* **2008**, *7* (2), 105–114.

(12) Zhao, W.; Ding, J.; Zou, Y.; Di, C. A.; Zhu, D. Chemical Doping of Organic Semiconductors for Thermoelectric Applications. *Chem. Soc. Rev.* **2020**, *49* (20), 7210–7228.

(13) Kroon, R.; Mengistie, D. A.; Kiefer, D.; Hynynen, J.; Ryan, J. D.; Yu, L.; Müller, C. Thermoelectric Plastics: From Design to Synthesis, Processing and Structure-Property Relationships. *Chem. Soc. Rev.* **2016**, *45* (22), 6147–6164.

(14) Jacobs, I. E.; Moulé, A. J. *Controlling Molecular Doping in Organic Semiconductors*. *Advanced Materials*. 2017.

(15) Scholes, D. T.; Hawks, S. A.; Yee, P. Y.; Wu, H.; Jeffrey, R.; Tolbert, S. H.; Schwartz, B. J.; Lindemuth, J. R.; Tolbert, S. H.; Schwartz, B. J. Overcoming Film Quality Issues for Conjugated Polymers Doped with F4TCNQ by Solution Sequential Processing: Hall Effect, Structural, and Optical Measurements. *J. Phys. Chem. Lett.* **2015**, *6* (23), 4786–4793.

(16) Jacobs, I. E.; Aasen, E. W.; Oliveira, J. L.; Fonseca, T. N.; Roehling, J. D.; Li, J.; Zhang, G.; Augustine, M. P.; Mascal, M.; Moulé, A. J. Comparison of Solution-Mixed and Sequentially Processed P3HT:F4TCNQ Films: Effect of Doping-Induced Aggregation on Film Morphology. *J. Mater. Chem. C* **2016**, *4* (16), 3454–3466.

(17) Hynynen, J.; Kiefer, D.; Yu, L.; Kroon, R.; Munir, R.; Amassian, A.; Kemerink, M.; Müller, C. Enhanced Electrical Conductivity of Molecularly P-Doped Poly(3-Hexylthiophene) through Understanding the Correlation with Solid-State Order. *Macromolecules* **2017**, *50* (20), 8140–8148.

(18) Patel, S. N.; Glaudell, A. M.; Kiefer, D.; Chabinyc, M. L. Increasing the Thermoelectric Power Factor of a Semiconducting Polymer by Doping from the Vapor Phase. *ACS Macro Lett.* **2016**, *5* (3).

(19) Lim, E.; Peterson, K. A.; Su, G. M.; Chabinyc, M. L. Thermoelectric Properties of Poly(3-Hexylthiophene) (P3HT) Doped with 2,3,5,6-Tetrafluoro-7,7,8,8-Tetracyanoquinodimethane (F4TCNQ) by Vapor-Phase Infiltration. *Chem. Mater.* **2018**, *30* (3), 998–1010.

(20) Li, J.; Zhang, G.; Holm, D. M.; Jacobs, I. E.; Yin, B.; Stroeve, P.; Mascal, M.; Moulé, A. J. Introducing Solubility Control for Improved Organic P-Type Dopants. *Chem. Mater.* **2015**, *27* (16), 5765–5774.

(21) Kiefer, D.; Kroon, R.; Hofmann, A. I.; Sun, H.; Liu, X.; Giovannitti, A.; Stegerer, D.; Cano, A.; Hynynen, J.; Yu, L.; Zhang, Y.; Nai, D.; Harrelson, T. F.; Sommer, M.; Moulé, A. J.; Kemerink, M.; Marder, S. R.; McCulloch, I.; Fahlman, M.; Fabiano, S.; Müller, C. Double Doping of Conjugated Polymers with Monomer Molecular Dopants. *Nat. Mater.* **2019**, *18* (2), 149–155.

(22) Patel, S. N.; Glaudell, A. M.; Peterson, K. A.; Thomas, E. M.; O'Hara, K. A.; Lim, E.; Chabinyc, M. L. Morphology Controls the Thermoelectric Power Factor of a Doped Semiconducting Polymer. *Sci. Adv.* **2017**, *3* (6), e1700434.

(23) Dong, B. X.; Nowak, C.; Onorato, J. W.; Ma, T.; Niklas, J.; Poluektov, O. G.; Grocke, G.; DiTusa, M. F.; Escobedo, F. A.; Luscombe, C. K.; Nealey, P. F.; Patel, S. N. Complex Relationship between Side-Chain Polarity, Conductivity, and Thermal Stability in Molecularly Doped Conjugated Polymers. *Chem. Mater.* **2021**, *33* (2), 741–753.

(24) Hu, P.; Du, K.; Wei, F.; Jiang, H.; Kloc, C. Crystal Growth, HOMO-LUMO Engineering, and Charge Transfer Degree in Perylene-FxTCNQ (x = 1, 2, 4) Organic Charge Transfer Binary Compounds. *Cryst. Growth Des.* **2016**, *16* (5), 3019–3027.

(25) Glaudell, A. M.; Cochran, J. E.; Patel, S. N.; Chabinyc, M. L. Impact of the Doping Method on Conductivity and Thermopower in Semiconducting Polythiophenes. *Adv. Energy Mater.* **2015**, *5* (4).

(26) Dongmin Kang, S.; Jeffrey Snyder, G. Charge-Transport Model for Conducting Polymers. *Nat. Mater.* **2017**, *16* (2), 252–257.

(27) Watanabe, S.; Ohno, M.; Yamashita, Y.; Terashige, T.; Okamoto, H.; Takeya, J. Validity of the Mott Formula and the Origin of Thermopower in π-Conjugated Semicrystalline Polymers. *Phys. Rev. B* **2019**, *10* (24), 241201.

(28) Boyle, C. J.; Upadhyaya, M.; Wang, P.; Renna, L. A.; Lu-Díaz, M.; Pyo Jeong, S.; Hight-Huf, N.; Korugic-Karasz, L.; Barnes, M. D.; Aksamija, Z.; Venkataraman, D. Tuning Charge Transport Dynamics via Clustering of Doping in Organic Semiconductor Thin Films. *Nat. Commun.* **2019**, *10* (1), 2827.

(29) Gregory, S. A.; Hanus, R.; Atassi, A.; Rinehart, J. M.; Wooding, J. P.; Menon, A. K.; Losego, M. D.; Snyder, G. J.; Yee, S. K. Quantifying Charge Carrier Localization in Chemically Doped Semiconducting Polymers. *Nat. Mater.* **2021**.

(30) Thomas, E. M.; Popere, B. C.; Fang, H.; Chabinyc, M. L.; Segalman, R. A. Role of Disorder Induced by Doping on the Thermoelectric Properties of Semiconducting Polymers. *Chem. Mater.* **2018**, *30* (9), 2965–2972.

(31) Mott, N. F.; Davis, E. A. *Electronic Processes in Materials*; Oxford Classic Texts in the Physical Sciences; OUP Oxford, 1963; Vol. 276.

(32) Kang, K.; Schott, S.; Venkateshvaran, D.; Broch, K.; Schweicher, G.; Harkin, D.; Jellett, C.; Nielsen, C. B.; McCulloch, I.; Sirringhaus, H. Investigation of the Thermoelectric Response in Conducting Polymers Doped by Solid-State Diffusion. *Mater. Today Phys.* **2019**, *8*, 112–122.

(33) Lee, Y.; Park, J.; Son, J.; Woo, H. Y.; Kwak, J. Degenerately Doped Semi-Crystalline Polymers for High Performance Thermoelectrics. *Adv. Funct. Mater.* **2021**, *31* (9), 2006900.

(34) Abutaha, A.; Kumar, P.; Yildirim, E.; Shi, W.; Yang, S. W.; Wu, G.; Hippalgaonkar, K. Correlating Charge and Thermoelectric Transport to Paracrystallinity in Conducting Polymers. *Nat. Commun.* **2020**, *11* (1), 1737.

(35) Tanaka, H.; Kanahashi, K.; Takekoshi, N.; Mada, H.; Ito, H.; Shimoi, Y.; Ohta, H.; Takenobu, T. Thermoelectric Properties of a Semicrystalline Polymer Doped beyond the Insulator-to-Metal Transition by Electrolyte Gating. *Sci. Adv.* **2020**, *6* (7), eaay8065.

(36) Kroon, R.; Kiefer, D.; Stegerer, D.; Yu, L.; Sommer, M.; Müller, C. Polar Side Chains Enhance Processability, Electrical Conductivity, and Thermal Stability of a Molecularly p-Doped Polythiophene. *Adv. Mater.* **2017**, *29* (24).

(37) Li, J.; Rochester, C. W.; Jacobs, I. E.; Aasen, E. W.; Friedrich, S.; Stroeve, P.; Moulé, A. J. The Effect of Thermal Annealing on Dopant Site Choice in Conjugated Polymers. *Org.*

Electron. physics, Mater. Appl. **2016**, *33*, 23–31.

(38) Flagg, L. Q.; Bischak, C. G.; Onorato, J. W.; Rashid, R. B.; Luscombe, C. K.; Ginger, D. S. Polymer Crystallinity Controls Water Uptake in Glycol Side-Chain Polymer Organic Electrochemical Transistors. *J. Am. Chem. Soc.* **2019**, *141* (10), 4345–4354.

(39) Meng, B.; Liu, J.; Wang, L. Oligo(Ethylene Glycol) as Side Chains of Conjugated Polymers for Optoelectronic Applications. *Polym. Chem.* **2020**, *11* (7), 1261–1270.

(40) Finn, P. A.; Jacobs, I. E.; Armitage, J.; Wu, R.; Paulsen, B. D.; Freeley, M.; Palma, M.; Rivnay, J.; Sirringhaus, H.; Nielsen, C. B. Effect of Polar Side Chains on Neutral and P-Doped Polythiophene. *J. Mater. Chem. C* **2020**, *8* (45), 16216–16223.

(41) Schmode, P.; Savva, A.; Kahl, R.; Ohayon, D.; Meichsner, F.; Dolynchuk, O.; Thurn-Albrecht, T.; Inal, S.; Thelakkat, M. The Key Role of Side Chain Linkage in Structure Formation and Mixed Conduction of Ethylene Glycol Substituted Polythiophenes. *ACS Appl. Mater. Interfaces* **2020**.

(42) Dong, B. X.; Nowak, C.; Onorato, J. W.; Strzalka, J.; Escobedo, F. A.; Luscombe, C. K.; Nealey, P. F.; Patel, S. N. Influence of Side-Chain Chemistry on Structure and Ionic Conduction Characteristics of Polythiophene Derivatives: A Computational and Experimental Study. *Chem. Mater.* **2019**, *31* (4), 1418–1429.

(43) Wegner, B.; Lungwitz, D.; Mansour, A. E.; Tait, C. E.; Tanaka, N.; Zhai, T.; Duhm, S.; Forster, M.; Behrends, J.; Shoji, Y.; Opitz, A.; Scherf, U.; List-Kratochvil, E. J. W.; Fukushima, T.; Koch, N. An Organic Borate Salt with Superior P-Doping Capability for Organic Semiconductors. *Adv. Sci.* **2020**, *7* (17), 2001322.

(44) Scholes, D. T.; Yee, P. Y.; McKeown, G. R.; Li, S.; Kang, H.; Lindemuth, J. R.; Xia, X.; King, S. C.; Seferos, D. S.; Tolbert, S. H.; Schwartz, B. J. Designing Conjugated Polymers for Molecular Doping: The Roles of Crystallinity, Swelling, and Conductivity in Sequentially-Doped Selenophene-Based Copolymers. *Chem. Mater.* **2019**, *31* (1), 73–82.

(45) Gordon, M. P.; Gregory, S. A.; Wooding, J. P.; Ye, S.; Su, G. M.; Seferos, D. S.; Losego, M. D.; Urban, J. J.; Yee, S. K.; Menon, A. K. Microstructure and Heteroatom Dictate the Doping Mechanism and Thermoelectric Properties of Poly(Alkyl-Chalcogenophenes). *Appl. Phys. Lett.* **2021**, *118* (23), 233301.

(46) Gregory, S. A.; Ponder, J. F.; Pittelli, S. L.; Losego, M. D.; Reynolds, J. R.; Yee, S. K. Thermoelectric and Charge Transport Properties of Solution-Processable and Chemically Doped Dioxythienothiophene Copolymers. *ACS Appl. Polym. Mater.* **2021**, *3* (5), 2316–2324.

(47) Lim, E.; Glaudell, A. M.; Miller, R.; Chabinyc, M. L. The Role of Ordering on the Thermoelectric Properties of Blends of Regioregular and Regiorandom Poly(3-Hexylthiophene). *Adv. Electron. Mater.* **2019**, *5* (11), 1–11.

(48) Scholes, D. T.; Yee, P. Y.; Lindemuth, J. R.; Kang, H.; Onorato, J.; Ghosh, R.; Luscombe, C. K.; Spano, F. C.; Tolbert, S. H.; Schwartz, B. J. The Effects of Crystallinity on Charge

Transport and the Structure of Sequentially Processed F4TCNQ-Doped Conjugated Polymer Films. *Adv. Funct. Mater.* **2017**, *27* (44), 1–13.

(49) Ma, T.; Kent, W.; Dong, B. X.; Grocke, G. L.; Patel, S. N. Continuously Graded Doped Semiconducting Polymers Enhance Thermoelectric Cooling. *Appl. Phys. Lett.* **2021**, *119* (1), 13902.

(50) Ma, T.; Dong, B. X.; Grocke, G. L.; Strzalka, J.; Patel, S. N. Leveraging Sequential Doping of Semiconducting Polymers to Enable Functionally Graded Materials for Organic Thermoelectrics. *Macromolecules* **2020**, *53* (8), 2882–2892.

(51) Wood, S.; Hollis, J. R.; Kim, J.-S. Raman Spectroscopy as an Advanced Structural Nanoprobe for Conjugated Molecular Semiconductors. *J. Phys. D. Appl. Phys.* **2017**, *50* (7), 73001.

(52) Tsoi, W. C.; James, D. T.; Kim, J. S.; Nicholson, P. G.; Murphy, C. E.; Bradley, D. D. C.; Nelson, J.; Kim, J. S. The Nature of In-Plane Skeleton Raman Modes of P3HT and Their Correlation to the Degree of Molecular Order in P3HT:PCBM Blend Thin Films. *J. Am. Chem. Soc.* **2011**, *133* (25), 9834–9843.

(53) Chew, A. R.; Ghosh, R.; Shang, Z.; Spano, F. C.; Salleo, A. Sequential Doping Reveals the Importance of Amorphous Chain Rigidity in Charge Transport of Semi-Crystalline Polymers. *J. Phys. Chem. Lett.* **2017**, *8* (20), 4974–4980.

(54) Fujimoto, R.; Yamashita, Y.; Kumagai, S.; Tsurumi, J.; Hinderhofer, A.; Broch, K.; Schreiber, F.; Watanabe, S.; Takeya, J. Molecular Doping in Organic Semiconductors: Fully Solution-Processed, Vacuum-Free Doping with Metal-Organic Complexes in an Orthogonal Solvent. *J. Mater. Chem. C* **2017**, *5* (46), 12023–12030.

(55) DeLongchamp, D. M.; Kline, R. J.; Lin, E. K.; Fischer, D. A.; Richter, L. J.; Lucas, L. A.; Heeney, M.; McCulloch, I.; Northrup, J. E. High Carrier Mobility Polythiophene Thin Films: Structure Determination by Experiment and Theory. *Adv. Mater.* **2007**, *19* (6), 833–837.

(56) Northrup, J. E. Atomic and Electronic Structure of Polymer Organic Semiconductors: P3HT, PQT, and PBTTT. *Phys. Rev. B - Condens. Matter Mater. Phys.* **2007**, *76* (24), 245202.

(57) Pingel, P.; Zhu, L.; Park, K. S.; Vogel, J. O.; Janietz, S.; Kim, E. G.; Rabe, J. P.; Brédas, J. L.; Koch, N. Charge-Transfer Localization in Molecularly Doped Thiophene-Based Donor Polymers. *J. Phys. Chem. Lett.* **2010**.

(58) Bredas, J. L.; Street, G. B. Polarons, Bipolarons, and Solitons in Conducting Polymers. *Acc. Chem. Res.* **1985**, *18* (10), 309–315.

(59) Liang, Z.; Ho Choi, H.; Luo, X.; Liu, T.; Abtahi, A.; Shantini Ramasamy, U.; Andrew Hitron, J.; Baustert, K. N.; Hempel, J. L.; Boehm, A. M.; Ansary, A.; Strachan, D. R.; Mei, J.; Risko, C.; Podzorov, V.; Graham, K. R. N-Type Charge Transport in Heavily p-Doped Polymers. *Nat. Mater.*

Chapter 7: CONCLUSION

The research in this dissertation were designed and conducted in the aim of enabling organic functionally graded materials by leveraging molecularly doped semiconducting conjugated polymers. The findings in this thesis showcase creative strategies to tailor the thermoelectric properties across the length of polymer film, e.g. formation of dopant compositional and microstructure gradients, and provide guidelines on utilizing functionally graded polymer films to enhance the TE performance, especially in the case of cooling applications.

In Chapter 2, we present a facile process in fabricating the first organic FG polymer film, symmetric double-segmented PBTTT thin films where each segment is sequentially doped with molecular dopant F4TCNQ from the vapor phase. The approach for this study employs compositional control of the F4TCNQ to modulate doping level (carrier concentration) within each macroscopic segment. This work showcases how sequential vapor doping is an enabling technique for applying the principles of functional grading for organic thermoelectrics. By design, the focus of the work is not motivated by device optimization but centered around a fundamental understanding of spatial structure-transport properties of molecularly doped semiconducting polymers through double-segmented thin films. Chapter 3 reports on continuously graded thin films relevant to improved thermoelectric (Peltier) cooling. Spatial compositional control of the F4TCNQ in PBTTT yield 1D profiles in σ and α. Moreover, first principle calculations based on linear Onsager theory and conservation of charge and energy are used to model the cooling performance using the experimentally derived σ and α spatial profiles. The grading σ and α

profiles allow for efficient redistribution of the Joule heating and Peltier cooling effects to improve cooling compared to equivalent uniform films.

In Chapter 4, we study the structural and transport properties of a molecularly doped thiophene-based polymer, PQT, upon thermal annealing. Polymorphism is observed in PQT resulting from different phase transitions, where polymorphs with interdigitated side-chains coexist. The interdigitation of side-chain significantly affects the doping efficiency, which leads to a large variation in thermoelectric properties upon vapor doping with F4TCNQ. Chapter 5 follows the work from the previous chapter and realize spatial gradient in σ and α by tuning the morphology of PQT. The variation in morphology is achieved by apply a temperature gradient across the polymer film, which is captured directly through IR imaging. The cooling performance of the graded PQT film is predicted and compared with the uniform equivalent. In Chapter 6, we investigate the thermoelectric properties of a polythiophene derivatives with polar side-chain, P3MEET, doped with FnTCNQ (n = 1, 2 and 4). A combination of X-ray scattering and spectroscopy (UV-Vis and Raman) indicated that both crystalline and amorphous regions of the polymer are doped. Kang-Snyder transport model is used to modele the α-σ relationship of our FnTCNQ-doped P3MEET films where s = 1 was found to give the best fit. Despite having the lowest EA, films doped with F1TCNQ were found to have the highest average mobility, resulting from less carriers generated in the amorphous region, which eventually led to an optimized PF. Our findings illustrate the importance of understanding the role of crystalline and amorphous domains in charge transport studies on existing and designing molecularly doped semiconducting polymers.

Moving forward, the fundamental investigation in $\alpha - \sigma$ relationship of conjugated polymers will benefit the design of future molecularly doped CPs by leveraging the charge transport models. During my PhD, I have conducted hundreds of conductivity and Seebeck

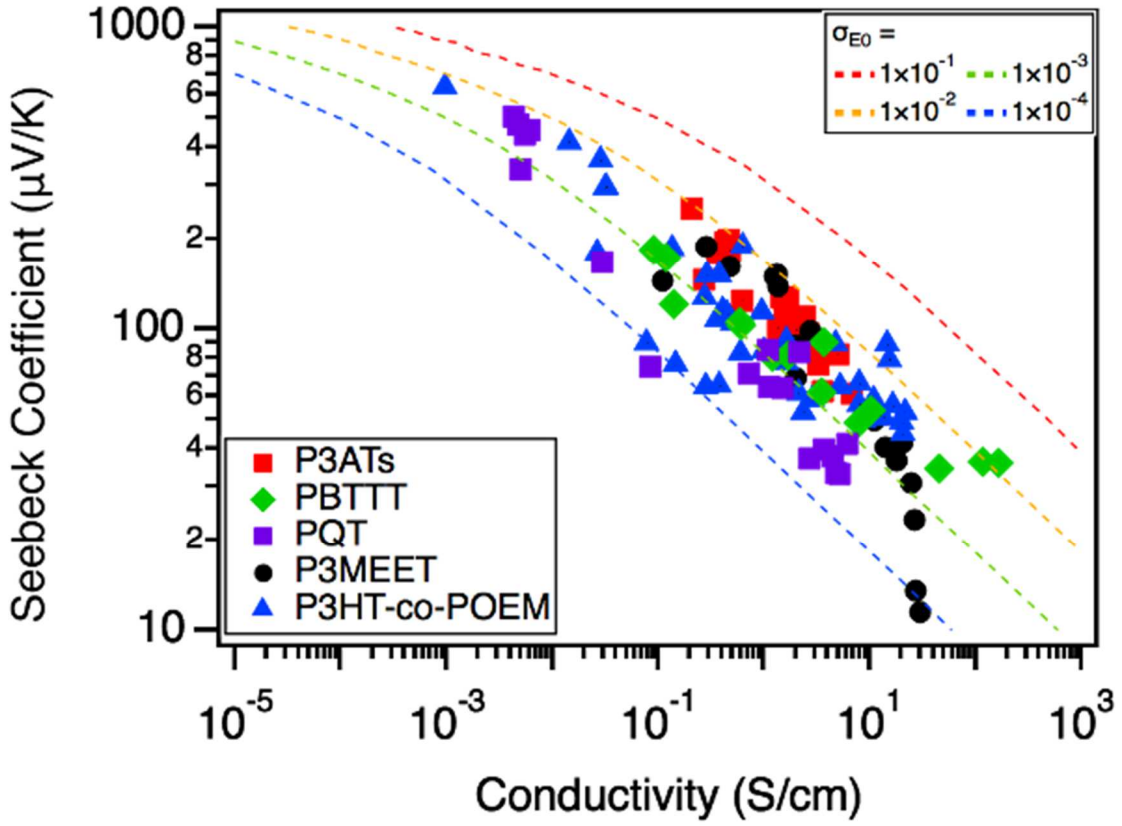

Figure 7.1: Compilation of Seebeck coefficient vs conductivity data collected: FnTCNQ (n = 1, 2 or 4) doped P3ATs (red square, A = B, H, O, D or DD), PBTTT (green diamond), PQT (purple square), P3MEET (black circle) and copolymer, P3HT-co-POEM (blue triangle). The dashed lines represent for fits generated from Kang-Snyder transport model with s = 3 and the values of σ_{E0} ranging from 1×10^{-4} S/cm to 1×10^{-1} S/cm.

coefficient measurements for variety of semiconducting CPs, particularly polythiophene-based polymers, including P3ATs (P3BT, P3HT, P3OT and P3DDT), PBTTT, PQT, P3MEET and copolymer P3HT-POEM. By collecting and organizing the whole database, it helps to directly visualize the $\alpha - \sigma$ relationship of these conjugated polymers as shown in Figure 7.1. The dash lines calculated from Kang-Snyder model and shift up with increasing σ_{E0}, indicating improved

relative carrier mobility. Generally speaking, the model fits well over the full range of our data, covering over 6 orders of magnitude in σ values and 3 orders in α values. By understanding the correlation between α and σ allows us to design the future functional grading motifs more precisely by tailoring the values and profiles of conductivity and Seebeck coefficient.